CHARACTERIZATION AND MODELING OF THE FUNDAMENTAL ASPECTS OF OIL TRANSPORT IN THE PISTON RING PACK OF INTERNAL COMBUSTION ENGINES

by

Benoist Thirouard

M.S., Engines (1996)
Ecole Nationale Supérieure du Pétrole et des Moteurs, Paris

DEA, Energy Conversion (1995)
Université Paris VI

Engineering Degree, Mechanics (1995)
Ecole Supérieure de l'Energie et des Matériaux, Orléans

BARKER

MASSACHUSETTS INSTITUTE OF TECHNOLOGY
JUL 16 2001
LIBRARIES

Submitted to the Department of Mechanical Engineering
in Partial Fulfillment of the Requirements for the Degree of

DOCTOR OF PHILOSOPHY

at the
MASSACHUSETTS INSTITUTE OF TECHNOLOGY

June 2001

© Massachusetts Institute of Technology
All Rights Reserved

Signature of the Author.....
Department of Mechanical Engineering
June 2001

Certified by.....
Douglas P. Hart
Associate Professor, Department of Mechanical Engineering
Thesis Supervisor

Accepted by.....
Ain A. Sonin
Chairman, Department Committee on Graduate Studies

CHARACTERIZATION AND MODELING OF THE FUNDAMENTAL ASPECTS OF OIL TRANSPORT IN THE PISTON RING PACK OF INTERNAL COMBUSTION ENGINES

by

Benoist Thirouard

Submitted to the Department of Mechanical Engineering
on May 10, 2001
in Partial Fulfillment of the Requirements
for the Degree of Doctor of Philosophy

ABSTRACT

Engine oil consumption is one of the primary interests for the automotive industry in controlling emissions and reducing service cost. Due to a lack of understanding of the mechanisms of oil transport along the piston, reducing oil consumption from the ring pack of internal combustion engines has been extremely challenging for engine manufacturers and suppliers. This work addressed the fundamental aspects of oil transport in the piston ring pack through experiments and modeling.

A two-dimensional multiple-dye Laser-Induced Fluorescence (LIF) visualization system was successfully implemented in a diesel and a spark-ignition engine. Real time high resolution images of the ring pack oil distribution were acquired and analyzed for the entire range of operating conditions typically encountered by passenger car engines.

Based on experimental observations, major oil flow patterns in the piston ring pack were identified and characterized. Physically based models were proposed to describe each individual oil transport process, such as, oil flows on the piston lands in both axial and circumferential directions and oil flows through the ring grooves and gaps. Modeling results showed good agreement with the experimental data.

Then, using the individual oil transport models, the contributions of the different oil transport mechanisms to oil flow in and between the piston regions and the effects of piston and ring designs were analyzed. Finally, a global oil transport scheme was presented by integrating all major paths and mechanisms of oil transport along the piston. It highlighted that the rate at which oil is lost to the combustion chamber is mostly determined by the competing oil transport processes occurring on the piston lands. While the effect of the inertia force results in a net oil flow toward the top of the piston, the dragging action of the blow-by gases removes oil from the piston lands and recycles it to the crankcase.

This work was the first comprehensive investigation of the mechanisms of oil transport in the piston ring pack of internal combustion engines. It constitutes a major step in the development of analytical tools for oil consumption reduction.

Thesis Supervisor: Douglas P. Hart
Title: Associate Professor, Department of Mechanical Engineering

ACKNOWLEGMENTS

I would like to thank my committee members for their guidance and constructive advice. In particular, I would like to thank Professor Douglas Hart, my advisor, and Professor John Heywood, Director of the Sloan Automotive Laboratory, for giving me the opportunity to conduct my doctoral studies at MIT. Furthermore, I would like to express the most special thanks to Tian Tian who has contributed to every part of my work at MIT. Tian Tian has been involved in my doctoral research as one of my committee members, as an everyday advisor and most importantly as a supportive friend. Among other things, I would like to thank Tian for his encouragement through the easy and most meaningfully the difficult and stressful moments. I would also like to thank Tian for his everyday inputs from which I gained insights on how to apply scientific knowledge to engineering problems. Not only Tian has been a key contributor to this project but he also taught me how to get the best out of my stay at MIT and has been the most supportive friend during the four and a half years spent in the Sloan Lab.

I would like to use this opportunity to thank the people from the industry sponsors of this project. First of all, I would like to thanks people from PSA Peugeot Citroen for their continuing and extensive support in this project. Especially, I would like to thank the PSA Research Department for providing the prototype single-cylinder research engine that was used to build the unique testing facility used in this project. I would like to express special thanks to Bernard Cousyn who gave me the opportunity to go to MIT as a visiting engineer and who strongly supported this project by encouraging PSA contribution to the Lubrication Consortium. I am particularly thankful to Bernard for his trust and very valuable advice. Inside PSA, I would also like to thank Thierry Duverger for dedicating part of his time to the design and assembly of the prototype engine and Jacques Theron for his expertise in the design of the optical access and the cooling jacket. I would also like to thanks Nick Lee for his help and support in this project. Eventually, I would like to thanks Nicolas Charollais, who have been a very supportive friend, for his very valuable inputs on engine control.

I would like to express special thanks to Rémi Rabuté from Perfect Circle Europe (Dana Corp.), not only for his numerous and pertinent technical inputs and suggestions but also for his strong support in this project and its friendship. I also would like to thank Rémi Rabuté for supplying prototype rings for both engines used in this work. I would like to thank Steve Systma, Kim Karrip and Randy Lunsford from Dana Corp. for their technical inputs. I would also like to thank Dr Mokhtar Maamouri from Renault for its valuable inputs and numerous advice, Adam Bloomberg, Frederick Stromstedt, Jonas Rick, and Bengt Olsson from Volvo for their support and interest in the project. Eventually, I would like to thank Mr. Kopf and Mr. Fiedler from Mahle GmbH for their technical expertise.

I would like to thank Dr. Victor Wong, Sloan Lab Manager, for his support and his help. Among the supporting staff, I would like to thank Brian Corkum, Pete Menard, John Baron and Thane Dewitt for their technical help and advice, and Nancy Cook, Suzanne Lutin and Karla Striker for their help and pleasant conversations. Eventually, I would like to express my gratitude to Leslie Reagan for the tremendous help she provides to the students of the Mechanical Engineering Department.

Among the graduate students and visiting engineers with whom I have shared time in the Sloan Lab I would like to thank Mark Kiesel from Caterpillar and Pierre Mulgrave for designing the optical access in the Kubota engine. I would like to express special thanks to Ertan Yilmaz, Bertrand Lecointe, Gerald Chamarre, Conor McNally and Liang Liu for their technical contribution and most importantly for making my time at MIT both enjoyable and fulfilling.

My stay at MIT has constituted my first experience of living abroad, away from my family and my friends at home with whom I had shared much of my free time in the past. Many persons outside the Sloan Lab have in their way contributed to make this experience unique and enjoyable. Among others I want to thank Booke Noordjig, Geoffrey Adams, Nicolai Cauchy, Mehri Sater, Marie-Laure Grillet, Steve Patterson, Michael Boccara, Micha Wiegel and Cornelius O'Sullivan. I also would like to express special thanks to my friends at home for their continuous esteem. Eventually, I want to thanks my family and especially my parents for their encouragement, trust and support.

This work was sponsored by the Consortium on Lubrication in Internal Combustion Engines, whose current members are Dana Corporation, Mahle GmbH, PSA Peugeot Citroën, Renault SA and Volvo.

Benoist Thirouard, June 2001.

TABLES OF CONTENTS

Abstract 2
Acknowledgments 3
Tables of Contents 4
List of Figures 8
List of Tables 14

CHAPTER 1. INTRODUCTION 18
1.1 Background 18
1.2 Lubrication versus Oil Consumption: Oil Transport 19
1.3 Related Previous Work 20
1.4 Thesis Objectives and Approach 21

CHAPTER 2. EXPERIMENTAL SETUP 22
2.1 Experimental Strategy 22
2.1.1 Experimental objectives 22
2.1.2 Measurement and diagnostic choices 22
2.1.3 Times scales 23
2.2 Experiments Configurations 25
2.2.1 Engine operating conditions 25
2.2.2 Window positions 27
2.2.3 Ring gap positions 28
2.2.4 Ring designs 31
2.3 Engines and Optical Access Design 34
2.3.1 The Kubota engine 34
2.3.1.1 Engine characteristics 34
2.3.1.2 Optical access 34
2.3.2 The PSA single-cylinder engine 36
2.3.2.1 Engine characteristics 36
2.3.2.2 Optical access and window design 37
2.3.2.3 Cooling system design 40
2.3.2.4 Lubrication system 40

2.4 Diagnostics 42
2.4.1 Laser-Induced Fluorescence 42
2.4.1.1 Principle 42
2.4.1.2 Theory 43
2.4.1.3 Application 47
2.4.2 Calibration of the LIF signal 48
2.4.2.1 Temperature effect 36
2.4.2.2 Calibration challenges 49
2.4.2.3 Dual emission LIF technique 54
2.4.2.4 Dual emission calibration (applied in the Kubota engine) 60
2.4.2.5 Improved in-situ calibration (applied in the PSA engine) 64
2.4.3 Imaging system 71
2.4.3.1 Laser 72
2.4.3.2 Detection device 73
2.4.3.3 Control and timing 75
2.4.3.4 Complete optical setup 77
2.4.4 Blow-by measuring system 78
2.4.4.1 Challenges 78
2.4.4.2 Dampening system 80
2.4.4.3 Blow-by flowmeter 83

CHAPTER 3. CHARACTERIZATION OF OIL TRANSPORT MECHANISMS 85
3.1 Oil Transport on the Piston Lands 85
3.1.1 Inertia driven oil transport 85
3.1.1.1 Observation and description 85
3.1.1.2 Modeling 96
3.1.1.3 Results analysis 102
3.1.1.4 3-Dimensional aspects 111
3.1.2 Gas flow driven circumferential oil transport 115
3.1.2.1 Observations and description 115
3.1.2.2 Modeling 123
3.1.2.3 Effect of gas flow dragging on the uniformity of the oil layer 130
3.1.2.4 Effect of the uniformity of the oil layer on the oil transport rate 133
3.1.2.5 Practical results 137

3.1.3 Gas flow driven axial oil transport 145
3.1.3.1 Effect of the axial gas flow resulting from the piston/liner relative motion 146
3.1.3.2 Effect of gas exchange with the ring grooves and with adjacent lands 149
3.2 Oil Transport between the Liner and the Piston Lands 152
3.2.1 Ring scraping 152
3.2.1.1 Description 152
3.2.1.3 Scraping observations 153
3.2.1.4 Implications for oil transport on the piston 154
3.2.2 Oil release 155
3.2.2.1 Observations 155
3.2.2.2 Description 158
3.2.2.3 Implications for oil transport 159
3.3 Oil Transport Through the Ring Groove 161
3.3.1 Oil transport from the lands into the grooves 161
3.3.1.1 Ring pumping 163
3.3.1.2 Pressure gradient due the inertia force 168
3.3.1.3 Lateral motion of the piston relative to the rings 170
3.3.1.4 Dragging of the gas flow from the lands to the grooves 171
3.3.1.5 Conclusions 172
3.3.2 Oil transport from the grooves to the lands 173
3.3.2.1 Ring squeezing 173
3.3.2.2 Gas flow in the ring/groove clearances 178
3.3.3 Conclusions 188
3.4 Oil Flow Through the Ring Gaps 189
3.4.1 Mechanisms 189
3.4.1.1 Gas driven flow 189
3.4.1.2 Inertia driven flow 195
3.4.2 Low load and closed throttle situations 196
3.4.2.1 Low load engine operation 196
3.4.2.2 Closed throttle situation 201

CHAPTER 4. OIL TRANSPOR ROUTES IN THE PISTON RING PACK 202
4.1 Dividing the Ring Pack Into Three Regions 202
4.2 Region 1: Controlling the Oil Supply to the Upper Ring Pack 204
4.2.1 Oil Supply

4.2.1.1 Twin-land oil control ring 205
4.2.1.2 Three-piece oil control ring 210
4.2.1.3 U-Flex oil control ring 211
4.2.1.4 Oil supply through the OCR gap 214
4.2.2 Internal Flow Pattern 214
4.2.2.1 Scraper ring with hook 215
4.2.2.2 Scraper ring without hook 218
4.2.2.3 Third land circumferential oil flow 219
4.2.3 Outward oil flows and net oil transports 219
4.2.3.1 Oil flow pass the OCR 220
4.2.3.2 Oil flow pass the scraper ring 223
4.3 Region2: Controlling the Oil Supply to the Top Ring Groove 228
4.3.1 Oil flows in and out of region 2 228
4.3.1.1 Through the second ring gap 228
4.3.1.2 From the second ring groove 229
4.3.1.3 To the top ring groove 229
4.3.1.4 Through the top ring gap 231
4.3.1.4 Top ring down scraping 232
4.3.2 Effect of the total amount of oil stored on the second land 233
4.3.2.1 Oil supply to the top ring groove lower clearance 233
4.3.2.2 Second land oil balance 234
4.4 Region 3: The Oil Consuming Region 240
4.4.1 Oil supply 241
4.4.2 Oil flow to the combustion chamber 242
4.5 Global Oil Transport Scheme 244
4.5.1 Reference case: Diesel engine and SI engines at high load 244
4.5.1.1 Upward oil transport 245
4.5.1.2 Downward oil transport 245
4.5.1.3 Occasional oil transport processes 245
4.5.1.4 Liquid oil consumption and main controlling points 246
4.5.2 SI engine running at low load and closed-throttle engine operation 247

CHAPTER 5. CONCLUSIONS 249
REFERENCES 253
ANNEX 1. 258
ANNEX 2. 259

LIST OF FIGURES

Figure 2.1	Kubota engine operating range and tested operating conditions	26
Figure 2.2	PSA single-cylinder engine operating range and tested operating conditions	27
Figure 2.3	Description of the transient test conducted in the PSA single-cylinder engine	27
Figure 2.4a	Ring pinned at the gap (method used in two-stroke engines)	29
Figure 2.4b	Ring pinned away from the gap (method used in this project)	29
Figure 2.5	Kubota engine – Description of the ring gap positions for the experiments conducted with top two ring pinned	30
Figure 2.6	PSA single-cylinder engine. Description of the ring gap positions for the experiments conducted with top two ring pinned.	30
Figure 2.7	Most commonly used ring designs for spark ignition and small diesel engines	32
Figure 2.8	Description of ring configurations tested on the Kubota engine	33
Figure 2.9	PSA single-cylinder engine. Description of the tested ring gap geometry	33
Figure 2.10	Dimension and position of the quartz window installed in the liner of the Kubota engine	35
Figure 2.11	Cooling jacket modification on the Kubota engine	36
Figure 2.12	Dimension and position of the sapphire window installed in the PSA engine	39
Figure 2.13	Cooling jacket design and clamping system in the PSA engine	39
Figure 2.14	Lubrication system of the PSA single-cylinder engine	41
Figure 2.15	Fluorescence process	41
Figure 2.16	Excitation and Absorption spectrum	43
Figure 2.17	Solid angle of fluorescence signal acquired	46
Figure 2.18	Example of Laser-Induced-Fluorescence image of the piston oil distribution (PSA engine – 3500 rpm 500 mbar – Intake stroke 33)	47
Figure 2.19	Piston operating temperatures in vehicle engines at full load. (Source: Mahle Mini Piston Manual)	49
Figure 2.20	Mineral oil oxidation (Source: IFP Lubricant Booklet)	50
Figure 2.21	Absorption and emission spectra for two dyes with small emission spectrum overlap and significant pumping effect	53
Figure 2.22	Absorption and emission spectra for two dyes with large emission spectrum overlap	53
Figure 2.23	Selection of potential dye combinations	58

Figure 2.24	Temperature response of Pyrro 567 (5.0 10^{-4} mol/liter) and Rhd 640 (2.0 10^{-4} mol/liter) while mixed together (Emission of Pyrro 567 measured at 570 nm with a 10 nm narrow-band filter, emission of Rhd 640 measured at 650 nm with a 10 nm narrow band filter)	59
Figure 2.25	Thickness and temperature response of Pyrro 567 (5.0 10^{-4} mol/liter) and Rhd 640 (2.0 10^{-4} mol/liter) while mixed together (Emission of Pyrro 567 measured at 570 nm with a 10 nm narrow-band filter, emission of Rhd 640 measured at 650 nm with a 10 nm narrow band filter).	59
Figure 2.26	Curves of iso-intensity of fluorescence emission for Pyrro 567 (5.0 10^{-4} mol/liter) and Rhd 640 (2.0 10^{-4} mol/liter) while mixed together (Emission of Pyrro 567 measured at 570 nm with a 10 nm narrow-band filter, emission of Rhd 640 measured at 650 nm with a 10 nm narrow band filter)	60
Figure 2.27	Oil film thickness profile calibrated with Dual Emission Fluorescence technique. Kubota engine – 1200 RPM No load – Expansion stroke	63
Figure 2.28	Evolution of absorptivity and quantum yield efficiency with temperature for Rhd 640 and Pyrro 567	65
Figure 2.29	Evolution of the function G (σ_{g1}.x)	67
Figure 2.30	Temperature response of Pyrro 567 (1.0 10^{-4} mol/liter) and Rhd 640 (1.0 10^{-4} mol/liter) while mixed together (Emission of Pyrro 567 measured at 570 nm with a 10 nm narrow-band filter, emission of Rhd 640 measured at 650 nm with a 10 nm narrow band filter)	68
Figure 2.31	Thickness and temperature response of Pyrro 567 (1.0 10^{-4} mol/liter) and Rhd 640 (1.0 10^{-4} mol/liter) while mixed together (Emission of Pyrro 567 measured at 570 nm with a 10 nm narrow-band filter, emission of Rhd 640 measured at 650 nm with a 10 nm narrow band filter)	69
Figure 2.32	Aspect of the oil layer on the piston lands with toll marks (shown for an average oil thickness of 30 μm)	70
Figure 2.33	Oil film thickness profile calibrated with Dual Emission Fluorescence technique. Kubota engine – 1200 RPM No load – Expansion stroke	70
Figure 2.34	Camera and laser timing	74
Figure 2.35	Example of burst acquisition for stroke to stroke oil distribution observation. (Using frame transfer mode)	75

Figure 2.36	Timing of the LIF images acquisition and video frame rate	76
Figure 2.37	Complete optical setup	77
Figure 2.38	Engine and acquisition control diagram	78
Figure 2.39	Blow-by oscillations due to the piston motion	79
Figure 2.40	Fourth order acoustic filter (Electrical analogy)	80
Figure 2.41	Designed acoustic filter (Components and dimensions)	81
Figure 2.42	Performance of the blow-by acoustic filter: attenuation of the flow oscillations	83
Figure 2.43	Performance of the blow-by acoustic filter: oscillations of the crankcase pressure	84
Figure 2.44	Blow-by meter design	84
Figure 3.1	Oil distribution on the piston lands of the Kubota engine, showing the effect of the inertia force on the second oil accumulation	86
Figure 3.2	Inertia force computed for the Kubota engine running at 1200 rpm (Timing of the LIF image acquisition)	86
Figure 3.3	Effect of the engine speed on the inertia-driven oil displacement	87
Figure 3.4	Effect of the volume of the oil accumulation on the inertia-driven displacement	88
Figure 3.5a	Cycle resolved evolution of the third land oil distribution, showing the effect of the inertia force (I)	89
Figure 3.5b	Cycle resolved evolution of the third land oil distribution, showing the effect of the inertia force (II)	90
Figure 3.6	Description of the parameters used for the thin film modeling	91
Figure 3.7	Description of the formation of a steep edge at the front of oil puddles	93
Figure 3.8	Formation of a steep edge at the front of oil puddles observed in the Kubota engine	94
Figure 3.9	Rolling-over process occurring a the front edge of oil puddles displaced by the inertia force	95
Figure 3.10	Puddle motion. Description of the oil flow and modeling approach	96
Figure 3.11	Description of the computation scheme used to determine the position of the front edge of puddles moving under the effect of the inertia force	98
Figure 3.12	Modeling of the spreading of an oil puddle undergoing the inertia force (Assumptions and results)	100
Figure 3.13	Computed evolution of the shape and position of a two-dimensional oil puddle with repeated oil supply	101

Figure 3.14	Comparison between the computed and measured axial distribution of the oil accumulated on the second land	103
Figure 3.15	Computed effect of the engine speed and oil volume on the distance traveled by the front edge of a two-dimensional puddle	103
Figure 3.16	Description of the inertia-driven oil transport across the piston lands (I)	105
Figure 3.17	Description of the inertia-driven oil transport across the piston lands (II)	106
Figure 3.18	Computed effect of the engine speed and oil volume on the maximum height of a two-dimensional puddle	107
Figure 3.19	Computed effect of the engine speed and oil volume on the aspect ratio of a two-dimensional puddle	108
Figure 3.20	Computed non-dimensional puddle width (The surface was generated with linear interpolation of the data points)	109
Figure 3.21	Computed non-dimensional puddle maximum height (The surface was generated with linear interpolation of the data points)	109
Figure 3.22	Surface showing the non-dimensional puddle width computed with the analytical function fitted to the data points obtained with the inertia-driven flow model	110
Figure 3.23	Surface showing the non-dimensional puddle maximum height computed with the analytical function fitted to the data points obtained with the inertia-driven flow model	110
Figure 3.24a	3-dimensional aspect of the third land oil distribution (I)	113
Figure 3.24b	3-dimensional aspect of the second land oil distribution(II)	114
Figure 3.25	Circumferential oil flow observed on the second land of the Kubota engine (I)	115
Figure 3.26	Circumferential oil flow observed on the second land of the Kubota engine (II)	116
Figure 3.27	Lands pressures and gas flow rate at the gaps in the Kubota engine at 1200 rpm 1N.m load (Results computed with RINGPACK-OC)	117
Figure 3.28	Circumferential oil transport observed on the second land of the PSA engine	117
Figure 3.29	Circumferential oil transport observed on the third land of the PSA engine	118
Figure 3.30	Circumferential oil transport observed on the second land of the PSA engine while the blow-by was negative	119
Figure 3.31	Description of the gas flow and oil profile used for modeling the dragging action of the blow-by gases	120
Figure 3.32	Wavy aspect of the second land oil layer (PSA engine – Compression stroke)	122
Figure 3.33	Wavy aspect of the second land oil layer (PSA engine – Expansion stroke)	123

Figure 3.34	Reynolds number and flow rate of the gas flow sweeping the second land (Calculated for the PSA engine with RINGPACK-OC)	124
Figure 3.35	Ratio of the convection and viscous dissipation terms for the gas sweeping the second land (Calculated for the PSA engine with RINGPACK-OC)	125
Figure 3.36	Definition of the piston land sectors	128
Figure 3.37	Definition of the two types of oil distribution used for the modeling of oil transport induced by the dragging action of the blow-by gases	129
Figure 3.38	Computed evolution of the shape and position of a two-dimensional oil puddle dragged by gas flow (Initial shape corresponding to the wave-type oil distribution)	131
Figure 3.39	Computed evolution of the shape and position of a two-dimensional oil puddle dragged by gas flow (Initial shape corresponding to the puddle-type oil distribution)	132
Figure 3.40	Computed evolution of the rate of oil transport with the cumulative volumetric gas flow (Initial puddle shape corresponding to the puddle-type oil distribution)	135
Figure 3.41	Computed evolution of the rate of oil transport with the cumulative volumetric gas flow (Initial puddle shape corresponding to the wave-type oil distribution)	136
Figure 3.42	Definition of the control volume for the evaluation of the second land circumferential oil distribution	138
Figure 3.43	Circumferential repartition of the oil around a piston land (second or third) plotted as a function of the relative positions of the ring gaps	139
Figure 3.44	Effect of the relative position of the top two ring gaps observed in the Kubota engine	140
Figure 3.45	Total volume of oil accumulated on a land plotted as a function of the relative positions of the gaps	141
Figure 3.46	Blow-by flow rate measured in the PSA engine and rate of the circumferential gas flows sweeping the second and third land (calculated with RINGPACK-OC)	143
Figure 3.47	Description of the axial gas flow induced by the piston/liner relative motion (secondary gas flow)	144
Figure 3.48	Comparison between oil displacement induced by the secondary gas flow and the inertia force	148

Figure 3.49	Scraping mechanism	152
Figure 3.50	Oil scraping by the upper land of the OCR observed in the PSA engine	154
Figure 3.51	Oil scraping by the scraper ring observed in the PSA engine	155
Figure 3.52	Oil release from the hook of the Napier ring observed in the PSA engine	156
Figure 3.53	Oil release from the hook of the Napier ring observe in the Kubota engine	157
Figure 3.54	Description of the oil release mechanism	157
Figure 3.55	Oil flow out of the ring grooves observed in the PSA engine (I)	162
Figure 3.56	Oil flow out of the ring grooves observed in the PSA engine (II).	163
Figure 3.57	Oil pumping and squeezing observed in the Kubota engine	164
Figure 3.58	Oil flow through the top ring groove following a sudden increase of the amount of oil on the second land	165
Figure 3.59	Ring lift and inertia force computed for the Kubota	166
Figure 3.60	Oil transport to the ring groove, timing of the inertia force and ring lift	166
Figure 3.61	Description of the oil transport into the ring groove resulting from the pressure gradient generated by the inertia force	168
Figure 3.62	Description of the oil transport into the ring groove resulting from the lateral motion of the piston relative to the rings	170
Figure 3.63	Main squeezing direction for inside and outside sealing configurations	174
Figure 3.64	Effect of the ring static twist on the rate of oil squeezing on both side of the ring (assuming rectangular groove).	174
Figure 3.65	Determination of the direction of the net oil transport through the ring groove (assuming that there is no ring flutter)	175
Figure 3.66	Instantaneous oil squeezing rate at the lower clearance of the top ring groove (Calculated with RINGPACK-OC for the PSA engine running at 2500 rpm 500 mbar)	177
Figure 3.67	Cycle-averaged oil squeezing rate at the lower clearance of the top ring groove (Calculated for the PSA engine running at 2500 rpm 500 mbar)	177
Figure 3.68	Computed rate of oil transports induced the dragging action of the blow-by gases in the side clearances of the top ring groove (Computed for the PSA engine)	180
Figure 3.69	Computed rate of oil transports induced the dragging action of the blow-by gases in the side clearances of the second ring groove (Computed for the PSA engine)	180

Figure 3.70	Computed rate of oil transports induced the dragging action of the blow-by gases in the upper side clearance of the OCR (Computed for the PSA engine)	181
Figure 3.71	Top and second ring lift computed for the PSA engine running at 2500 rpm 300 mbar. Left figure: average cylinder pressure trace and top ring groove oil filling 20%.Right figure: lower than average cylinder pressure trace and top ring groove oil filling 80%	181
Figure 3.72	Intermittent top ring fluttering observed in the PSA engine running at 2500 rpm 300 mbar	184
Figure 3.73	Oil flow through the second ring gap and mist formation observed in the Kubota engine	190
Figure 3.74	Left figure: width of the gas flow close to the gap. Right figure: description of the oil control volume used to compute the rate of oil transport at the gaps	191
Figure 3.75	OCR gap observed in the Kubota engine	192
Figure 3.76	Description of the gas-driven mechanism of oil transport through the ring gaps	193
Figure 3.77	Large oil accumulation observed above the OCR gap in the PSA engine running at low load	195
Figure 3.78	Top ring gap observed at low load in the PSA engine	197
Figure 3.79	Oil flow from the third to the second land observed at the second ring gap in the PSA engine running at low load (4500 rpm)	199
Figure 3.80	Oil flow from the third to the second land observed at the second ring gap in the PSA engine running at low load (2500 rpm)	200
Figure 3.81	Oil flow from the third to the second land observed at the second ring gap in the PSA engine running at low load (3500 rpm)	200
Figure 4.1	Definition of the ring pack regions	203
Figure 4.2	Piston tilt and land/liner clearances of the twin-land OCR, calculated for the PSA engine running at 2500 rpm 500-mbar intake pressure	206
Figure 4.3	Wetting conditions of the scraper ring when used with a twin-land OCR, calculated for the PSA engine at 2500 rpm 500-mbar intake pressure	207
Figure 4.4	Second ring scraping observed in the PSA engine	208
Figure 4.5	Second ring scraping observed in the Kubota engine	208
Figure 4.6	Effect of the twin-land OCR tension on the second and third land oil accumulation (observed in the Kubota engine)	209
Figure 4.7	Three-piece OCR side sealing	210

Figure 4.8	Oil squeezed from the OCR groove to the third land, observed in the Kubota engine while using a U-flex OCR	212
Figure 4.9	U-flex structure and deformation of the U-flex flanks	213
Figure 4.10	Oil transport from the third land to the hook of the Napier ring	216
Figure 4.11	Oil transport from the hook to the third land and to the liner (Observed in the PSA engine)	216
Figure 4.12	Oil and gas flows through gaps U-flex OCR	221
Figure 4.13	Effect of various OCR designs on oil transports between the upper skirt region and the third land region	222
Figure 4.14	Effect of the second ring/third land geometry on the second land oil accumulation (I)	223
Figure 4.15	Effect of the second ring/third land geometry on the second land oil accumulation (II)	224
Figure 4.16	Computed second ring lift for the Kubota engine running at 2000 rpm 35% load	225
Figure 4.17	Effect of various scraper ring design on oil transports in and out of the third land region	227
Figure 4.18	Description of top ring flutter and reverse flutter	230
Figure 4.19	Second land oil balance	236
Figure 4.20	Schematic description of engine speed and load effect on the second land oil balance	237
Figure 4.21	Effect of engine load on the second land oil accumulation (measured in the PSA engine)	238
Figure 4.22	Effect of engine speed on the second land oil balance (measured in the PSA engine)	239
Figure 4.23	Oil squeezed out of the top ring groove toward the crown land (observed in the PSA engine)	239
Figure 4.24	Top ring oil squeezing and inertia-driven oil transport observed on the crown land of the PSA engine	242
Figure 4.25	Description of oil transport on the crown land	243
Figure 4.26	Global oil transport scheme for diesel engine and spark ignition engine at high load (Intake pressure > ~500 mbar)	244

Figure 4.27 Global oil transport scheme for spark ignition engine running at low load (Intake pressure 300 ~500 mbar) 247

Figure 4.28 Global oil transport scheme for spark ignition engine with closed or near to closed throttle (intake pressure < ~200 mbar) 248

LIST OF TABLES

Table 2.1	Potential driving forces for oil transport in the piston ring pack	24
Table 2.2	Description of the engine configurations and running conditions tested in the PSA single-cylinder engine	255
Table 2.3	Description of the engine configurations and running conditions tested in the Kubota single-cylinder engine	258
Table 2.4	Kubota engine characteristics	34
Table 2.5	PSA single-cylinder engine characteristics	37
Table 2.6	Optical material properties	38
Table 2.7	Fluorescing dye selection	58

CHAPTER 1. INTRODUCTION

1.1 Background

Today's research in internal combustion engines is driven by the demand for reduced pollutant emissions and improved fuel economy and customer satisfaction. The performances of the piston ring pack, which are measured in terms of friction loss, oil consumption, oil degradation and wear, affect all these three factors. Unburned and partially burned oil flowing into the exhaust accounts for hydrocarbon and particulate emissions [1, 2, 3, 4]. Additionally, some of the chemical compounds present in oil additives, mainly high sulfur content ones, are poisonous to catalytic converters and thus dramatically reduce their conversion efficiency [5, 6]. Oil flow to the combustion chamber through the piston/liner interface is estimated to account for 40 to 80% of the total engine oil consumption [7]. Minimizing oil consumption from the piston ring pack is therefore of primary interest when trying to reduce lubricant originated emissions. The ring friction, which is an increasing function of the ring sealing ability [8] and hence inversely related to oil consumption, is estimated to account for 10 to 20% of the total engine friction power loss [9, 10]. Eventually, the degradation of the oil properties, which results from high temperature oxidation and combustion soot contamination occurring in the piston ring pack [1, 11], limits the lubricant lifetime and thus affect the customer satisfaction.

In order to meet the increasingly stringent regulations on emissions and fuel economy, new engine designs such as direct injection gasoline and diesel engines are now implemented in passenger cars. Meanwhile the specific power output is increased by allowing higher engine speed and lighter materials such as aluminum alloys are used in the design of new engine blocks. As a result, the thermal and mechanical stresses and deformation have been greatly enhanced, making the ring pack lubrication and sealing ability more critical. Consequently, designing efficient and reliable piston and piston rings for new engine development is increasingly challenging for engine manufacturers and suppliers.

1.2 Lubrication versus Oil Consumption: Oil transport

The primary function of the piston rings is to prevent the leakage of gases from the combustion chamber to the crankcase, and to create a heat path for the cooling of the piston crown. Because the rings are sliding along the liner and the groove sides, lubrication is needed to minimize friction and wear. Consequently, a sufficient lubricant supply must be allowed to the contact regions, whose most critical ones, namely the top ring running surface and groove, constitute direct links to the combustion chamber. The performance of the piston ring pack can thus be regarded as a compromise between friction, wear, and oil consumption. The key to minimizing oil consumption is to optimize oil transport within the piston ring pack. Because the regions above the oil control ring are only partly flooded with oil [12, 13], the rate at which oil flows from the upper skirt region to the combustion chamber is the result of numerous oil transport processes between the various regions defined by the ring pack geometry, namely the piston lands, the ring grooves, and the liner [14].

One of the major difficulties for oil transport analysis lies in the number of sub-regions and the multitude of flow paths. For instance, oil may flow from one land to another through the grooves, the gaps or the ring liner interface. Furthermore, due to the motion of the rings in their grooves, connections between ring grooves and piston lands are repeatedly opened and closed, making the gas and oil flows highly coupled with the ring dynamics [14]. Potential driving forces for oil transports between the different part of the piston ring pack are pressure gradients, shear stress from gas flows, ring/liner and ring/groove relative motion and inertia forces. Pressure gradients and resulting gas flows greatly vary in amplitude and direction with the engine load. For instance, in typical passenger car spark ignition engine, from closed to wide opened throttle (WOT) the blow-by flow rate varies from negative values (toward the combustion chamber) to several liters per minute per cylinder toward the crankcase; the absolute intake pressure varies from about 170 mbar to 1 bar, and the peak cylinder pressure from several bars to about 60 bar. Besides, from 1000 to 6000 rpm, the average inertia force induced by the piston alternating motion varies from 280 to 10 000 m/s^2. Consequently, oil transports are expected to exhibit great variations over the range of potential engine operating conditions. Eventually, oil consumption and thus oil transports were found to be significantly affected by the detailed geometry of the ring pack components, to name a few, ring and groove relative angles, ring running surfaces [15, 16, 17], piston land geometry [18, 19] and bore thermal and mechanical deformations [20, 21].

Due to the underlined complexities associated with the optimization of the ring pack lubrication and sealing ability, a thorough characterization of the fundamental aspects of oil transport is critical for further improvements of piston and piston ring designs. Moreover, to reduce development lead-time

and costs, the demand for analytical tools to predict oil consumption has increased. Consequently, there is a strong need for physically based oil transport models.

1.3 Previous related work

Oil may flow through the piston ring pack along two routes, namely, the liner and the piston. These paths are geometrically connected by the rings and thus oil may be transported between the liner and the piston. Oil displacements along the liner, which are governed by the ring/liner lubricating conditions, have been thoroughly studied [22, 23, 24, 14] and are now very well modeled [25, 26, 27]. Oil transport along the piston involves oil flow across the lands, through the ring grooves and gaps. The oil flows through the ring grooves require oil from the piston lands to be supplied to the ring/groove clearances and are therefore highly related to oil displacements on the lands. The oil flows out of the ring/groove side clearances are mostly determined by the ring/groove interactions and the resulting oil squeezing process, which have been studied and modeled in great details by T. Tian [14]. A few attempts to model oil transport driven by the flow of blow-by gases through the ring gaps have been reported [28]. However, due to the lack of experimental validations and the absence of model to predict the oil supply to the region upstream of the gaps, the significance of the results was limited. As today, due to lack of direct experimental observations and theoretical efforts, the oil mechanical behavior on the piston lands has never been thoroughly investigated. Consequently, even though some of the controlling factors for flows within the piston ring pack such as the ring and piston dynamics have been extensively studied [29, 30, 31, 32, 33, 14], very little success was achieved in modeling the oil flow along the piston. Accordingly, no comprehensive study of oil transports through the piston/liner interface was yet conducted.

Although well-developed one-point Laser-Induced-Fluorescence technique have had success in quantifying the oil film thickness between the rings and the liner [34, 35, 36, 37, 38, 39, 40, 41], it was not sufficient for studying oil transport processes on the piston as oil moves both axially and circumferentially. Other than observations of oil flows in non-firing glass-liner engine, which for obvious reasons were of little interest, there is a limited amount of published work reporting two-dimensional visualization of oil transport on the piston. In 1995 Inagaki and al. [42], using a flash lamp as light source, developed the first two-dimensional LIF oil film measuring system. Their work demonstrated the benefits of having a two dimensional view of the evolution of the oil distribution during engine operation.

1.4 Thesis objectives and Approach

Controlling the oil transport among various regions of the piston ring pack is the key to optimization of oil consumption in internal combustion engines. The major obstacle for the development of analytical tools that could help reducing oil consumption has been the lack of understanding of oil transport processes on the piston lands and of their interactions with oil transports through the ring grooves and gaps. Accordingly, the primary objectives of this thesis are to:

1. Based on experiments, identify and characterize the different oil transport mechanisms between the various sub-regions of the piston ring pack.
2. Propose a physically based model to describe the oil transport processes on the piston lands and their coupling with the oil flows to the other sub-regions.
3. Propose a mass-conserving oil transport scheme describing the main oil routes through the piston ring pack.
4. Study the effect of engine operating conditions and piston ring designs on the oil flows along the piston.

In this work, a two-dimensional visualization system, based on multiple-dye LIF technique, was designed to conduct direct real-time observation of the oil distribution in the piston ring pack during engine operation (Chapter 2). The setup was implemented in both a diesel and a spark ignition single cylinder engine. In order to correlate observed oil displacements with potential driving forces, simulation codes developed in the Sloan Automotive Laboratory by T. Tian [25, 26, 27, 33] were used to compute the ring dynamics and the gas flows between the various sub-regions of the piston ring pack. First, each type of oil transport, namely, oil transport on the lands, through the grooves, through the gaps and between the lands and the liner, were identified and characterized. Then, the physical mechanisms governing each oil transport process were proposed (Chapter 3). A specific theoretical effort was devoted to modeling the oil transport on the piston lands. Then, dividing the ring pack in three zones, oil transport processes were analyzed region by region, emphasizing the effect of the ring design and engine operating conditions on the ability to control the oil supply to the critical areas that are the top ring groove and the crown land (Chapter 4). Eventually, in an attempt to provide a comprehensive description of the routes of oil transport through the piston ring pack, a global oil transport scheme was proposed.

CHAPTER 2. EXPERIMENTAL SETUP

2.1 Experimental Strategy

2.1.1 Experimental Objectives

In order to achieve a full characterization of the various oil transport processes taking place in the piston ring pack, the oil flux and oil distribution need to be qualitatively and quantitatively related to the forces driving the oil motions. Therefore, the paths and rates of oil flows as well as the amplitude and direction of the driving forces must be accurately determined. Accordingly, the experimental objective can be divided in four tasks:

1- Identification of the main oil routes.

2-Understanding the driving forces and governing factors behind each oil transport mechanisms.

3- Provide quantitative data on oil flow rates and oil distribution in the piston ring pack.

4- Provide the measurements needed to compute the amplitude of the driving forces.

2.1.2 Measurement and Diagnostic Choices

Due to the complexity of the ring pack geometry and the resulting multitude of potential flow paths, 2-dimensional direct observation of the oil distribution was found to be the most suited way to identify the main oil routes through the piston ring pack. This method implies the design of an optical access in the cylinder liner and the use of an adequate visualization technique. Laser-Induced-Fluorescence (LIF) was chosen as the visualization technique because it can provide clear images of a correctly doped media. Moreover, the fluorescence intensity is a function of the volume of media that is excited and therefore the optical signal can be converted into quantitative measurements. By using a laser as excitation source very short exposure time (~a few nanoseconds) can be achieved. In fact, exposure time must be less than 1 μs to obtain sharp images of the piston at 5000 rpm. Eventually, in order to develop and validate oil transport models it was necessary to obtain quantitative oil distribution data. Consequently, a great deal of effort was put in developing a reliable calibration technique.

The forces that may drive oil through the piston ring pack are of four types:

- Mechanical actions: the lubricant can be displaced by a moving part like for instance the piston moving relative to the liner or a ring moving in its groove.
- Body force: the alternative piston motion creates a strong body force (up to 2000g) that is acting on the lubricant moving with the piston. This force will be called inertia force in this work.
- Pressure drop and pressure gradient: the significant pressure difference between the combustion chamber and the crankcase results in a series of pressure gradients and pressure drops within the ring pack.
- Shear stress on the surface on the lubricant layer: gas flows between the different regions of the ring pack induce shear stress at the interface between the gas and the oil layers.

The computation of the inertia force is trivial and therefore its amplitude and direction is perfectly known at any time during the engine cycle. The piston and ring dynamics as well as the gas flows and pressure distribution have to be computed with an elaborate simulation code. RINGPACK-OC, which is the main code used in this work, was developed in the Sloan Auto Lab by T.Tian [14]. The accuracy of this code on predicting ring dynamics, gas flows and pressures mainly depends on the accuracy of the input parameters such as cylinder pressure and piston and liner geometry during engine operation. In particular, piston and liner clearances all along the stroke must be known with a great accuracy and thus thermal deformations must be taken into account. Even though the exact piston and liner dimensions can be very difficult to evaluate, the critical values such as the amplitude of the bore and piston deformation can be obtained by tuning the model to match blow-by measurements. This procedure requires having accurate measurements of the blow-by flow rate for the engine operating conditions tested. For this reason, a great deal of effort was put into the design of a reliable blow-by measurement device. Using the cylinder pressure trace and the blow-by measurements, the RINGPACK_OC simulation code was used to provide detailed descriptions of the ring dynamics and the gas flows through the gaps and grooves.

2.1.3 Time Scales

The time scale of the different oil transport driving factors varies from a few crank angle degrees for the motion of the rings in their grooves to one complete engine cycle for the flow of blow-by gases through the entire ring pack. Moreover, as oil transports are repeated every cycle, some of them may lead to oil accumulation processes that last for hundreds of engine cycles. Therefore, to study the evolution of the oil distribution, experiments had to be conducted over time periods ranging from a

few milliseconds to several minutes. The optical diagnostic system was designed to accommodate these constraints. To study oil transports that take place at a specific time interval with a span of a few crank angle degrees, the optical window must cover the piston position that corresponds to this particular timing. Therefore, to maximize the possibility of oil transport observations, the optical access had to be designed such that the longest possible part of the piston stroke could be seen.

Oil Transport Potential Driving Forces	Types of transport induced	Characterization of the driving forces	Measurement required
Relative motion of: Piston and the liner Rings in their groove Rings along the liner	Scraping, Squeezing, Pumping	Using RINGPACK-OC Simulation code	Blow-by Cylinder pressure
Inertia force	Body force driven flow	Computation of the piston acceleration	
Pressure gradient	Poiseuille flow	Using RINGPACK-OC Simulation code	Blow-by Cylinder pressure
Shear-stress at the oil surface	Couette flow	Using RINGPACK-OC Simulation code	Blow-by Cylinder pressure

Table 2.1 – Potential-driving forces for oil transports in the piston ring pack.

2.2 Experiment Configurations

2.2.1 Engine Operating Conditions

One of the main objectives of this project was to study oil transports over the whole range of operating conditions encountered by today's passenger car engines. The oil transport driving forces are greatly affected by the engine speed and load variations. For instance, the inertia force typically varies from 400 m/s^2 at 1000 rpm to 20 000 m/s^2 at 6000 rpm. On a spark-ignition engine the blow-by flow rate per cylinder (net flow rate of gases flowing through the ring pack) can vary from zero (or even negative values) to several liters per minutes as the throttle is moved from a closed to a fully opened position. The two engines used for this work allowed us to cover the entire range of operating conditions needed for a complete characterization of oil transport mechanisms. Both engines were coupled with a motoring dynamometer and could thus be spun independently of the engine load. The Kubota engine is a diesel engine with a speed range that spans from 800 to 3000 rpm. As any naturally-aspirated diesel engine its intake-manifold pressure is constant and almost equal to atmospheric pressure through the entire load range. As a result, the combustion chamber pressure is always equal or larger than the crankcase pressure, and therefore gases flowing through the ring pack are mostly flowing toward the crankcase. In order to cover most of its operating range, the Kubota engine was tested in nine different running conditions shown in Figure 2.1, which were all firing conditions with positive torque was output. The PSA single cylinder engine is a spark-ignited engine with a speed range that spans from 1000 rpm to 6000 rpm. Its load variation is obtained by changing the intake manifold pressure. The domain of operating conditions of the PSA single-cylinder engine and the steady-state running conditions tested are shown in Figure 2.2. Due to the presence of a complete valve train and four balancing shafts the friction losses and thus the torque output of the single-cylinder engine was not representative of a real car engine. Accordingly, the line separating the negative and positive torque output shown in Figure 2.2 was measured on the four-cylinder engine (two-liter displacement) from which the single-cylinder engine is derived.

In real driving conditions, negative loads are typically encountered when the accelerator is suddenly released while driving at a significant speed. In this case, the throttle is closed and the engine is driven by the car inertia. As a result, the pressure in the intake manifold can decrease below 200 mbar. In spark ignition engines, when the intake pressure is decreased below the crankcase pressure (~ atmospheric pressure), gases and oil in the ring pack region are pulled toward the combustion chamber. This phenomenon can lead to dramatic oil consumption level if the intake pressure is

maintained very low [42]. Therefore, it was important to exactly duplicate and thoroughly study the engine operating conditions leading to very low intake manifold pressure. In today's production engine the minimum intake manifold pressure is limited by action of the ECU on the throttle position. Typically, the minimum accepted intake manifold pressure is between 170 and 200 mbar. At such low level of intake pressure the engine always output negative torque. Consequently, in a car, very low intake manifold pressure can only be obtained during transient operating conditions (typically accelerator release while the car is cruising) and thus can not be maintained for more than 30 seconds. Moreover, during this type of transient engine operation from high load to closed throttle, the injection is shut off to save gasoline and therefore the engine is not firing. Transient tests representative of the transient engine operations described above were conducted (see Figure 2.3).

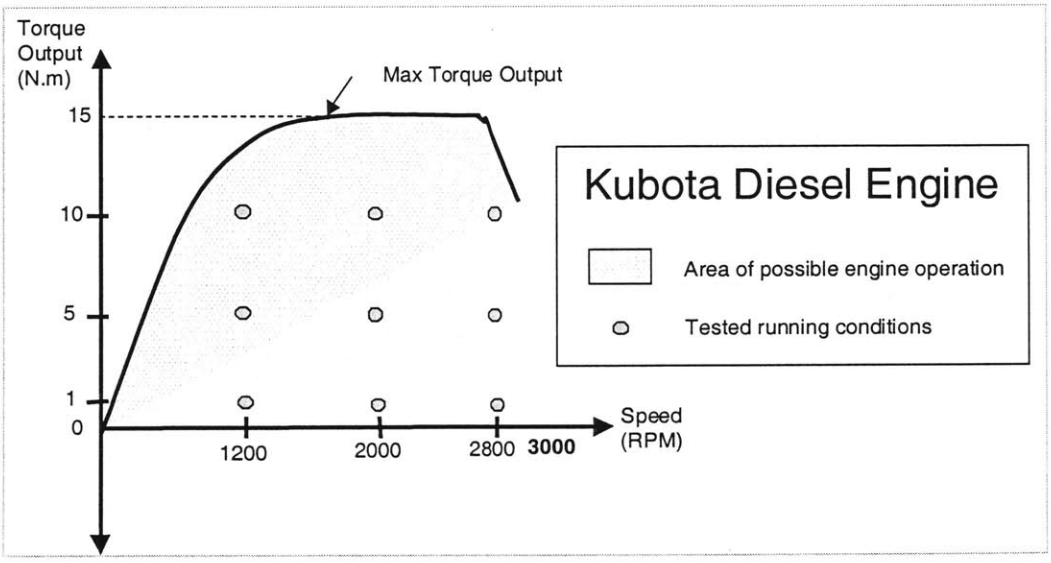


Figure 2.1 - Kubota engine operating range and tested running conditions.

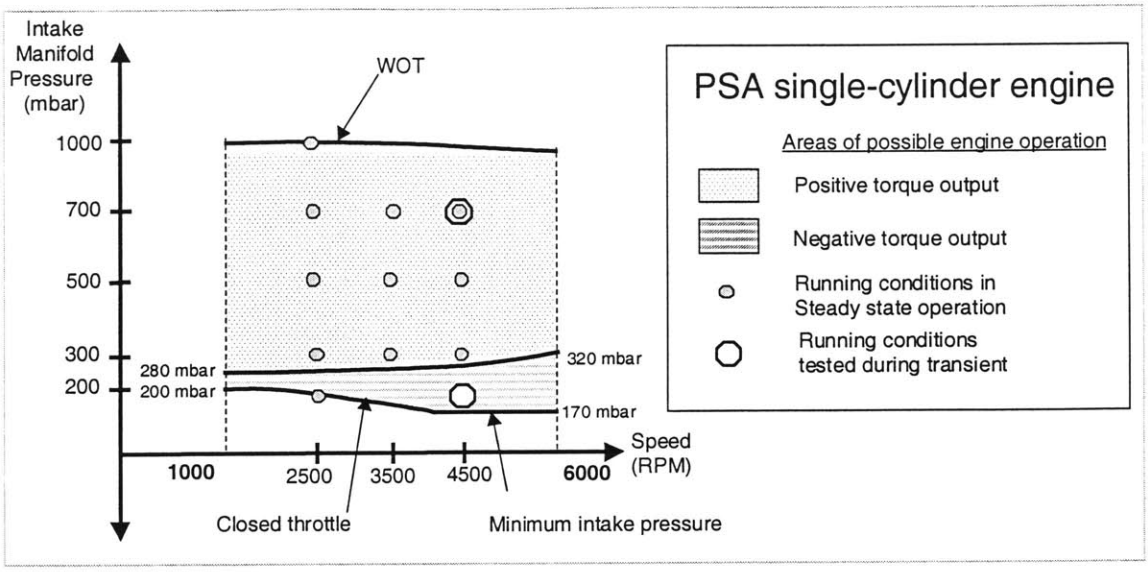


Figure 2.2 – PSA single cylinder engine and tested operating conditions.

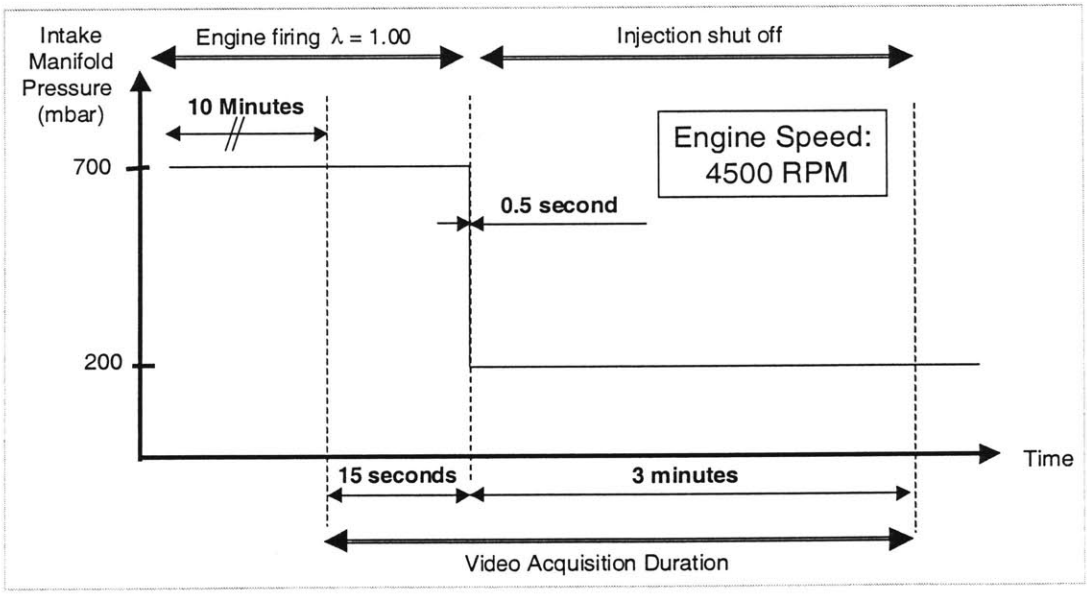


Figure 2.3 – Description of the transient test conducted in the PSA single-cylinder engine.

2.2.2 Window positions

In the Kubota engine the window was located on the anti-thrust side and could not be moved. Therefore, all the observations were conducted at the same circumferential location. The liner of the PSA single cylinder engine was designed so that it could be turned 180 degrees to allow the window

to be located either on the thrust side or on the anti-thrust side. The piston secondary motion can locally affect ring motions [27, 43] and gas flows and thus has an effect on oil transport and oil consumption [44]. In order to study the effect of the piston secondary motion on the lubricant behavior in the piston ring pack, observations were conducted on both the thrust and the anti-thrust side for most of the operating conditions tested on the PSA single-cylinder engine (see Table 2.2 in annex 2).

2.2.3 Ring gap positions

First, due to the presence of the ring end gaps the oil distribution in the piston ring pack is not axi-symmetric. Therefore, it was necessary to conduct oil distribution observations with the ring gaps located at different circumferential positions relative to the observation window. Moreover, the relative angle between the ring gaps has an effect on the repartition of the circumferential gas flows sweeping the piston lands and thus on oil transports. Accordingly, experiments had to be conducted for different relative positions of the gaps. Consequently the positions of the ring gaps had to be measured or fixed.

Secondly, observations of the lubricant behavior in the piston ring pack have shown that the oil distribution on the piston lands was not reaching a steady state during stabilized engine operation. The amount of oil accumulated in the different regions of the piston ring pack was continuously changing on a time scale of several thousands engine cycles (several minutes). As a consequence, the oil distribution data were very difficult to interpret. Furthermore, the unsteady aspect of the oil distribution was found to be directly related to the evolution of the gap locations while the rings were rotating around the piston. In order to facilitate the identification and understanding of oil transport mechanisms, the unsteady lubricant behavior had to be suppressed and therefore the ring rotation prevented. This was achieved by pinning the ring in their groove. Finally, by pinning the rings, the position of the ring gaps relative to each other and relative to the observation window could be set and fixed.

In order to not alter oil transports, it was necessary to pin the ring without restricting the ring axial motion (ring lift in its groove) and the gas flows through the ring grooves and gaps. For this reason, the rings were not pinned at the gap like it is usually done in two stoke engines (see Figure 2.4a). Instead the rings were pinned away from the gap as shown in Figure 2.4b. With this method the gap geometry is not modified and the gas flows through gaps and grooves are not altered. The only drawback of this method is that the local ring tension is slightly affected by the presence of the slot machined on the backside of the ring. In the experiments conducted with pinned rings, only the top

two rings were pinned. The oil control ring was not pinned for the following reasons. First, due to their complex geometry, twin-land OCR and three-piece OCR are difficult to pin without restricting their axial motion. In the case of U-flex OCRs, there is no need to prevent them from rotating since they are completely axi-symmetric once assembled. Secondly, due to their high tension, OCRs rotate around the piston much slower than the top two rings and therefore their rotation does not introduce strong unsteady oil distribution.

The different configurations of ring gap positions tested in the pinned-ring experiments are described in Figure 2.5 for the Kubota engine and in Figure 2.6 for the PSA single cylinder engine.

Eventually, to investigate the effect of the ring rotation on the lubricant behavior and to observe oil transports in configuration identical to a production engine, experiments with non-pinned rings were conducted for all the tested engine operating conditions.

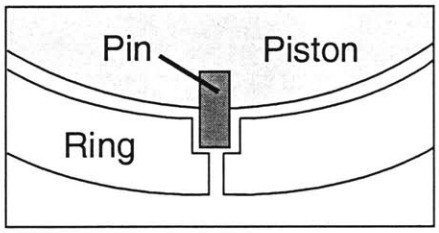


Figure 2.4a – Ring pinned at the gap.
Method used in two-stroke engine.

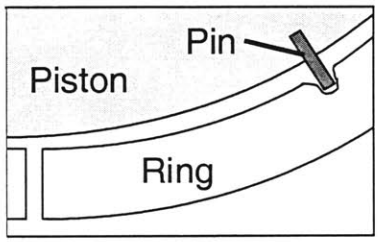


Figure 2.4b – Ring pinned away from the gap
Method used in this project.

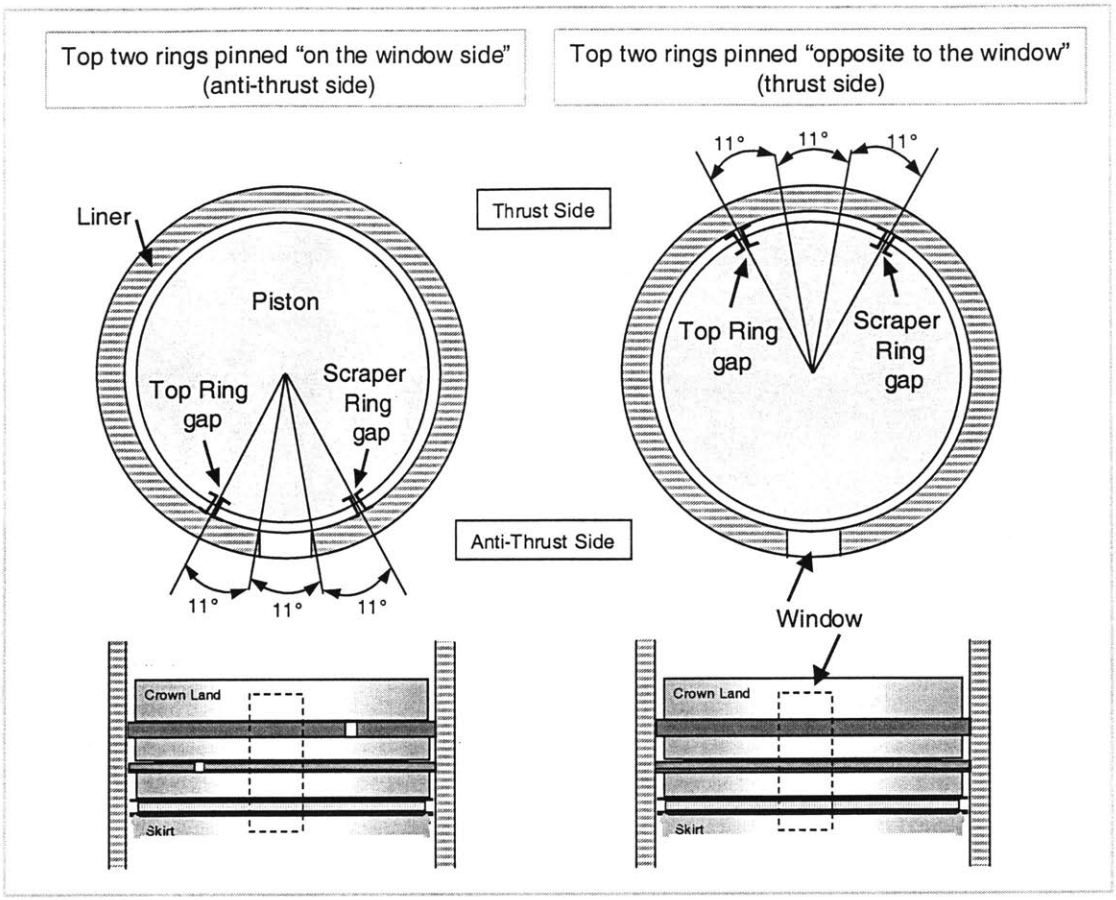


Figure 2.5 – Kubota engine – Description of the ring gap positions for the experiments conducted with top two ring pinned.

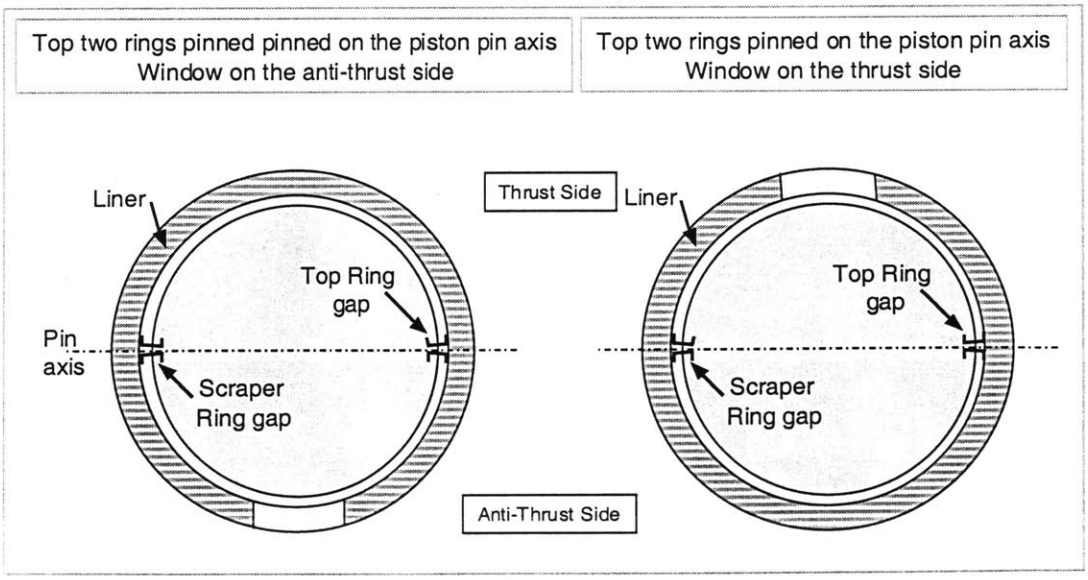


Figure 2.6 – PSA single-cylinder engine. Description of the ring gap positions for the experiments conducted with top two ring pinned.

2.2.4 Ring Designs

The ring designs that are most commonly used in today's small diesel and spark-ignition engines are presented in Figure 2.7. In this project, the mechanisms of oil transports were first investigated using the original ring pack of each engine (see Figure 2.8 and 2.9). Then, different ring designs chosen among the most commonly used ones were tested. By observing the effects of changing ring geometry, a better understanding on the ring-related oil transport mechanisms can be gained and the benefits and drawbacks of the different ring designs can be analyzed.

The original ring pack of the Kubota engine, described in Figure 2.8, is composed of a half-keystone top ring, a scraper ring with hook (hereinafter called Napier ring) and a twin-land oil control ring. Four design variations were tested in the Kubota engine (Figure 2.8). Two of them were made to study how oil transports are affected by the specific geometrical features associated with the Napier ring, namely the hook and the third land cut-off. These two design changes are described below:

1- The Napier ring was replaced by a scraper ring without hook. This scraper ring had no torsion chamfer. It had a tapered face and therefore had a slight negative twist. Scraper rings without hook and without torsion chamfer are not commonly used but by using one we were able to specifically study the effect of the hook on oil transports.

2- A cut-off was machined in the upper part of the third land and the original Napier ring was used. In most applications, Napier rings are used in association with a third-land cut-off that matches the hook geometry. As the original design of the Kubota piston does not have any cut-off, this configuration was used to observe the effect of the third land cut-off on oil transports.

The two other design variations made on the Kubota engine ring pack consisted in changing the oil control ring type. As all the oil supply to the upper ring pack has to flow by the oil control ring, it was important to examine the effect of any of the three typical OCR designs on the lubricant behavior. Therefore a three-piece OCR and a U-Flex OCR were tested in the Kubota engine. Additionally, oil distribution was observed for three different tensions of the twin-land oil control ring.

The half keystone top ring, which is an intermediate design between the keystone ring used in heavy-duty diesel engines and the rectangular ring used in light-duty ones, is not commonly used in recently designed engines. Therefore, the effect of the half-keystone geometry on oil transports seems to be of little interest. However, a half-keystone top ring has a positive static twist, and therefore the data obtained with this ring were used to gain insights on how positively-twisted top rings affect oil transports in other engines.

The original ring pack of the PSA single-cylinder engine, described in Figure 2.9, is composed of a rectangular top ring, a scraper ring with hook and a twin-land oil control ring. In the PSA engine the original design of the third land has a cut-off that matches the dimension of the scraper ring hook (see Figure 2.9). No design variations were tested in the PSA single cylinder engine.

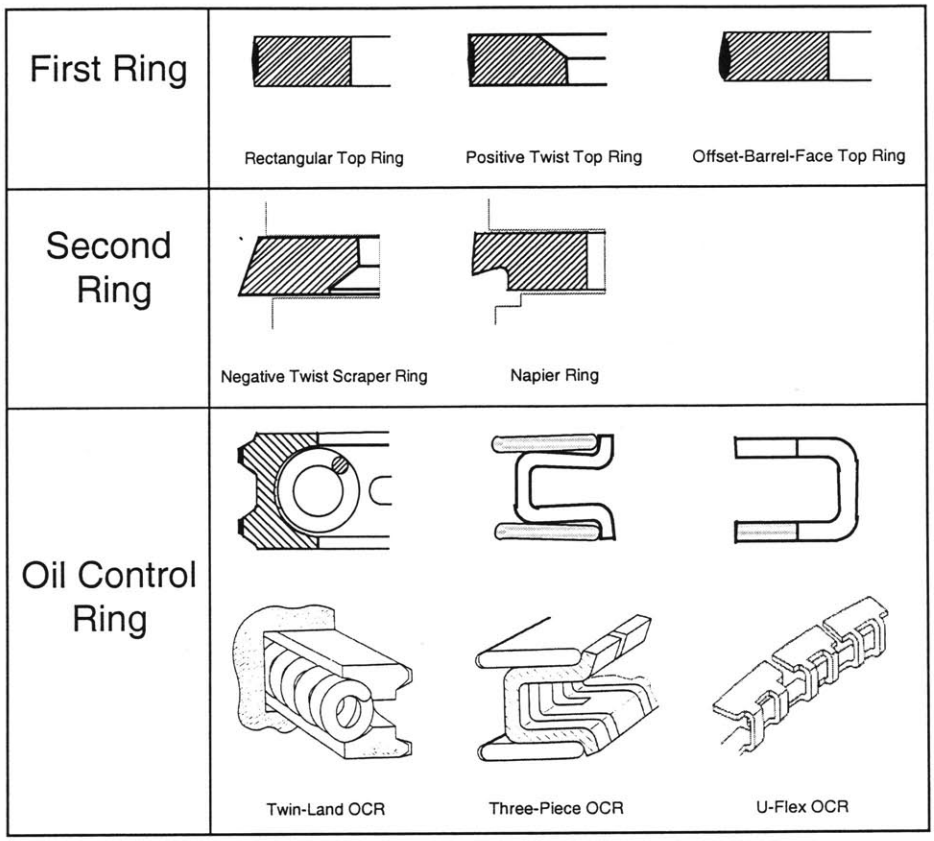


Figure 2.7 – Most commonly used ring designs for spark ignition and small diesel engines.

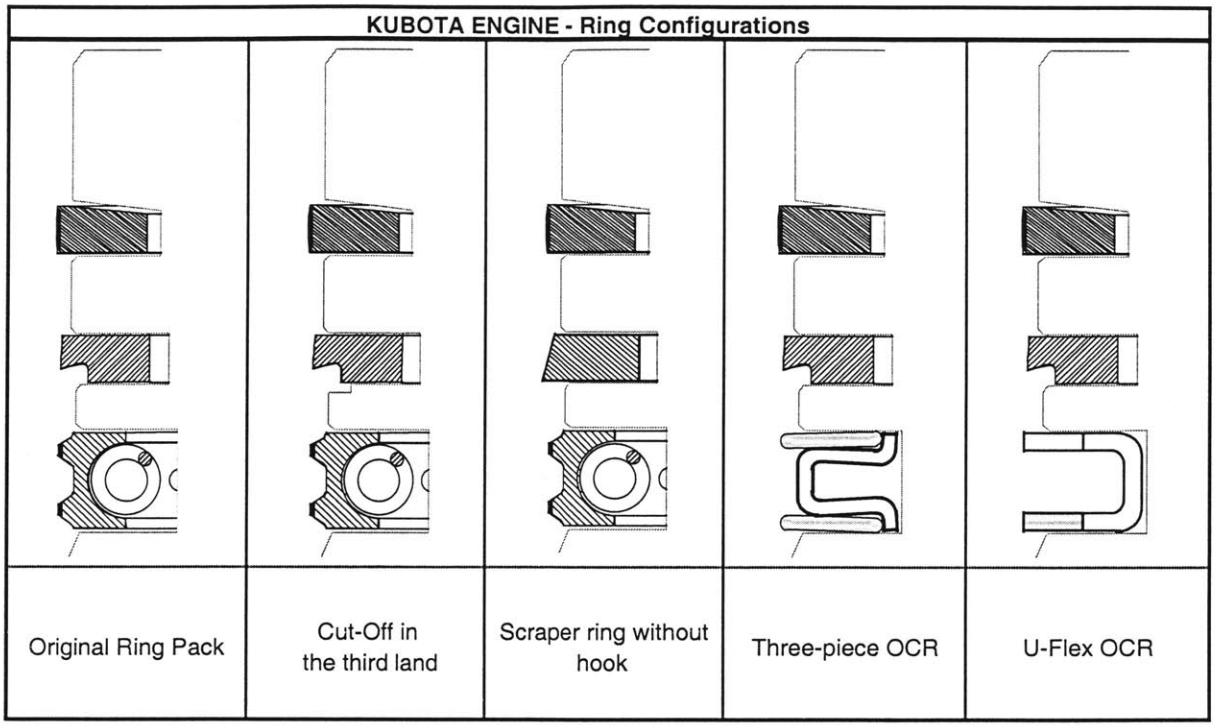


Figure 2.8 – Description of ring configurations tested on the Kubota engine.

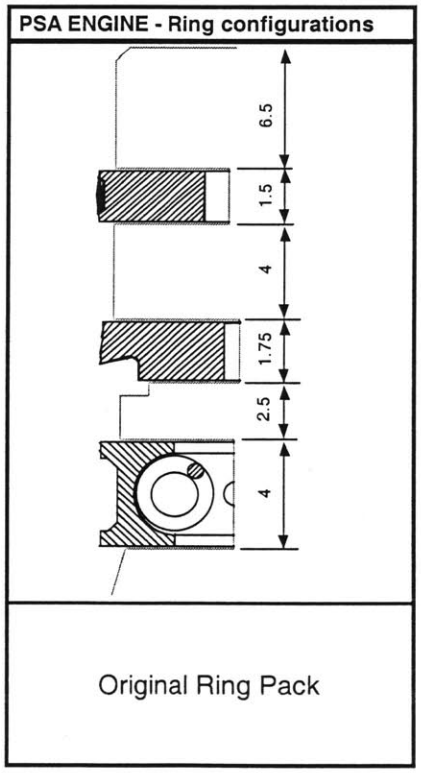


Figure 2.9 – PSA single-cylinder engine. Description of the tested ring gap geometry.

2.3 Engines and Optical Access Design

2.3.1 The Kubota Engine

The Kubota engine was first used to conduct a feasibility study and develop the optical diagnostic system used to visualize the oil behavior in the piston ring pack. Then, it was used to investigate the governing factors involved in oil transport on the piston lands. Eventually, it was utilized to study the impact of several ring designs on oil transport.

2.3.1.1 Engine Characteristics

The Kubota engine is a single-cylinder diesel engine designed for stationary applications. This engine was initially chosen to develop the two-dimensional laser-induced-fluorescence technique because it could be easily equipped with an optical access in the liner. Moreover, it had already been used in the Sloan Automotive Lab to study oil film thickness at the ring/liner interface [12], using one-point LIF technique. The general characteristics of the Kubota EA300 engine are shown in Table 2.4.

Engine Model	Kubota EA300
Type	Diesel with precombustion chamber
Bore	75mm
Stroke	70mm
Displacement	0.309 liter
Max Speed	3000 rpm
Max Specific Power	20.4 kW/liter at 3000 rpm
Max Specific Torque	63.5 N.m/liter at 2400 rpm

Table 2.4 – Kubota engine characteristics.

The lubrication system of the Kubota engine was not modified and thus the oil temperature was not controlled. As a consequence the oil temperature varied from 50 °C at 1200 rpm low load to 65 °C at 2800 rpm 70% load. The oil pressure was generated by a trochoid pump and regulated by a relief valve. The cooling system was modified so that the coolant temperature could be regulated. The coolant temperature was maintained constant at 50°C during all the engine tests. Finally, the blow-by was not re-circulated.

2.3.1.2 Optical Access

A quartz (Synthetic Fused Silica) window was installed in the removable liner of the Kubota engine. The window was designed with a trapezoidal section in both vertical and horizontal direction to better

support the combustion pressure [45]. The dimensions and location of the window, which are shown in Figure 2.10, were limited by the position of the cylinder head bolts. The window offers a 20-mm long and 8-mm wide viewing area. The whole ring pack could be observed through the window when the piston was located at 88 crank angle degrees before or after TDC. The window was glued with high temperature epoxy glue and was honed in place with standard honing stones. After the honing process, the window was flush with the liner. The surface characteristics of the quartz window were not measured. However, it is known from previous experiments that the roughness of the window was higher than the roughness obtained on the cast iron part of the liner. As shown in Figure 2.11, the coolant jacket was modified to allow optical access to the window.

Synthetic fused silica was chosen for this application for the following reasons:

- Good optical quality: excellent transmittance of the visible wavelength.
- Good mechanical properties: very scratch resistant.
- Inexpensive raw material and inexpensive to machine.

The low thermal conductivity of the synthetic fused silica was not an issue for this application because:

- The window was relatively small and inserted in a well-cooled cast iron cylinder liner.
- The window was located below mid-stroke and was therefore not exposed to the very high temperatures encountered during the combustion process.

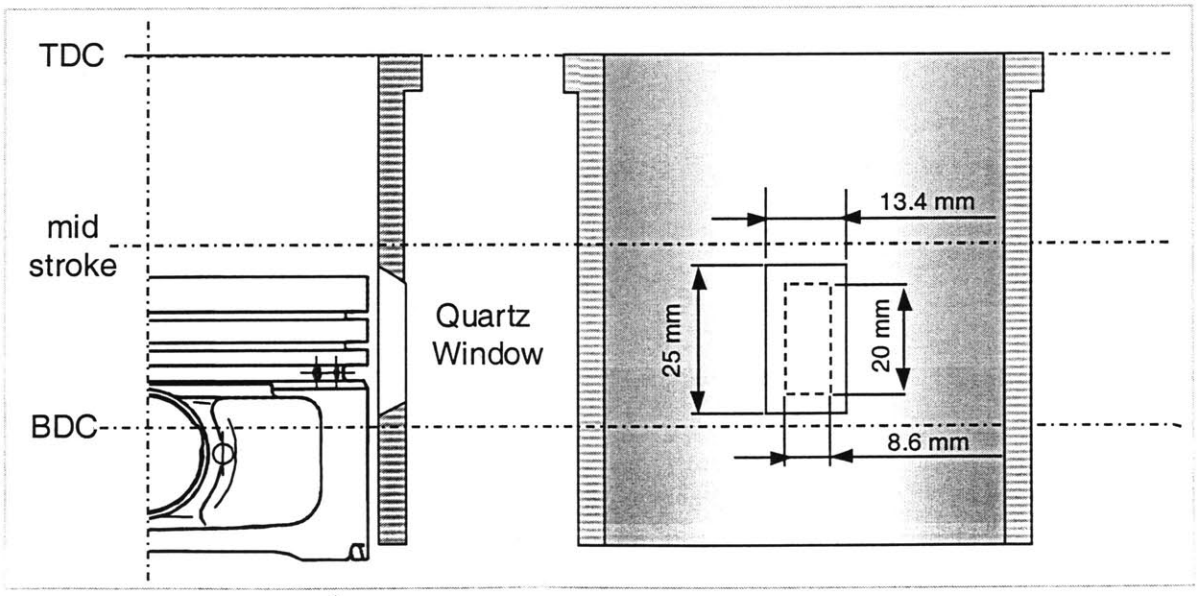


Figure 2.10 – Dimensions and position of the quartz window installed in the liner of the Kubota engine.

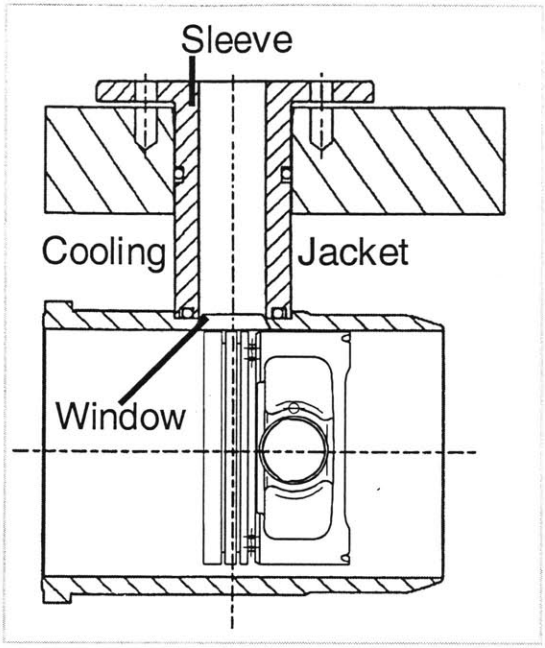


Figure 2.11 – Cooling jacket modification on the Kubota engine.

2.3.2 The PSA Single-Cylinder Engine

As the Kubota single-cylinder engine could not reproduce some of the operating conditions experienced by modern passenger car SI engines. A gasoline engine was needed to complete the investigation of oil transport mechanisms. Additionally, due to the position and the limited size of the window in the Kubota engine oil distribution could only be observed at one piston position and at one circumferential location. Consequently, many oil transport aspects could not be experimentally verified. Therefore, it was decided to equip a spark-ignition engine with a longer optical access that could be positioned on both the thrust and the anti-thrust side. The PSA single-cylinder research engine was chosen because it offered a unique possibility of optical access design. In this thesis work, this engine was used to study the effect of high engine speed and low intake pressure on oil transport by observing the oil distribution along the whole piston stroke and on both the thrust and the anti thrust sides.

2.3.2.1 Engine Characteristics

The PSA single-cylinder engine is a spark-ignited engine that was specially developed for research purposes. The cylinder head, the connecting rod, the piston and the rings are from a XU10J4R Peugeot engine. The cylinder head was heavily modified to be adapted on a single-cylinder engine.

Moreover, to gain more freedom in the design of the liner cooling jacket and optical access, the cooling jacket of the cylinder head has been isolated from the cylinder cooling jacket. An AVL pressure transducer was fitted in the cylinder head to record the combustion chamber pressure. The engine was equipped with four balancing shafts, and can therefore run smoothly up to 6000 rpm. The general characteristics of the PSA single cylinder engine are shown in Table 2.5.

Engine	PSA Research Single-Cylinder
Type	Spark-Ignition - 4 valves - Pentroof chamber
Bore	86.6 mm
Stroke	88 mm
Displacement	0.511 liter
Max Specific Power*	37.3 kW/liter at 5400 rpm
Max Specific Torque*	80 N.m/liter at 4200 rpm

Table 2.5 – PSA single-cylinder characteristics. (* The specific torque and specific power are given for the 4-cylinder engine from which the single-cylinder engine is derived)

2.3.2.2 Optical Access and Window Design

Most engines with large optical access can not be operated at high load and/or high speed for more than 20~30 seconds because effective cooling of the optical widow can not be achieved. For investigation of oil transports in the piston ring pack, it was very important to be able to duplicate all engine operating conditions, including the most severe ones. As a matter of fact, high speed/high load and high speed/low load are among the most critical conditions for oil consumption. Moreover, gas flows in the ring pack and ring motions are very sensitive to the exact geometry of the piston. Consequently, thermal deformations can significantly affect oil distribution and oil transports. Therefore, the engine has to be operated long enough to achieve a steady temperature distribution before conclusive data could be acquired. Consequently, the challenge of designing the optical window was to have a large optical access without preventing normal engine operation.

The cylinder liner of the PSA engine was designed in collaboration with the PSA Research Department (DRIA). In order to accommodate the largest possible window, the cylinder liner was designed so that the liner deformation would be minimized and the cooling efficiency maximized in window area. To limit mechanical and thermal deformation, the massive piece of steel used to support the back of the window was utilized to clamp the two sides of the slot machined in the cylinder (see Figure 2.13). The optimization of the cooling jacket is discussed in Section 2.3.3.3. Since the dimensions of the window are large (104.5 x 18 mm), the thermal conductivity of the

material was critical. For this reason sapphire was chosen over synthetic fused silica. Additionally, sapphire has superior mechanical properties (see Table 2.6) and is therefore more likely to resist the stress induced by the combustion chamber pressure. Eventually, sapphire and cast iron have very similar thermal expansion coefficient and therefore with a sapphire window the gap between the window and the liner will not increase as the temperature rises. As a result, the risk of leakage was minimized.

The window was glued in the liner. A high temperature resistant (up to 230 °C), high thermal conductivity (1.4 W/m.K) epoxy glue (ECCOBOND 276) was used. Once glued in place, the liner and the window had to be ground with a diamond tool so that the window and the liner would be perfectly flush and the bore diameter extended to the nominal bore size. The final bore size was measured and was found to be well within the tolerances (18 μm). Roughness measurement on the liner and on the window showed that Ra was between 0.30 and 0.48 μm.

The window offers a viewing area of 98.5 x 18 mm that extends from the BDC of the OCR to the TDC of the scraper ring (see Figure 2.12).

		Synthetic Fused Silica	Sapphire	Cast Iron
Mechanical Properties	Compression Strength (Mpa)	650-1100	2000	
	Tensile Strength (Mpa)	48	250-400	
	Flexural Strength (Mpa)	80	760-1035	
Thermal Properties	Thermal Expansion (μm/m.K)	0.45	8	6
	Thermal Conductivity	1.4	25...40	15
Optical Properties	Index of Refraction	1.52	1.77	

Table 2.6 – Optical material properties.

Both widows, namely, the quartz one in the Kubota engine and the sapphire one in the PSA engine were polished on the outside and honed on the inside. The honed surfaces are not optically clear. However, the oil refraction index (1.55) is very close to the refraction index of both the quartz and the sapphire, and therefore, once the roughness cavities are filled up with oil, the honed surfaces become transparent enough so that sharp and clear observations can be made.

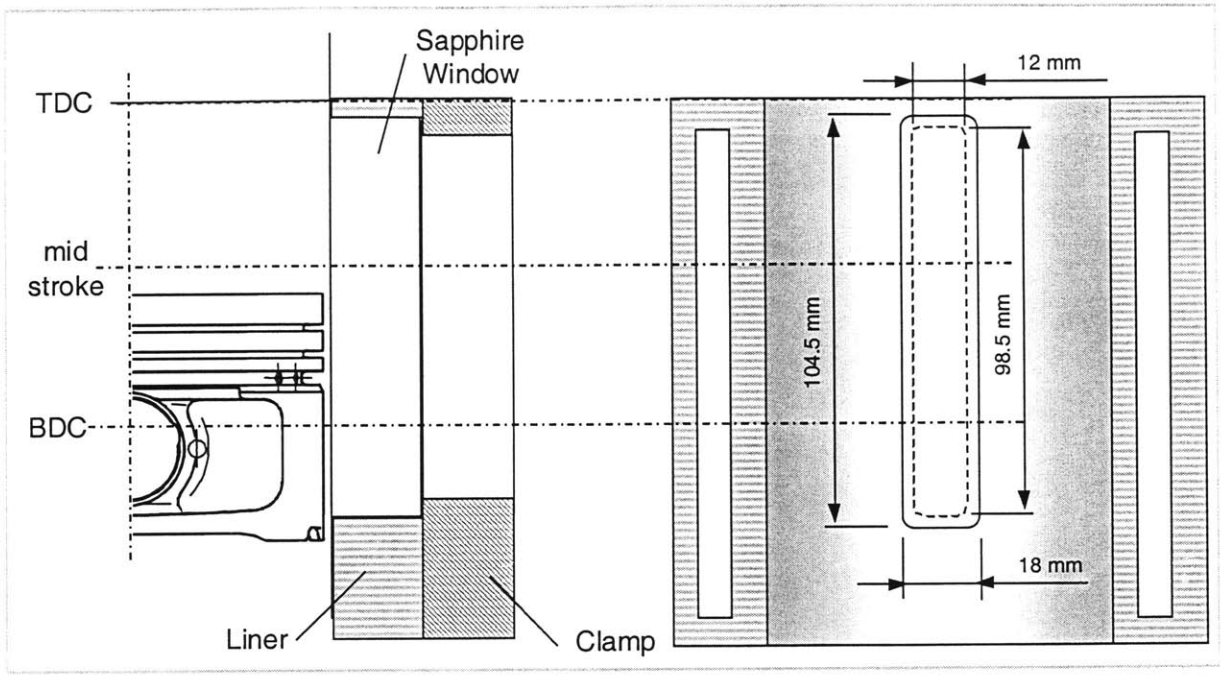


Figure 2.12 – Dimensions and position of the sapphire window installed in the PSA engine.

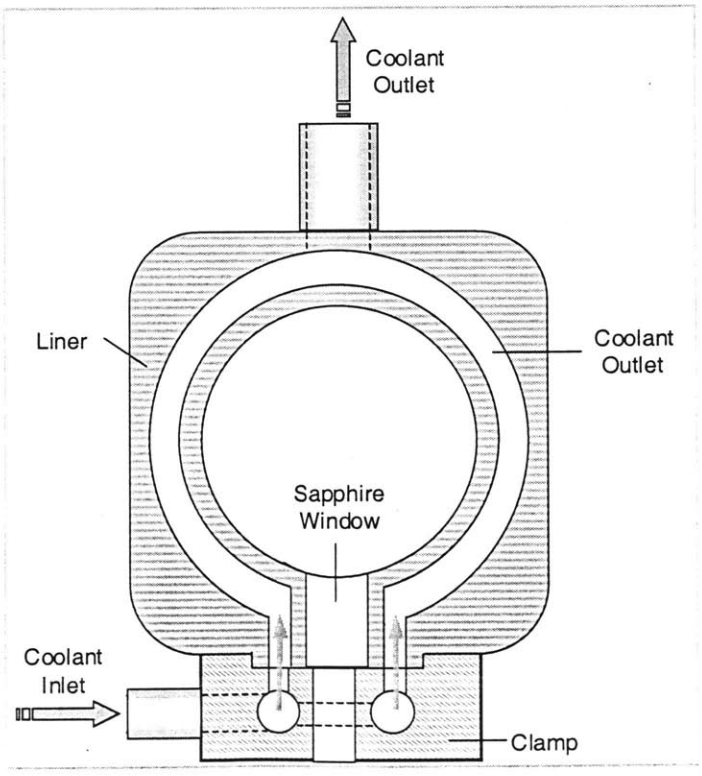


Figure 2.13 –Cooling jacket design and clamping system in the PSA engine.

2.3.2.3 Cooling System Design

The cooling jacket was designed to optimize the cooling efficiency in the window area (see Figure 2.13). First, the coolant goes through the steel clamp. Then, the coolant flows into to the coolant jacket through six holes located around the window (three holes along the length of the window on each side). The resulting repartition of the coolant around the window insures an efficient and homogenous cooling of the window. Afterwards, the coolant flows around the liner and exits the coolant jacket on the side opposite to the window.

In order to obtain a homogeneous liner temperature, it was important to minimize the increase of the coolant temperature between the inlet and outlet of the cooling jacket. Therefore a high-flow-rate coolant pump was used. The pump can sustain up to 50-liter/min flow rate with a back pressure of 2 bar. This flow rate is four times of the flow rate usually used for a single cylinder engine of this size. The coolant temperature at the inlet of the cooling jacket was regulated and was set at 50 °C for all the tests.

2.3.2.4 Lubrication System

While setting up the PSA single-cylinder engine, the lubrication and crankcase ventilation system were carefully designed so that the engine would behave as a production engine. Since the engine was dedicated to the study of oil transports, it was necessary to control the conditions in which the oil was delivered to the engine. Consequently, the lubrication system, which is described in Figure 2.14, was designed to provide a means of accurately regulating the temperature and the pressure of the lubricant entering the engine. As this engine was operated with a dry sump, the lubricant was stored in an external tank where the cooling heat exchanger and the heater were installed. As a result, the large volume of oil contained in the tank acts as a thermal inertia and the oil temperature was controlled without overshooting even though on/off-type controllers and actuators are used. The pressure was regulated with a standard relief valve and a pressure release line. The dry sump requires the use of two pumps: one to scavenge the crankcase, the other to pressurize the lubricant into the engine. The scavenging pump was speed regulated to minimize the amount of crankcase vapor recirculated through the oil tank. For this project, it was very important not to modify the crankcase pressure with the scavenging pump. Variation in the crankcase pressure would have altered the blow-by that was one of the primary interests. Therefore, a connection was made between the crankcase

and the oil tank to avoid building up of pressure difference between them and to help maintain the crankcase pressure very close to atmospheric pressure.

The flow rate of the oil jet that cools the piston is adjustable. However, as no specification was available for this engine, The flow rate was maintained constant and close to its maximum value for all the tests.

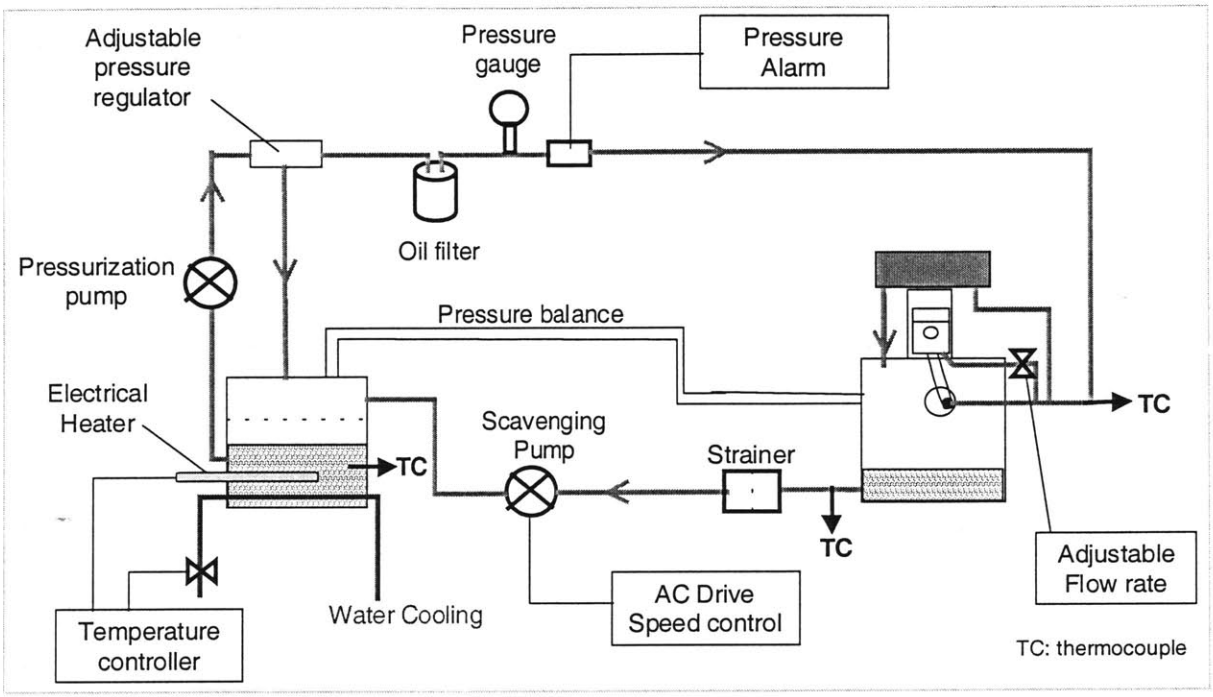


Figure 2.14 – Lubrication system of the PSA single-cylinder engine.

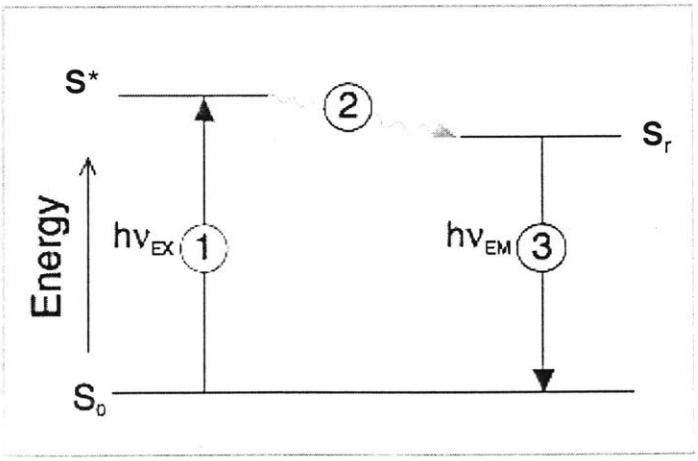


Figure 2.15 – Fluorescence process.

2.4 Diagnostics

2.4.1 Laser-Induced Fluorescence

2.4.1.1 Principle

The Fluorescence Process [46]: Fluorescence is the result of a three-stage process that occurs in certain molecules (generally polyaromatic hydrocarbons or heterocycles) called fluorophores or fluorescent dyes. The process responsible for the fluorescence of fluorescent dyes is explained by the simple electronic state diagram shown in Figure 2.15.

Stage 1: Excitation.

A photon of energy h_{ex} (wavelength ν_{ex}) is supplied by an external source such as a flash lamp or a laser and is absorbed by the fluorescent dye, creating an excited electronic singlet-state S*.

Stage 2: Excited-State lifetime.

The excited state exists for a finite time (typically 1 to 10 nanoseconds). During this time, the fluorophore undergoes conformational changes and is also subject to a multitude of possible interactions with its molecular environment. These processes have two important consequences. First, the energy of S* is partially dissipated, yielding to a relaxed singlet excited state (S_r) from which fluorescence emission originates. Second, not all the molecules initially excited by absorption return to the ground state (S_0) by fluorescence emission. Other processes such as collisional quenching and fluorescence energy transfer may also depopulate S_r. The fluorescence quantum yield, which is the ratio of the number of fluorescence photons emitted to the number of photons absorbed, is a measure of the relative extent to which these processes occur.

Stage 3: Fluorescence Emission.

A photon of energy h_{em} (wavelength ν_{em}) is emitted as the fluorophore returns to its ground state S_0. Due to the energy dissipation during the excited-state lifetime, the energy of this photon is lower and therefore its wavelength longer than the excitation one. The wavelength difference represented by (h_{ex}-h_{em}) is called the Stokes shift. The Stokes shift is the foundation of fluorescence technique because it allows emission photons to be isolated from excitation photons. The entire fluorescence process is cyclical. Unless the fluorescent dye is irreversibly destroyed in the excited state (photobleaching), the same dye molecule can be repeatedly excited and detected.

The Fluorescence Spectra [46]: For polyatomic molecules in solution, the discrete electronic transitions represented in Figure 2.15 are replaced by rather broad energy spectra called the fluorescence excitation spectrum and the fluorescence emission spectrum (see Figure 2.16). The bandwidths of these spectra are parameters of particular importance for applications in which two or more different fluorescing dyes are simultaneously used. Under the same conditions, the fluorescence emission spectrum is independent of the excitation wavelength, due to the partial dissipation of excitation energy during the excited-state lifetime.

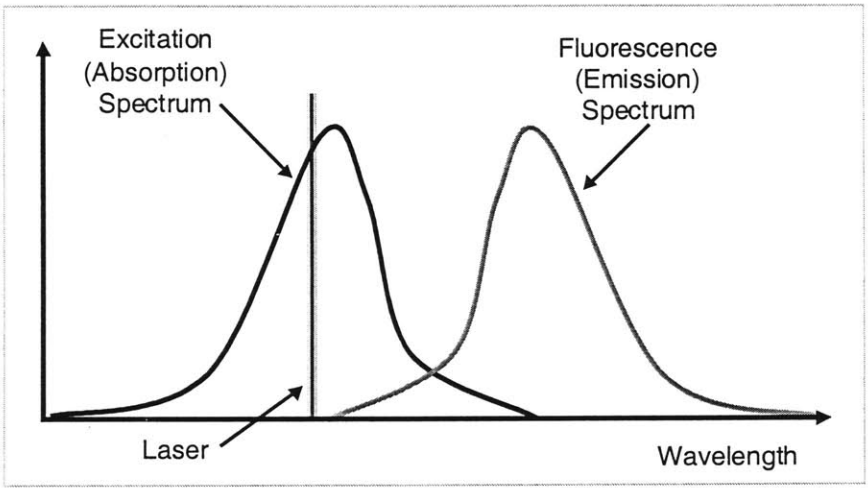


Figure 2.16 – Excitation and Absorption spectrum.

2.4.1.2 Theory

In order to estimate the intensity of the emitted fluorescence, the amount of photons absorbed by the dye must be evaluated first. This is done by using the Lambert law that expresses the amount of transmitted light as a function of the absorbing medium thickness [47]:

$$\frac{I_{tr}}{I_0}(h) = \exp(-\sigma.h) \tag{2.1}$$

With I_{tr}: transmitted light intensity (number of photons/m^2.s)

I_0: excitation intensity (number of photons/m^2.s)

σ: medium absorbance (m^{-1})

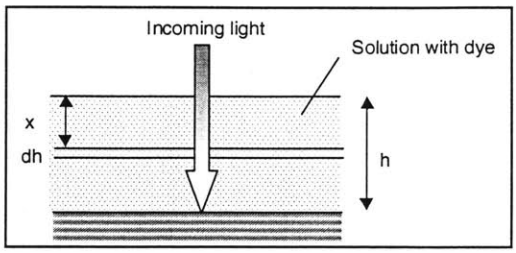
h: medium thickness (m)

Note that the medium absorbance is a function of the wavelength. The amount of light absorbed can be expressed as follows:

$$I_{abs} = I_0(1 - \exp(-\sigma.h)) \tag{2.2}$$

In the case where the fluorescing dye is in solution, the absorbance is equal to the product of the molar extinction coefficient ε (also called absorptivity coefficient), the optical path length h and the dye molar concentration C. The intensity of light absorbed by the dye within a layer of thickness dh can be expressed by the following equation:

$$dI_{abs\,dye} = I(x) \cdot C_{dye} \cdot \varepsilon_{dye} \cdot dh \tag{2.3}$$



With C_{dye}: dye concentration ($mol.m^{-3}$)

ε_{dye}: dye absorptivity coefficient ($m^2.mol^{-1}$)

I(x): light intensity incoming on the layer of thickness dh.

The intensity of excitation light available at the depth x depends on the amount of light absorbed by the dye molecule and the solvent (in our case engine oil) contained in the upper layer of thickness x, and is given by Equation 2.4.

$$I(x) = I_0.\exp(-(C_{dye} \cdot \varepsilon_{dye} + \sigma_{oil}) \cdot x) \tag{2.4}$$

With σ_{oil}: oil absorbance (m^{-1})

In Equation 2.4, the total absorbance of the solution was assumed to be equal to the sum of the absorbance of the oil and the absorbance of the dye. This assumption was experimentally verified by S. Saeki and al [48].

Substituting (2.4) into (2.3) gives:

$$dI_{abs\,dye} = I_0.\exp(-(C_{dye} \cdot \varepsilon_{dye} + \sigma_{oil}) \cdot x) \cdot C_{dye} \cdot \varepsilon_{dye} \cdot dh \tag{2.5}$$

Then, the intensity of fluorescence signal emitted in the layer of thickness dh is given by:

$$dI_{fluo\,dye} = \phi.I_0.\exp(-(C_{dye} \cdot \varepsilon_{dye} + \sigma_{oil}) \cdot x) \cdot C_{dye} \cdot \varepsilon_{dye} \cdot dh \tag{2.6}$$

With ϕ: quantum yield efficiency (non-dimensional)

The photons resulting from the fluorescence process are emitted in all directions. As these photons are traveling through the oil, they are being absorbed. Therefore, only a fraction of the emitted

fluorescence signal exits the oil layer and is available for detection. In order to determine the proportion of photons absorbed one has to estimate the length of the optical path through which the photons detected by the camera travels. As shown on Figure 2.17, the photons that are detected by the camera are those that are inside the solid angle α_s defined by the camera aperture and the focusing distance. Since the focusing distance is large compare to the aperture diameter, α_s is very small. Consequently, it is fair to consider that the optical length traveled by the detected photons that were emitted in the layer of thickness dh is equal to x. As a result, the number of photons emitted in the layer dh that is detectable by the camera is given by the following equation:

$$dI_{\text{fluo dye detectable}} = \frac{\alpha_s}{4\pi} \cdot S_p \ \exp(-\sigma_{oil}.x) \cdot \phi.I_0.\exp(-(C_{\text{dye}} \cdot \varepsilon_{dye} + \sigma_{oil}) \cdot x) \cdot C_{\text{dye}} \cdot \varepsilon_{dye} \cdot dh \qquad (2.7)$$

With S_p: area of the oil layer that corresponds to one pixel on the CCD panel.

By integrating Equation 2.7 from 0 to h we obtained the total amount of fluorescence photons intercepted by one pixel:

$$I_{\text{fluo dye detectable}} = \frac{\alpha_s}{4\pi} \cdot \frac{S_p \ \cdot \phi \cdot I_0 \cdot C_{\text{dye}} \cdot \varepsilon_{dye}}{C_{\text{dye}} \cdot \varepsilon_{dye} + 2 \cdot \sigma_{oil}} \cdot \left[1 - \exp(-(C_{\text{dye}} \cdot \varepsilon_{dye} + 2 \cdot \sigma_{oil}) \cdot h)\right] \qquad (2.8)$$

In Equation 2.8, the absorptivity coefficient of the dye ε_{dye} and the oil absorbance σ_{oil} are functions of the excitation wavelength ν_{ex}. Therefore, integration over the absorption spectrum would be required if a broadband excitation source (flash lamp) were used. This is not the case here since the excitation was a laser beam. Similarly, the quantum yield efficiency of the dye ϕ is function of the wavelength at which the emission is observed ν_{em}. Moreover, the fluorescence emission is detected through a narrow band filter whose transmission efficiency if function of the wavelength. Consequently, to calculate the total intensity of fluorescence detected by the camera, Equation 2.8 must be multiplied by the filter transmittance $f(\lambda)$ and integrated between the two bounds of the narrow band filter.

$$I_{\text{fluo dye dected}} = \frac{\alpha_s}{4\pi} \cdot \frac{S_p \ \cdot I_0 \cdot C_{\text{dye}} \cdot \varepsilon_{dye}}{C_{\text{dye}} \cdot \varepsilon_{dye} + 2 \cdot \sigma_{oil}} \cdot \left[1 - \exp(-(C_{\text{dye}} \cdot \varepsilon_{dye} + 2 \cdot \sigma_{oil}) \cdot h)\right] \cdot \int_{\nu_1}^{\nu_2} f(\lambda) \cdot \phi(\lambda) \cdot d\lambda \qquad (2.9)$$

With $f(\lambda)$: Filter transmittance at wavelength λ.

ν_1: Minimum wavelength transmitted by the narrow band filter.

ν_2: Maximum wavelength transmitted by the narrow band filter.

Effect of dye concentration:

We defined the global absorbance of the oil+dye solution as $\sigma_g = C_{dye}.\varepsilon_{dye} + 2.\sigma_{oil}$.

For $\sigma_g.h << 1$ (thin oil film), Equation 2.9 can be approximated as:

$$I_{\text{fluo dye detected}} \approx \frac{\alpha_s}{4\pi} \cdot \frac{S_p \cdot I_0 \cdot C_{dye} \cdot \varepsilon_{dye}}{C_{dye} \cdot \varepsilon_{dye} + 2 \cdot \sigma_{oil}} \cdot \left[(C_{dye} \cdot \varepsilon_{dye} + 2 \cdot \sigma_{oil}) \cdot h \right] \cdot \int_{\nu_1}^{\nu_2} f(\lambda) \cdot \phi(\lambda) \cdot d\lambda \qquad (2.10)$$

Therefore, for thin oil film, the fluorescence signal is quasi-proportional to the film thickness. It can be deduced from Equation 2.9 that the range of linearity is in the order of $1/\sigma_g$. Consequently, reducing the concentration of dye increases the linearity range of the diagnostic technique. However, the range of linearity is limited by the fact that reducing the dye concentration proportionally reduce the signal intensity and therefore increases the signal to noise ratio.

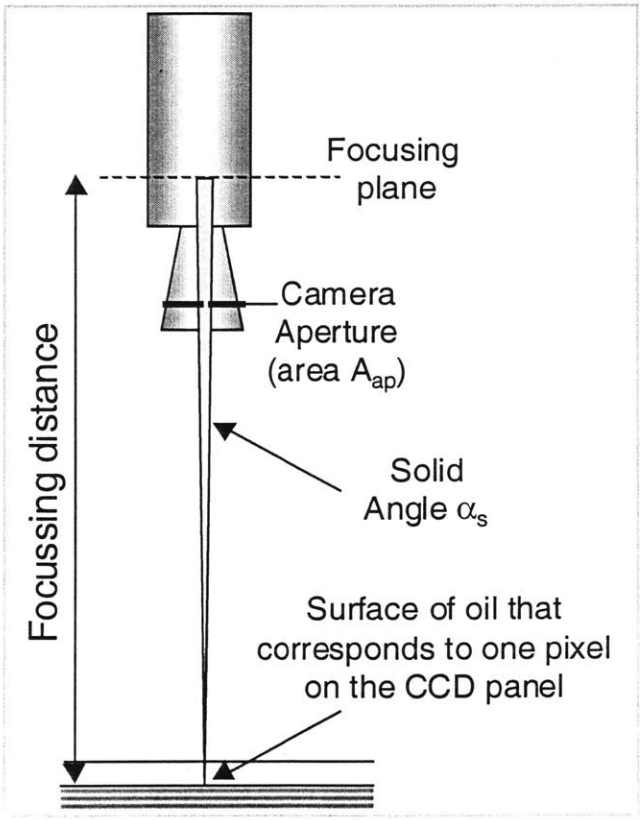


Figure 2.17 – Solid angle of fluorescence signal acquired.

2.4.1.3 Application

In this project, the engine oil was doped with a combination of fluorescing dyes that were excited by the second harmonic of a Nd-Yag pulsed laser (wavelength 532 nm). The fluorescence signal emitted by the dye molecules was isolated from the laser light by a narrow band-pass filter and was acquired by an intensified CCD camera. Details of the optical setup are provided in Section 2.4.3.4. Figure 2.18 shows an example of oil distribution image obtained with the Laser-Induced-Fluorescence Technique. The image was obtained at 3500 rpm 500 mbar intake pressure. On both the LIF image and the florescence intensity profile, the detail geometrical features of the rings and piston can be identified.

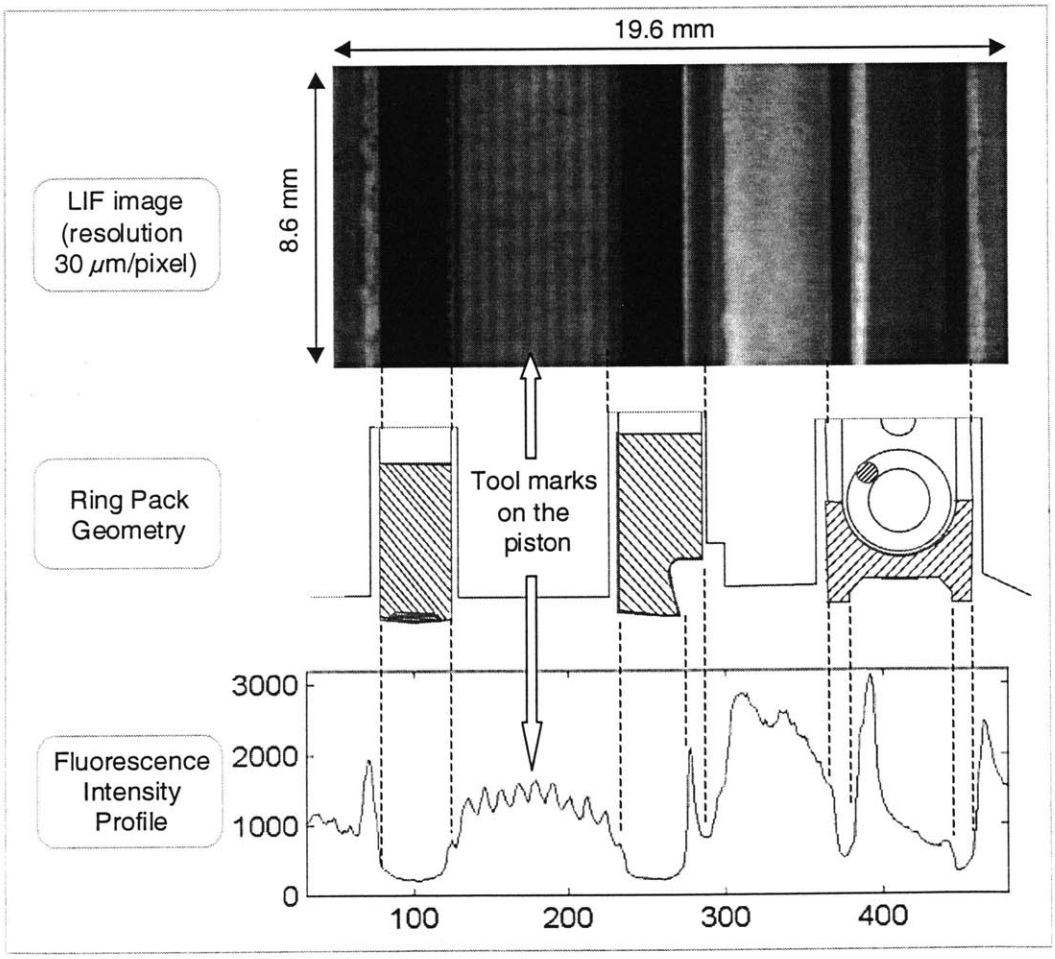


Figure 2.18 – Example of Laser-Induced-Fluorescence image of the piston oil distribution (PSA engine – 3500 rpm 500 mbar – Intake stroke 33)

2.4.2 Calibration of the LIF Signal

2.4.2.1 Temperature Effect

Temperature effect on fluorescence:

Fluorescence is strongly affected by temperature. The fluorescing properties of dyes can be permanently or temporary affected by temperature. First of all, for any dye, if the temperature is elevated high enough, the chemical structure of molecules will be modified and the dye will lose its ability to fluoresce. This phenomenon, which is called thermal bleaching, must be avoided by choosing dyes that can stand the temperature variations experienced by the dye/solvent solution. Secondly, below the thermal bleaching temperature, the absorptivity ε_{dye}, and the quantum yield efficiency ϕ and the absorption and emission spectrum of a dye are function of temperature. Absorptivity usually decreases as temperature increases. According to F.P Schäfer [49], the decay of absorptivity results from a broadening of the absorption spectra induced by an increased molecular vibration level. The quantum yield efficiency ϕ usually decreases with temperature. The main reasons described in the literature [47, 49, 50] are also related to the increased level of molecular vibration. According to F.P Schäfer [49], the non-radiative decay (so-called relaxation) from the excited state to the ground state is enhanced by molecular vibrations. F.P Schäfer also states that the phenomena is more likely to happen in molecules that have a branch that can rotate like -(NH_3)-, -(COOH) or -(SO_2OH). According to F.J Duarte [50] and G. Guilbault [49], the decay of the quantum yield efficiency can be explained by the increasing probability of collisional quenching as the temperature rises. Additionally, G. Guilbault observed that the quantum yield efficiency was decreasing if the viscosity of the solvent was reduced. In many solvents and certainly in engine oil, the viscosity dependency of the fluorescence efficiency will result in an additional temperature-induced decay of fluorescence. Eventually, as long as the chemical structure of the dye molecule is not altered, the temperature effects are reversible.

All the temperature-related phenomena that affect the fluorescence emission are strongly related to the chemical structure of the molecule and are thus very dye specific. Moreover, due to the complexity of the phenomena involved, the amplitude of the temperature effect on the dye fluorescing properties are very difficult to predict and must therefore be experimentally studied.

Temperature variation on the piston: The temperature of the oil/dye solution lying on the piston can be assumed to be equal to the piston surface temperature. It is well known, that there is a significant temperature gradient along the piston when the engine is firing (see Figure 2.19) [51]. This gradient, which increases which the engine load, can be such that the crown land surface temperature is above

250 °C while the skirt temperature is only 80 °C. The fluorescence efficiency of any dye is strongly affected over such a wide range of temperature. This was found to be a problem in previous oil film thickness measurement using LIF technique [34, 48]. Experiments conducted during this work showed that, at 170 °C, the fluorescence emission of some commonly used dyes could be decreased to an extent that it was not detectable. Consequently, LIF images of the oil distribution on the piston lands are very likely to be greatly altered by the oil temperature distribution. Not only the quantitative data but also the qualitative information may be lost. In order to observe the oil distribution at any engine load and to be able to extract the film thickness information from the fluorescence intensity, the dyes had to be very carefully selected.

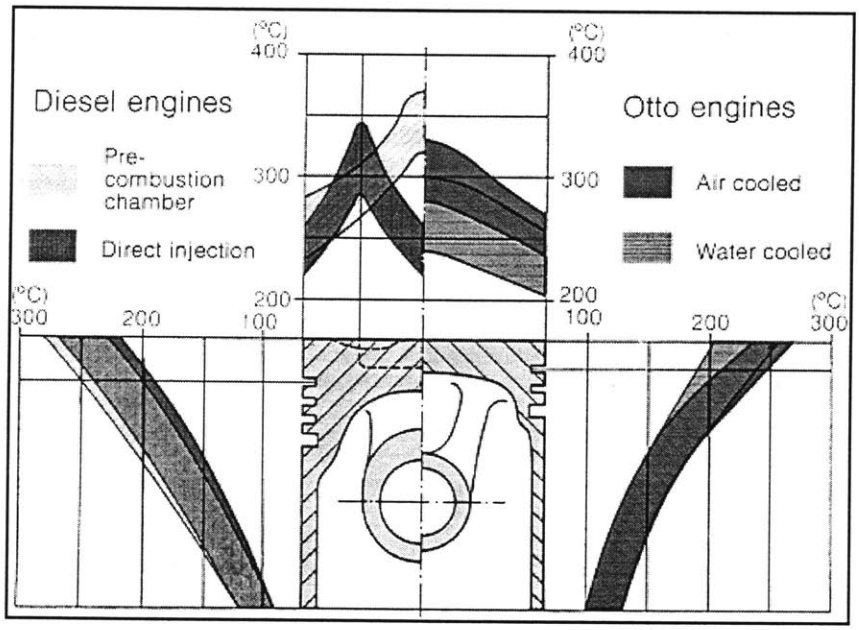


Figure 2.19 – Piston operating temperatures in vehicle engines at full load.
(Source: Mahle Mini Piston Manual)

2.4.2.2 Calibration Challenges

Previous work: The technique that has been most extensively used in the past to calibrate oil film thickness measurement at the piston/liner interface is an in-situ calibration technique. This technique calibrates the fluorescence signal by assuming a specific part of piston or ring of known dimension being filled with oil. D. P. Hoult and G. Tamai [12, 34] used the ring profiles, D. Richardson [39] used a groove machined in the ring, B. Noordjig [13] used machined marks on the piston skirt. In all these cases, the calibration feature was located in a place where it was most likely to be filled with oil,

and the calibration coefficient calculated from the calibration mark was used to calibrate the fluorescence signal from the entire piston ring pack. First of all, this technique is only valid in the thickness range inside which the fluorescence signal is quasi-linear to the film thickness. Secondly, due to the significant temperature gradient on the piston surface, the computed thickness of the oil film along the piston ring was very erroneous. Consequently, for this project, it was decided to specifically address the problem of the fluorescence temperature dependency by developing a more elaborate calibration method.

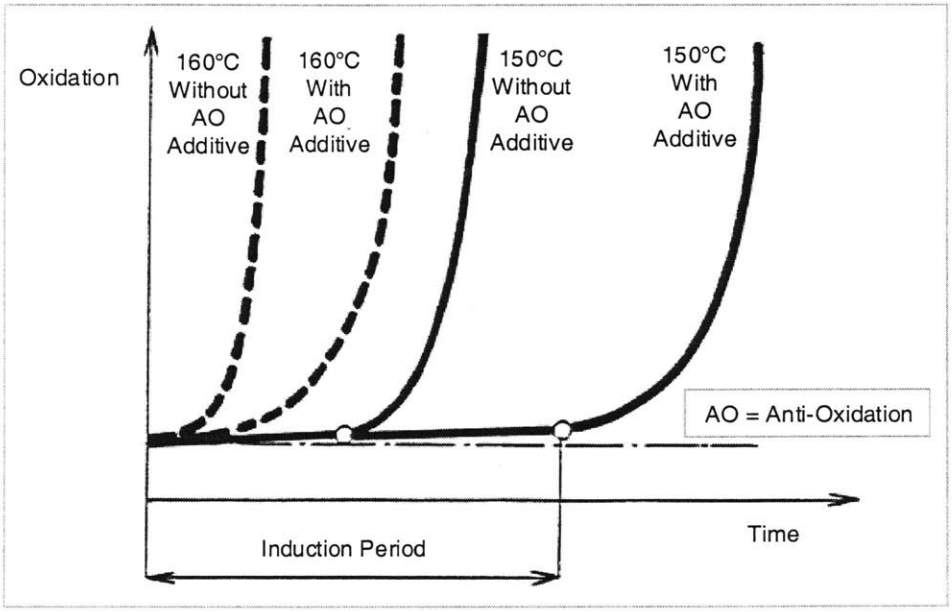


Figure 2.20 – Mineral oil oxidation (Source: IFP Lubricant Booklet).

Calibration issues:

$$I_{\text{fluo dye dected}} = \frac{\alpha_s}{4\pi} \cdot \frac{S_p \cdot I_0 \cdot C_{\text{dye}} \cdot \varepsilon_{dye}}{C_{\text{dye}} \cdot \varepsilon_{dye} + 2 \cdot \sigma_{oil}} \cdot \left[1 - \exp(-(C_{\text{dye}} \cdot \varepsilon_{dye} + 2 \cdot \sigma_{oil}) \cdot h)\right] \cdot \int_{\nu_1}^{\nu_2} f(\lambda) \cdot \phi(\lambda) \cdot d\lambda \quad (2.9)$$

The relationship between the measured fluorescence intensity and the oil film thickness is expressed by Equation 2.9. In order to calibrate the signal intensity $I_{\text{fluo detected}}$ as a function of the film thickness x, all the parameters involved in Equation 2.9 must be either directly measured or deduced from a acquisition made on an oil film of known thickness. The known reference thickness can be located either on the piston surface, in which case the reference measurement is made in-situ while the ring pack oil distribution image is acquired, or in a external calibration device. It is important to note here that when the reference thickness calibration is made with an external calibration device, the group of

parameters to be evaluated must have identical values during the acquisition of the oil distribution image inside the engine and the calibration experiment. Before evaluating the potential of the different calibration techniques, the difficulty of measuring and/or controlling each of the parameters of Equation 2.9 must be discussed.

- $\frac{\alpha_s}{4\pi}$, S_p, C_{dye} and $f(\lambda)$ can all be measured and easily kept identical during engine data acquisition and calibration experiment.
- I_0 is the local laser intensity (number of photons hitting the area S_p). Due to the spatial variation of the laser beam intensity and the pulse to pulse variation of the beam profile and beam total energy, I_0 is a function of the spatial location and time. The amplitude of the intensity variation depends on the laser type and construction. These aspects are discussed in Section 2.4.2. On one hand, the total laser beam energy (mJ per pulse) can be easily measured and controlled so that it remains constant from one experiment to another. On the other hand, measuring the spatial distribution of the laser beam intensity during the acquisition of the fluorescence signal requires an additional CCD camera and was therefore not considered as an option. However, the effect of the spatial variations of the laser beam intensity can be suppressed by averaging a large number of LIF images and correcting the average oil distribution images with an normalized image of the average laser beam profile. This averaging method requires that the observed phenomenon is steady enough so that no significant change in the oil distribution occurs while the large number of LIF images are acquired.
- σ_{oil} is the oil absorbance. It increases when oil get oxidized and/or contaminated with combustion soot. Oil oxidation is a process that depends on temperature and time as described in Figure 2.20. Oil oxidation starts above 140°C. Except in no-load conditions, the temperature of the piston crown land is above 140 °C. This temperature (140°) is also exceeded on the upper part of the liner when the engine in significantly loaded. Therefore, oil oxidation can be considered to be a continuous process in a firing engine. The process is slow and is thus limited by the residence time of the oil in the hot areas. Increasing the total amount of oil used to lubricate the engine can reduce the effect of the oil oxidation and soot contamination on the oil absorbance. For new oil and typical dye concentration, the oil absorbance usually account for less than 15% of the total absorbance of the solution [42, 48]. After 20 hours of running, it can account for more than half of the solution absorbance. It would be difficult to continuously monitor the oil absorbance. However, the oil absorbance can be maintained to a level close to its minimum by frequently replacing the oil/dye solution.

- The dye absorptivity and quantum yield efficiency have strong dependencies on temperature that can be fully characterized using a spectrofluorometer or a well designed calibration setup. However, temperature remains an unknown. There are two ways to address the temperature dependency issue. The first one is to develop a technique to measure the temperature distribution simultaneously with the acquisition of the fluorescence image. The second one is to somehow significantly reduce the temperature effect on the detected fluorescence emission. Both ways were investigated in this work.

To summarize, first it can be stated that the calibration equation has three unknowns: the oil film thickness x, the local piston temperature T and the local laser intensity I_0. Second, the number of unknowns can be reduced to two if the image averaging process, the beam profile correction and the monitoring of the energy per laser pulse are used to eliminate the effect of I_0 variation. Moreover, the piston temperature distribution has to be measured or the thermal effect on the detected fluorescence has to be reduced to an extent that satisfying estimation of oil film thickness can be obtained without accounting for the temperature variation. Possible approaches to both options are explained below.

1. Measuring the temperature distribution: The piston temperature distribution can only be measured optically. H.S Chang [52] has demonstrated the possibility of using infrared spectroscopy to measure the piston and ring surface temperature. However, this method requires its own optical setup and thus can not be coupled with the one for oil distribution observation that is our primary interest. A more common approach to measure two-dimensional temperature distribution consists of using a combination of two fluorescing dyes (Dual Emission LIF Technique). First, the two dyes must have different emission spectra so that the fluorescence of each dye can be separately measured while both dyes are in solution. Then, if the fluorescence decay induced by temperature is significantly different for the two dyes, the LIF images of the emission of each dye can be used to solve for both temperature and film thickness. Practically, the two images can either be acquired simultaneously with two different CCD cameras or one after the other if only one camera is available. If only one CCD camera is used, the observed phenomena has to be steady enough so that there will be no significant oil distribution variation between the acquisition of the two images. The Dual LIF Technique is explained in details in Section 2.4.1.3 and the selection of the appropriate dyes is discussed in Section 2.4.1.4.

2. Reducing the temperature effect on the detected fluorescence emission: Different dyes have different fluorescence emission response to temperature variation. However, even the least

temperature sensitive dye found in this work had a fluorescence efficiency decay of 25 % at 150 °C and 50% at 170 °C. Even though the temperature effect on the dye absorptivity and quantum yield efficiency can not be modified, it was found that the total absorbance of the solution σ_g can be made temperature dependent so that the sensitivity to temperature of the detectable fluorescence emission can be reduced. This technique, which was used to improve the accuracy of the in-situ calibration method, is described in details in Section 2.4.1.5.

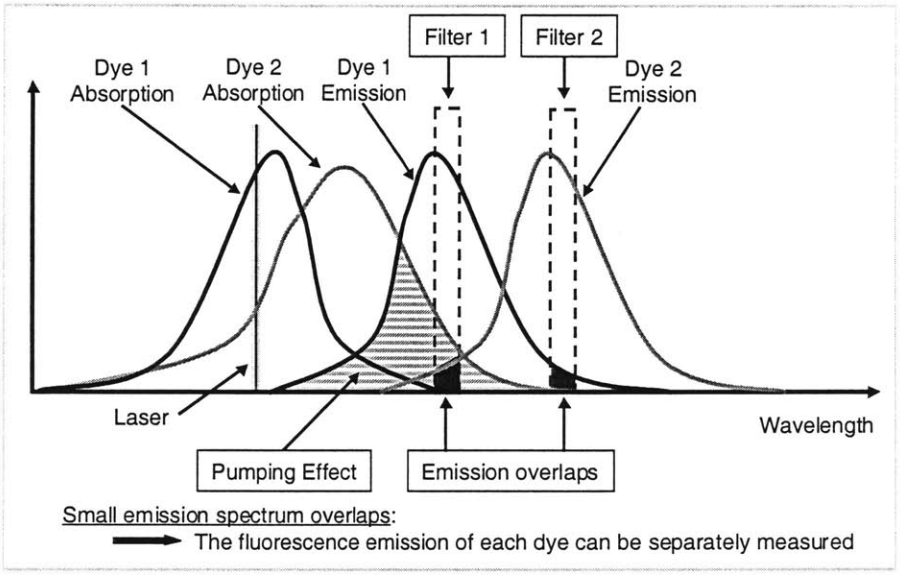


Figure 2.21 – Absorption and emission spectra for two dyes with small emission spectrum overlap and significant pumping effect.

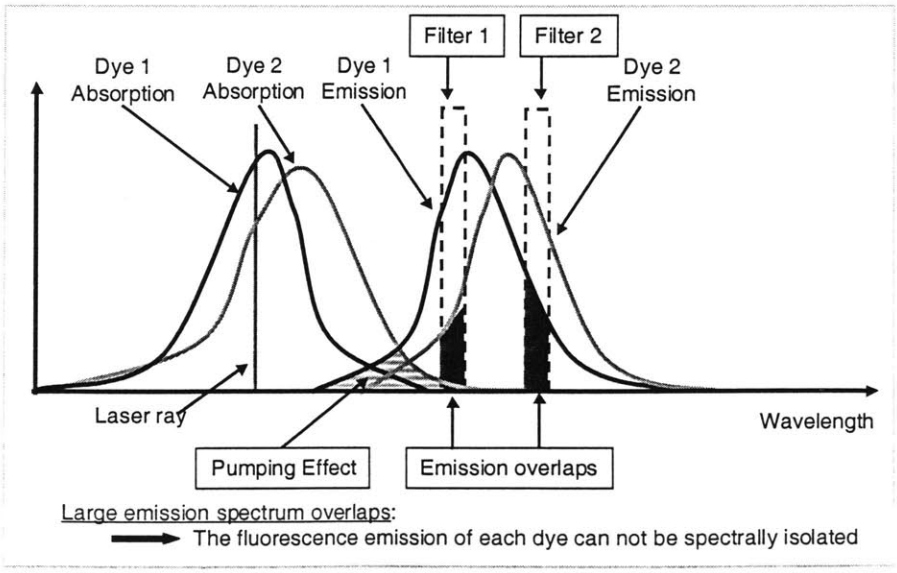


Figure 2.22 – Absorption and emission spectra for two dyes with large emission spectrum overlap. added to clean the rotameter between the measurements.

2.4.2.3 Dual Emission LIF Techniques

Principles: As previously explained, Dual Emission LIF technique consists of measuring the fluorescence emissions of two different dyes mixed in solution to calibrate measurements where two unknowns need to be solved from optical signals [53, 54, 55]. Before discussing dye selection, potential spectral interactions that can occur when two dyes are mixed together must be studied.

First of all, when a combination of two dyes is used with one excitation source, both dyes must have absorption spectra that overlap the wavelength of excitation so that they can both be excited. Second, the two emission spectra must be apart enough so that the fluorescence of each dye can be measured separately (see Figure 2.21). The Stokes shift of dyes that can be excited by the type of laser used for this work rarely exceed 30 to 40 nm. Therefore, as shown in Figures 2.21 and 2.22, if two dyes can be excited with the same wavelength and their fluorescence emission can be spectrally isolated, in most cases, there will be an overlap between the emission spectrum of one dye and the absorption spectrum of the other. This means that the fluorescence signal emitted by one dye is partially absorbed by the second one. This phenomenon is called pumping. Referring to a solution with two dyes: dye 1 and dye 2, and assuming that dye 1 is pumping dye 2, two effects will result from this spectral conflict. First of all, the detectable fluorescence emission of dye1 will be reduced since it is being partly reabsorbed by dye 2. Secondly, the fluorescence emission of dye 2 will be increased since it is now the results of two excitation processes: the laser excitation and the pumping effect of dye 1 (see Equations 2.14, 2.15 and 2.17). Usually, the increase in fluorescence of the second dye is relatively small since the external excitation source, the laser, is much more intense than the fluorescence emission of the first dye. The analytical expressions of the detectable fluorescence emissions of a two-dye combination have been computed taking into account the effect of pumping on both dyes:

- Detectable fluorescence of dye 1:

$$I_{fluo1}(\lambda_1) = \frac{\alpha_s}{4\pi} \cdot \frac{S_p \cdot I_0 \cdot C_{dye1} \cdot \varepsilon_{dye1}(\lambda_{laser})}{\sigma_{g1}} \cdot \left[1 - \exp(-(\sigma_{g1}) \cdot h)\right] \cdot \phi(\lambda_1) \cdot d\lambda_1 \qquad (2.11)$$

With $$\sigma_{g1} = C_{dye1} \cdot \varepsilon_{dye1}(\lambda_{laser}) + C_{dye2} \cdot \varepsilon_{dye2}(\lambda_{laser}) + \alpha_2 \cdot C_{dye2} \cdot \varepsilon_{dye2}(\lambda_1) + 2 \cdot \sigma_{oil} \qquad (2.12)$$

α_2: Non-dimensional coefficient such that $0 < \alpha \leq 1$. α_2 represents the proportion of dye 2 molecules that are in the ground state while photons emitted by dye 1 are travelling out of the oil layer.

- Linear approximation of Equation 2.11: for $\sigma_{g1}.x << 1$ (condition 1)

$$I_{fluo\,1}(\lambda_1) \approx \frac{\alpha_s}{4\pi} \cdot S_p \cdot I_0 \cdot C_{dye\,1} \cdot \varepsilon_{dye1}(\lambda_{laser}, T) \cdot x \cdot \phi(\lambda_1, T) \cdot d\lambda_1 \quad (2.13)$$

♦ Detectable fluorescence of dye 2:

- $I_{fluo\,2} = I_{fluo\,2\,laser} + I_{fluo\,2\,pump}$ (2.14)

With $I_{fluo\,2\,laser}$: Fluorescence emission of dye 2 due to direct laser excitation.

$I_{fluo\,2\,pump}$: Fluorescence emission of dye 2 due to the pumping effect of dye 1.

$$I_{fluo\,2\,laser}(\lambda_2) = \frac{\alpha_s}{4\pi} \cdot \frac{S_p \cdot I_0 \cdot C_{dye\,2} \cdot \varepsilon_{dye2}(\lambda_{laser})}{\sigma_{g2}} \cdot \left[1 - \exp(-(\sigma_{g2}) \cdot h)\right] \cdot \phi(\lambda_2) \cdot d\lambda_2 \quad (2.15)$$

With $\sigma_{g2} = C_{dye\,1} \cdot \varepsilon_{dye1}(\lambda_{laser}) + C_{dye\,2} \cdot \varepsilon_{dye2}(\lambda_{laser}) + 2 \cdot \sigma_{oil}$ (2.16)

$$I_{fluo\,2\,pump}(\lambda_2) = \frac{\alpha_s}{8\pi} \cdot S_p \cdot I_0 \cdot C_{dye\,1} \cdot \varepsilon_{dye1}(\lambda_{laser}) \cdot \alpha_2 \cdot C_{dye\,2} \cdot \int_{\lambda_1} \phi_1(\lambda_1) \cdot \varepsilon(\lambda_1) \left[\int_0^h f(x, h, \lambda_1) \cdot \exp(-\sigma_{oil} \cdot h) \cdot dh \right] \cdot d\lambda_2 \quad (2.17)$$

Where $f(x,h.\lambda_1)$ is a function of positive value given in Annex 1.

- Approximation of Equation 2.15: for $x \cdot \sigma_{g2} << 1$ (condition2)

$$I_{fluo\,2\,laser}(\lambda_2) \approx \frac{\alpha_s}{4\pi} \cdot S_p \cdot I_0 \cdot C_{dye\,2} \cdot \varepsilon_{dye2}(\lambda_{laser}, T) \cdot h \cdot \phi(\lambda_2, T) \cdot d\lambda_2 \quad (2.18)$$

- Approximation of Equation 2.17: for $x \cdot (\alpha \cdot_2 \cdot C_{dye\,2} \cdot \varepsilon_{dye2}(\lambda_1) + 2 \cdot \sigma_{oil}) << 1$ (condition 3)

$$I_{fluo\,2\,pump}(\lambda_2) = \frac{\alpha_s}{8\pi} \cdot S_p \cdot I_0 \cdot C_{dye\,1} \cdot \varepsilon_{dye1}(\lambda_{laser}) \cdot \alpha_2 \cdot C_{dye\,2} \cdot h^2 \cdot \int_{\lambda_1} \phi_1(\lambda_1) \cdot \varepsilon(\lambda_1) \cdot d\lambda_2 \quad (2.19)$$

- Using Equations 2.18 and 2.19, the following condition can be establish to neglect the pumping effect on dye_2 emission:

$$\text{If} \quad \frac{I_{fluo\,2\,pump}}{I_{fluo\,2\,laser}} = \frac{C_{dye\,1}\cdot\varepsilon_{dye1}(\lambda_{laser})\cdot\alpha_2\cdot C_{dye\,2}\cdot h\cdot\int_{\lambda_1}\phi_1(\lambda_1)\cdot\varepsilon(\lambda_1)\cdot d\lambda}{\varepsilon_2(\lambda_{laser})} << 1 \qquad \text{(condition 4)}$$

$$\text{Then} \quad I_{fluo\,2} = I_{fluo\,2\,laser} \approx \frac{\alpha_s}{4\pi}\cdot S_p \cdot I_0 \cdot C_{dye\,2}\cdot\varepsilon_{dye2}(\lambda_{laser},T)\cdot h\cdot\phi(\lambda_2,T)\cdot d\lambda_2 \qquad (2.20)$$

In Equation 2.12, the absorption of dye_1 emission by dye_2 (pumping effect) is represented by the term $\alpha_2 \cdot C_{dye\,2}\cdot\varepsilon_{dye2}(\lambda_1)$. Since this additional term increases the solution absorbance σ_{g1} seen by dye_1, the range of linearity of dye_1 emission is reduced by the occurrence of pumping. Therefore, lower dye concentrations have to be used to respect condition 1 and have a quasi-linear relationship between thickness and dye_1 fluorescence emission. Similarly, for the emission of dye 2 to be proportional to film thickness, dye concentrations must be low enough so that conditions 2, 3 and 4 are respected. If dye concentrations can be lowered enough so that the fluorescence of both dyes is quasi-linear with oil film thickness, Equations 2.13 and 2.20 can be used to relate fluorescence intensity to the thickness and temperature of the oil film. Furthermore, the ratio of dye_1 and dye_2 fluorescence intensities is then only a function of temperature. In these conditions, the use of the ratio $I_{fluo\ 1}/I_{fluo\ 2}$ (ratiometric techniques) greatly simplifies the calibration process [53, 55]. However, reducing dye concentrations may lower the fluorescence emission below detectable level. Consequently, to work in the linear range of fluorescence emission, one might have to restrict the selection of potential dyes to a few high quantum yield efficiency dyes.

Chosen approach: The work done by Inagaki and Sanda [55] was the first application of Dual Emission LIF to oil film measurement in IC engines found in literature. They attempted to simultaneously measure the thickness and the temperature of the oil film in the piston ring pack using one-point LIF technique and a He-Cd laser as light source. Their calibration was made using the linear approximation of the fluorescence/oil film thickness relationship. Recently, C. Hidrovo [54] developed a technique using the pumping effect of a two-dye solution to measure oil film thickness while minimizing errors caused by variation of the laser beam profile. This technique was proven to be successful in measuring oil film thickness when the effect of laser intensity variations must be corrected. However, because the technique can not correct none-linear effect, the variation of the

fluorescence intensity with temperature can not be corrected and therefore this technique could not be applied in this project.

In this work, effort was made to search the best dye combination to simultaneously solve for temperature and oil film thickness using the second harmonic of Nd-Yag laser (532 nm) as excitation source. Since the number of dyes that can be excited at 532 nm is limited, the search was not restricted to the dye combinations that could only be used in the linear range.

Dye selection: All the dyes available from Exciton Inc. that could be excited by the second harmonic of a Nd-Yag laser (532 nm) were initially considered. Then, considering the extreme thermal environment that can be encountered on the piston crown land, only the dyes with a melting point temperature above 200 °C were selected. Finally, ten dyes, which were found to be soluble in oil, were tested for quantum yield efficiency, thermal bleaching, and temperature sensitivity (see table 2.5). The baseline chosen for the dye evaluation was Rhodamine 590 chlorate. This dye was first selected because it had been used extensively for oil film thickness measurement in shaft seal [Hugo]. Then, Rhodamine 590 was excluded because it was found to cause significant oxidation to the engine bearings (Copper oxide was identified in the oil doped with Rhd 590 after only a few hours of engine operation).

Table 2.7 shows the results of the dye testing. Three dyes from the Rhodamine family and three dyes from the Pyrromethene family were found to be suitable for oil distribution observation in internal combustion engines. To be able to effectively use dual emission LIF calibration, the emission spectra of the two selected dyes must be as fart apart as possible so that the fluorescence signal of each dye can be measured separately. Dye combinations involving either Pyrro 597 or Rhd 610 were tested and rejected since the fluorescence emission of each dye could not be separately measured because of emission spectra overlap. After all, two dye combinations could have been chosen from the six selected dyes presented in Figure 2.23: Pyrromethene 567 + Rhodamine 640 and Pyrromethene 650 + Rhodamine 590.

To calibrate for oil film thickness and temperature, the two dyes chosen must have significantly different temperature response. Since Rhd 590 and Pyrro 650 were found to have a very similar temperature behavior, the best dye combination appeared to be Pyrromethene 567 + Rhodamine 640. As shown in Figure 2.24, where fluorescence was measured at 570 nm for Pyrro 567 and 650 nm for Rhd 640, Rhd 640 and Pyrro 567 have significantly different temperature response and thus appear suitable for dual emission calibration.

Dye Families	Name	Melting Point Temperature(°C)	Observations	Dyes selected
Rhodamine	590 Chloride	315	Oxidize engine bearings	
	590 Tetrafluoroborate	255		X
	610 Chloride	210		X
	610 Perchlorate	112	Melting temperaure too low	
	640 Perchlorate	210		X
Pyrromethene	556	>400	Not soluble	
	567	208		X
	580	183	Melting temperaure too low	
	597	247		X
	605	176	Melting temperaure too low	
	650	255		X
LDS	698	202	Quantum yield efficiency too low	
	720	283	Not soluble	
	722	246	Not soluble	
Sulfurhodamine	620	>310	Not soluble	
	640	>310	Not soluble	
Others				
	DCM	212	Quantum yield efficiency too low	
	LD688	290	Quantum yield efficiency too low	

Table 2.7 – Fluorescing dye selection.

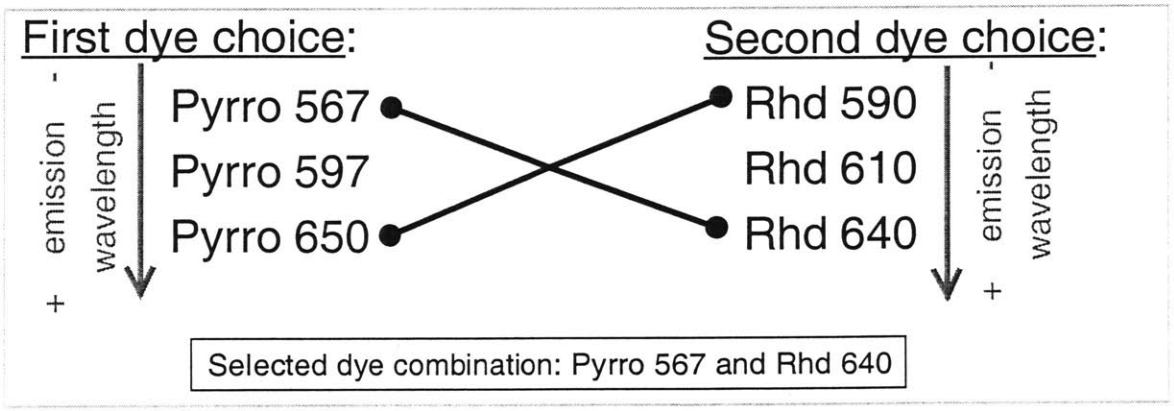


Figure 2.23 – Selection of potential dye combinations.

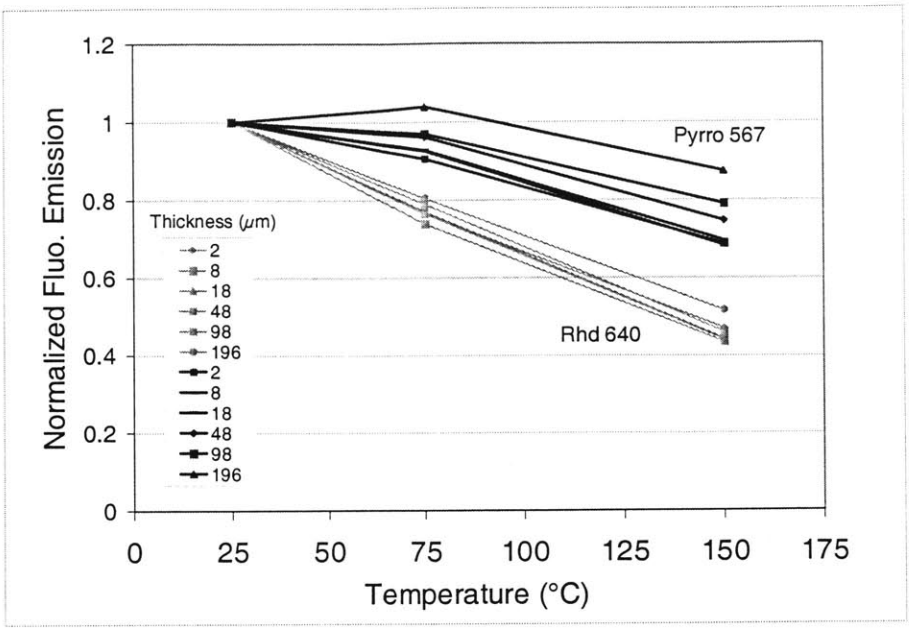


Figure 2.24 – Temperature response of Pyrro 567 (5.0 10^{-4} mol/liter) and Rhd 640 (2.0 10^{-4} mol/liter) while mixed together (Emission of Pyrro 567 measured at 570 nm with a 10 nm narrow-band filter, emission of Rhd 640 measured at 650 nm with a 10 nm narrow band filter).

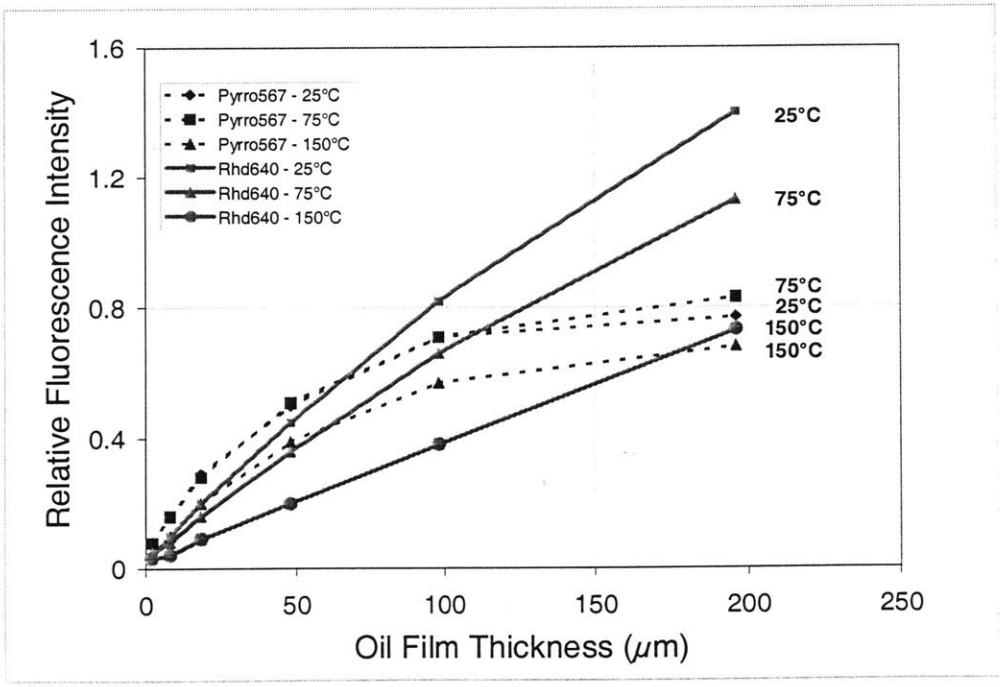


Figure 2.25 – Thickness and temperature response of Pyrro 567 (5.0 10^{-4} mol/liter) and Rhd 640 (2.0 10^{-4} mol/liter) while mixed together (Emission of Pyrro 567 measured at 570 nm with a 10 nm narrow-band filter, emission of Rhd 640 measured at 650 nm with a 10 nm narrow band filter).

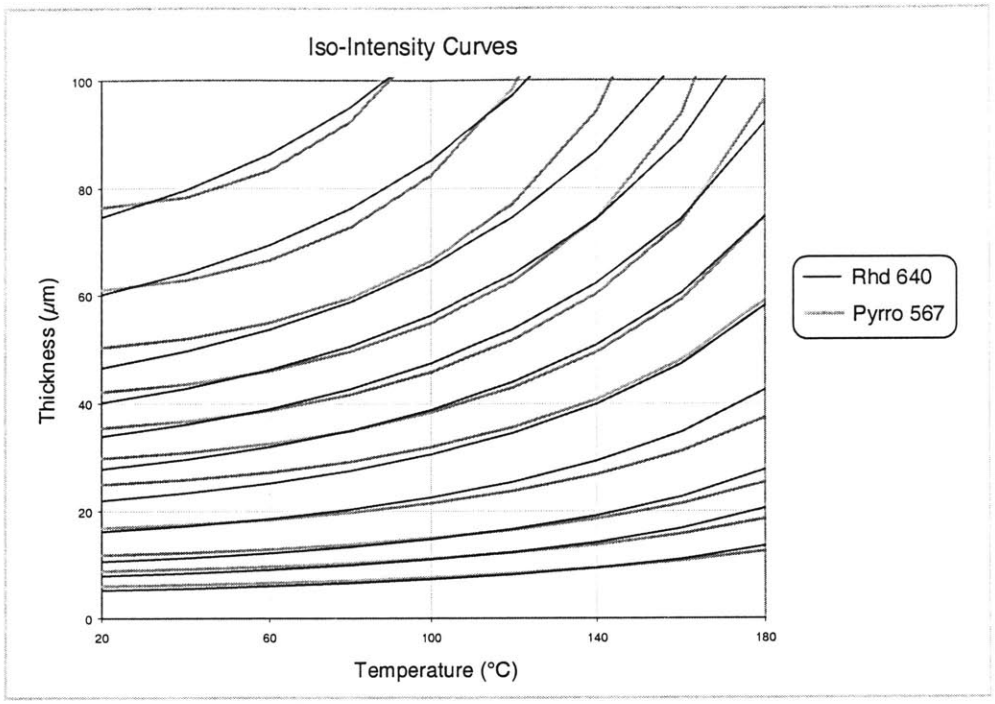


Figure 2.26 – Curves of iso-intensity of fluorescence emission for Pyrro 567 ($5.0\ 10^{-4}$ mol/liter) and Rhd 640 ($2.0\ 10^{-4}$ mol/liter) while mixed together (Emission of Pyrro 567 measured at 570 nm with a 10 nm narrow-band filter, emission of Rhd 640 measured at 650 nm with a 10 nm narrow band filter).

2.4.2.4 Dual Emission Calibration (applied to the Kubota Engine)

Optimization of the dye combination: First of all, the concentration of Rhd 640 and Pyrro 567 were optimized so that the level of fluorescence emission of both dyes were very similar and high enough to be easily detected by the CCD camera. As a result, Rhd 640 was first used at $5.0\ 10^{-4}$ mol/liter of oil and Pyrro 567 at $2.0\ 10^{-4}$ mol/liter of oil. The characteristics of the fluorescence emission obtained with these dye concentrations are shown in Figure 2.25. It can be noticed that due to the re-absorption of Pyrro 567 fluorescence by Rhd 640 (pumping effect), Pyrro 567 signal saturates above 50 μm.

In order to estimate all the coefficients needed to compute the two equations relating the fluorescence intensity of each dye to the oil film thickness and temperature, the behavior of Pyrro 567/Rhd 640 combination was fully characterized. Equation 2.11 was used to simulate the behavior of Pyrro 567 emission. Equation 2.15 was used to represent the behavior of Rhd 640 fluorescence. The additional contribution to the fluorescence of Rhd 640 due to the pumping effect (Equation 2.17) was neglected.

Calibrating oil film thickness and temperature is achieved by solving the system of equations made by Equations 2.11 and 2.15. Solving this system is equivalent to find the crossing point of two iso-intensity curves in a temperature vs. thickness plot (see Figure 2.26). Consequently, by examining the Iso-Intensity curves (IIC) on Figure 2.26, the number of solution of the system can be determined and the accuracy of the solution can be estimated. First of all, in order for the system to have only one solution, an IIC of one dye must cross IICs of the other dye only once. Secondly, the larger is the angle between IICs at their crossing point, the more accurate the solution (temperature, thickness) is. From Figure 2.26, we can see that, in our case, the IICs have two crossing points and are parallel in some areas of the plot. Therefore, even though the two dyes have different temperature responses (see Figure 2.24), the actual dye combination can not be used to measure simultaneously the temperature and the thickness of the oil film.

In order to improve the characteristics of the selected dye combination, it was necessary to understand why the IICs could have two crossing points, and thus to analyze the factors affecting the slope of Pyrro 567 IICs. As the fluorescence intensity is a function of thickness and temperature, we have:

$$I_{fluo\,i} = f(h,T) \qquad \text{and} \quad dI_{fluo\,i} = \frac{\partial f}{\partial h}\cdot dh + \frac{\partial f}{\partial T}\cdot dT$$

Along an iso-intensity curve $dI_{fluo\ i} = 0$, therefore the slope of the IIC can be estimated with the following equation:

$$\frac{dh}{dT} = -\frac{\dfrac{\partial f}{\partial T}}{\dfrac{\partial f}{\partial h}} \tag{2.21}$$

In Figure 2.26, we can see that, the IICs that have two crossing points are the ones corresponding to large film thickness (upper part of the plot). First of all, at low temperature (upper left part of the plot), it can be seen that Pyrro IICs have a smaller slope than Rhd 640 IICs. This reflects the fact Pyrro 567 is less sensitive to temperature than Rhd 640 and leads to the existence of the first crossing point. Secondly, at high temperature (upper right part of the plot), Pyrro 567 IICs have larger slope than Rhd 640 IICs leading to the existence of the second crossing point. The reason for which Pyrro 567 IICs slope is increasing with temperature for thick film can be seen from Equation 2.21. Due to the re-absorption of Pyrro 567 emission by Rhd 640, the fluorescence signal of Pyrro 567 saturates above 50 μm (see Figure 2.23) and thus $\left.\dfrac{\partial f}{\partial h}\right|_{Pyrro\,567}$ decreases as the thickness h increases. IICs go from low to high film thickness as they go from low to high temperature. Moreover,

$\left.\frac{\partial f}{\partial h}\right|_{Pyrro\,567}$ decreases as the thickness increases. Consequently, the IIC slope $\frac{dh}{dT}$ increases with temperature along an IIC. Furthermore, this effect is enhanced at high temperature (above 100 °C) where the temperature sensitivity of Pyrro 567 ($\left.\frac{\partial f}{\partial T}\right|_{Pyrro\,567}$) is greater.

There were two ways to improve the characteristics of the dye combination so that the system of Equations 2.11 and 2.15 could be correctly solved. The first and the best one was to replace the two dyes so that the dye with the strong temperature dependency was the one whose fluorescence emission was being reabsorbed. In this case, the re-absorption effect (pumping) would had enhanced the calibration accuracy instead of reducing it. Unfortunately, no dye with the adequate characteristics was found. The second way, which was used in this work, was to greatly attenuate the re-absorption effect by significantly decreasing Rhd 640 concentration. Rhd 640 concentration was therefore divided by 10 (down to 5.0 10^{-5} mol/liter). Pyrro 567 concentration was divided by 10 (down to 2.0 10^{-5} mol/liter) as well in order to maintain the fluorescence intensity of both dyes at similar levels. The dye concentrations could not be further reduced without significantly increasing the signal to noise ratio. Using the reduced concentrations, calibrations were attempted on oil distribution profiles acquired in the Kubota engines.

Results and applications: Figure 2.27 shows a typical result of dual emission calibration conducted with the optimized Pyrro567/Rhd640 dye combination. Temperature and thickness of the oil film were determined on the second and third land of the piston. The sensitivity of the calibration technique to temperature was found to be very limited and consequently the accuracy of the determined temperature was poor (+ or – 20 °C). The temperature and film thickness on the crown land could not be evaluated using the dual emission calibration. Overall, it was found that with the developed technique, oil film thickness could be correctly evaluated only in regions were temperature was below 110 °C. Despite the significant reduction of the dye concentrations, the temperature range in which the calibration technique could be used was still limited by the effects of pumping.
Considering the limitation of the technique, dual emission calibrations were only conducted to measure oil film thickness on the piston second and third land at low engine load. The results obtained were satisfying and were used for the preliminary development of the models of oil transport on the piston lands.

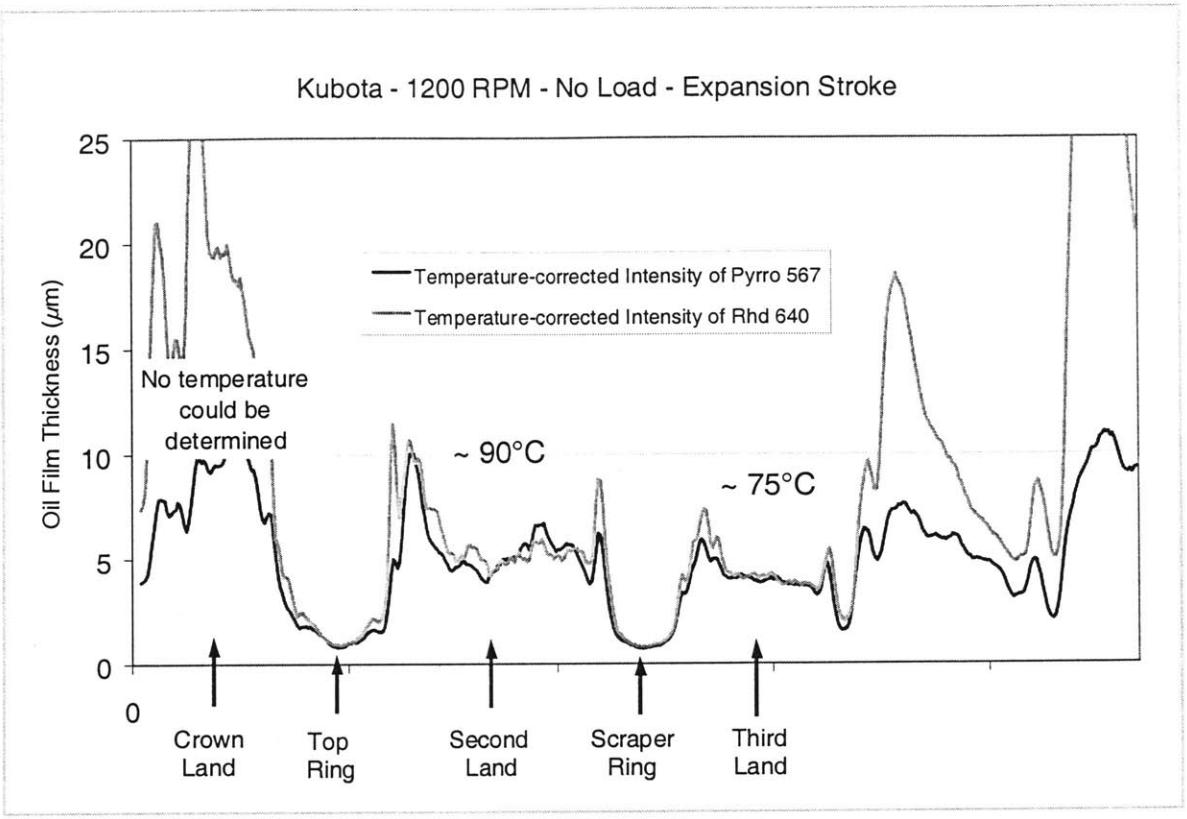


Figure 2.27 – Oil film thickness profile calibrated with Dual Emission Fluorescence technique. Kubota engine – 1200 RPM No load – Expansion stroke.

Summary and conclusions: As explained in Section 2.4.1.3, to use dyes without emission overlap, we had to select a dye combination that could exhibit significant pumping. Besides, it was found that due to the absorption of the fluorescence emission of one dye by the other, the behavior of both dyes could be significantly coupled. As a consequence, the pumping effect can greatly alter the capability of the dual emission calibration in accurately determining the oil film thickness and temperature. Eventually, this coupling effect was found to be a greater problem at high temperature (above 110 °C) where dyes becomes noticeably more sensitive to temperature.

There are two possibilities to extend the temperature range of the dual emission calibration technique and to improve the accuracy of the temperature measurement:

1. If one of the two dyes has a large Stokes shift (> 70 nm), the behavior of both dyes can be completely de-coupled since both emission spectra overlap and emission/absorption spectra overlap can be avoided.
2. If the fluorescence emission of the dye that is more sensitive to temperature is re-absorbed, the pumping effect can be beneficial as it can enhance the accuracy of the technique.

These two options were not tested since no suitable dye was found when the work was conducted. It is believed that, unless one of the above options is implemented, the capability of dual emission LIF technique to simultaneously measure temperature and thickness of the oil film in internal combustion engines will remain very limited.

2.4.2.5 Improved In-Situ Calibration (applied to the PSA Engine)

Principles: Since the dual fluorescence emission technique could not be used above 110 ° C, an improved in-situ calibration technique was developed. The main drawback of standard in-situ calibration techniques is that they fail to account for the effect of temperature on the fluorescence emission [39]. In this work, using the knowledge we gained on the behavior of fluorescence emission from multiple dye solution, we elaborated a two-dye combination with reduced sensitivity to temperature. First of all, among the selected dyes (see Section 2.4.1.3 – Dye selection), one of the least temperature sensitive dye was chosen: Pyrromethene 567. Secondly, effort was made to reduce the temperature sensitivity of the detectable fluorescence emitted by Pyrro 567. Here, it is very important to distinguish emitted fluorescence from detectable fluorescence. The temperature response of the emitted fluorescence depends on the dye chemical structure and thus can not be modified. The detectable fluorescence corresponds to the photons that exit the oil layer. In other words, the detectable fluorescence is the part of the emitted fluorescence that is not absorbed by the oil or by other dyes. If the absorbance of the solution at the wavelength of Pyrro 567 emission (570 nm) is made temperature sensitive, the decay of the emitted fluorescence due to temperature increase could be compensated by a decrease of the solution absorbance. An easy way to modify the solution absorbance at a specific wavelength is to add a dye whose absorption spectrum corresponds to that wavelength. Accordingly, the solution absorbance σ_{g1} seen by Pyrro 567 emission can be modified by adding Rhd 640 in the solution. In order to further analyze the effect of temperature on the detectable emission, it is necessary to look at the equation relating the fluorescence intensity to the solution characteristics:

$$I_{567}(\lambda) = \frac{\alpha_s}{4\pi} \cdot \frac{S_p \cdot I_0 \cdot C_{567} \cdot \varepsilon_{567}(\lambda_{laser}, T) \cdot \phi_{567}(\lambda, T)}{\sigma_{g1}} \cdot \left[1 - \exp(-(\sigma_{g1}) \cdot h)\right] \cdot d\lambda \qquad (2.22)$$

$$\sigma_{g1} = C_{567} \cdot \varepsilon_{567}(\lambda_{laser}, T) + C_{640} \cdot \varepsilon_{640}(\lambda_{laser}, T) + \alpha \cdot C_{640} \cdot \varepsilon_{640}(\lambda, T) + 2 \cdot \sigma_{oil} \qquad (2.23)$$

According to Equation 2.21, the temperature effect on Pyrro 567 detectable emission can be analyzed by examing two different terms A and B such that:

$I_{567} = Ct \cdot A(T) \cdot B(T)$ where Ct is a constant

$$A = C_{567} \cdot \varepsilon_{567}(\lambda_{laser}, T) \cdot \phi_{567}(\lambda, T) \qquad B = \frac{1 - \exp(-(\sigma_{g1}) \cdot x)}{\sigma_{g1}} \qquad (2.24)$$

A, which follows the evolution of the absorptivity and quantum yield efficiency (see Figure 2.28), decreases with temperature. B increases when σ_{g1} decreases. σ_{g1} is a linear function of the absorptivity of both dyes and therefore decreases with temperature. Consequently, B inceases with temperature. As a result, the effects of temperature on both terms could theoretically compensate each other. In reality, the decay of A is usually greater than the increase of B, and the intensity of the detectable fluorescence decreases with temperature. However, as B is a function of σ_{g1}, its temperature sensitivity can be increased by changing the dye concentrations.

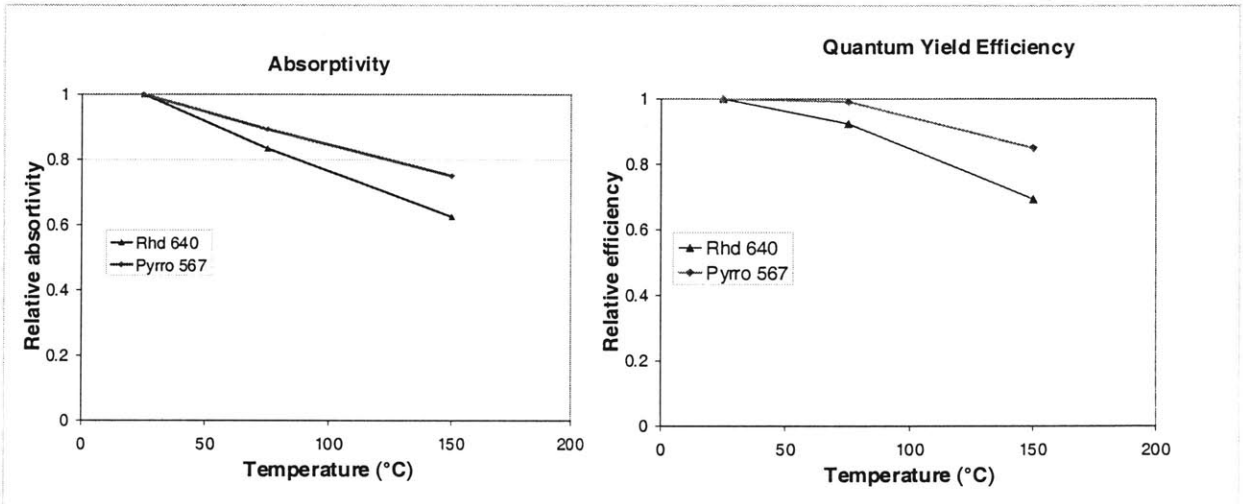


Figure 2.28 – Evolution of absorptivity and quantum yield efficiency with temperature for Rhd 640 and Pyrro 567.

Dye concentration optimization: In order to optimize the dye concentrations, it is needed to further analyze the relationship between σ_{g1} and the temperature sensitivity of I_{567}. Ideally, we would like to have:

$$\frac{\partial I_{567}}{\partial T} = Ct \cdot \left(A \cdot \frac{\partial B}{\partial T} + B \cdot \frac{\partial A}{\partial T} \right) = 0 \text{ which is equivalent to } \frac{1}{B} \cdot \frac{\partial B}{\partial T} = -\frac{1}{A} \cdot \frac{\partial A}{\partial T} \qquad (2.25)$$

Where $$\frac{1}{A} \cdot \frac{\partial A}{\partial T} = \frac{1}{\varepsilon_{567}(\lambda_{laser}, T)} \cdot \frac{\partial \varepsilon_{567}(\lambda_{laser}, T)}{\partial T} + \frac{1}{\phi_{567}(\lambda, T)} \cdot \frac{\partial \phi_{567}(\lambda, T)}{\partial T} \qquad (2.26)$$

From Equation 2.26, we can see that $\frac{1}{A}\cdot\frac{\partial A}{\partial T}$ is negative and independent of dye concentrations. In order to reduce the temperature sensitivity of I_{567}, $\frac{1}{B}\cdot\frac{\partial B}{\partial T}$ should be increased so that Equation 2.25 is satisfied. From Equation 2.24, we have:

$$\frac{1}{B}\frac{\partial B}{\partial T}=\frac{1}{\sigma_{g1}}\cdot\frac{\left(\exp\left(-\sigma_{g1}\cdot x\right)\left(1+\sigma_{g1}\cdot x\right)-1\right)}{1-\exp(-\sigma_{g1}\cdot x)}\cdot\frac{\partial\sigma_{g1}}{\partial T} \tag{2.27}$$

Since the dye concentrations are usually changed proportionally, in order to maintain similar fluorescence intensity levels for both dyes, σ_{g1} and its derivative with respect to temperature can be expressed as follows:

$$\sigma_{g1}=\kappa\cdot\sigma_{g1}^{0} \quad \text{with} \quad \sigma_{g1}^{0}=C_{567}^{0}\cdot\varepsilon_{567}\left(\lambda_{laser},T\right)+C_{640}^{0}\cdot\varepsilon_{640}\left(\lambda_{laser},T\right)+\alpha\cdot C_{640}^{0}\cdot\varepsilon_{640}\left(\lambda\ ,T\right)$$

$$\frac{\partial\sigma_{g1}}{\partial T}=\kappa\cdot\frac{\partial\sigma_{g1}^{0}}{\partial T} \quad \text{where} \quad \frac{\partial\sigma_{g1}^{0}}{\partial T} \text{ is a constant.}$$

(Here, the absorbance of oil, which is very small compare to the absorbance of both dyes, was neglected)

Then, Equation 2.27 can be written as:

$$\frac{1}{B}\cdot\frac{\partial B}{\partial T}=\frac{\left(\exp\left(-\sigma_{g1}^{0}\cdot\kappa\cdot x\right)\cdot\left(1+\sigma_{g1}^{0}\cdot\kappa\cdot x\right)-1\right)}{1-\exp(-\sigma_{g1}^{0}\cdot\kappa\cdot x)}\cdot\frac{\partial\sigma_{g1}^{0}}{\partial T}\cdot\frac{1}{\sigma_{g1}^{0}} \tag{2.28}$$

where $\frac{\partial\sigma_{g1}^{0}}{\partial T}\cdot\frac{1}{\sigma_{g1}^{0}}$ is constant. Here, the analysis is conducted for the part of Equation 2.28 that is function of κ, and for convenience we study it as function of $\kappa\cdot\sigma_{g1}^{0}\cdot x$:

$$G=\frac{\left(\exp\left(-\sigma_{g1}^{0}\cdot\kappa\cdot x\right)\cdot\left(1+\sigma_{g1}^{0}\cdot\kappa\cdot x\right)-1\right)}{1-\exp(-\sigma_{g1}^{0}\cdot\kappa\cdot x)} \tag{2.29}$$

$\kappa\cdot\sigma_{g1}^{0}\cdot x$ represents the "optical thickness" of the solution. If $\kappa\cdot\sigma_{g1}^{0}\cdot x$ is much less than 1, the solution is optically thin and vice-versa.

In Figure 2.29, which shows the evolution of G as a function of $\kappa\cdot\sigma_{g1}^{0}\cdot x$, it can be seen that the larger $\sigma^{0}_{g1}.x$ is, the greater $\frac{1}{B}\cdot\frac{\partial B}{\partial T}$ and therefore the less temperature sensitive I_{567} is. Accordingly, the dye concentrations should be increased to minimize the temperature sensitivity of the detectable fluorescence intensity. However, since the dye combination is to be used for in-situ calibration of the

oil film thickness, the absorbance σ_{gl} of the solution has to be small enough so that the fluorescence intensity is proportional to the thickness at constant temperature. Using the above analysis and test results, the following quantity of Pyrro 567 and Rhd 640 were selected to be used for in-situ calibration:

- Concentration of Pyrro 567: 1.0 10^{-4} mol/liter,
- Concentration of Rhd 640: 1.0 10^{-4} mol/liter.

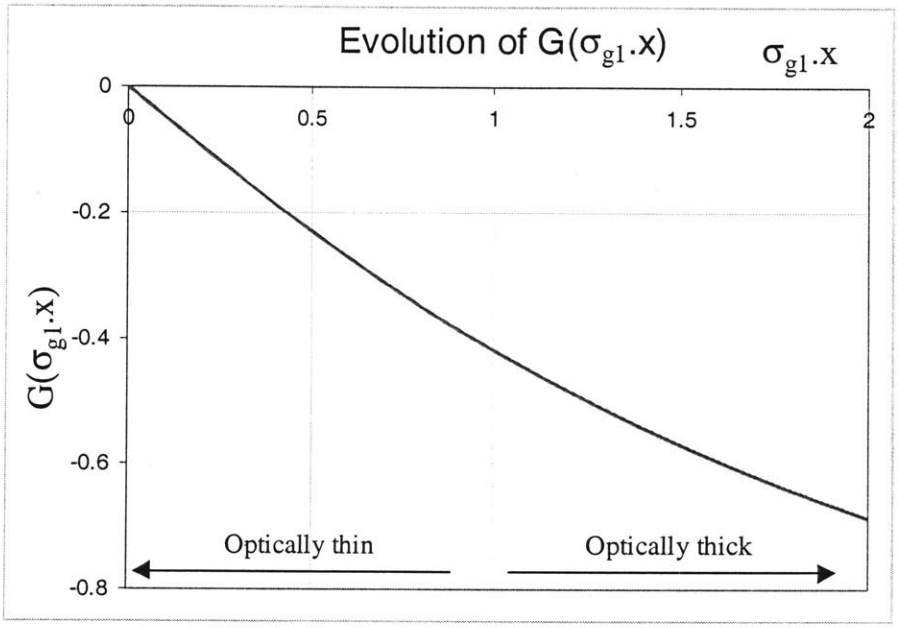


Figure 2.29 – Evolution of the function G (σ_{gl}.x).

Results: The temperature behavior of the obtained dye combination is shown in Figure 2.30. The detectable fluorescence emitted by Pyrro 567 slightly increases with temperature from 25 to 70°C, showing the effect of the decrease of Rhd 640 absorptivity. At 100°C the level of detectable fluorescence emitted by Pyrro 567 is almost equal to the level of fluorescence emitted at 25°C. Above 100°C, the decrease of Pyrro 567 quantum yield efficiency is larger and can not be completely compensated by the decay of Rhd 640 absorptivity. As a result, the level of Pyrro 567 detectable fluorescence slightly decreases with temperature. Since during engine operation the minimum temperature encountered on the piston lands is around 100°C (at low load, on the third land with coolant temperature regulated at 50°C), the level of fluorescence emission detectable at 100°C can be chosen as the reference level. Accordingly, the fluorescence emission at 150°C shows a decay of maximum 15%. At 170°C the maximum temperature dependency was found to be 30 %. It can be noticed that with this dye combination, the temperature dependency of Pyrro 567 depends on the thickness on the oil film. This is due to the fact that the technique used to compensate the effect of

temperature is based on the modification of the solution absorptivity and is therefore more efficient for thick oil layers. Overall, among all the single dyes and dye combinations tested in this work, this particular combination of Pyrro 567 and Rhd 640 produced the least temperature sensitive fluorescence emission.

As shown in Figure 2.31, the linearity range of the Pyrro 567 emission obtained with the selected dye concentrations extends above 100 μm. Above 150 μm, Pyrro 567 emission starts to saturate due to the significant re-absorption by Pyrro 640. Rhd 640 emission was found to be strictly linear up to 75 μm. Above 75 μm, the pumping of Rhd 640 by Pyrro 567 emission significantly contribute to Rhd 640 excitation. The additional fluorescence emission due to the pumping effect is proportional to the square of the oil layer thickness (see Equation 2.19). As a result, the level of Rhd 640 fluorescence emission measured above 75 μm is slightly superior to the level that would be predicted with linear approximation. Furthermore, with the selected dye concentrations, for oil thickness lower than 50 μm, the level of fluorescence obtained from Pyrro 567 (using a 570 nm narrow-band filter) is significantly greater than the level obtained from Rhd 640 (using a 650 nm narrow-band filter). As a result, the signal to noise ratio is significantly less. Consequently, Pyrro 567 fluorescence emission was used to observe thin oil accumulation. On the other hand, Rhd 640 was found to be more suitable to observe oil accumulation thicker than 100 μm for which Pyrro 567 exhibits appreciable saturation.

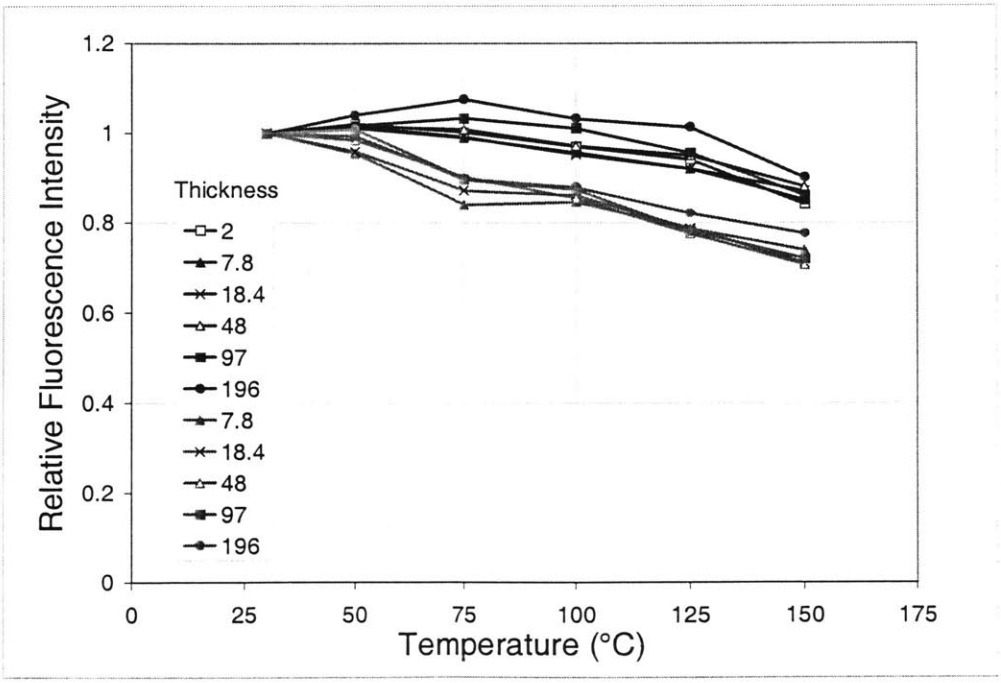


Figure 2.30 – Temperature response of Pyrro 567 (1.0 10^{-4} mol/liter) and Rhd 640 (1.0 10^{-4} mol/liter) while mixed together (Emission of Pyrro 567 measured at 570 nm with a 10 nm narrow-band filter, emission of Rhd 640 measured at 650 nm with a 10 nm narrow band filter).

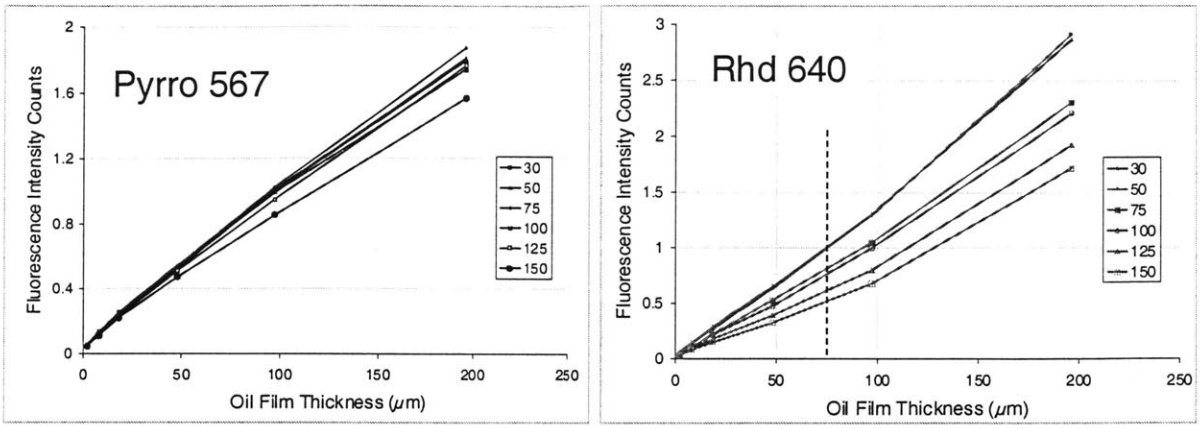


Figure 2.31 – Thickness and temperature response of Pyrro 567 ($1.0\ 10^{-4}$ mol/liter) and Rhd 640 ($1.0\ 10^{-4}$ mol/liter) while mixed together (Emission of Pyrro 567 measured at 570 nm with a 10 nm narrow-band filter, emission of Rhd 640 measured at 650 nm with a 10 nm narrow band filter).

Applications: The selected dye combination and dye concentrations were used to conduct in-situ calibration on data acquired in the PSA single-cylinder engine. In-situ calibration requires the use of a geometrical feature of known depth as a reference thickness. The geometrical feature, which is usually a step or a groove machined on the piston, has to be wide enough so that it covers several pixels on the CCD camera and deep enough so that the signal to noise ratio of the corresponding signal is small. Ideally, to maximize the signal to noise ratio, the depth of the groove should be close to the linear range of the fluorescence signal. To satisfy all these requirements there needs to machine a 100-μm deep groove on the piston land. On the other hand, such a deep groove would modify the oil transport pattern on the land where it is located and therefore could not be used. In this work, the tool marks resulting from the piston surface machining were used for the calibration. The tool marks are 10-μm deep grooves that are 300 μm apart. These tool marks exist on the first and second land and on the piston skirt. The best approach to calibrate the oil film thickness on the piston lands would have been to use the signal emitted by the oil trapped in the tool marks located on the second and top land. By doing so, the effect of temperature would have been best minimized. However, even though the average oil film thickness on the lands was usually greater than 10 μm, the tool marks located on the top two lands of the piston were almost never full of oil (see Figure 32), and thus could not be used for calibration. Consequently, the in-situ calibration was done using the tool marks located on the upper part of the piston skirt. Even though, the tool marks located on the skirt provided an adequate reference for the in-situ calibration, the author believes that a more systematic calibration could be obtain if specific reference marks were machined. An example of a calibrated oil film profile acquired in the PSA single-cylinder engine is shown in Figure 2.33.

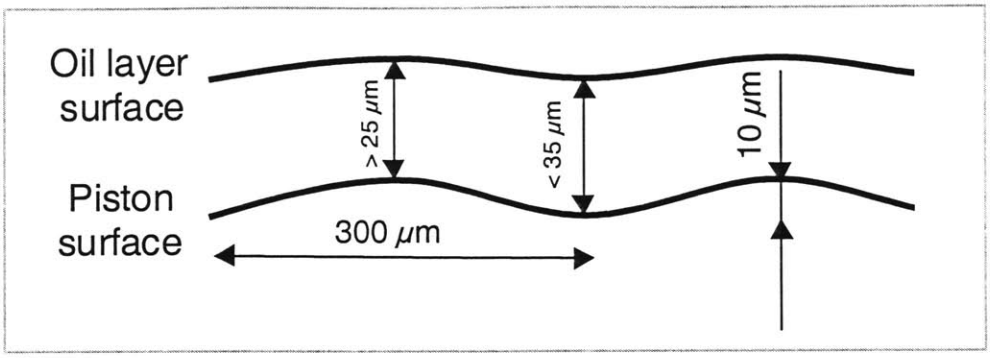


Figure 2.32 – Aspect of the oil layer on the piston lands with toll marks
(shown for an average oil thickness of 30 μm).

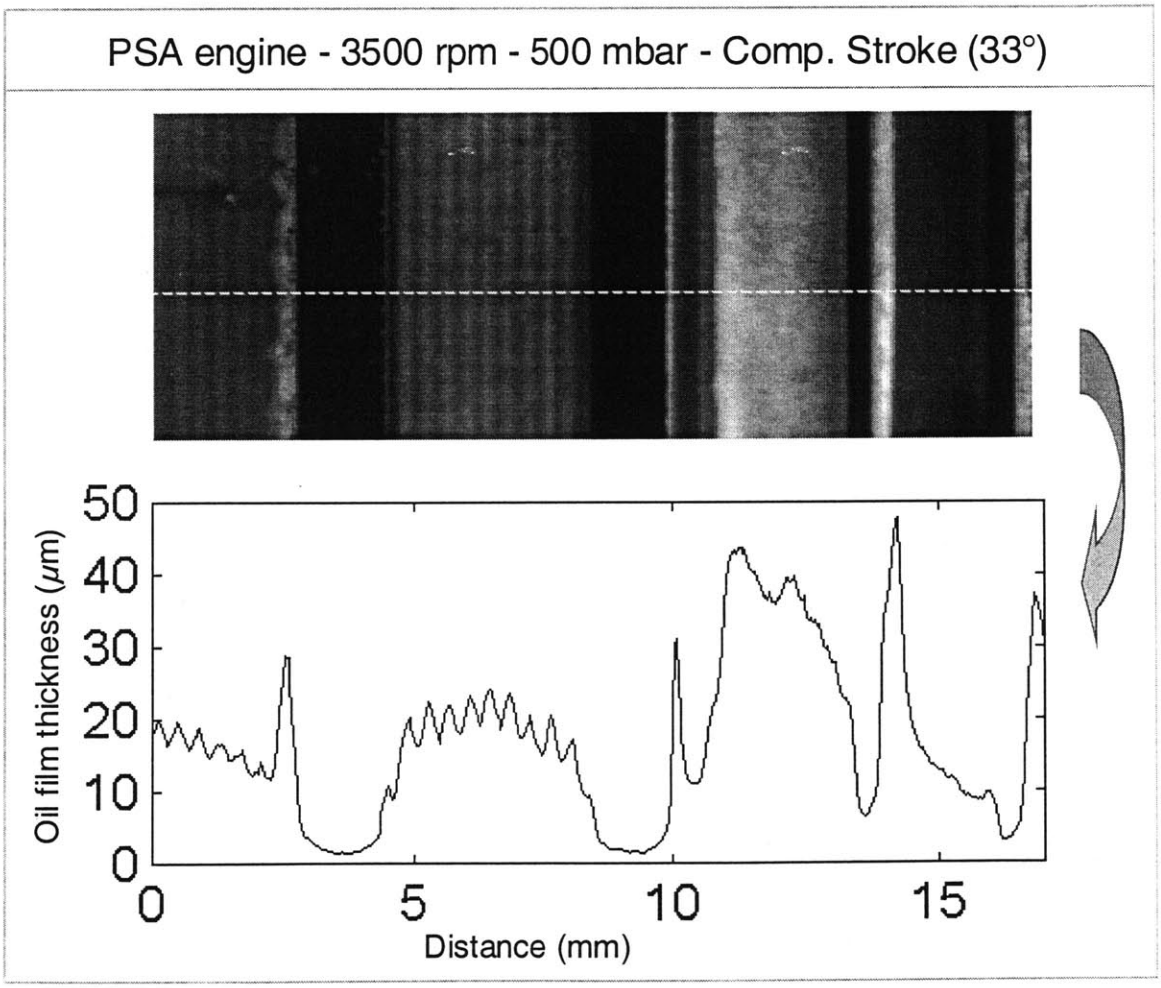


Figure 2.33 – Oil film thickness profile calibrated with Dual Emission Fluorescence technique.
Kubota engine – 1200 RPM No load – Expansion stroke.

2.4.3 Imaging System

2.4.3.1 Laser

In this project the second harmonic (532 nm) of a Nd-Yag pulsed laser was used as the fluorescence excitation source. The main characteristics of the laser and their effects on the performance of the visualization system are discussed in this section.

Wavelength: For LIF experiments, the wavelength of the laser is very critical since it limits the choice of fluorescing dyes. Ideally, ultraviolet lasers are more suitable for LIF since they can be used in combination with wide variety of dyes. The 532-nm wavelength of the laser used in this work appeared to be a strong limitation for the choice of suitable dyes for calibration.

Pulse duration: In order to obtain sharp image of the piston up to 6000 rpm, the exposure time had to be less than 1 μs. Such short exposure time can either be achieved by pulsing the light source or by using a high-speed electronic shutter on the camera. In this work, the short duration of the laser pulse was used to limit the exposure time. The laser pulse itself was 6 nanoseconds long. The fluorescence process, which is triggered by the laser excitation, typically lasts from 1 to 10 nanoseconds. Therefore, the fluorescence emission lasts between 6 and 16 nanoseconds. On the camera used for this project, the shuttering was done by activating and deactivating the image intensifier. This operation was controlled by a 1000-volt pulse and the minimum duration of the shutter cycle was limited by the capability of the high voltage pulse generator. With the equipment used in this project the minimum duration of the intensifier operation was 1 ms. Consequently, the signal acquired by the camera was the integration of the fluorescence emission over the 16 ns of the fluorescence process.

Energy output: The power output of the laser was about 15~25 mJ/pulse. This level of energy output was found to be adequate for the visualization purpose. However, it is believed that 50 to 100 mJ/pulse is more suitable since less intensifier gain and/or smaller lens aperture is needed. The level of intensification was not so much of a problem since the signal to noise ratio was relatively low. However, decreasing the aperture can increases the depth of field and can ease the subtle focusing process.

Laser pulsation frequency: The laser is composed of two laser heads. Each of them can pulse at rate up to 20 Hz and can produce between 15~25 mJ/pulse. The laser could be used in various configurations depending on the need of the experiment conducted:

1. The two lasers could be used alternately to generate a beam pulsing at rates up the 40 Hz.
2. The two lasers could be used to generate two pulses separated by a very short time interval. This timing was used in conjunction with the frame transfer feature of the CCD camera (described in Section 2.4.4) to generate snapshots of the oil distribution acquired from one to a few milliseconds apart.
3. The lasers could be used simultaneously to double the power output.

Since it was difficult to maintain the two lasers at comparable output levels, experiments requiring the use of both lasers were only conducted to address some specific visualization needs.

Beam profile: The profile of the beam at the output of the laser (near field) was roughly Gaussian. Due to divergence of the beam, its profile changes along the beam path. The beam was found to exhibit a "top hat" profile approximately two meters away from the laser heads (far field). Since the top hat profile results in an almost uniform intensity distribution, it is more appropriate for quantitative LIF measurement. Consequently, the laser was purposely used in the far field where its profile was found to be optimum for oil film thickness evaluation.

Laser intensity variation: First of all, the total energy delivered during each pulse was found to vary from pulse to pulse. This variation was reduced to an acceptable level (+ or – 3%) by allowing the laser to warm up for 45 minutes and maintaining the cavity chamber free of oxidation. Second, from pulse to pulse the laser beam was found to have significant intensity variation across the beam profile. These variations are due to the continuously changing thermal loading of the Nd-Yag rod and are thus set by the laser construction. However, it was found that in the far field these variations were significantly attenuated by beam divergence.

To conduct Dual LIF calibration, the laser beam temporal and spatial intensity variations were corrected. The correction involved three steps:

1. Generate an average image of the oil distribution
2. Generate a normalized average image of the laser beam
3. Divide the average oil distribution by the normalized average beam image.

To conduct in-situ calibrations, the global laser intensity variations were not an issue and thus were not accounted for. Moreover, when the oil distribution was relatively steady, the LIF images were averaged to minimize the effect of the local beam intensity variation.

Laser beam conditioning: The diameter of the beam at the exit of the laser was 2.5 mm. In order to cover the entire ring pack the beam was expanded by a factor of 10. Due to geometrical limitations of the optical access, a cube beamsplitter had to be used to reflect the laser beam toward the visualization window (see Figure 2.37). A cube beamsplitter was preferred to a dichroic mirror because it does not produce ghost images. The disadvantage of cube beamsplitter is that they usually equally transmit and reflect all the wavelengths. As a result, with a setup like the one presented in Figure 2.36, 50% of the incoming light is transmitted away from the engine and 50% of the emitted fluorescence is reflected away from the camera. Overall 75 % of the laser energy is not used to produce the detected signal. In this application, the reflection of the laser into the optical access was greatly improved by using the sensitivity of the beam splitter to the incoming light polarization. This improvement was made by taking advantage of the fact that for a cube beamsplitter, the portion of transmitted and reflected light depends on the direction of polarization of the incoming light. The laser beam was polarized to optimize the portion of laser light reflected into the engine. As a result, only 52% of the laser intensity was wasted.

2.4.3.2 Detection device

An intensified CCD camera (Princeton Instrument Pentamax 512) was used to acquire the two-dimensional images of the oil distribution. The Pentamax 512 CCD camera was chosen for its compromised overall characteristics:

Intensifier: With the laser used in this work, the intensification feature was needed to be able to detect the fluorescence signal emitted by the dyes. The intensifier was used at half of its gain (Hidrovo and al. [54] conducted oil film visualization experiments using the same excitation wavelength and without using intensifier, however, they used a laser 5 times more powerful and up to 100 times larger dye concentrations).

CCD panel: The 1024x512-pixel CCD panel is divided into two parts. One side (512x512) is exposed for image acquisition and the other (also 512x512) is permanently masked and is used as a buffer memory. By transferring frames from the exposed side to the buffer part, one image can be acquired while the previous one is being read, converted and downloaded to the computer. As a result, the minimum duration between two consecutive frames is determined by the time required to shift frames from one side of the CCD to the other one (1 ms). Using a 120-macro lens, the 512x512-pixel CCD panel produced images with resolution as high as 30 μm/pixel. Finally, the cooling

feature of the camera was used to maintain the CCD panel at –20 °C and thus limit the noise resulting from thermally induced charge buildup.

Fast A/D converter: The camera is equipped with a 12-bit 5MHz A/D converter. With this converter, in continuous operation the camera can output up to 15 full frames per second (fps) and up to 30 half-size fps. The rectangular shape of the engine optical access favored the used of a rectangular portion of the CCD panel. Accordingly, a portion of 512x256 pixels was used and the camera was allowed to output up to 30 frames per seconds. With this maximum frame rate, one frame every cycle could be acquired up to 3600 rpm. Finally, the 12-bit dynamic range was found to be optimal for the range of oil film thickness measured in this work.

Signal outputs: The camera is equipped with one digital and one video output. As a result video recordings and snapshots images of the oil distribution could be acquired simultaneously.

The camera was found to have two unexpected limitations. First, the 1000-volt pulse required to drive the intensifier had a rising time of about 0.5 to 1 ms. Consequently, full intensification was obtained only after 1 ms of intensifier operation. Accordingly, the acquisition of LIF images was timed such that the intensifier was activated 2 ms before the laser pulse (see Figure 2.34). Second, the CCD panel exhibited significant blooming. As a result, the thickness of very thin oil film adjacent to very thick oil accumulation could not be measured. In particular, the oil film thickness between the land of the oil control ring and the liner could not be evaluated.

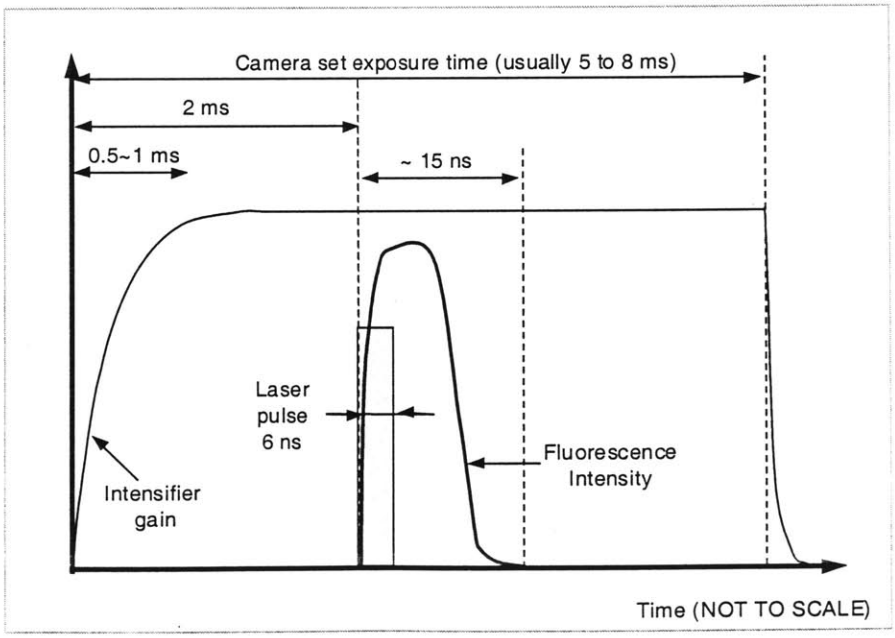


Figure 2.34 – Camera and laser timing.

2.4.3.3 Control and Timing

Snapshot acquisition timing: A programmable counter-board was used to time the acquisition of the LIF images with the piston position. Two major acquisition modes were used:

1. Continuous acquisition mode: In this mode one image of the oil distribution was acquired every engine cycle at a preset crank angle degree. Only one laser was used and therefore the acquisition frequency was limited to 20 Hz. Accordingly, acquisitions were conducted every other cycles above 2400 rpm and every 3 cycles above 4800 rpm. This mode was used to study oil transport over time scales ranging from one to several engine cycles.
2. Frame transfer mode: In this mode the two lasers were used to generate two LIF images one or a few milliseconds apart. The two images were acquired and stored on the CCD panel. Then, the camera was given the necessary time (66 ms for two half-size frames) to convert the two images and download them to the frame grabber. Depending on the engine speed and the time interval between the two images, one or more engine cycles had to be skipped before the following burst acquisition could be completed. This acquisition mode was used to investigate oil transport mechanisms with time scales ranging from a few crank angle degrees to one engine revolution. Figure 2.35 shows an example where the frame transfer mode was used to study stroke to stroke oil distribution variation.

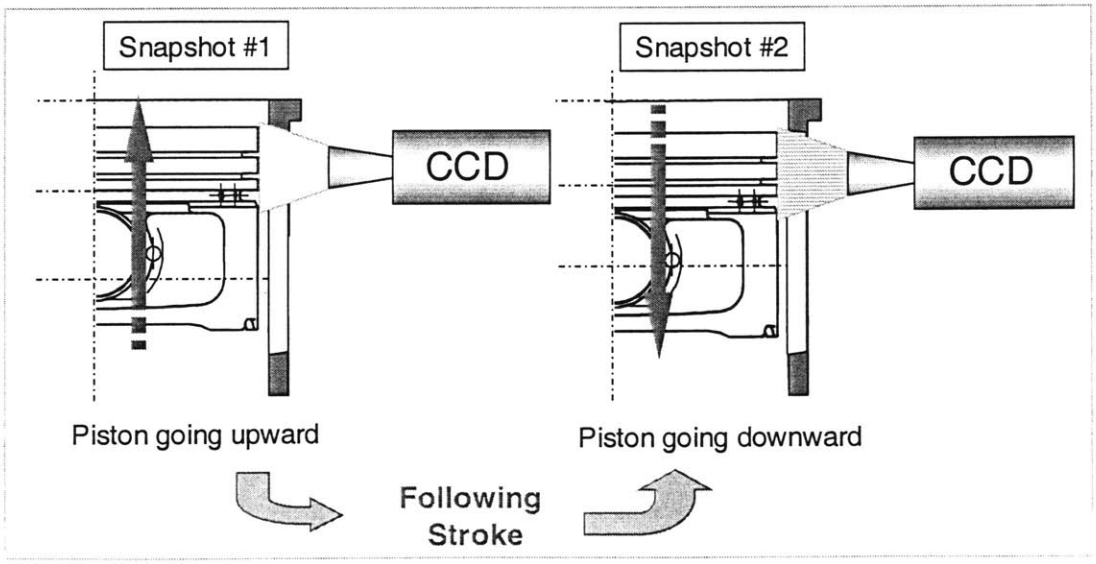


Figure 2.35 – Example of burst acquisition for stroke to stroke oil distribution observation. (Using frame transfer mode).

Video acquisition timing: The real time evolution of the oil distribution over periods of several minutes was recorded using the video output of the camera and a digital video recorder. For the video recording the imaging system was working in the continuous acquisition mode defined above. Therefore, the videos contained images of the oil distribution acquired every 720 crank angle degrees at one specific piston position. Accordingly, between each frame the crankshaft had turned two full revolutions, and therefore, unrecorded phenomena may have happened between two consecutive frames.

Since the video rate is fixed at 30 frames per second and thus independent of the engine rotation speed, each new video frame did not always correspond to a new oil distribution image. Every time the video signal was refreshed (30 times per second), the last frame acquired by the CCD panel was supplied to the video output. Since in continuous acquisition mode, the acquisition frequency was limited at 20Hz, the video rate was always greater than the acquisition rate. Accordingly, at any engine speed every image acquired was displayed on the video. The timing of the image acquisitions, the engine cycles and the video frame output is shown in Figure 2.36.

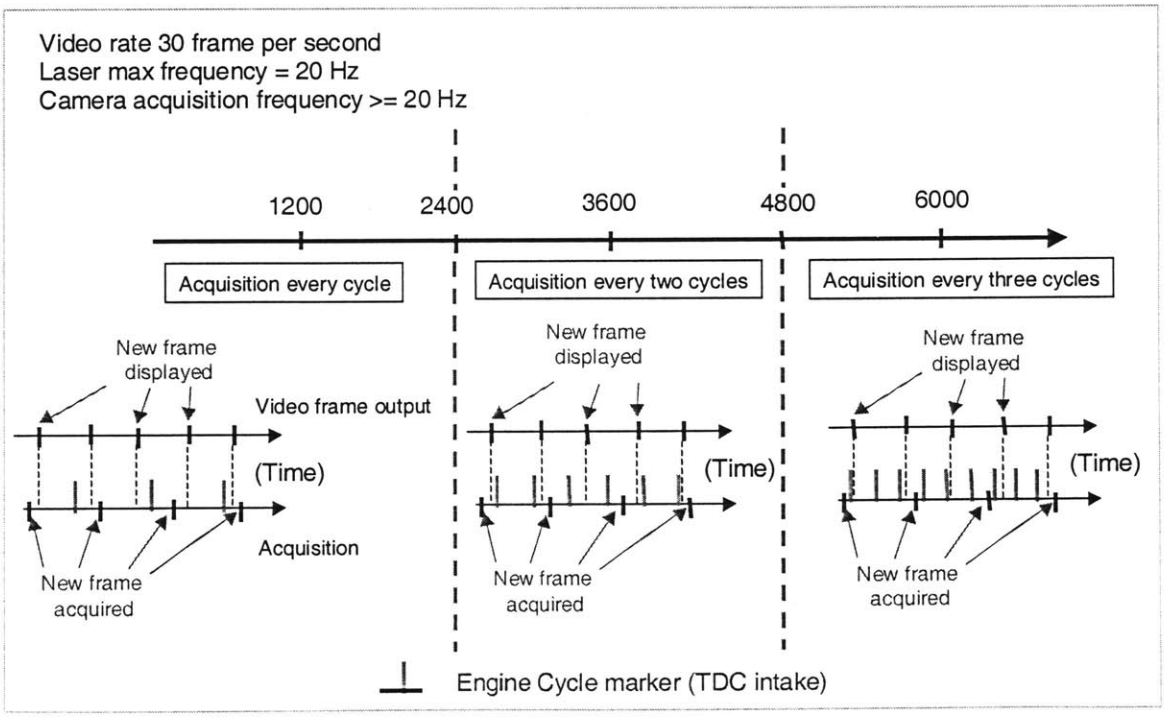


Figure 2.36 – Timing of the LIF images acquisition and video frame rate.

2.4.3.4 Complete Optical Setup

Figure 2.37 described the complete optical setup used in this work and Figure 2.38 shows the structure of the control diagram used to time various events related to the engine operation and the LIF image acquisition.

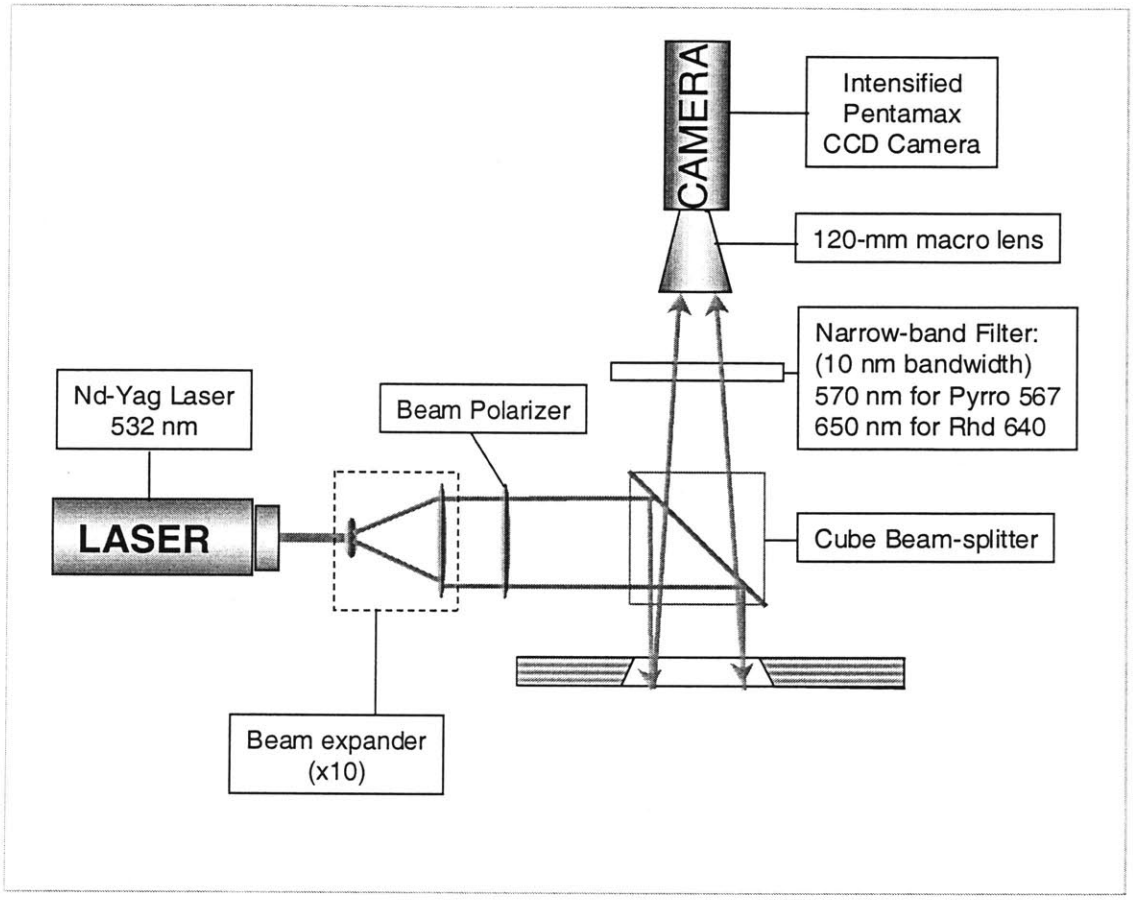


Figure 2.37 – Complete optical setup.

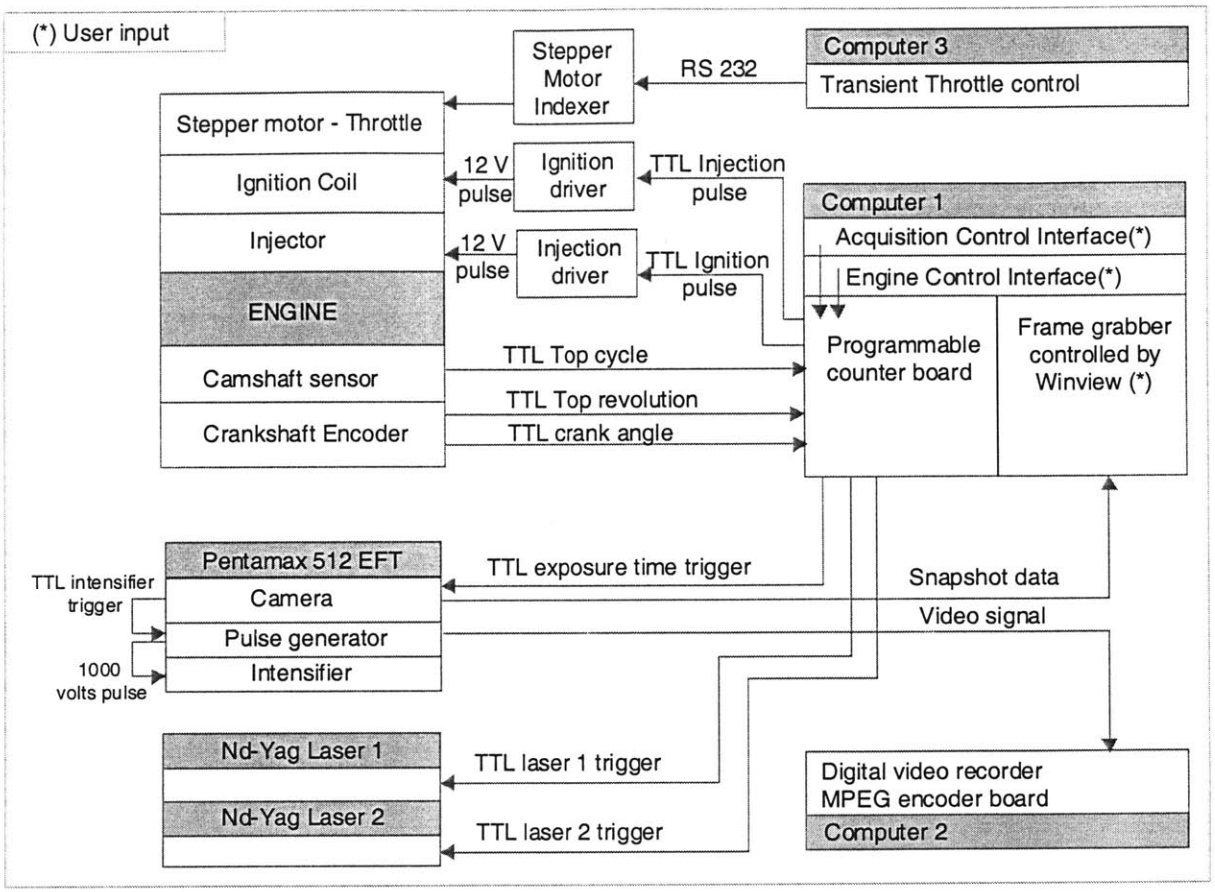


Figure 2.38 – Engine and acquisition control diagram.

2.4.4 Blow-by Measuring System

2.4.4.1 Challenges

As it is explained in Section 2.1.2, for the completion of this project it was essential to have a mean of accurately measuring the blow-by flow rate in all the tested engine operating conditions. Measuring the blow-by flow rate of a single-cylinder engine is a difficult task for the two following reasons:

1. Because of the nature of blow-by gases, blow-rate measurement can not be conducted with any kind of flowmeter. Blow-by gases contain combustion soot, oil droplets and vapors and a significant percentage of water. Therefore, only equipment that can tolerate these various contaminants may be used. Laminar elements, rotameters and hot wire are thus to be excluded. Displacement flowmeters could be used, however, they require a relatively long measuring period (over several minutes) and they induce relatively high back pressure. The two most commonly used techniques are the vortex shading technique and the orifice pressure drop measurement.

Both methods can provide accurate blow-by measurement for flow rate ranging from 4 to several hundreds liters per minute (lpm). Typically, the blow-by flow rate of a 0.5-liter displacement single cylinder engine range from 0.2 to 15 lpm. Consequently, neither the vortex shading technique nor the orifice pressure drop measurement could be used to measure the lower range of blow-by flow rate encountered in the PSA engine. Since no appropriate measuring device was available in the market, a customized blow-by flowmeter was developed for this project.

2. The second major issue to be addressed when measuring blow-by in a single cylinder engine is the flow pulsations. The blow-by flow pulses have two origins: the cylinder pressure peaks and the piston alternating motion. For a multi-cylinder engine, the crankcase volume is constant since the volume displaced by one piston is always compensated by the volume swept by another one. Therefore, in passenger car engines, the piston motions do not create significant blow-by pulsations. On the other hand, for a single cylinder engine, the crankcase volume variation induced by the piston motion can create an oscillating flow that can be up to 10 000 times larger in amplitude than the average blow-by (see Figure 2.39). Consequently, an effective attenuation system was required to dampen the oscillations and make the average blow-by flow rate measurable. Accordingly, a low-pass acoustic filter was designed and implemented between the engine and the blow-by flowmeter. The pulsation due to the cylinder pressure variations are much smaller in amplitude and occur at half the frequency of the flow oscillations resulting from the piston motion. Therefore, the low-pass filter designed to filter out the oscillations resulting from the piston displacement easily suppressed the pulsations induced by the cylinder pressure variations.

	At 1000 rpm	At 6000 rpm
Blow-by Oscillation (liter/minute)	1600	9600
Pressure oscillation in the crankcase (bar)	~ 0.08	~0.08

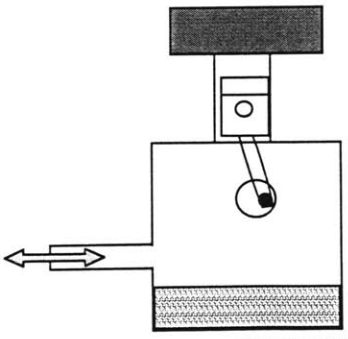


Figure 2.39 – Blow-by oscillations due to the piston motion.

2.4.4.2 Dampening System

The maximum acceptable oscillation level was considered to be about 0.1 liter/min. Accordingly, the filter had to be designed to achieve a minimum attenuation of 80 dB at 16 Hz (1000 rpm) and 100 dB at 100 Hz (6000 rpm). Moreover, in order not to alter the gas flow through the ring pack, it was necessary to maintain the crankcase pressure variations at a low level (< 10 mbar). Therefore, the acoustic filter had to be designed such that the resonance frequency associated with the crankcase pressure would be lower than the frequency corresponding to the minimum engine speed (1000 rpm). An acoustic filter is composed of various volumes, which acts as capacitance, and hose, which acts as inductance. A first order filter, which would have been composed of just one volume (capacitance), would have required a container of 120 m^3 to produce the attenuation needed. Consequently, to achieve the required levels of attenuation without using enormous components it was necessary to design a higher order filter. Accordingly, it was decided to use a fourth order low pass filter composed of two capacitances and two inductances. The crankcase volume was used as the first capacitance. Two hoses and one container were added to complete the filter (see Figure 2.40). An acoustic model was developed to correctly dimension each element.

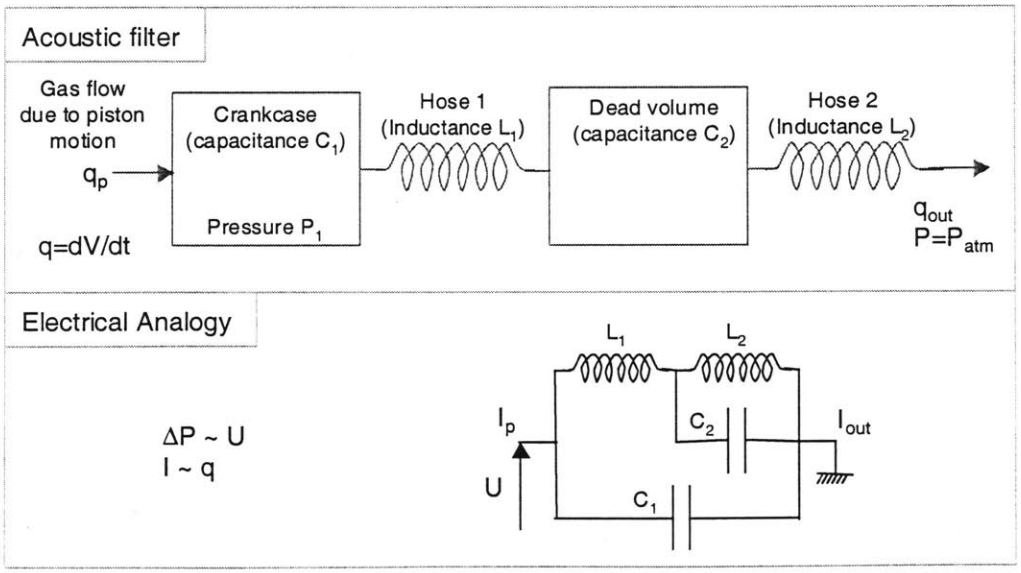


Figure 2.40 – Fourth order acoustic filter (Electrical analogy).

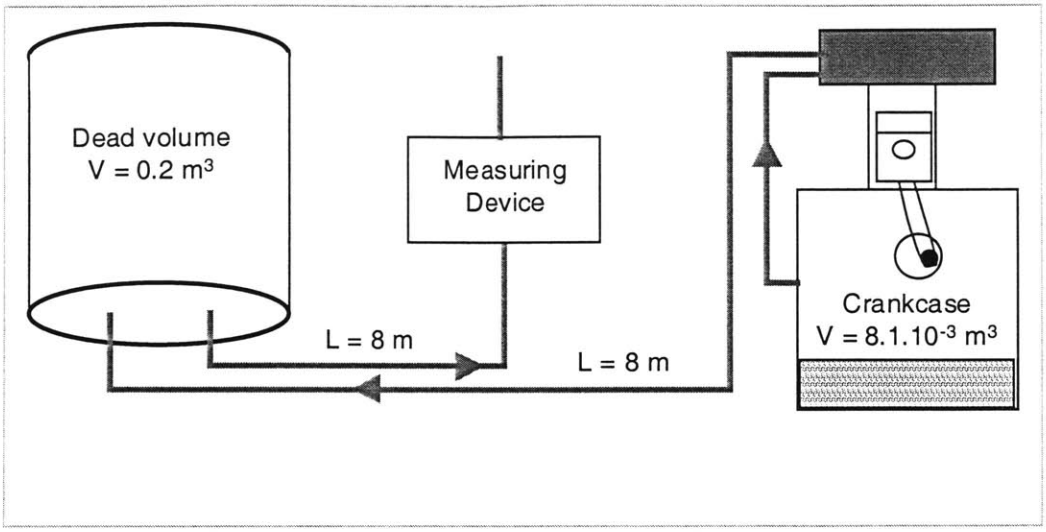


Figure 2.41 – Designed acoustic filter (Components and dimensions).

Acoustic model: An electrical analogy was used to model the acoustic filter (see Figure 2.40). The acoustic capacitance and inductance are defined as follows:

$$\text{Capacitance: } C = \frac{\Delta V}{\Delta P} \tag{2.30}$$

$$\text{Inductance: } L = \Delta P \cdot \left(\frac{dt}{dq} \right) \tag{2.31}$$

For an ideal gas undergoing an isentropic transformation, for small pressure variations Equation 2.30 can be expressed as:

$$C = \frac{V_0}{\gamma \cdot \rho \cdot r \cdot T} \tag{2.32}$$

With V_0: volume of the element (m^3)

γ: Ratio of the specific heats (γ = 1.4 was used)

ρ: gas density (kg/m^3)

r: ideal gas constant (r= 287 J/kg.K was used)

T: temperature

Using Bernoulli's relationship, Equation 2.31 can be expressed as:

$$L = \frac{\rho \cdot l}{A} \tag{2.33}$$

With l: length of hose (m)

A: section of the hose (m^2)

The impedance of each element is obtained with the following equations:

$$\text{Volumes:} \qquad Z = \frac{1}{j \cdot C \cdot \omega} \tag{2.34}$$

$$\text{Hoses:} \qquad Z = j \cdot L \cdot \omega \tag{2.35}$$

With ω: pulsation (rad.s^{-1})

Using the electrical analogy the amplitude of the crankcase pressure variation and the oscillation of the flow rate of gases exiting the acoustic filter were expressed as follows (see Figure 2.39 for notations):

$$\left|\frac{P_1 - P_{atm}}{q_p}\right| = \frac{\omega \cdot L_1 \cdot \left(1 - C_2 \cdot L_2 \cdot \omega^2\right) + L_2 \cdot \omega}{1 - \left(C_1 \cdot L_1 \cdot \omega^2 \left(1 - C_2 \cdot L_2 \cdot \omega^2\right) + L_2 \cdot C_1 \cdot \omega^2 + C_2 \cdot L_2 \cdot \omega^2\right)} \tag{2.36}$$

$$\left|\frac{q_{out}}{q_p}\right| = \frac{C_2 \cdot L_2 \cdot \omega^2 - 1}{\left(1 - C_2 \cdot L_2 \cdot \omega^2\right)\left(1 - \left(C_1 \cdot L_1 \cdot \omega^2 \left(1 - C_2 \cdot L_2 \cdot \omega^2\right) + L_2 \cdot C_1 \cdot \omega^2 + C_2 \cdot L_2 \cdot \omega^2\right)\right)} \tag{2.37}$$

Where q_p was approximated by:

$$q_p = \frac{\pi \cdot D \cdot S}{2} \cdot \sin(\omega \cdot t) \quad \text{And} \quad \omega = \frac{N \cdot \pi}{30}$$

With D: bore diameter (m)

S: stroke length (m)

t: time (s)

N: engine speed (rpm)

Using Equations 2.36 and 2.37 to model the performances of the acoustic filter, the size of the different elements was determined such that:

- The required attenuation of the blow-by oscillations was achieved.
- The oscillation of the crankcase pressure did not exceed 10 mbar.
- The size of the "dead volume" element of the filter was minimized.

Designed acoustic filter: Figure 2.41 shows the dimensions of the various components of he designed acoustic filter. On Figure 2.42, which shows the attenuation achieved with the filter, one can see that the amplitude of the filtered blow-by oscillations is lower than 0.1 liter/min at any engine speed between 1000 and 6000 rpm. Furthermore, on Figure 2.43 it can be seen that the resonance frequency of the crankcase pressure, which is about 3 Hz (~180 rpm) is below the speed range of usual engine

operation. Therefore, the designed acoustic filter achieved the required attenuation without amplifying the crankcase pressure variations.

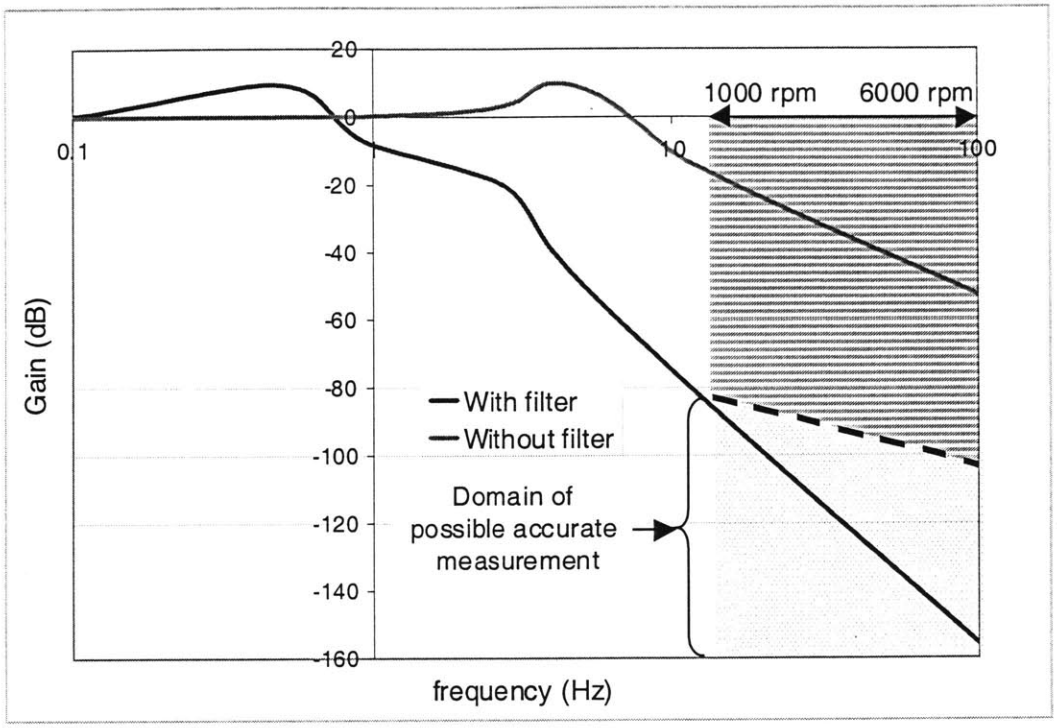


Figure 2.42 – Performance of the blow-by acoustic filter: attenuation of the flow oscillations.

2.4.4.3 Blow-by flowmeter

Considering the range of flow rates to be measured, the most adequate flowmeters appeared to be the rotameter-type ones. With these flowmeters the flow rate is determined by the position of a spherical ball in a vertical conic tube through which the gases are flowing. The major problem to be solved when using a rotameter to measure blow-by flow rates is the contamination of the ball and the tube with oil and water. In order to prevent oil and water to reach the flowmeter, the blow-by measuring circuit was modified in two places:

1. In order to prevent large oil droplets to be carried out of the crankcase along with the blow-by gas stream, a screen was installed at the location of the blow-by pickup in the crankcase.
2. Two condensers and two condensate traps were added upstream of the flowmeter (see Figure 2.44).

Finally, a nitrogen flushing circuit was added to clean the rotameter between the measurements.

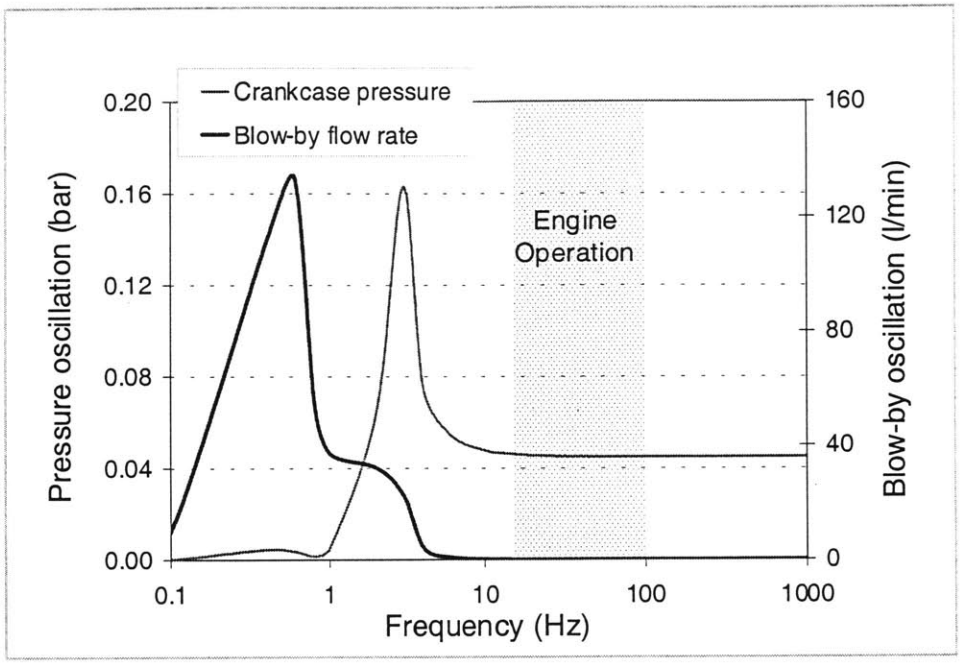


Figure 2.43 – Performance of the blow-by acoustic filter: oscillations of the crankcase pressure.

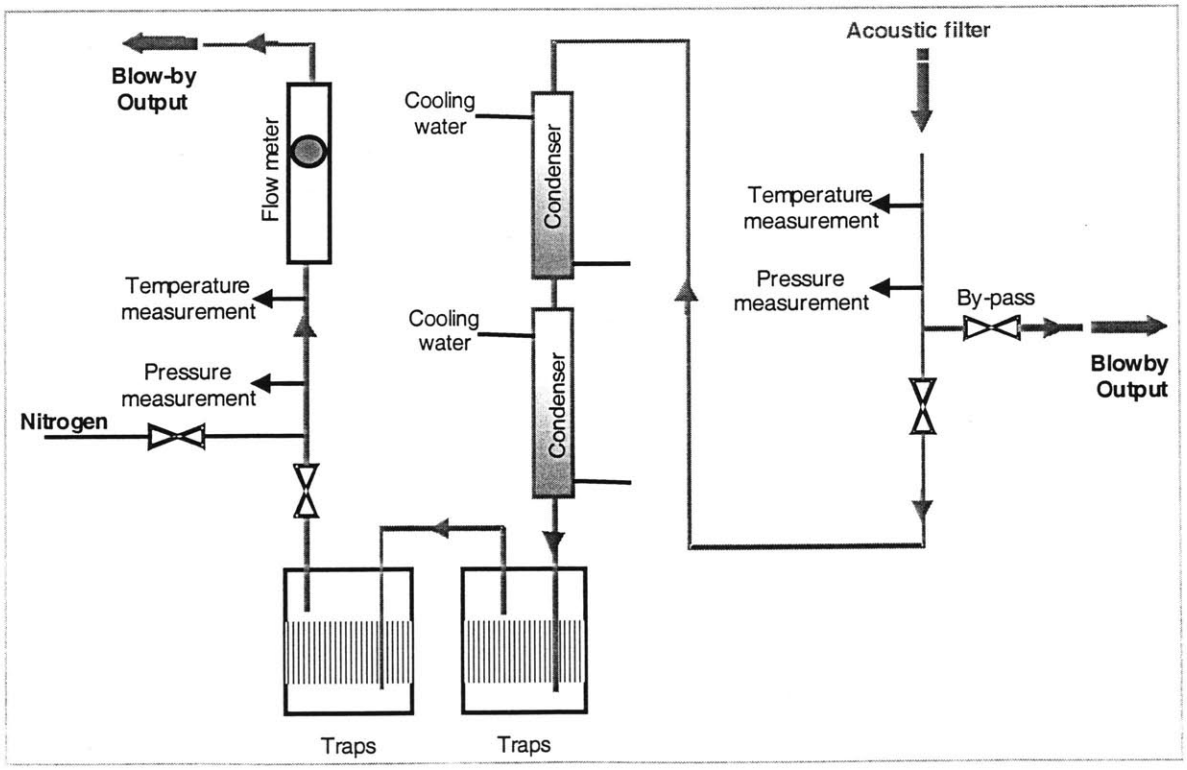


Figure 2.44 – Blow-by meter design.

CHAPTER 3. CHARACTERIZATION OF OIL TRANSPORT MECHANISMS

3.1 Oil Transport on the Piston Lands

The understanding of oil transport processes on the piston lands is essential to analyze the oil flow patterns leading to oil consumption. In this section, oil transport mechanisms that were experimentally identified are characterized and physically based models are proposed to describe the oil flows on the piston land surfaces.

3.1.1 Inertia Driven Oil Transport

3.1.1.1 Observation and Description

It was observed that oil accumulated on the piston lands move up and down in the axial direction – the direction of the piston primary motion. The consistent phasing of the observed axial displacement of the lubricant with the piston motion implied that the oil motion was driven by the body force resulting from the piston alternative accelerations and decelerations. The existence of this body force, so called inertia force, can be seen as the consequence of the fact that the reference frame attached to the piston, in which the oil motion is studied, is a non-inertial one. The computation of the inertia force is trivial and is directly related to the piston acceleration:

$$f_I = -\rho_{oil} \cdot a_p \tag{3.1}$$

With ρ_{oil}: oil density [kg/m^3]

a_p: piston acceleration [m/s^2].

Observations on the second land (Kubota engine): Figure 3.1 shows oil displacements resulting from the action of the inertia force on oil accumulated on the piston second land of the Kubota engine running at 2800 rpm. Each picture was acquired at 88 crank angle degrees either before (compression and exhaust stoke) or after (expansion and intake stroke) the top dead center. At this particular piston position, in intake and expansion stroke, the inertia force, which is plotted is Figure 3.2, had been pointing upward (toward the combustion chamber) for about 180 crank angle degrees. Similarly, in compression and exhaust stroke the inertia force had been pointing downward (toward the crankcase) for about half a crankshaft revolution. Consequently, LIF images acquired at this piston position

show the greatest effect of the inertia force on the oil distribution in both directions. On images 2 and 4, it can be seen that oil that was initially about half way down on the second land (see images 1 and 3) flowed upward and accumulated just below the top ring. On images 1 and 3 (intake and expansion stroke) of Figure 3.1, we can see that oil that was originally accumulated just below the top ring moved down on the second land. Thus, one can conclude that the alternating oil motion is directly related to the direction of the inertia force: when the inertia force is pointing upward the lubricant is moving upward and vice-versa.

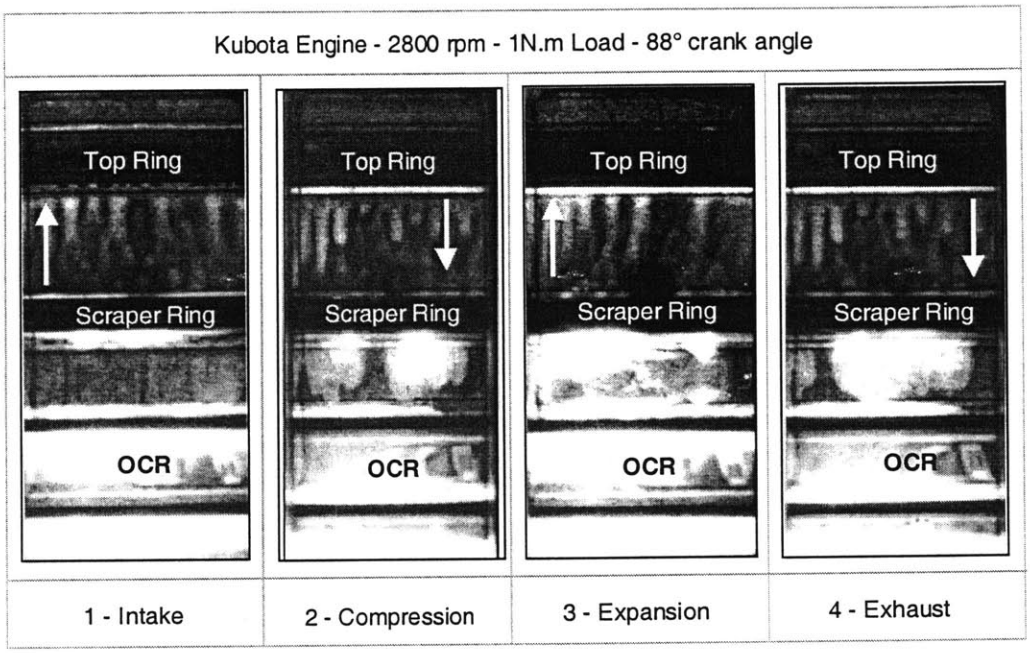


Figure 3.1 – Oil distribution on the piston lands of the Kubota engine, showing the effect of the inertia force on the second oil accumulation.

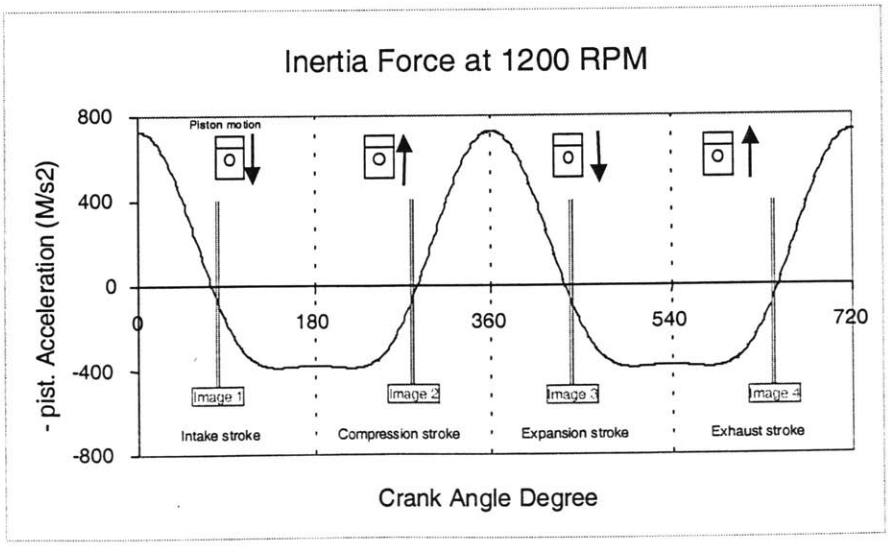


Figure 3.2 – Inertia force computed for the Kubota engine running at 1200 rpm (Timing of the LIF image acquisition).

Figure 3.3 shows the effect of the amplitude of the inertia force on the axial motion of the lubricant accumulated on the piston lands. The top image was acquired during compression stroke at 1200 rpm. At this engine speed, the downward inertia force in the Kubota engine peaks at 400 m/s^2. The resulting oil displacement was about 1 mm. The bottom image shows the oil distribution during compression stroke at 2800 rpm. At this speed, the downward inertia force peaks at 2180 m/s^2 and the resulting oil displacement was about 2 to 3 mm. Therefore, it is clear that the inertia force resulting from the piston alternating motion drives oil up and down on the piton lands and that the distance traveled by the lubricant is a function of the inertia force amplitude, which depends directly on the engine speed.

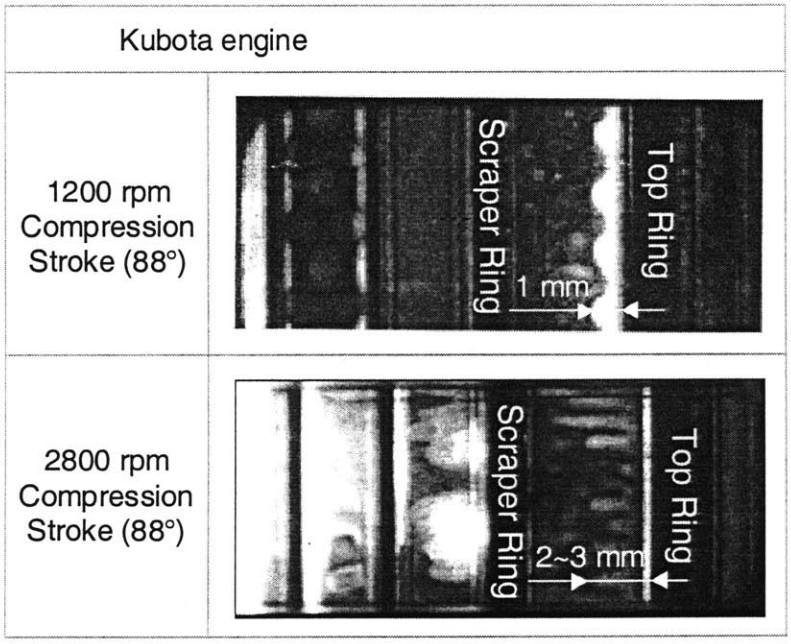


Figure 3.3 – Effect of the engine speed on the inertia-driven oil displacement.

Furthermore, Figure 3.4 is used to illustrate that the oil displacement induced by the inertia force depends on the volume of oil accumulated. On the bottom picture, according to the low LIF intensity signal, the amount of oil accumulated below the top ring is small and no downward oil motion can be detected from the oil pattern. On the other hand, on the top image, there was a larger quantity of oil accumulated the downward oil displacement induced by the inertia force could be clearly identified. Overall, we can conclude that:

1. Oil was observed to move axially on the piston lands and the inertia force resulting from the piston motion was identified as the driving force.
2. The amplitude of the oil displacement was found to depend on the engine speed and the oil accumulation volume.

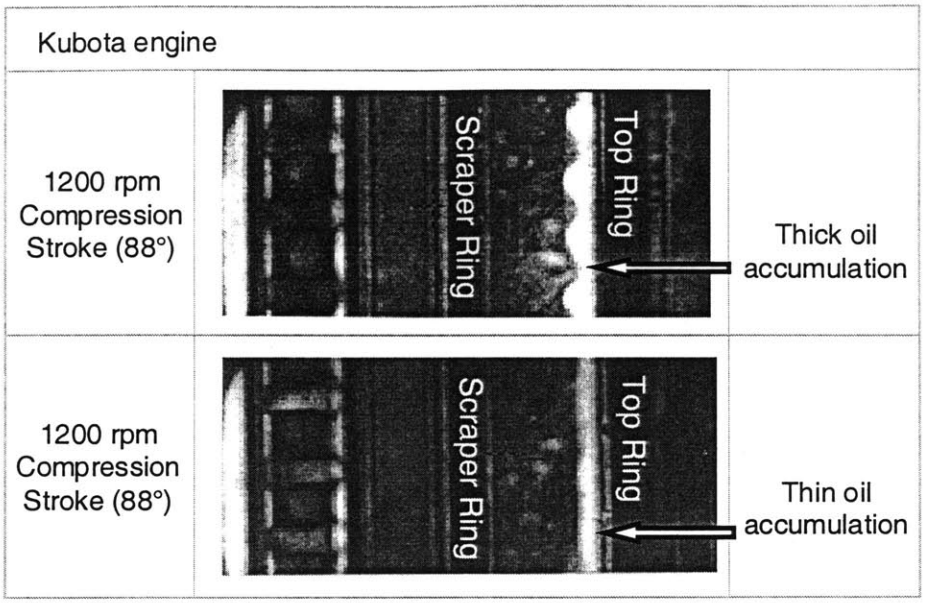


Figure 3.4 – Effect of the volume of the oil accumulation on the inertia-driven displacement.

Observations on the third land (PSA single-cylinder engine): Figures 3.5a and 3.5b shows the evolution of the oil distribution on the third land of the PSA single-cylinder engine running at 3500 rpm and 300 mbar intake pressure. Since images presented in Figures 3.5a and 3.5b were acquired at different times, the total amount of oil accumulated on the third land might have varied from one image to another. Therefore, when comparing the images in Figures 3.5a and 3.5b, one should focus on the oil position and not on the oil quantity. The evolution of the oil pattern with inertia force is presented for one engine revolution, from the beginning of intake stroke (33 crank angle degrees) to the end of compression stroke (330 crank angle degrees). Due to the more complex geometry (third land cutoff, hook in the Napier ring), the evolution of the third land oil accumulation is slightly different than the second land one. In particular, as it can be seen in images 3, 4 and 5 oil is stored in and released from the buffer region formed by the cutoff and the hook. On images 5, 6 and 7 one can see that the inertia force was strong enough to drive the oil across the third land from the scraper ring to the oil control ring and vice-versa. Eventually, one can see than the 3-dimensionnal patterns of the oil accumulation on the second land (Figure 3.1) and on the third land (Figures 3.5a and 3.5b) were different. This was found to be due to the geometrical differences of the two regions and is further discussed in Section 3.1.1.4.

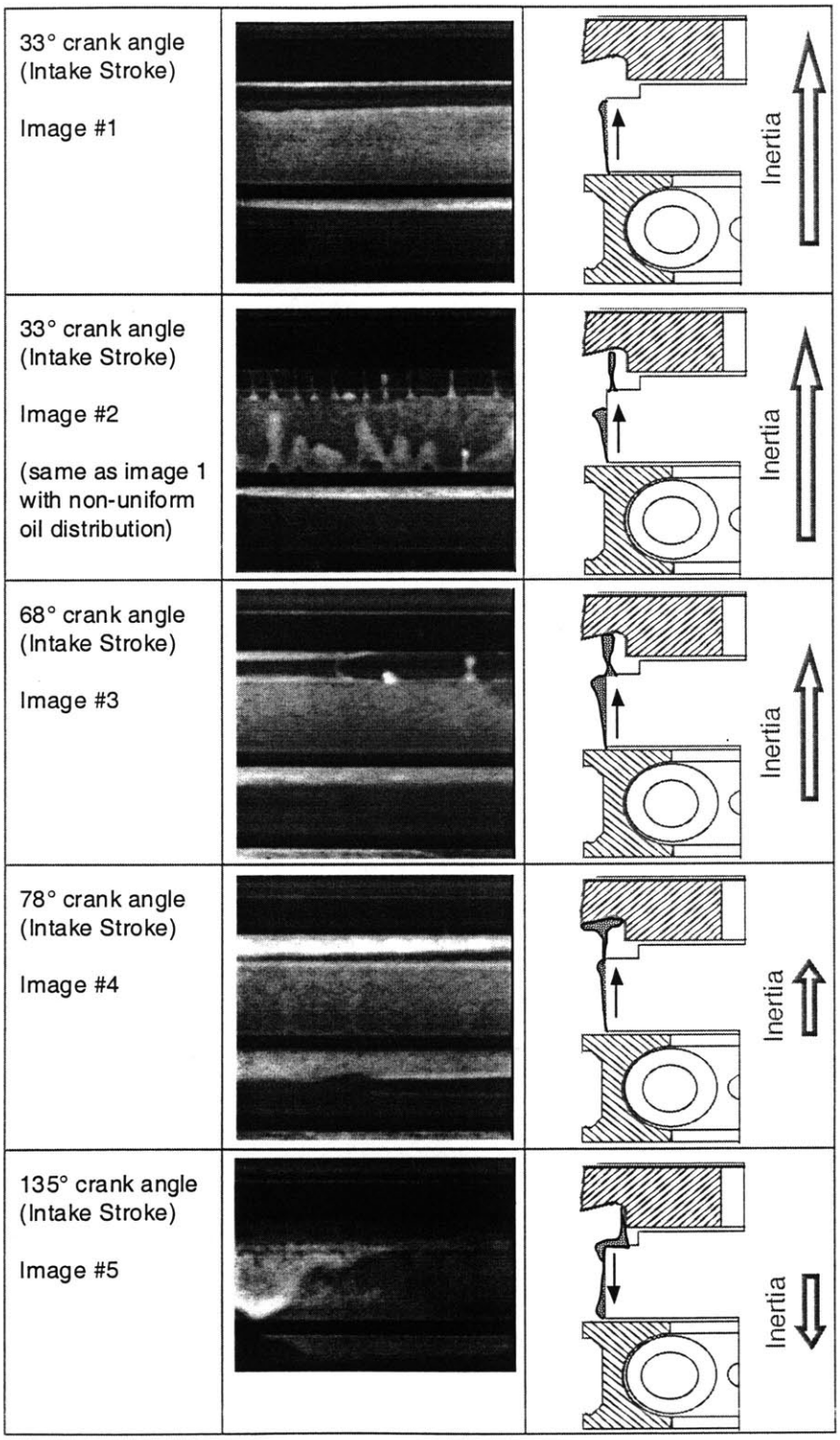


Figure 3.5a – Cycle resolved evolution of the third land oil distribution, showing the effect of the inertia force(I).

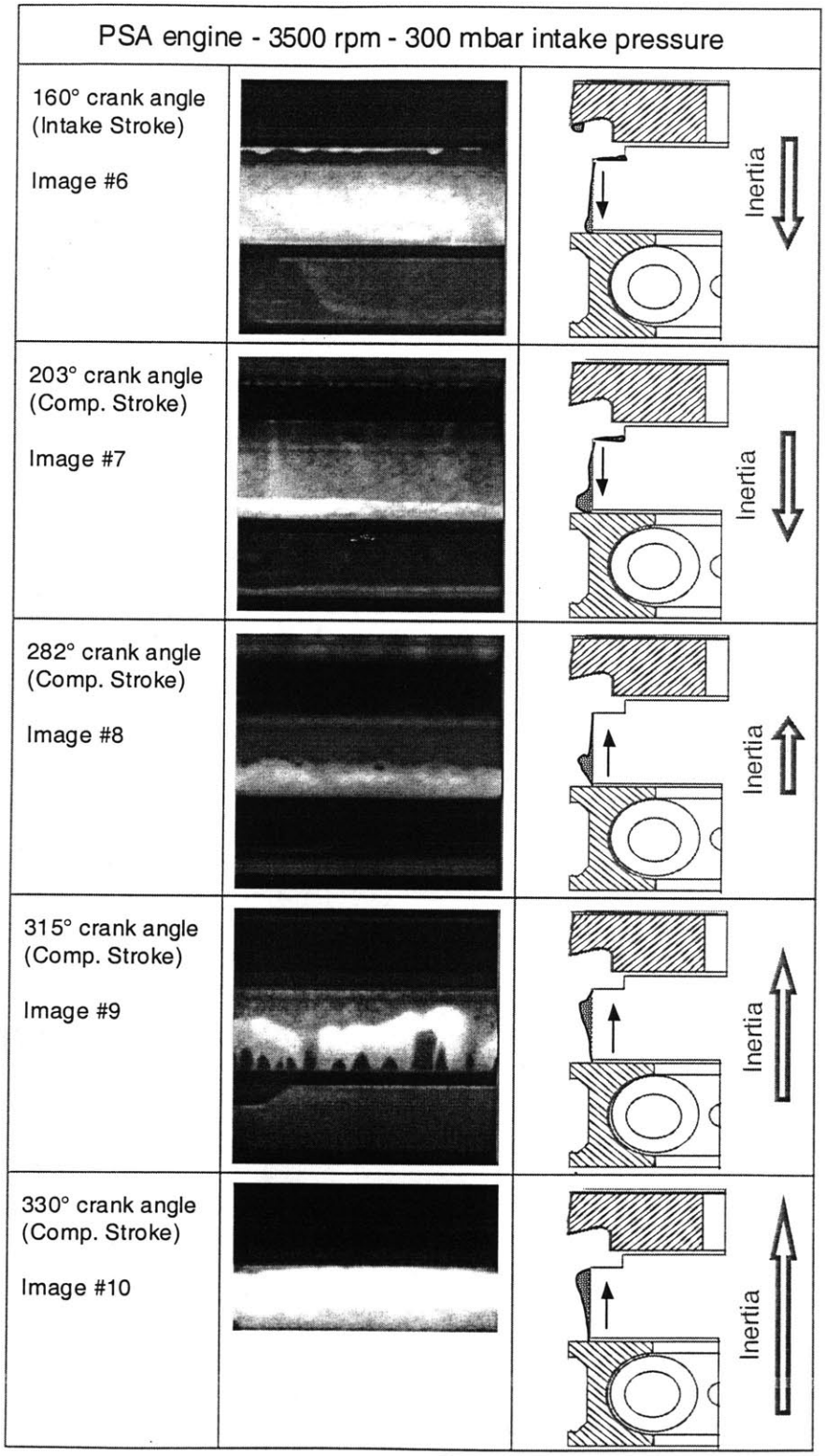


Figure 3.5b – Cycle resolved evolution of the third land oil distribution, showing the effect of the inertia force(II).

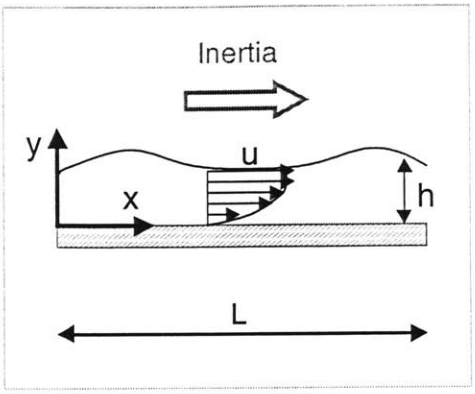


Figure 3.6 – Description of the parameters used for the thin film modeling.

One-dimensional description of the oil flow: Assuming that the oil layer at the surface of the piston land is a thin film (h<<L), the oil motion induced by the inertia force can be described as a one-dimensional flow driven by a body force parallel to the film (see Figure 36). For this type of flow, the Navier-Stokes equations can be reduced to:

$$\frac{\partial u}{\partial t} + u\frac{\partial u}{\partial x} + v\frac{\partial u}{\partial y} = \upsilon \cdot \frac{\partial^2 u}{\partial y^2} + \frac{f_I}{\rho_{oil}} \tag{3.2}$$

With u: oil velocity along the x-axis

v: oil velocity along the y-axis

ν: kinematic oil viscosity.

Equation 3.2 does not account for pressure variation that would result from surface tension effect. It is therefore only valid when the radius of curvature of the oil surface is large enough so that surface tension can be neglected.

The Reynolds number for this flow can be computed using an estimation of the oil velocity derived for a fully developed viscous flow:

$$\tilde{u} = \frac{a_p \cdot h^2}{3 \cdot \upsilon} \tag{3.3}$$

$$R_e = \frac{\tilde{u} \cdot \tilde{h}}{\upsilon} \approx \frac{a_p \cdot h^3}{6 \cdot \upsilon^2} \tag{3.4}$$

In Equation 3.2, the ratio of the convection terms to the viscous dissipation term can be estimated by the following expression:

$$Re \cdot \left(\frac{h}{L}\right) = \frac{a_p \cdot h^3}{6 \cdot \upsilon^2} \cdot \left(\frac{h}{L}\right) \tag{3.5}$$

With: $h = 20\ \mu m$

$L = 1$ mm

$\nu = 7.10^{-6}\ m^2/s$ (Low shear viscosity of a Shell 15W40 oil at 130°C).

The numerical value of Equation 3.5 varies from 4.10^{-4} to 10^{-1} as the piston acceleration a_p varies from 400 (at 1200 rpm) to 10000 m/s^2 (at 6000 rpm). Accordingly, in the rest of the analysis, the convection terms were assumed to be negligible and the flow was considered fully viscous. It is interesting to notice that for a significantly thicker oil accumulation (~100 μm) or at higher engine speed (racing engines) the convection terms would have a non-negligible effect on the oil motion.

Since the inertia force is cyclically changing with a period of one engine revolution, the time scale of the problem is defined by the duration of one engine revolution: $T = N.\pi/30$, where N is the engine speed in revolution per minute (rpm). In order to determine if the viscous flow induced by the inertia force is fully developed, T has to be compared with the viscous diffusion time $T_\nu = h^2/\nu$.

$$\frac{T}{T_\nu} = \frac{h^2 \cdot N \cdot \pi}{30 \cdot \upsilon} \sim 10^{-2} \tag{3.6}$$

With $h = 20\ \mu m$

$\nu = 7.10^{-6}\ m^2/s$

$N = 6000$ rpm.

According to Equation 3.6, the viscous diffusion time is always small compare to the time scale of the inertia force variation and therefore the flow can be considered to be a fully developed viscous flow. As a result, Equation 3.2 can be simplified to:

$$\frac{\partial^2 u}{\partial x^2} = \frac{a_p}{\upsilon} \tag{3.7}$$

With the following boundary conditions:

$$u(y = 0) = 0 \text{ and } \left.\frac{\partial u}{\partial y}\right|_{y=h} = 0$$

Equation 3.7 can be integrated to:

$$u = -\left(\frac{a_p}{\upsilon}\right)\left(\frac{y^2}{2} - h \cdot y\right) \tag{3.8}$$

Moreover, from mass conservation, we have:

$$\frac{dh}{dt} + \frac{dq}{dx} = 0 \tag{3.9}$$

With: $$q(x) = \int_0^h u(y)dy = -\frac{a_p \cdot h^3}{3.\upsilon}$$

Combining Equations 3.8 and 3.9 we obtain:

$$\frac{\partial h}{\partial t} - \frac{a_p \cdot h^2}{\upsilon} \cdot \frac{\partial h}{\partial x} = 0 \qquad (3.10)$$

Equation 3.10 is a wave-type equation (first order quasi-nonlinear) for which the wave speed is $\frac{a_p \cdot h^2}{\upsilon}$. The wave speed dependency on the square of the oil layer thickness and the piston acceleration is in good agreement with the experimentally observed effects of the oil volume and engine speed on inertia driven flow. As illustrated on Figure 3.7, due to the h^2 dependency of the "wave speed", positive sloping oil surface (dh/dx>0) flattens under the effect of the inertia force, and negative sloping surface (dh/dx<0) becomes steeper. Consequently, any disturbance of the oil layer surface will develop and create a steep front (see Figure 3.7). The formation of steep front at the surface of the oil layer was consistently observed from experiments. Figure 3.8 shows the oil distribution profiles measured in the axial direction along the piston second and third land. On both lands, it can be seen that the oil moving under the inertia force effect has developed a puddle shape with a steep edge at the front. Equation 3.10 has been derived for a film flow with the assumption that the flow was essentially one-dimensional. When the thickness of oil layer varies greatly in the flow direction, like in the vicinity of the front edge of the puddles, the flow becomes locally two-dimensional. Consequently, the previously developed one-dimensional representation of the flow can not be used to describe the displacement of the puddle front edges.

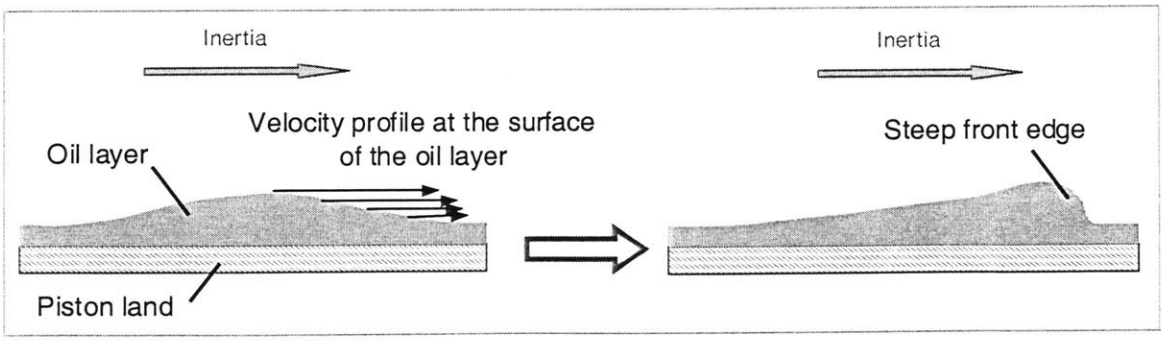


Figure 3.7 – Description of the formation of a steep edge at the front of oil puddles.

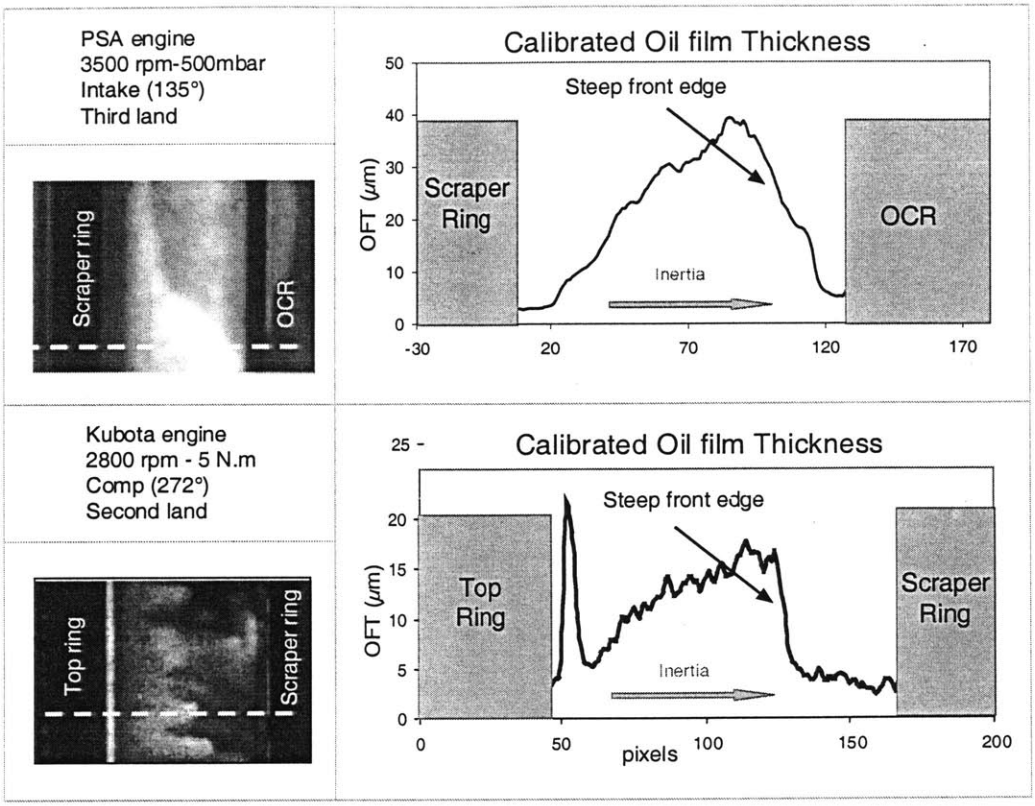


Figure 3.8 – Formation of a steep edge at the front of oil puddles observed in the Kubota engine.

Description of the oil flow at the front edge of the puddle: At the steep edge of the oil puddle, the flow is two-dimensional and surface tension plays an important role as it prevents the viscous layer from breaking up. Indeed, the oil motion in the vertical direction is driven by a pressure gradient resulting from the fact that surface tension constrains the shape of the oil surface. The oil approaching the steep front from the top of the puddle is forced to "roll over". As a result the front edge of the puddle moves forward (see Figure 3.9). The flow pattern shown in Figure 3.9 was experimentally observed by tracking the trajectory of fine chalk particulate sprayed on the surface of a puddle of oil rolling on an oil-wetted inclined surface. The slope and length of the steep edge at the front of the puddle is determined by the extent of the surface tension effect. To roughly determine the portion of the puddle where the oil flow is truly two-dimensional, we can estimate the radius of curvature necessary for the pressure gradient resulting for the effect of surface tension to be comparable in magnitude with the pressure drop due to viscous forces. The ratio of viscous and surface tension force is the Capillary number.

$$Ca = \frac{\mu \cdot \tilde{u} \cdot R}{\sigma \cdot h} \tag{3.11}$$

With: σ: oil surface tension

R: local radius of curvature

$\tilde{u}$: average oil velocity

μ: dynamic oil viscosity

Using Equation 3.8, the Capillary number can be expressed as:

$$Ca = \frac{\rho \cdot a_p \cdot h \cdot R}{3 \cdot \sigma \cdot} \tag{3.12}$$

For surface tension to have a significant impact on the oil motion, the Capillary number must be in the order of unity or smaller. Therefore, according to Equation 3.12, the radius of curvature of the oil surface should in the order of 100 μm or smaller. This value was computed using the following numerical values.

σ = 0.02 N/m (Pennzoil 15W40 oil at 130°C)

h = 20 μm

ρ = 800 kg/m^3

As expected, this result shows that at the front edge of the puddle where the radius of curvature might be in the order of the oil thickness (10~30 μm), the effect of surface tension can be significant. Moreover, surface radius of curvature smaller than 100 μm can only exist in the portion of puddle located right behind the front edge (see Figure 3.10a). The length of this portion can be assumed to be in the order of the puddle thickness and is thus very small compare to the puddle length. Consequently, except in the close vicinity of the steep front, surface tension effects are negligible and the oil flow can be represented by the one-dimensional approach previously developed. Eventually, since the oil flow rate is known everywhere expect in the region of the steep front, the position and height of the front edge of the puddle may be determined using mass conservation applied to a small control volume including the leading edge of the puddle.

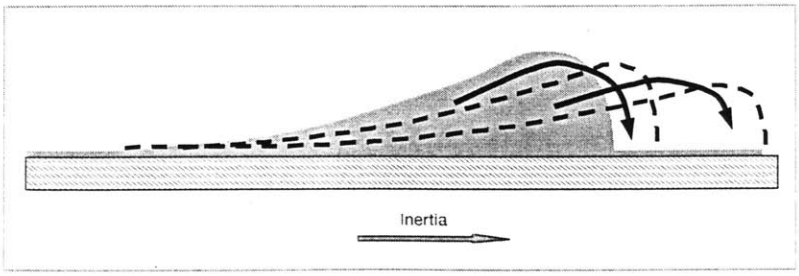


Figure 3.9 – Rolling-over process occurring a the front edge of oil puddles displaced by the inertia force.

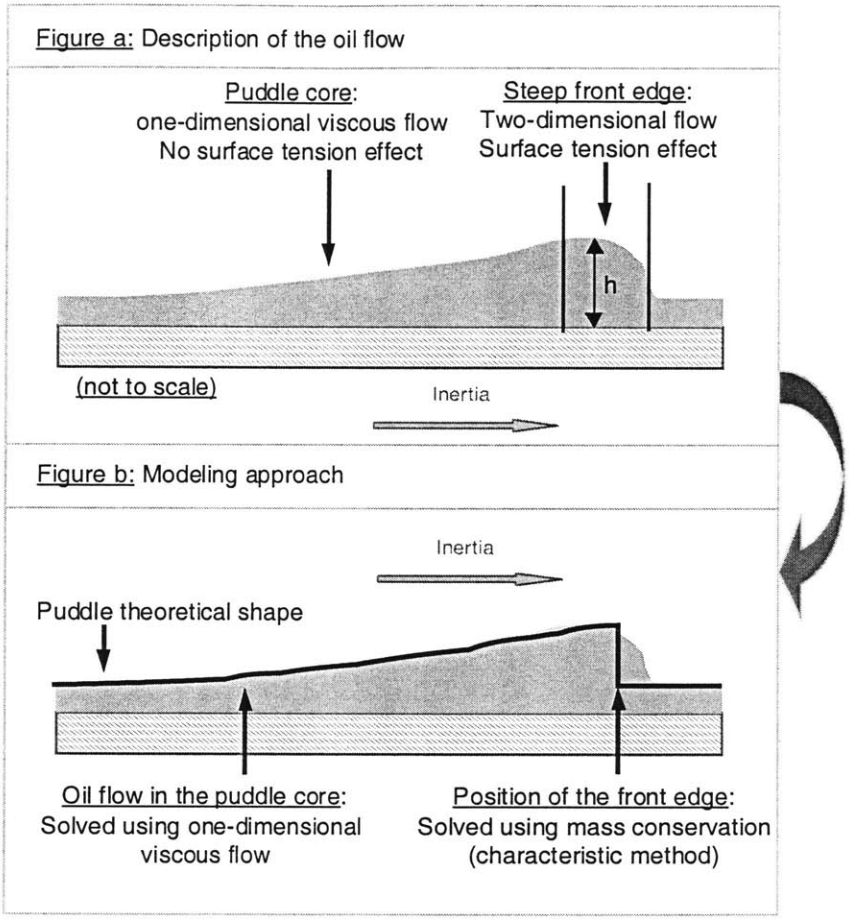


Figure 3.10 – Puddle motion. Description of the oil flow and modeling approach.

3.1.1.2 Modeling

Modeling approach: The purpose of the modeling effort was to provide a physical-based model that could be used to predict the effect of the inertia force on the oil motion and the aspect ratio of oil puddles located on the piston lands. As discussed in the previous section the motion of the oil in the core of the puddle can be described by Equation 3.10. In this equation, the wave speed depends on the piston acceleration and is therefore time dependent. By dividing Equation 3.10 by the piston acceleration $a_p = dV_p/dt$, one can obtained Equation 3.13 where the wave speed is not dependent on time.

$$\frac{\partial h}{\partial V_p} - \frac{h^2}{\upsilon} \cdot \frac{\partial h}{\partial x} = 0 \qquad (3.13)$$

It is important to notice that in Equation 3.13 the piston speed V_p "plays the role" of time. As a consequence, the oil motion is found to be function of the amplitude and not the duration of the piston speed variations. Since the part of the puddle in which the one-dimensional approximation is not valid is small compare to the puddle width, the front edge of the puddle can be treated in a way analogous to shock wave in compressible fluids. Accordingly, the position of the front edge will be solved using mass conservation while the rest of the flow will be computed using the wave equation (Equation 3.13). The main advantage of this technique is that the position of the oil puddle is correctly predicted without conducting a two-dimensional flow computation. The method used to compute the evolution of the shape and position of the puddle is based on the characteristic method. Accordingly, the modification of the puddle shape due to the effect of the inertia force while the piston decelerates from Vp_{max} to $-Vp_{max}$ is computed with the following equation (see Equation 3.14):

$$X = X_0 + \frac{h^2}{\upsilon} \cdot 2 \cdot Vp_{max} \tag{3.14}$$

If a steep edge is created, the computed oil profile has a multi-valued region (see Figure 3.11) inside which the actual front edge of the puddle is located. The position S of the front edge is characterized by the following set of equations:

- $$S = X_{01} + \frac{h^2}{\upsilon} \cdot 2 \cdot Vp_{max} \tag{3.15}$$

- $$S = X_{02} + \frac{h^2}{\upsilon} \cdot 2 \cdot Vp_{max} \tag{3.16}$$

- $$\int_{(S,h_{01})}^{(S,h_{02})} h \cdot dx = 0 \tag{3.17}$$

With h_{01} and h_{02} defined by $h_{01} = h$ at $X = X_{01}$ and $h_{02} = h$ at $X = X_{02}$.

Where X_{01} is the x-coordinate of the point of the initial profile that moved to be bottom of the vertical front edge, and X_{02} is the x-coordinate of the point of the initial profile that moved to the top of the vertical front edge.

Equation 3.17, which expresses mass conservation at the front edge of the puddle, is an integral along the profile from the point of coordinates (S, h_{01}) to the point of coordinates (S, h_{02}). The system of equations was solved using the Newton algorithm. It is interesting to notice that the technique used to solve for the position of the front edge of the puddle can be applied in the case where one puddle front edge catches another one.

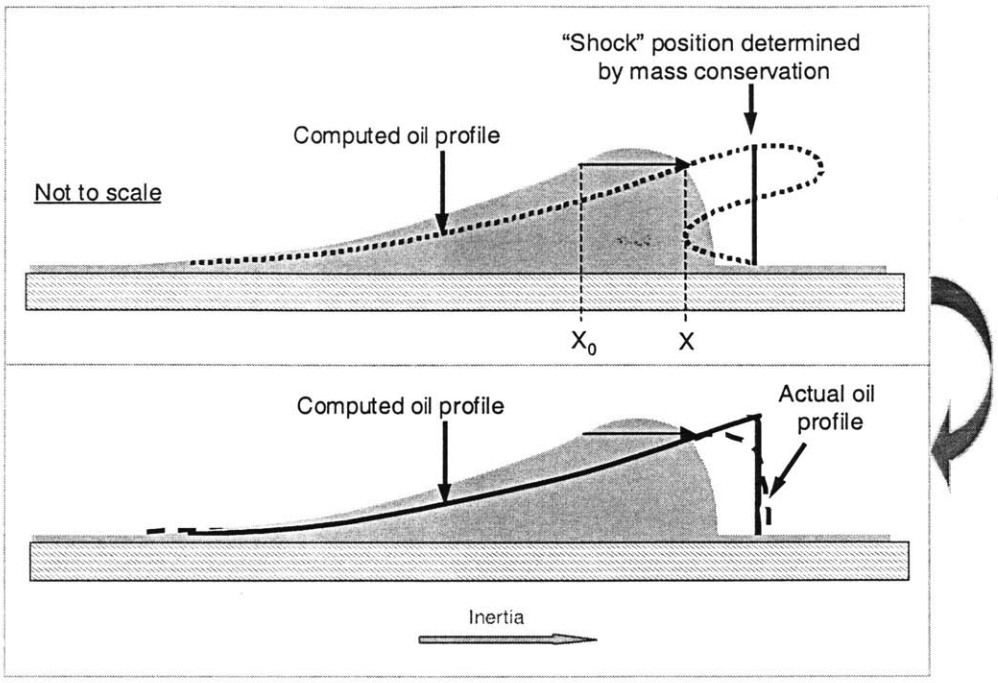


Figure 3.11 – Description of the computation scheme used to determine the position of the front edge of puddles moving under the effect of the inertia force.

Modeling process: As far as the inertia force is concerned, one engine revolution can be divided into two parts. First, we can consider the part during which the piston decelerates from its maximum upward velocity Vp_{max} to its maximum downward velocity –Vpmax. In the PSA single-cylinder engine, this part would extend from 76 crank angle degrees before TDC to 76 degrees after TDC. During this part the inertia force is pointing upward and thus the oil is driven toward the combustion chamber. Secondly, we can consider the part during which the piston accelerates from its maximum downward velocity to its maximum upward velocity. This part extends from 104° before BDC to 104° after BDC. During this part the inertia force is pointing downward and consequently the oil is driven towards the crankcase. Using the model and solving technique previously described, the evolution of the shape and position of an oil puddle driven by the inertia force during one engine revolution was computed.

For the computation it was assumed that at the beginning of the upward inertia period (76° before TDC) a given amount of oil was supplied at the lower end of the piston second or third land (see Figure 3.12a). The supplied oil puddle used in this calculation had a volume of 1.10^{-9} m^2. Since all calculations were conducted in two dimensions oil volumes are given as surface area (m^2). The initial shape of the puddle corresponded to the profile of the hump of a sinusoidal curve (see equation below) and its bottom width was 150 μm.

$$h(x) = h_i - (-1 \cdot (-1 + \cos\left(\frac{x \cdot 2 \cdot \pi}{oil_width}\right)) \cdot \frac{oil_volume}{oil_width}$$

With h(x): Oil film thickness (m)

h_i: Thickness of the uniform oil layer (m)

oil_width: Width of the oil puddle (m)

oil_volume: Volume of the oil puddle (m2)

The puddle was added on the top of 5-μm thick uniform oil layer. The uniform layer of oil was introduced to simulate the fact that during engine operation the piston lands are covered with a thin layer of oil. The inertia force was computed for an engine running at 2400 rpm. The shape and displacement of the oil puddle at the end of the upward inertia period (76° after TDC) and after one complete engine revolution were computed. The results are shown on Figure 3.12b.

Modeling results: First of all, we can see that, during the first part of the engine revolution (the upward inertia period), the puddle spreads in the direction of the inertia force and its height significantly reduces. The irreversible change of the puddle height is due to the "rolling-over" process that occurs at the front edge. Second, the modeling results showed that the height of the puddle is preserved during the downward inertia period (see Figure 3.12b). This result reflects the fact that because the variation of the piston speed during the upward and the downward inertia periods are equal, the rolling-over process can not occur during more than one inertia period unless additional oil is supplied to the puddle. Accordingly, continuing the computation of the puddle shape for the following engine revolutions showed that the puddle keeps moving back and forth between the positions reached during the first revolution (curves 2 and 3 in Figure 3.12b). At this point, it can be concluded that once the initial shape of the oil puddle has been altered during one full period of either upward or downward inertia force, the oil motion is cyclic and the resulting net oil flux along the axial direction of the land is zero. The latter conclusion can be seen as a direct consequence of the fact that the integral of the inertia force over one engine revolution is zero.

In the previous simulation, oil was supplied only once at the beginning of the first engine revolution. However, in a running engine, oil is probably supplied to the different regions of the piston every cycle. To duplicate the effect of repeated oil supply to the piston land, a simulation, in which a fixed amount of oil was added every cycle to the bottom part of the piston land was conducted. The results, presented in Figure 3.13, show that the distance traveled by the front edge of the puddle at the end of the upward inertia period is increasing every cycle as the volume of the puddle increases. After 53 cycles, the oil volume is large enough so that the front edge of the puddle can reach the upper end of

the piston land. Consequently, the computation shows that under the effect of inertia a net flux of oil across the piston land can be established if additional oil is repeatedly supplied.

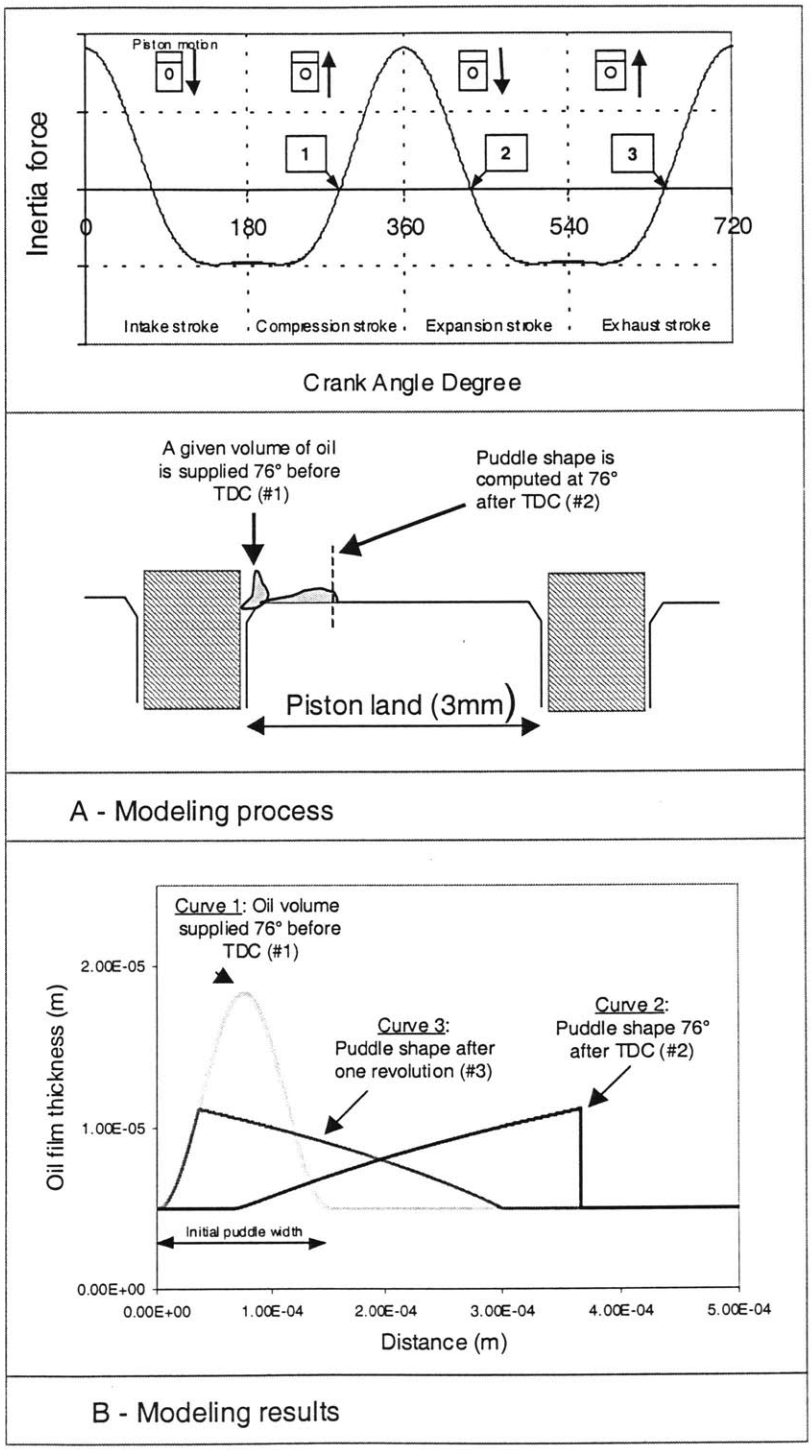


Figure 3.12 – Modeling of the spreading of an oil puddle under the effect of the inertia force. (Assumptions and results)

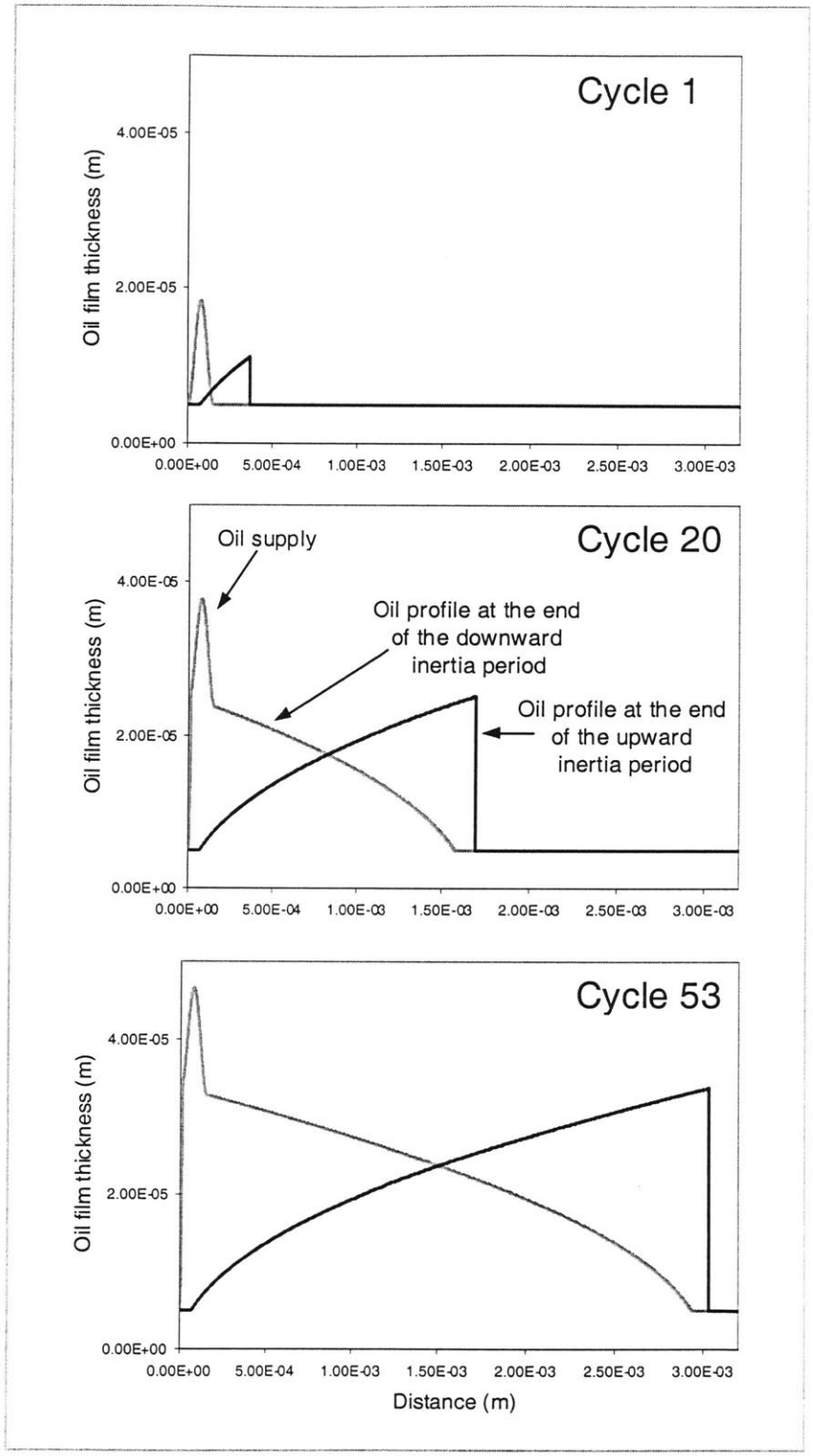


Figure 3.13 – Computed evolution of the shape and position of a two-dimensional oil puddle with repeated oil supply.

3.1.1.3 Results Analysis

Sensitivity of the model to the initial puddle geometry: In the developed model, the shape, the width and the height of the initial puddle were arbitrary chosen. In order to investigate the sensitivity of the model outputs to these parameters, the position of the front edge of the puddle at the end of the upward inertia period and its height were computed for puddles of identical volumes but different initial geometry. The results showed that:

1- If the puddle is steep enough so that the rolling-over process occurs, the puddle height and front edge position are independent of the initial height and shape.

2- The position of the front edge is significantly affected by the width of the initial puddle.

Oil transport observations have shown that in most engine operating conditions, oil puddles on the piston lands result from the accumulations of very small quantities of oil that have been supplied cycle after cycle. Therefore, a more realistic way to investigate the effect of the initial width of the supplied oil volume is to run the simulation for a large number of engine revolutions while supplying additional oil every cycle. In this case, the distance traveled by the front edge of the puddle at the end of the upward inertia period increases as the total volume of oil on the land increases. The relationship between the total oil volume and the distance traveled by the front edge of the oil accumulation was determined for different width of the oil volume that is supplied every cycle. The results show that as the total volume of oil accumulated on the land increases, the effect of the width of the oil volume that is supplied every cycle decreases. In fact, it was found that when the total oil volume is 20 to 25 times of the volume of the oil supply, the effect of the width of the supplied volume becomes negligible.

It can be concluded that if the oil supplied to the piston land at each revolution is much less than the volume of the oil puddle on the land, the oil motion computed by the developed model is independent of the arbitrary chosen parameters describing the oil supply. As a consequence, the motion and the aspect ratio of an oil puddle undergoing the effect of inertia are completely determined by the four following parameters: the engine speed, the total volume of the puddle, the thickness of the uniform oil layer covering the land and the kinematic viscosity of the oil.

Comparison with experiments: Figure 3.14 shows a comparison between a computed and a measured oil profile. The volume of the oil puddle observed on the LIF image was measured by integrating the calibrated oil thickness profile. The simulation was conducted by supplying every cycle a small amount of oil to the back of puddle. The simulation was stopped when the volume of the puddle created was equal to the measured oil volume. As it can be seen on Figure 3.14, that predicted and

measured aspect ratio and position of the front edge of the puddle match very well. Therefore, this physically based model is able to correctly duplicate the effect of the inertia force on the piston land oil distribution.

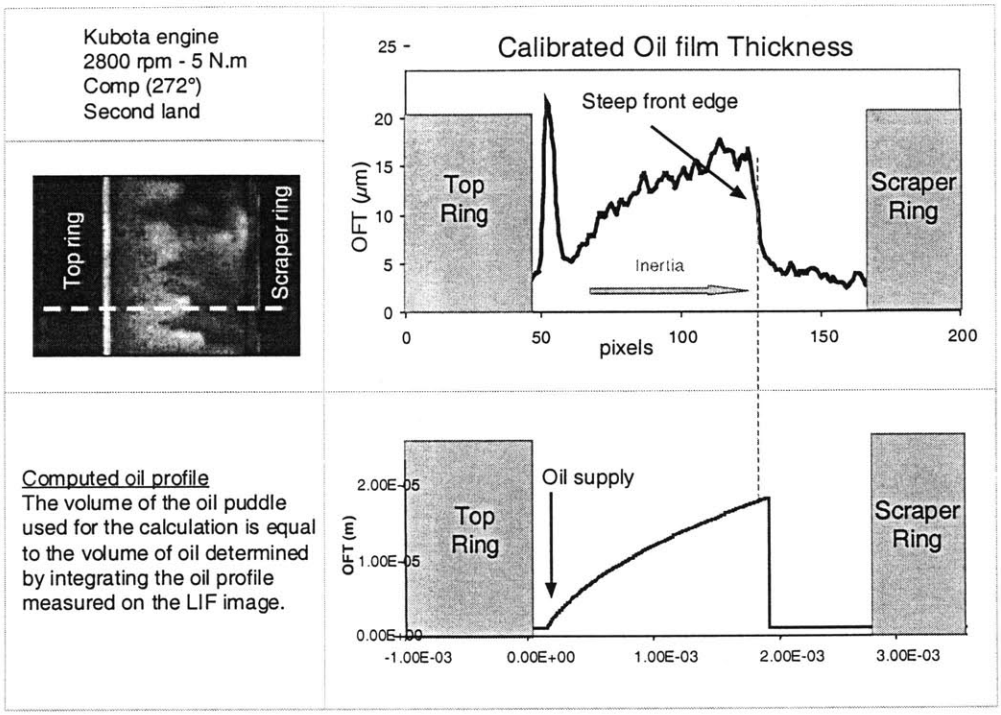


Figure 3.14 – Comparison between the computed and measured axial distribution of the oil accumulated on the second land.

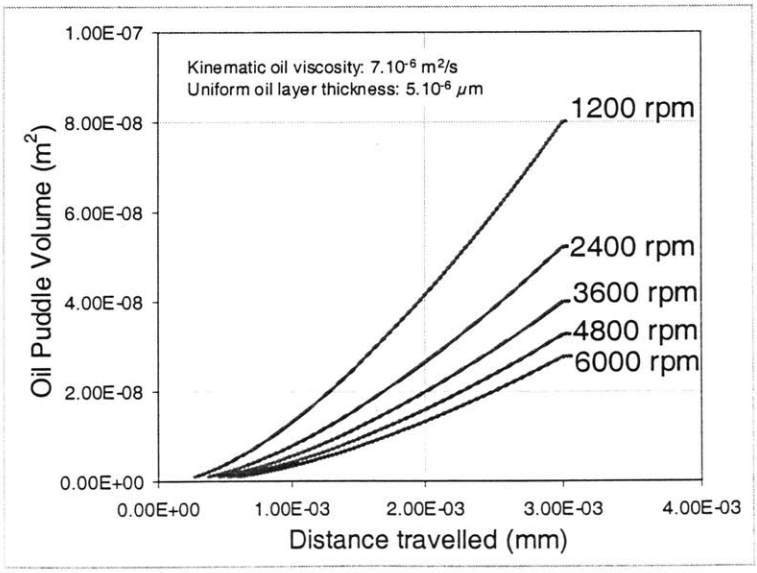


Figure 3.15 – Computed effect of the engine speed and oil volume on the distance traveled by the front edge of a two-dimensional puddle.

Inertia driven oil transport: In Figure 3.15, the computed evolution of the distance traveled by the front edge of the puddle was plotted as a function of the puddle volume for different engine speeds. As observed from the experiments, the model also predicts that the maximum distance traveled by the front edge of the puddle increases as the oil volume and/or the engine speed increase(s). These results show that for a given length of a piston land, at each engine speed, there is a minimum oil volume V_{oil_min} required for the oil to travel from one end of the piston land to the other within one engine revolution. As a consequence, if the amount of oil accumulated on the land is less than V_{oil_min}, no net oil flux across the land can be induced by the effect of the inertia force. On the other hand, if the amount of oil accumulated on the land is equal or greater than V_{oil_min}, a net transport of oil across the land can be established due the inertia force. It is important to notice that the direction of the net oil flux is determined by the location of the oil supply to the land and not by the driving force. As described in Figure 3.16, the oil flux resulting from the effect of the inertia force will be such that the oil will flow away from its source. Accordingly, since a large portion of the oil supplied to third land comes the OCR groove and most oil supplied to the second land comes from the second ring groove, the inertia force is likely to induce an oil flux in the direction of the combustion chamber. Furthermore, this net oil transport along the axial direction of the piston will increase with the engine speed and the rate of oil supply to the lands.

The piston second and third lands are bounded by one ring at each end. Even though significant oil leak through the ring grooves can occur, the volume of oil accumulated on these lands can increase such that it becomes significantly larger than V_{oil_min}. In this case the front edge of the puddle will reach the end of the land before the end of the upward or downward inertia period. As a result, before the inertia force switches direction, oil will accumulate against the ring (see Figure 3.17). Once oil reaches the ring at the end of the land, some oil may be transported out of the land region through the clearance between the ring and its groove. As far as oil transport from the land to the ring groove is concerned, the rate at which oil may be transported into the groove is greatly affected by the crank angle CA_r at which the oil reaches the ring, and the duration of the period T_{acc} during which oil accumulates against the ring (see paragraph 3.3.1). Therefore CA_r and Tacc are critical parameters to be determined to characterize oil flows into the ring grooves.

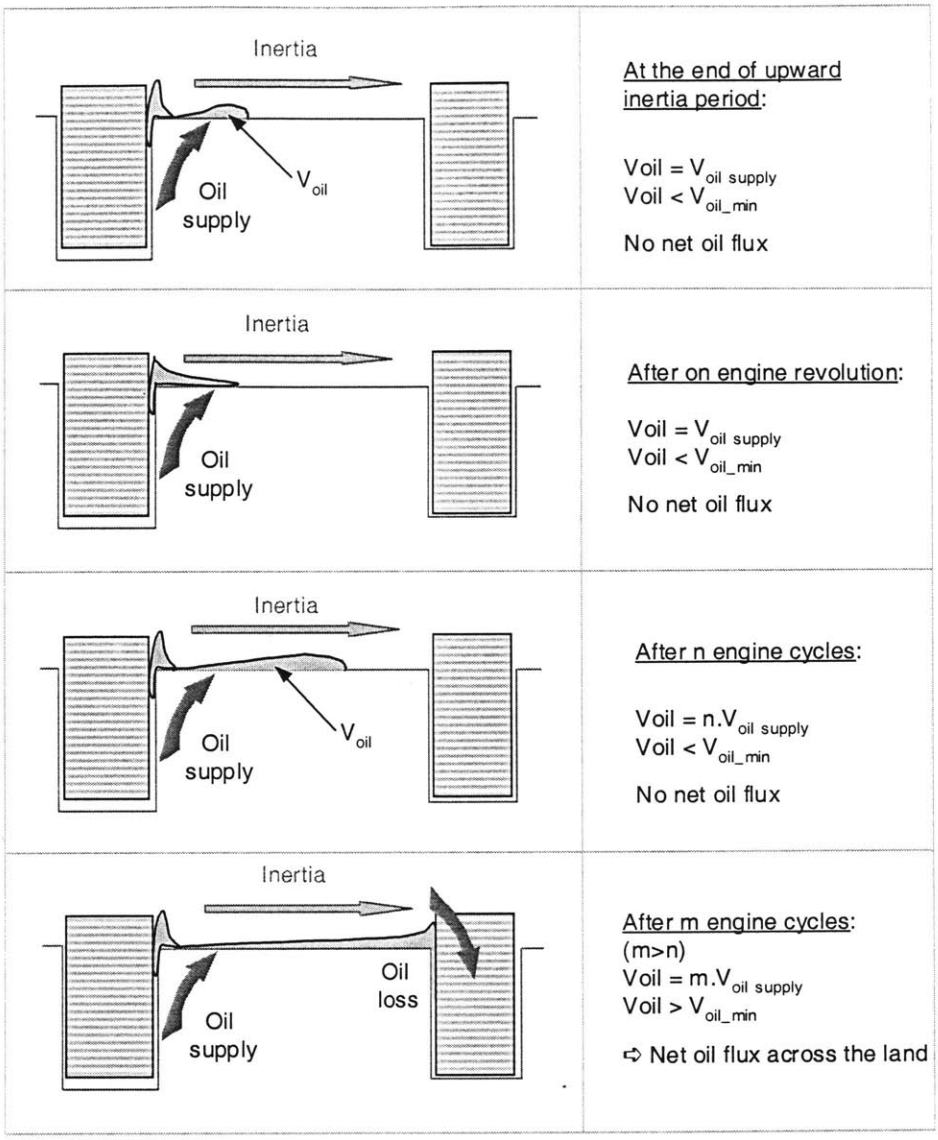


Figure 3.16 – Description of the inertia-driven oil transport across the piston lands (I).

The model developed for inertia driven oil transport can be used to evaluate V_{oil_min}, CA_r and T_{acc}. From the model, we have:

$$P_{fp}(CA) = F(N, V_{oil}, \upsilon, h_0, CA) \tag{3.18}$$

With P_{fp}: position of the front edge of the puddle

CA: crank angle specified

V_{oil}: Volume of oil accumulated on the land (puddle volume)

V_{oil_min} can be determined by solving Equation 3.19.

$$L_{ld} = F(N, V_{oil_min}, \upsilon, h_0, CA_i) \tag{3.19}$$

With L_{ld}: axial length of the land

CA_i: crank angle degree at which inertia changes direction

Then, for a given oil volume V_{oil} such that $V_{oil} > V_{oil_min}$, CA_r can be computed by solving Equation 3.20.

$$L_{ld} = F(N, V_{oil}, \upsilon, h_0, CA_r) \tag{3.20}$$

Eventually, Tacc can be simply determined by converting the duration CA_i-CA_r from crank angle degrees to seconds.

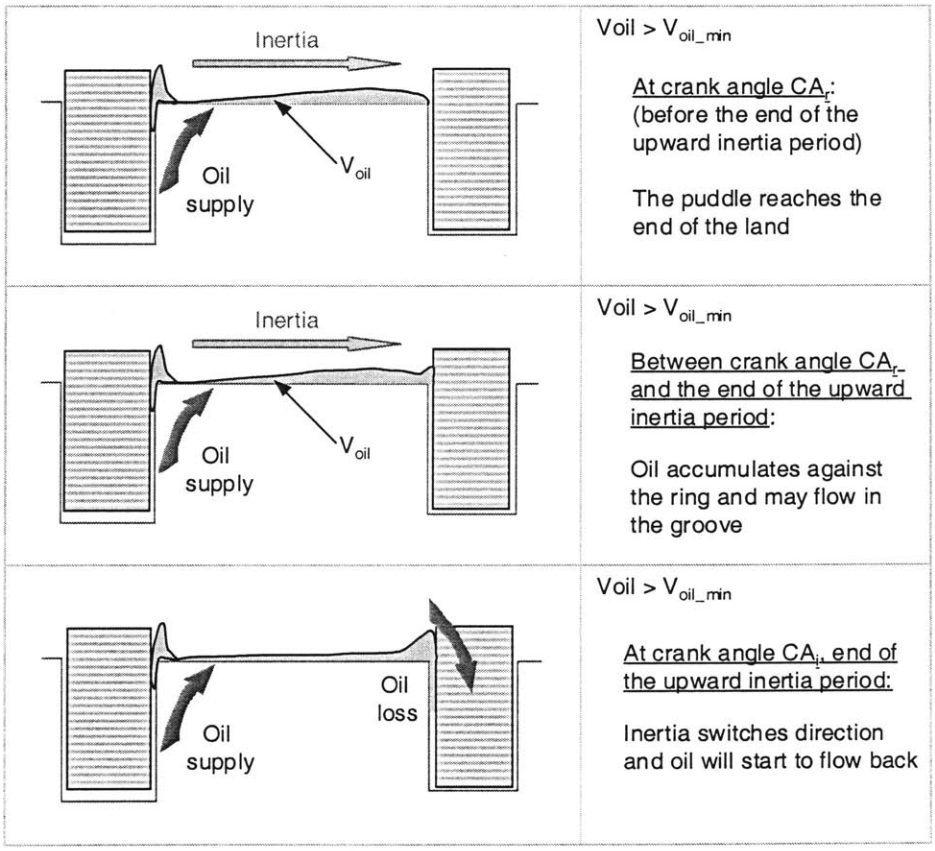


Figure 3.17 – Description of the inertia-driven oil transport across the piston lands (II).

The puddle aspect ratio: Due to the rolling-over process, the maximum height h and the aspect ratio of the puddle S_p/h, where Sp is the width of the puddle, are completely determined by the engine speed and the puddle volume. In Figure 3.18 and 3.19, where the evolution of S_p/h and h are plotted as a function of the puddle volume for different engine speeds, it can be seen that the oil puddle flattens as the engine speed and/or the puddle volume increases.

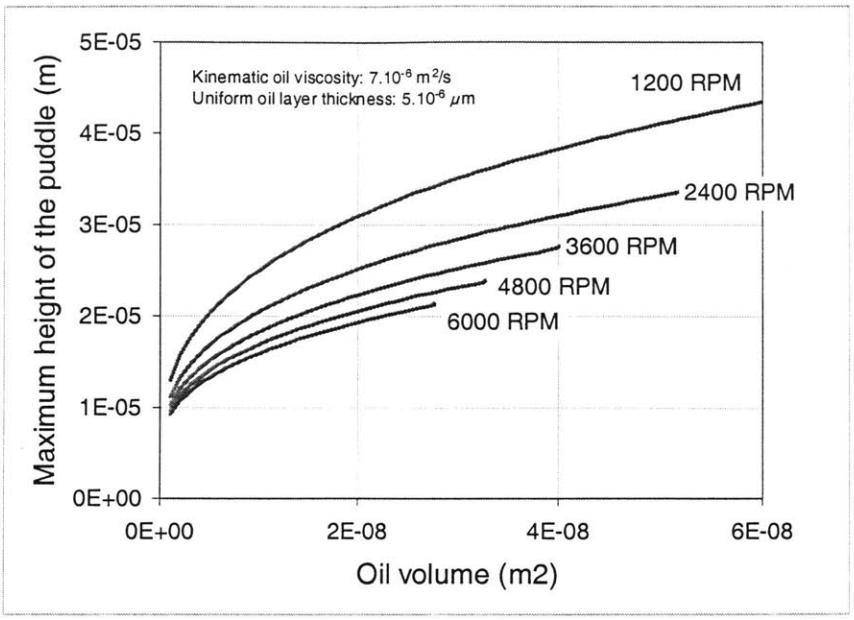


Figure 3.18 - Computed effect of the engine speed and oil volume on the maximum height of a two-dimensional puddle.

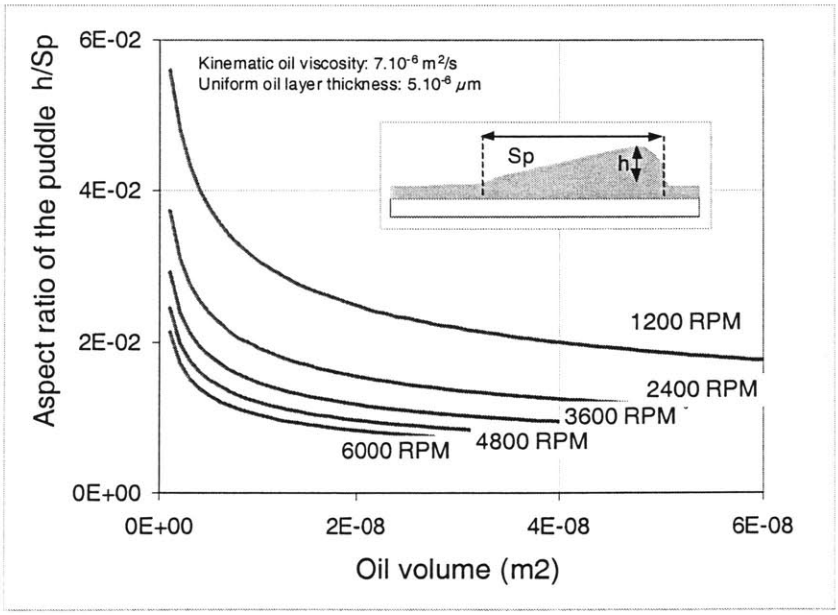


Figure 3.19 - Computed effect of the engine speed and oil volume on the aspect ratio of a two-dimensional puddle.

Dimension analysis: In order to find an analytical relationship that could relate the position and the aspect ratio of the puddle to the input parameters (puddle volume, engine speed, oil viscosity and thickness of the uniform oil layer) a dimension analysis was conducted. The variables to be determined were the puddle width S_p and the puddle maximum height h. The parameters taken into account were the piston maximum speed Vp_{max}, the puddle volume V_{oil}, the thickness h_0 of the uniform oil layer covering the land and the oil kinematic viscosity v. Since the oil displacement depends on the integral of the piston acceleration over time, the piston maximum speed was preferred to the piston acceleration. The dimension analysis provided the following relationships.

$$\frac{S_p}{\sqrt{V_{oil}}} = f\left(\frac{Vp_{max}\cdot\sqrt{V_{oil}}}{\upsilon}, \frac{h_0}{\sqrt{V_{oil}}}\right) \tag{3.21}$$

$$\frac{h_{max}}{\sqrt{V_{oil}}} = g\left(\frac{Vp_{max}\cdot\sqrt{V_{oil}}}{\upsilon}, \frac{h_0}{\sqrt{V_{oil}}}\right) \tag{3.22}$$

The shape of the functions *f* and *g* can be seen on Figure 3.20 and 3.21 where $\frac{S_p}{\sqrt{V_{oil}}}$ and $\frac{h_0}{\sqrt{V_{oil}}}$ are plotted as function of $\frac{Vp_{max}\cdot\sqrt{V_{oil}}}{\upsilon}$ and $\frac{h_0}{\sqrt{V_{oil}}}$. Each plot shows 41 points that have been computed with the model developed for inertia-driven oil transport. These points correspond to engine speed varying from 1000 to 6000 rpm, h_0 varying from 2 to 10 μm and oil accumulation volume varying from 5.10^{-9} to 9.10^{-8} m^2. The oil kinematic viscosity was fixed at 7.10^{-6} m^2/s. The surfaces on which the 41 data points lies have been fitted with the analytical functions given in Equations 3.23 and 3.24. On Figures 3.22 and 3.23, the data points and the fitted surfaces are plotted.

$$\frac{S_p}{\sqrt{V_{oil}}} = 7.29\cdot\left(\frac{Vp_{max}\cdot\sqrt{V_{oil}}}{\upsilon}\right)^{0.394}\cdot\left(\frac{h_0}{\sqrt{V_{oil}}}+0.163\right) \tag{3.23}$$

$$\frac{h_{max}}{\sqrt{V_{oil}}} = 2.91\cdot\left(\frac{Vp_{max}\cdot\sqrt{V_{oil}}}{\upsilon}\right)^{-0.286}\cdot\left(\frac{h_0}{\sqrt{V_{oil}}}+0.240\right) \tag{3.24}$$

Using Equation 3.23, the distance traveled at a crank angle degree CA by the front edge of the oil accumulated on a piston land can be directly computed.

$$D_p = 7.29\cdot\left(\frac{\left|V_p - Vp_{max}\right|\cdot\sqrt{V_{oil}}}{\upsilon}\right)^{0.394}\cdot\left(h_0+0.163\cdot\sqrt{V_{oil}}\right)+\frac{h_0^2}{\upsilon}\cdot\left|Vp - Vp_{max}\right| \tag{3.25}$$

With Vp: piston velocity at crank angle degree CA.

The oil sub-layer, which represents oil that permanently stays on the lands, is always very thin and therefore has little effect on the oil puddle displacements. For practical computation, the average depth of the piston tool marks gives a good estimation of the sub-layer thickness.

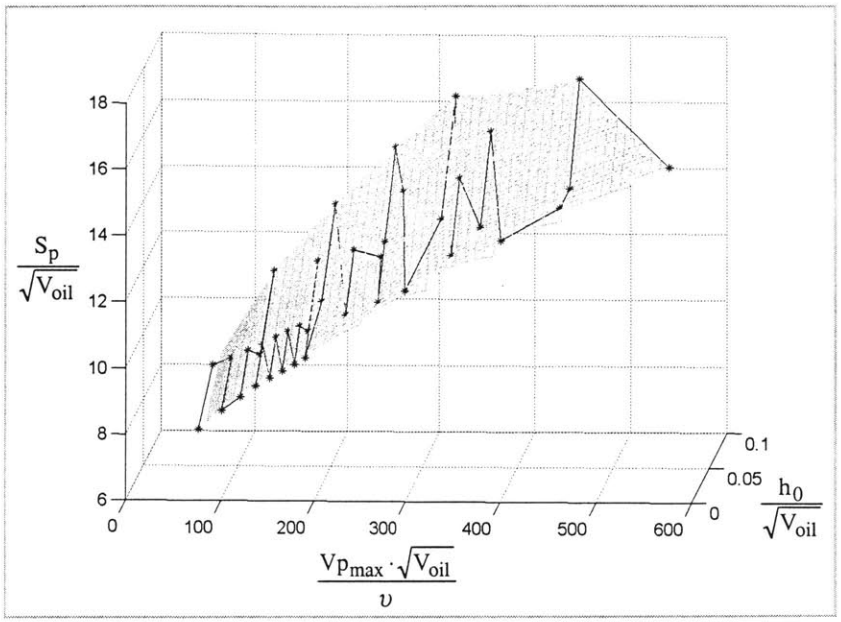


Figure 3.20 – Computed non-dimensional puddle width (The surface was generated with linear interpolation of the data points).

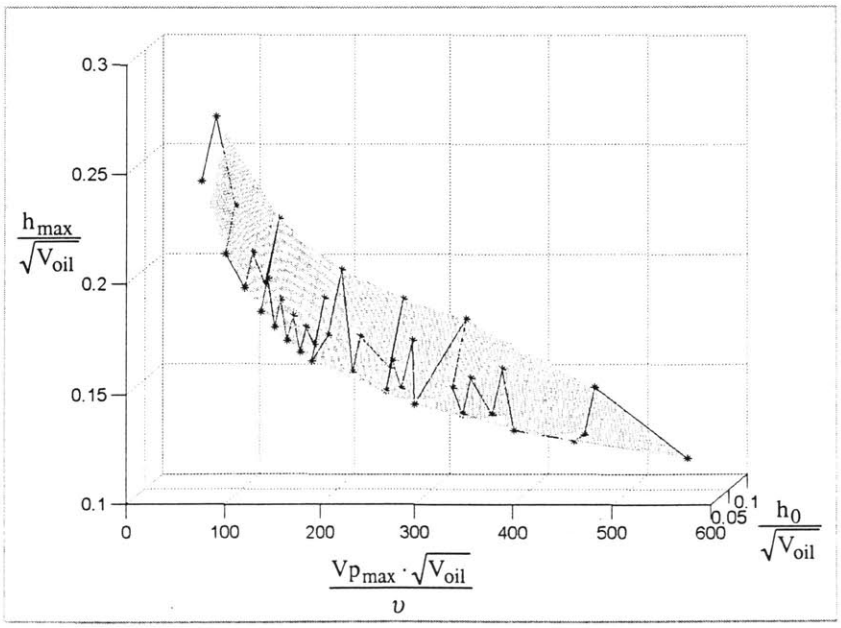


Figure 3.21 – Computed non-dimensional puddle maximum height (The surface was generated with linear interpolation of the data points).

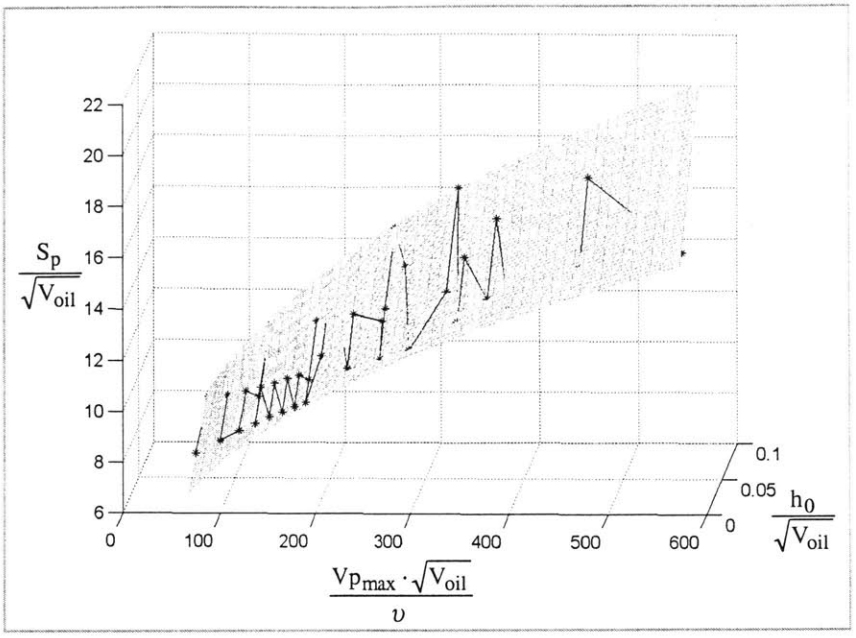


Figure 3.22 – Surface showing the non-dimensional puddle width computed with the analytical function fitted to the data points obtained with the inertia-driven flow model.

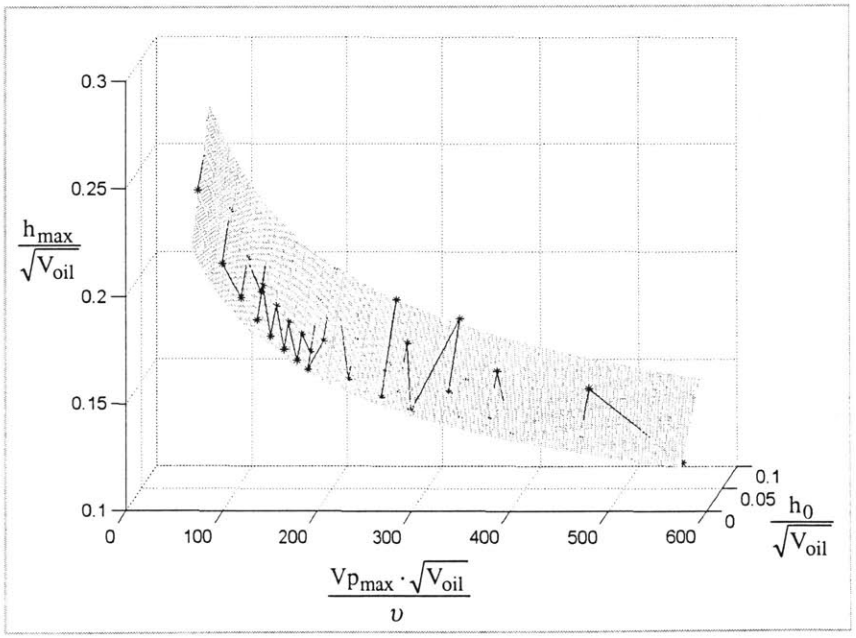


Figure 3.23 – Surface showing the non-dimensional puddle maximum height computed with the analytical function fitted to the data points obtained with the inertia-driven flow model.

3.1.1.4 3-Dimensional Aspects

Observations and description: Figure 3.24 shows various 3-dimensional oil patterns resulting from the effect of inertia on oil accumulated on or supplied to the piston second or third land. Experimental observations showed that the three dimensional aspect of the oil flowing under the effect of inertia force could vary depending on the way the oil is supplied to the piston land. Three different cases were distinguished:

1- The oil flowing on the land comes from a recessed area on the piston. For instance, oil comes from the cutoff on the top of the third land or from the hook of the Napier ring. In this case, oil on the land is the oil that could not be contained in the cutoff region. This excessive oil has spilled over the edge of the cutoff and flowed onto the land. The resulting oil circumferential distribution depends on the uniformity of the oil accumulation in the recessed area. As it can be seen on images 1, 2 and 3, in most cases the third land oil distribution obtained with the oil coming from the hook/cutoff region is almost 2-dimensional (no circumferential variation). In this case, the frequency at which oil is supplied from the cutoff region to the land depends on how often excessive oil has to be released and thus how fast the hook/cutoff region fills up. This may take from one to several hundreds cycles.

2- The oil on the land comes from the ring/groove interface and has been squeezed out of the groove due to the ring motion. In this case, the circumferential variations of the oil layer on the land depend on the uniformity of the oil accumulated in the ring/groove clearance. As it can be seen on images 4, 5, 6 and 7 (Figure 3.24), the resulting oil distribution can be either very non-uniform (see image 7) or almost 2-dimensional (see image 4).

3- Oil flowing on the land can come from a thick puddle of oil located at one end of the piston land. Such oil puddle results from the accumulation of small quantities of oil supplied to the land every cycle. In this particular case, when the puddle becomes large enough so that it can be affected by the inertia force, Raleigh-Taylor instability develops at the surface of the oil puddle. The resulting 3-dimensional shape (see image 8 and 9) is a series of lobes pointing in the direction of the inertia force. The development of Raleigh Taylor instability can only occur if a large enough quantity of oil can be accumulated at one end of the land, and if it occurs, the formation of the resulting non-uniform oil pattern will be repeated every engine cycle.

Raleigh-Taylor instability: The Raleigh-Taylor instability is a form of instability that can develop at the surface of an accelerated fluid. It results from the action of a body force, in our case the inertia force, and a stabilizing force, here the surface tension. The characteristic length associated with this instability can be roughly estimated by the following equation:

$$L_c \approx \sqrt{\frac{\sigma}{\rho \cdot a_p}} \tag{3.26}$$

Using $a_p = 200$ m/s^2 (average downward piston acceleration at 1200 rpm)

$\sigma = 0.02$ N.m

$\rho = 800$ kg.m^3

Equation 3.26 gives $L_c \sim 0.4$ mm. This number is in good agreement with the 2-mm instability characteristic length measured at 1200 rpm on image 8 of Figure 3.24. The ratio between L_c at 1200 and L_c at 2800 rpm was estimated using Equation 3.26:

$$\frac{L_c(1200\,\text{rpm})}{L_c(2800\,\text{rpm})} = \sqrt{\frac{a_p(2800\,\text{rpm})}{a_p(1200\,\text{rpm})}} = \frac{2800}{1200} = 2.3$$

The same ratio, measured experimentally from LIF images 8 and 9 of Figure 3.24 was found to be about 2.2.

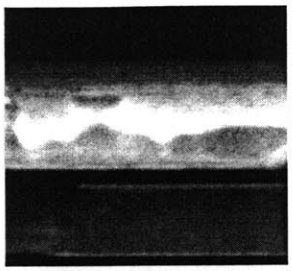
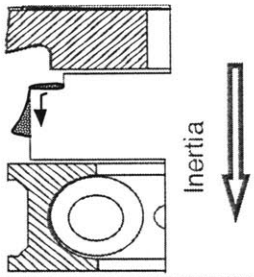
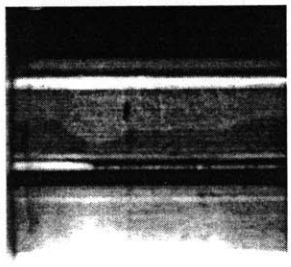
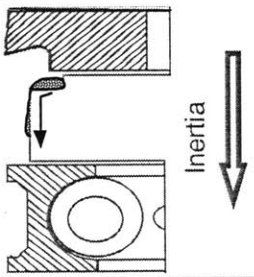
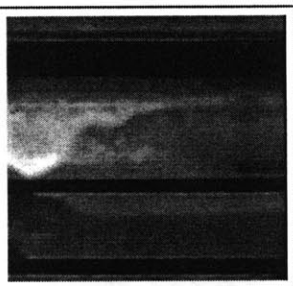
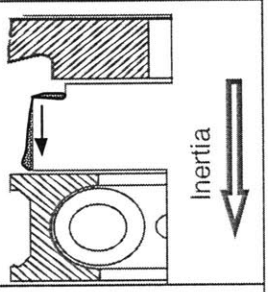
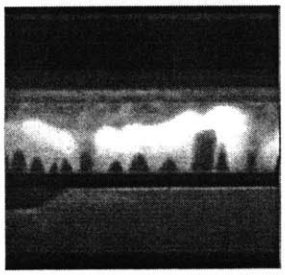
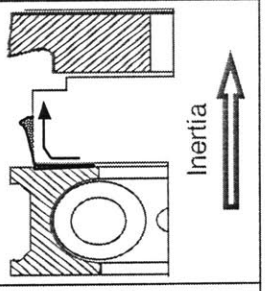
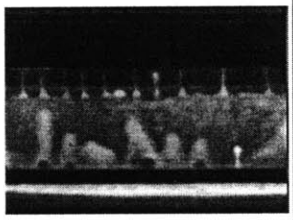
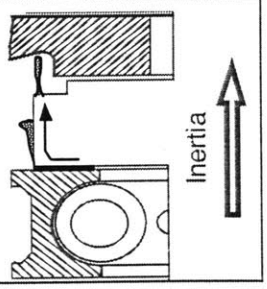
Image 1: PSA 3500 rpm • 122° crank angle (Intake Stroke) • Third land ⇨ Oil comes from the cutoff (spill over the corner)		
Image 2: Kub. 2800 rpm • 88° crank angle (Compression Stroke) • Third land ⇨ Oil comes from the hook (spill over the corner)		
Image 3: PSA 3500 rpm • 135° crank angle (Intake Stroke) • Third land ⇨ Oil comes from the cutoff (spill over the corner)		
Image 4: PSA 3500 rpm • 315° crank angle (Compression Stroke) • Third land ⇨ Oil comes from the clearance between OCR and its groove (gases comes out as well)		
Image 5: PSA 3500 rpm • 33° crank angle (Intake Stroke) • Third land ⇨ Oil comes from the clearance between OCR and its groove		

Figure 3.24a – 3-dimensional aspect of the third land oil distribution (I).

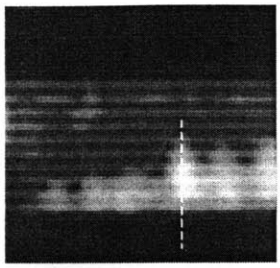
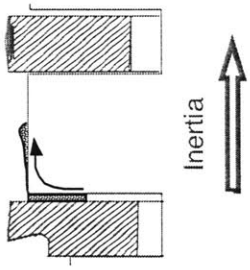
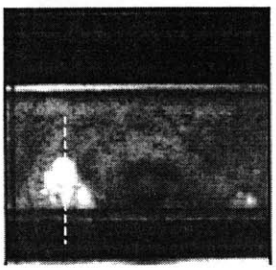
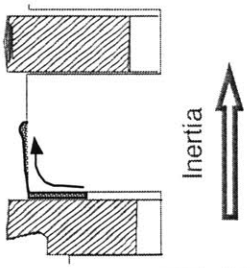
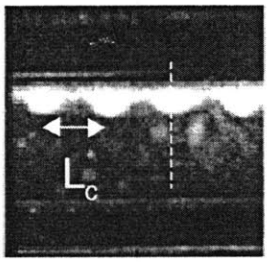
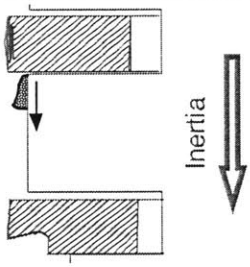
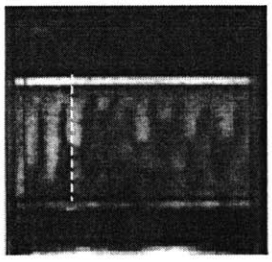
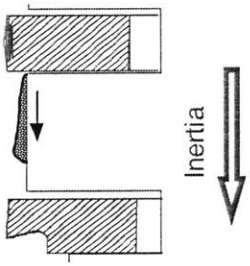
Image 6: PSA 2500 rpm • 78° crank angle (Intake Stroke) • Second land ⇨ Oil comes from the clearance between the scraper ring and its groove		
Image 7: Kub. 2000 rpm • 88° crank angle (Intake Stroke) • Second land ⇨ Oil comes from the clearance between the scraper ring and its groove		
Image 8: Kub. 1200 rpm • 88° crank angle (Compression Stroke) • Second land ⇨ Oil accumulated on the land flows downward (Raleigh-Taylor instability)		
Image 9: Kub. 2800 rpm • 88° crank angle (Compression Stroke) • Second land ⇨ Oil accumulated on the land flows downward (Raleigh-Taylor instability)		

Figure 3.24b – 3-dimensional aspect of the second land oil distribution (II).

3.1.2 Gas Flow Driven Circumferential Oil Transport

3.1.2.1 Observations and Descriptions

Oil accumulated on the piston lands was consistently observed to move in the circumferential direction. Multiple experimental observations have showed that the velocity and the direction of the circumferential oil motion depended on the relative position of ring gaps and on the amplitude and direction of the flow of blow-by gases. Indeed, the circumferential oil motion was found to be driven by the shear stress created by the gas flow at the surface of the oil layer. A few examples of observed circumferential oil flows are presented below.

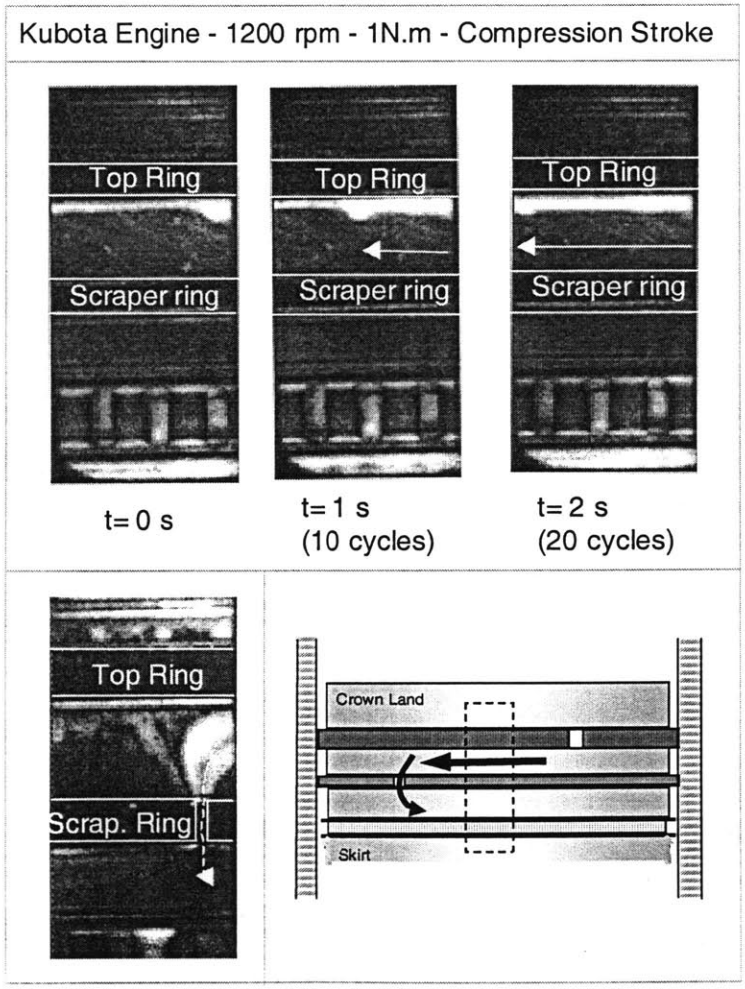


Figure 3.25 – Circumferential oil flow observed on the second land of the Kubota engine (I).

Observations in the Kubota engine: In Figure 3.25, the top three images, which were acquired one second apart, show the evolution of the oil distribution on the second land of the Kubota engine at 1200 rpm and 1 N.m load. On the first image (left), a puddle of oil can be distinguished on the right of the second land, just below the top ring. On the following two images, it can be seen that the oil puddle moved in the circumferential direction (from right to left) at a velocity of about 3 mm/s (0.3 mm/cycle). The bottom image, which was acquired a few minutes later while the scraper ring was rotating, shows the scraper ring gap. On this image, we can see that the oil that was moving in the circumferential direction toward the scraper ring gap is now being dragged into the gap. A similar oil motion can be identified on the images shown in Figure 3.26. But in this case, the top and second ring gaps had rotated and their positions were such that the oil flow toward the scraper ring gap was from left to right.

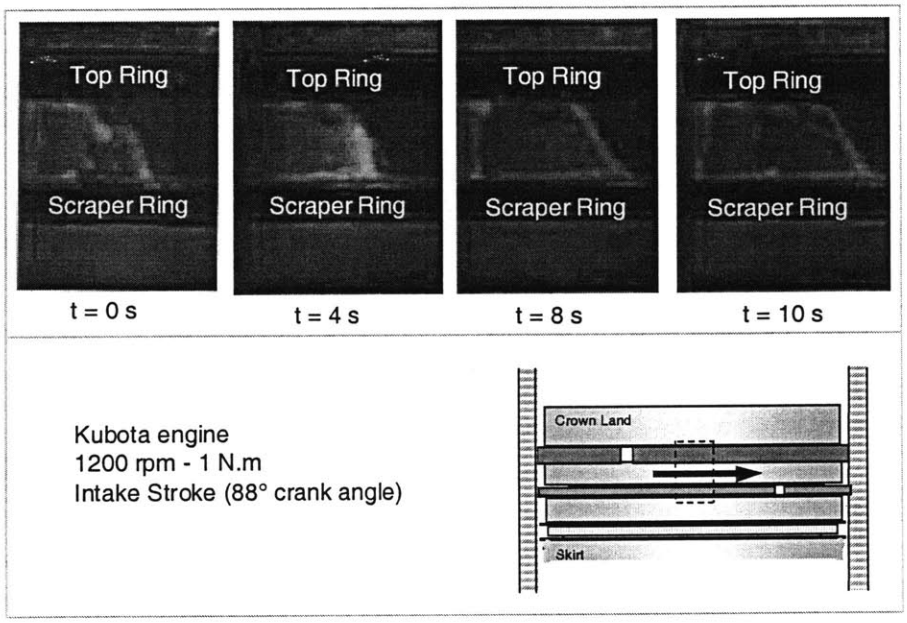


Figure 3.26 – Circumferential oil flow observed on the second land of the Kubota engine (II).

Using the simulation code RINGPACK-OC, the flow rates of gases flowing through the top and second ring gap were computed for the corresponding engine running conditions (1200 rpm, 1N.m). The results, which are plotted in Figure 3.27, show that during the compression stroke and the early part of expansion stroke blow-by gases were flowing from the top ring gap to the second ring gap across the second land. During the late part of expansion stroke blow-by gases were flowing out of the second land toward both the crown and the third land. Averaging the gas flows through the top and second ring gap and integrating the average over the engine cycle shows that overall the net flow of gases sweeping the second land was going from the top to the second ring gap. Accordingly, the

circumferential oil flow observed in Figure 3.25 and 3.26 was attributed to the dragging effect of the blow-by gases flowing around the piston.

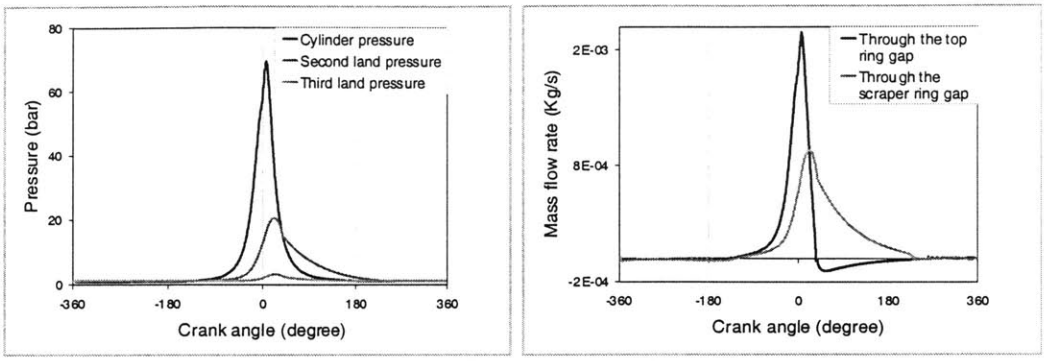


Figure 3.27 – Lands pressures and gas flow rate at the top two ring gaps in the Kubota engine running at 1200 rpm 1N.m load
(Results computed with RINGPACK-OC).

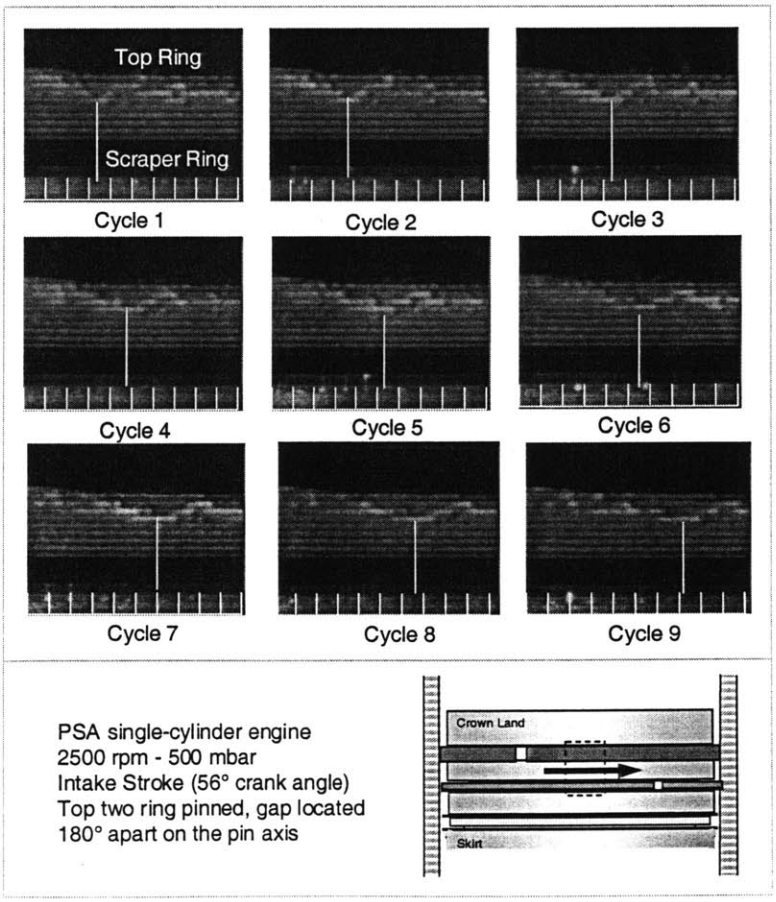


Figure 3.28 – Circumferential oil transport observed on the second land of the PSA engine.

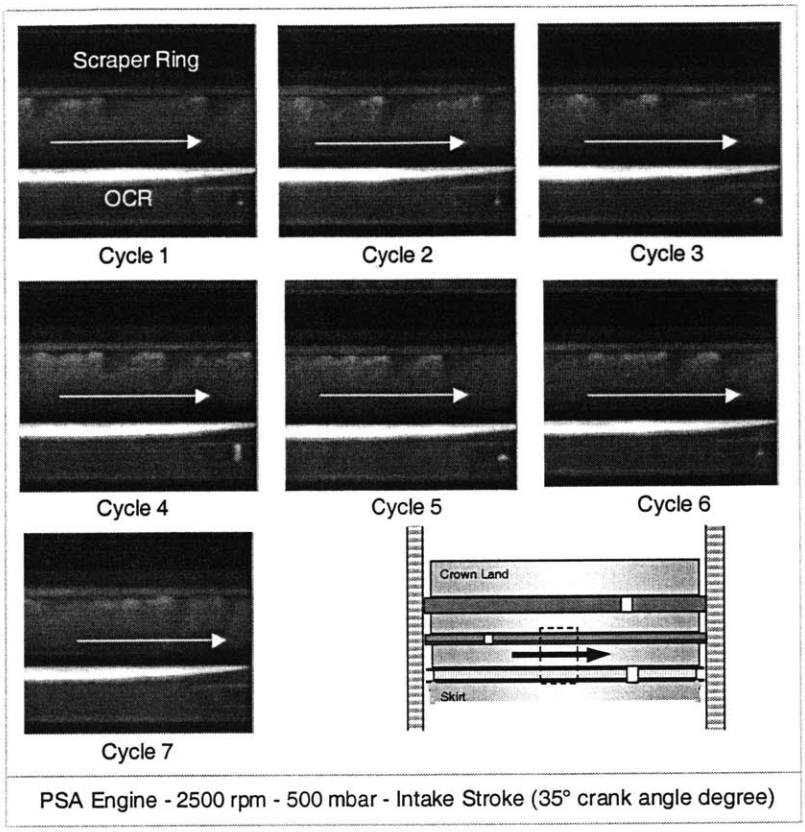


Figure 3.29 – Circumferential oil transport observed on the third land of the PSA engine.

Observations in the PSA single-cylinder engine: Figures 3.28 and 3.29 show the evolution of the oil distribution on the piston lands of the PSA engine while the engine was running at 2500 rpm with 500-mbar Absolute Intake Pressure (AIP). In this test, the top two rings were pinned and as a result the second land oil distribution was fairly uniform. Consequently, oil flow patterns were difficult to observe. However, in Figure 3.28 an oil accumulation pattern can be identified and tracked on the second land. It can be seen that oil was flowing from left to right – from the top ring gap position to the second ring gap. From the LIF images, the thicker part of the oil layer (~20 μm) was determined to move at about 0.6 mm/cycle. Similarly, an oil pattern can be tracked on Figure 3.29, which shows the evolution of the third land oil distribution during another test conducted at 2500 rpm 500 mbar AIP. In this case, the oil layer was about 35 μm thick and the oil was moving at 0.65 mm/cycle toward the OCR gap. For these running conditions, the average gas flows on the lands was computed using RINGPACK-OC. The results showed that on both lands the circumferential flow of blow-by gases was going from the upper ring gap to the lower ring gap. The integrated gas flow rate was $2.20.10^{-7}$ m^3/cycle on the second land and $2.71.10^{-7}$ m^3/cycle on the third land. Once again, the observed circumferential oil flow could be attributed to the dragging effect of the blow-by gases.

The argument that circumferential oil displacements are driven by the flow of blow-by gases was further confirmed by the observation results presented in Figure 3.30. The first image of Figure 3.30 was acquired while the engine was running at 4500 rpm two seconds after a fast transition (0.1 s) of the intake pressure from 700 down to 200 mbar. This particular test was conducted to study the effects of suddenly releasing the accelerator while cruising on the highway. Here, the interest is not the consequence of the sudden change of engine running conditions. Rather, the interest was to examine the effect of changing the gas flow rate on the oil flow. Simulation results show that in this condition the average flow of blow-by gases was going from the crankcase to the combustion chamber. In particular, the average flux of gases across the second land was found to direct from the second ring gap to the top ring gap at a rate of $2.7.10^{-9}$ m^3/cycle. On the sequence of four images presented in Figure 3.30, we can see that the oil accumulated on the second land was flowing from left to right, which according to the fixed ring gap positions means that the oil was being transported from the second to the top ring gap. Therefore, in this particular case where the flow of blow-by gases was reversed, the circumferential oil flow was observed to be reversed as well.

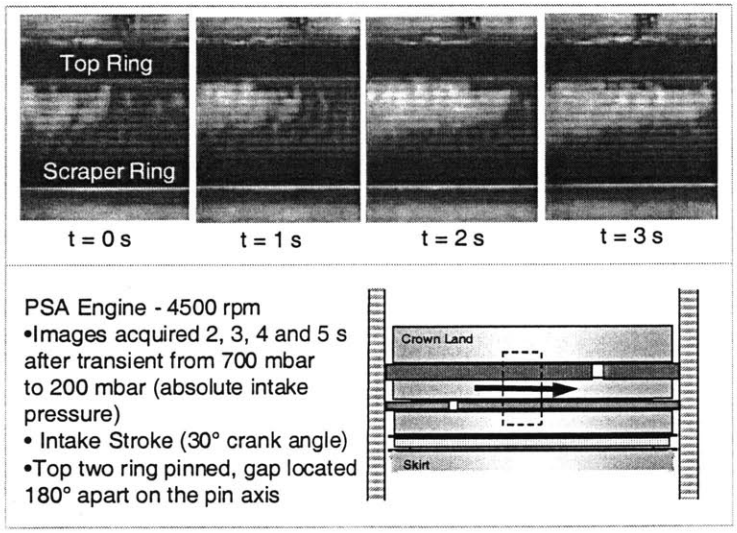


Figure 3.30 – Circumferential oil transport observed on the second land of the PSA engine while the blow-by was negative.

Description of the oil flow: Since the oil layer at the surface of the piston is very thin ($h_{oil} << L_{ld}$), we first assumed that the oil flow could be represented as a one-dimensional flow driven by a given shear stress at one of its boundary (see Figure 3.31). For such flow, the Navier-Stokes equations can be reduced to:

$$\frac{\partial u}{\partial t} + u\frac{\partial u}{\partial x} + v\frac{\partial u}{\partial y} = \upsilon_{oil} \cdot \frac{\partial^2 u}{\partial y^2} \tag{3.27}$$

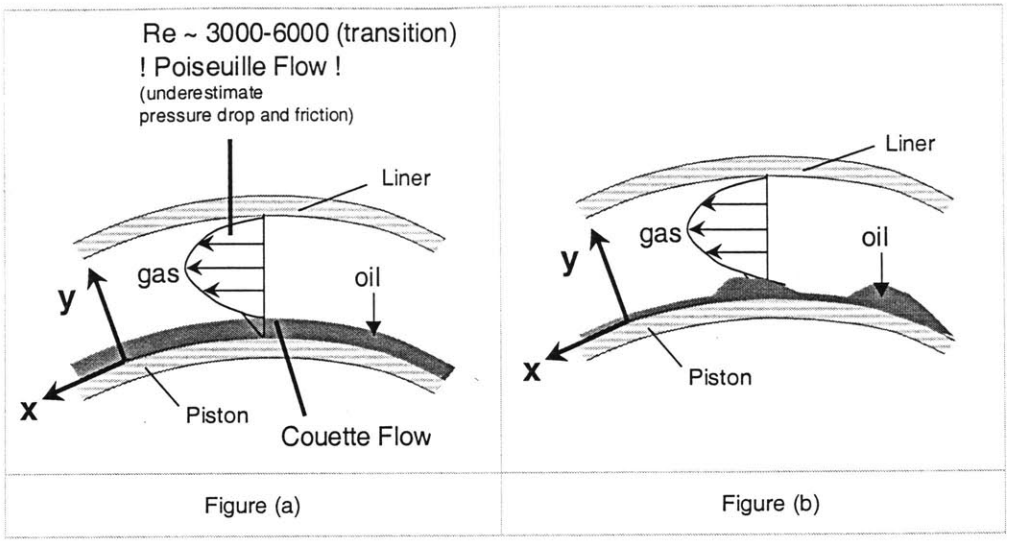


Figure 3.31 – Description of the gas flow and oil profile used for modeling the dragging action of the blow-by gases.

The comparison of the unsteady and convection terms with the viscous term was conducted using an estimation of the average oil velocity derived for a fully viscous flow. The results were as follows:

$$\tilde{u} = \frac{\tau_{gas}}{2\mu_{oil}} \cdot h_{oil} = \frac{3\mu_{gas}}{\mu_{oil} . h_{ld}^2} \cdot \frac{\tilde{q}_{gas}}{L_{ld}} \cdot h_{oil} \tag{3.28}$$

$$\frac{\partial u}{\partial t} \Big/ \upsilon_{oil} \frac{\partial^2 u}{\partial y^2} \sim \frac{h_{oil}^2 \cdot N \cdot \pi}{30 \cdot \upsilon_{oil}} \sim 1.10^{-2} \tag{3.29}$$

$$u \frac{\partial u}{\partial x} \Big/ \upsilon_{oil} \frac{\partial^2 u}{\partial y^2} \sim \left(\frac{h_{oil}}{\pi \cdot D} \right) \frac{\tilde{u} \cdot h_{oil}}{\upsilon_{oil}} \sim \frac{3 \cdot \rho_{oil} \cdot \mu_{gas} \cdot \tilde{q}_{gas} \cdot h_{oil}^3}{\mu_{oil\,s}^2 \cdot h_{ld}^2 \cdot L_{ld} \cdot \pi \cdot D} \sim 1.10^{-6} \tag{3.30}$$

Using $\tilde{q}_{gas} = 8.6.10^{-6}$ m^3/s (computed average gas flow on the second land at 2500 rpm WOT)

$\mu_{oil} = 5.6.10^{-3}$ Pa.s (low shear dynamic viscosity of Shell 15W40 oil at 130°C)

$\mu_{gas} = 2.10\text{-}5$ Pa.s (air dynamic viscosity at °C)

$h_{oil} = 20\ \mu$m

N = 2500 rpm

As one can see from Equations 3.29 and 3.30, the unsteady and convection terms are negligible, and therefore, the flow can be approximated as a Couette flow. As a result, the following equation and boundary conditions were used to compute the oil motion:

$$\upsilon_{oil} \frac{\partial^2 u}{\partial y^2} = 0 \tag{3.31}$$

$$\mu_{oil}\left.\frac{\partial u}{\partial y}\right|_{y=h_{oil}} = \tau_{gas} \qquad \text{And} \qquad u|_{h=0} = 0$$

Using Equation 3.31, the above boundary conditions and mass conservation, one can derived the following equation for the oil flow:

$$\frac{\partial h_{oil}}{dt} + \frac{\tau_{gas} \cdot h_{oil}}{\mu_{oil}} \cdot \frac{\partial h_{oil}}{dx} = 0 \tag{3.32}$$

Then combining Equations 3.32 and 3.33 we obtain:

$$\frac{\partial h_{oil}}{dt} + \frac{6 \cdot \mu_{air} \cdot q_{gas} \cdot h_{oil}}{\mu_{oil} \cdot h_{ld}^2 \cdot L_{ld}} \cdot \frac{\partial h_{oil}}{dx} = 0 \tag{3.33}$$

Equation 3.33 is a wave-type equation for which the wave speed is proportionally increasing with the oil thickness h_{oil}. Similarly to what was explained for the equation describing the inertia driven flow (Equation 3.10), due to the increase of the wave speed with the oil layer thickness, the positive sloping oil surface ($dh/dx > 0$) will flatten under the dragging effect of the gas flow, and the negative slopping surface will get steeper. Therefore, any disturbance of the oil thickness may develop into a steep front on the oil surface and thus create a zone in which the one-dimensional flow representation is not valid.

LIF observations showed that the oil layer covering the piston lands could be very non-uniform. The thickness of the oil film was found to have significant variations in both the axial and the circumferential direction. As it was explained in paragraph 3.1.1.4, the 3-dimensional aspect of the oil layer can be the result of a non-uniform oil supply to the land or of the development of Raleigh-Taylor instabilities at the surface of large oil accumulation. For instance, Figure 3.32 shows the three-dimensional aspect of a portion of the oil layer covering the second land in the PSA single-cylinder engine. The oil distribution profile was measured during compression stroke while the engine was running at 4500 rpm with 300 mbar AIP. As one can see, the oil distribution is fairly non-uniform and therefore steep fronts are very likely to develop at the surface of the oil layer. To see the effect of the gas flow on the shape of the oil surface, one should look at the oil distribution during the late part of expansion stroke, right after the peak of circumferential gas flow. Figure 3.33 shows a three-dimensional representation of the second land oil distribution measured 130 crank angle degrees after the combustion TDC. The effect of the gas flow on the local slope of the oil surface can be seen on the 1-D and 2-D profiles as well as on the LIF image. In particular, on the 1-dimensional oil thickness profile, we can see that the portion of the surface where dh/dx is negative (shown by the dashed lines) have steeper slope than the area where dh/dx is positive (shown by the full line).

Furthermore, steep fronts formed by the dragging action of the gas flow can clearly be identified on 3-D profile of the oil surface shown in Figure 3.33. The slope measured in these areas was between 1/10 and 1/5. Since the length of the steepest part of the oil profile is close to the camera resolution, these measurements probably give an underestimation of the real slope. For comparison the slope measured on the backside of the oil puddles was about 1/30 or less.

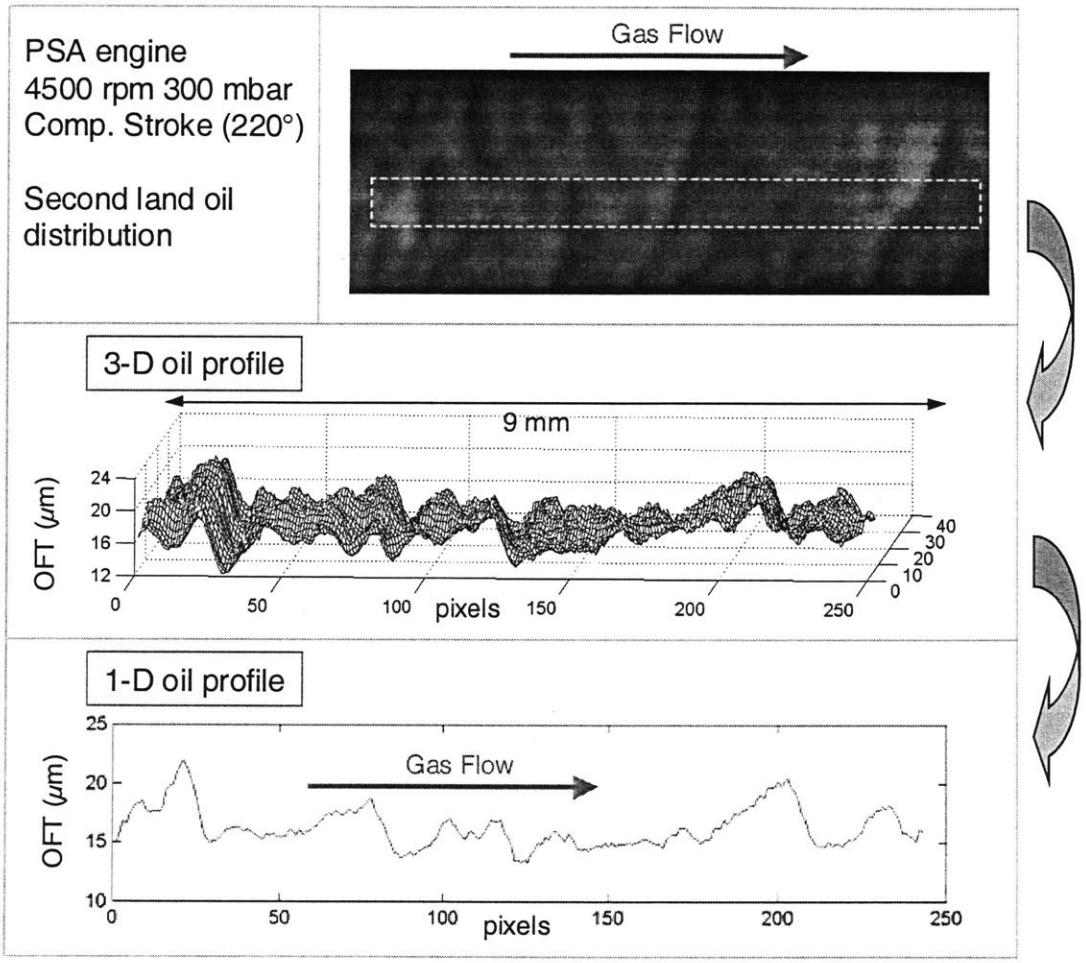


Figure 3.32 – Wavy aspect of the second land oil layer (PSA engine – Compression stroke).

Therefore, as predicted from the form of Equation 3.33, experimental observations showed that the combination of the dragging effect of blow-by gases and the inherent non-uniformity of the piston land oil distribution may result in the formation of steep fronts on the oil surface. Eventually, in the vicinity of these steep surface areas, the flow becomes locally 2-dimensional and the shape of the oil surface is constrained by surface tension. In particular, the oil flow at the steep front involves a rolling-over motion similar to the one described for inertia driven flow.

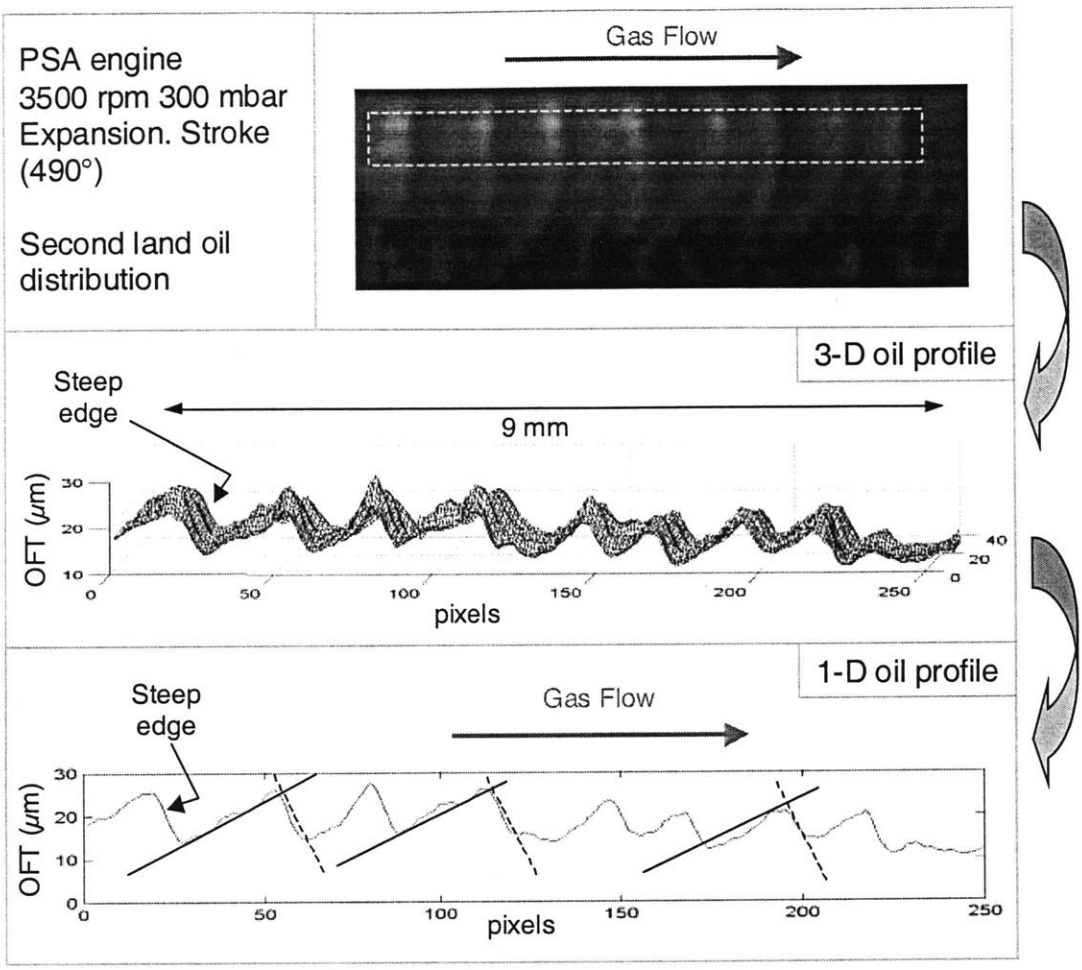


Figure 3.33 – Wavy aspect of the second land oil layer (PSA engine – Expansion stroke).

3.1.2.2 Modeling

Modeling of the blow-by gases flow: To model the oil motion induced by the dragging effect of the blow-by gases, we first need to describe the gas flow between the piston land and the liner. For a flow between parallel plates the transition to turbulence starts when the Reynolds number (Re) reaches 2800 and the turbulence becomes fully developed for Re greater than 10000. The evolution over one engine cycle of the volumetric flow rate and Reynolds number of the gas flow sweeping the second land was computed for two high load conditions and is plotted in Figure 3.34. Because the shear stress at the boundaries of the gas flow is function of the volumetric flow rate, the volumetric flow rate was preferred to the mass flow rate in this discussion. Moreover, because the circumferential gas flow rate is increasing with engine load and is higher on the second land than on the third land, the two cases plotted in Figure 3.34 are believed to show the upper limit of Reynolds numbers associated with circumferential gas flow. From the plots in Figure 3.34, it can be seen that

even though a significant portion of the flow occurs in the transition region, more than half of total volume of gases displaced flows in the laminar mode. Therefore, for the computation of the shear stress at the surface of the oil layer, the gas flow was assumed to be laminar. It is understood here that, at high engine load, the laminar flow assumption will lead to a slight underestimation of the average friction force exerted at the surface of the oil layer. However, the complexity involved in computing the effect of the flow transition is way beyond the scope of this work.

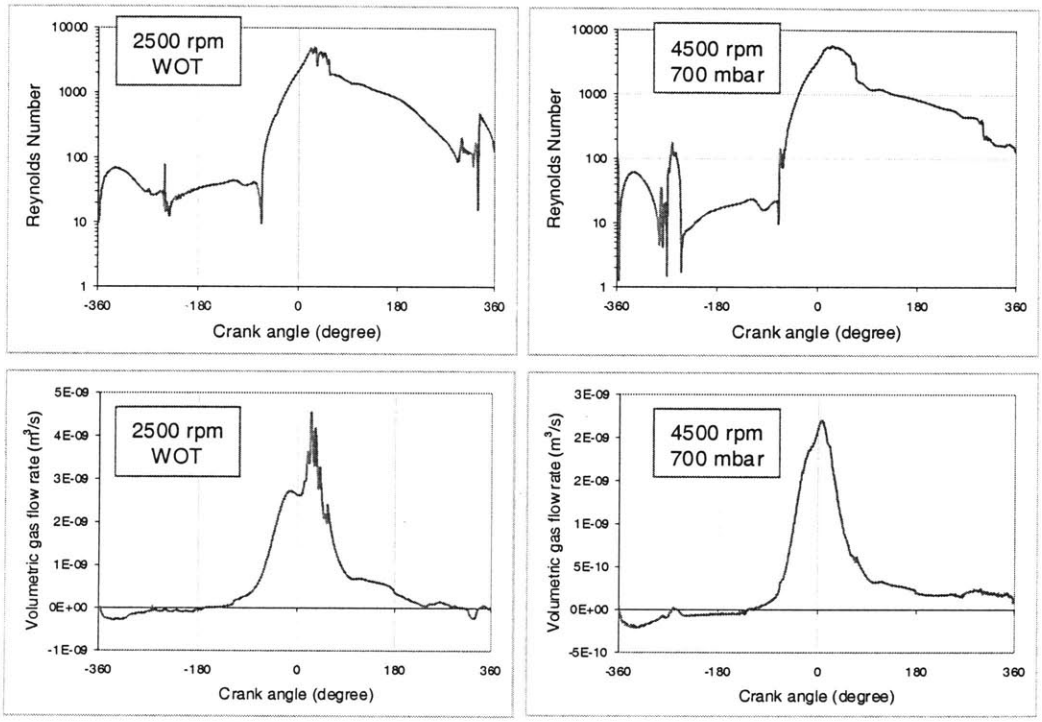


Figure 3.34 – Reynolds number and flow rate of the gas flow sweeping the second land (Calculated for the PSA engine with RINGPACK-OC).

Since the ratio of the land/liner clearance and the piston circumference is in the order of 10^{-3}, the flow was considered to be one-dimensional. Accordingly, for this type of flow the Navier-Stokes equations can be reduced to the following one:

$$\frac{\partial u}{\partial t} + u\frac{\partial u}{\partial x} + v\frac{\partial u}{\partial y} = \upsilon_{gas} \cdot \frac{\partial^2 u}{\partial y^2} - \frac{1}{\rho_{gas}}\frac{dP}{dx} \tag{3.34}$$

Comparison of the viscous diffusion time for the gas flow and the duration of one engine cycle gives the following result:

$$\frac{\text{Viscous diffusion time}}{\text{Engine cycle duration}} = \frac{h_{ld}^2 \cdot N}{\upsilon_{gas} \cdot 120} \sim 10^{-1}$$

With N = 6000 rpm

h_{ld} = 200 μm (clearance between the piston land and the liner)

$\nu_{gas} = 2.10^{-5}$ m^2/s (gas kinematic viscosity)

Since this value is obtained for 6000 rpm, it represents the upper limit. Therefore, the unsteady term of the Navier-Stokes equations was considered to be negligible. The ratio of the convection and viscous terms was estimated as follows:

$$R_{C/V} = \frac{u\dfrac{\partial u}{\partial x}}{\upsilon_{gas}\dfrac{\partial^2 u}{\partial y^2}} = \alpha \cdot \mathrm{Re}_{h_{le}} \text{ with } \mathrm{Re}_{h_{ld}} = \frac{u \cdot h_{ld}}{\upsilon_{gas}}$$

Where α is the angle between the liner and the piston land. This angle is quite difficult to determine since it depends on the piston ovality, the bore thermal deformation, the ring gap positions and the piston secondary motion. However, for the purpose of evaluating the ration of the convection and viscous term α can be approximated by the ratio of the land/liner clearance by the piston circumference. Therefore $R_{C/V}$ can be estimated by:

$$R_{C/V} = \frac{h_{ld}}{\pi \cdot D} \cdot \mathrm{Re}_{h_{le}}$$

With D: Bore diameter.

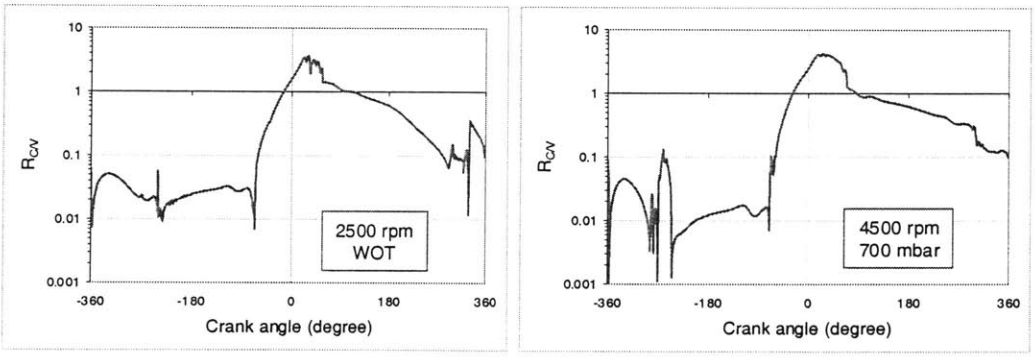


Figure 3.35 – Ratio of the convection and viscous dissipation terms for the gas sweeping the second land (Calculated for the PSA engine with RINGPACK-OC).

The evolution of $R_{C/V}$ over one engine cycle is plotted in Figure 3.35. As one can see, the convection term is not always negligible. It is even prominent over the viscous term in the early part of expansion stroke. This means that locally some part of the momentum is carried along with the flow, and therefore the friction does not exactly balance the pressure gradient. However, since the purpose here is to estimate the average oil transport induced by the gas flow over the entire piston land, the importance of the momentum convection is better estimated by considering a control volume defined

as the whole channel formed by the land/liner clearance. For instance, considering the second land, it can be assumed that the top and scraper ring gaps are located on the pin axis opposite to each other. In this case, the control volume is defined as the channel formed by the clearance between the second land and the liner on one side (thrust or anti-thrust) of the piston. Since the piston secondary motion does not affect the land/liner clearance on the pin sides, the flow sections at the entrance and the exit of the control volume are equal. Consequently, using mass conservation it can be shown that the momentum flux entering and exiting the control volume are equal, and thus that the friction at the boundaries of the control volume exactly balances the overall pressure drop. Therefore, in this particular case, it appears that neglecting the convection terms will only affect the local friction and not the average friction value that is representative of the overall dragging effect of the gas flow on the oil layer. In reality, the ring gaps are not pinned and they may be positioned anywhere around the piston. As a result, the difference between the momentum entering and exiting the control volume is not zero. Moreover, the angle α and thus the amount of convected momentum vary greatly within one engine cycle due to the piston secondary motion and the bore thermal deformation. As a result, the effect of the convection terms on the flow profile might be significant. An accurate computation of the gas flow structure would require, 1) to accurately know the angle α and its evolution within one cycle, 2) to solve the Navier-Stoke equations taking into account the convection terms, 3) to account for the rapidly moving boundaries during the piston slap.

Since this work was the first attempt to model the effect of gas dragging on the oil layer covering the piston lands, the objective here was to build a model that can be used to predict the trend and the order of magnitude of the oil flow. Thus, the requirement for the gas flow model was the ability to, 1) follow the trend of the boundary friction evolution when the gas flow rate is changing, and 2) be simple in computation. Accordingly, the convection terms were neglected and the flow assumed to be a Poiseuille flow. This assumption is equivalent to considering that the land/liner clearance is a straight channel ($\alpha = 0$). Despite the fact that this representation of the gas flow was highly simplified comparison of experimental data and computed results showed a good agreement between the observed and the calculated oil velocity in the circumferential direction. Therefore, the assumptions made to model the gas flow were considered to be appropriate.

Using the Poiseuille flow model, we have:

$$-\frac{dP}{dx} = \frac{q_{gas} \cdot 12 \cdot \mu_{gas}}{L_{ld} \cdot h_{ld}^3} \tag{3.35}$$

With q_{gas}: Gas volumetric flow rate (m3/s)

μ_{gas}: Gas dynamic viscosity (Pa.s).

Additionally, the shear stress at the boundary of the gas layer can be expressed as:

$$\tau_{gas} = \frac{1}{2}\left(-\frac{dP}{dx}\right)\cdot h_{ld} \tag{3.36}$$

Combining Equations 3.35 and 3.36, we obtain:

$$\tau_{gas} = \frac{6\mu_{gas}}{h_{ld}^2}\cdot\frac{q_{gas}}{L_{ld}} \tag{3.37}$$

At the interface between the oil and the gas layers the shear stress is balanced. Therefore, the shear stress in the oil is equal to the shear stress in the gases.

In this work, the value of q_{gas} was computed using the RINGPACK-OC model. Using this model and the measured cylinder pressure, one can compute the mass flow rate of blow-by gases through the ring gaps. To compute q_{gas}, the mass flow rate through the ring gaps have to be converted in volumetric flow rate, averaged and divided according to the ring gap positions. For instance, for the second land, the mass flow rate through the top and second ring gaps will be converted to volumetric flow rate using the calculated second land pressure and an input gas temperature. Then the average of the volumetric gas flow rate trough the top and second ring gap will be calculated. Finally the results will be divided according to the ring gap positions. In Figure 3.36, one can see that the ring gaps define two sectors on the piston land. The circumferential gas flow sweeping the sector defined by the angle θ is given by Equation 3.38 and the gas flow sweeping the sector defined by 2π-θ is given by Equation 3.39.

$$q_{gas}(\theta) = q_{gas_tot}\cdot\left(1-\frac{\theta}{2\pi}\right) \tag{3.38}$$

$$q_{gas}(2\pi-\theta) = q_{gas_tot}\cdot\left(\frac{\theta}{2\pi}\right) \tag{3.39}$$

With: $q_{gas_tot} = (q_{gap1} + q_{gap2})/2$

and q_{gap1}: instantaneous volumetric flow rate through the top ring gap (m^3/s)

q_{gap2}: instantaneous volumetric flow rate through the second ring gap (m^3/s).

For the computation results that are later described, whenever the gap positions were not specified, it was assumed that gaps were located on opposite sides of the piston ($\theta=\pi$).

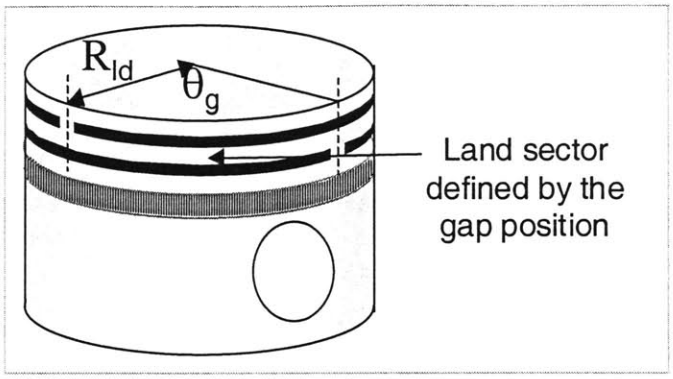


Figure 3.36 – Definition of the piston land sectors.

Modeling approach for the oil flow: Here, the objective of the modeling effort was to build a model that could be used to estimate the magnitude of the net circumferential oil transport induced by the gas dragging effect over one or more engine. As it was previously explained, the one-dimensional flow representation given by Equation 3.33 could only be used to compute the oil flow rate on the backside of the puddles. A more advanced model would have been required to predict the evolution of the oil velocity profile in the steep front areas. Nevertheless, the main interest was not in the details of the oil velocity profile but in an estimation of the average oil flow rate. Accordingly, the front edge of the puddles, which represents a small part of the total puddle width, was treated in a way analogous to what was done with inertia driven oil flows. Therefore, the position of the front edge was solved using mass conservation while the rest of the flow was computed using the one-dimensional approach previously described (Equation 3.33).

In order to use the characteristic method to solve for the evolution of the puddle position, the time dependency of the wave speed had to be eliminated. This was by dividing Equation 3.33 by Q_{gas}. Q_{gas}, which is the integrated volumetric gas flow rate, is given by the following equation:

$$Q_{gas} = \int_{\text{one cycle}} q_{gas} \cdot dt$$

$$\frac{dh_{oil}}{dQ_{gas}} + \frac{6 \cdot \mu_{air} \cdot h_{oil}}{\mu_{oil} \cdot h_{ld}^2 \cdot L_{ld}} \cdot \frac{dh_{oil}}{dx} \tag{3.40}$$

If Q_{gas} is the result of the integration over one cycle of the instantaneous volumetric gas flow, the calculated oil flow rate will represent a cycle-averaged oil transport rate. Eventually, the system of equations used to solve the evolution of the puddle position under the effect of gas dragging was composed of Equations 3.41, 3.42, 3.43 and 3.44. These equations were used analogously to Equations 3.14, 3.15, 3.16 and 3.17 for the inertia driven flow.

- $$X = X_0 + \frac{6 \cdot \mu_{air} \cdot h_{oil}}{\mu_{oil} \cdot h_{ld}^2 \cdot L_{ld}} \cdot Q_{gas} \quad (3.41)$$

- $$S = X_{01} + \frac{6 \cdot \mu_{air} \cdot h_{oil}}{\mu_{oil} \cdot h_{ld}^2 \cdot L_{ld}} \cdot Q_{gas} \quad (3.42)$$

- $$S = X_{02} + \frac{6 \cdot \mu_{air} \cdot h_{oil}}{\mu_{oil} \cdot h_{ld}^2 \cdot L_{ld}} \cdot Q_{gas} \quad (3.43)$$

- $$\int_{(S,h_{01})}^{(S,h_{02})} h \cdot dx = 0 \quad \text{with } h01 = h(X = X_{01}) \text{ and } h_{02} = h(X = X_{02}) \quad (3.44)$$

Where X_{01} is defined by is the x-coordinate of the point of the initial profile that moved to be bottom of the vertical front edge, and X_{02} is the x-coordinate of the point of the initial profile that moved to the top of the vertical front edge.

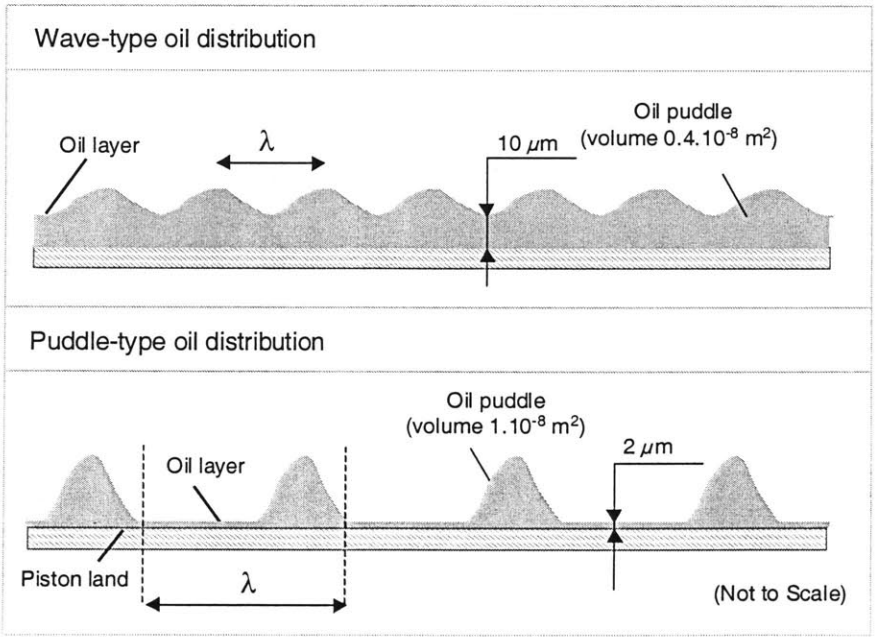


Figure 3.37 – Definition of the two types of oil distribution used for the modeling of oil transport induced by the dragging action of the blow-by gases.

Representation of the oil layer: The oil layer covering the piston land was modeled as a series of equally spaced oil puddles laid on the top of a uniform oil layer. Accordingly, the oil distribution used for modeling can be described by three parameters, the puddle volume V_{oil}, the thickness of the uniform oil layer h_0 and the distance between the front edge of the puddles λ (see Figure 3.37). Using this description of the oil layer, one can represent any type of oil distribution from a uniform oil layer

to isolated oil puddles. From the experimentally observed oil distribution patterns, two representative cases were chosen for the simulation (see Figure 3.37):

1- The puddle-type oil distribution: for the puddle-type oil distribution the oil was distributed in large puddles (1.10^{-8} m^2) separated by one puddle width and laying on a thin (~2 μm) oil layer. For this case the wavelength λ was equal to twice of the puddle width. The puddle-type oil distribution is representative of the oil profile observed on the second land of the Kubota engine when Raleigh-Taylor instabilities had developed at the surface of oil accumulated below the top ring. It corresponds to the least uniform oil distribution observed during experiments.

2- The wave-type oil distribution: for the wave-type oil distribution the oil was distributed in a fairly uniform oil layer with a wavy surface. The wavy surface was created by laying small puddles (4.10^{-9} m^2) right behind each other on the top of the 10-μm thick uniform oil layer. The initial height of the puddles was chosen to be 8-μm thick. For this case, the wavelength of the oil distribution was equal to the puddle width. This was representative of the most commonly observed oil distribution in the PSA single-cylinder engine.

3.1.2.3 Effect of gas flow dragging on the uniformity of the oil layer

In order to study the effect of gas flow dragging on the aspect ratio of oil puddles, and thus on the uniformity of the oil layer thickness, simulations were first conducted for isolated puddles of various aspect ratios. The evolution cycle after cycle of the puddle position, height and width was computed for up to 40 cycles. The integrated gas flow rate used for the simulations was obtained with RINGPACK-OC, and corresponds to the circumferential flow of blow-by gases sweeping the second land of the PSA single-cylinder engine at 2500 rpm and 500 mbar AIP. The computation was conducted for two sizes of puddles that represent each of the two types of oil distribution described in the previous section. Results are shown in Figure 3.38 and 3.39. Eventually, the initial oil distribution used for the computation of Figure 3.38 results was chosen to match the oil distribution observed in the PSA engine when the top two rings were pinned and the engine was running at 2500 rpm 500 mbar AIP. The calculated results could be directly compared with the observed oil motion shown in Figure 3.28.

In Figures 3.38 and 3.39, one can see that the aspect ratio (height/width) of the initial puddle quickly decreases as the puddle spreads over the land under the gas flow dragging action. Meanwhile the puddle is being transported away from its initial location and thus cycle after cycle a net oil transport is established in the direction of the gas flow. In order to check validity of the developed oil transport model, computed and observed oil displacements were compared. For the simulation results, the

displacement of the front edge of the puddle was averaged over 20 cycles. Using the simulation data shown in Figure 3.38, the average oil velocity was found to be 0.42 mm/cycle. From the experimental observations conducted in identical engine operating conditions (see Figure 3.28) oil lying on the second land was observed to move at about 0.6 mm/cycle. This good agreement between the observed and the computed oil displacement velocity shows that the model produce reasonable results despite all the simplifications.

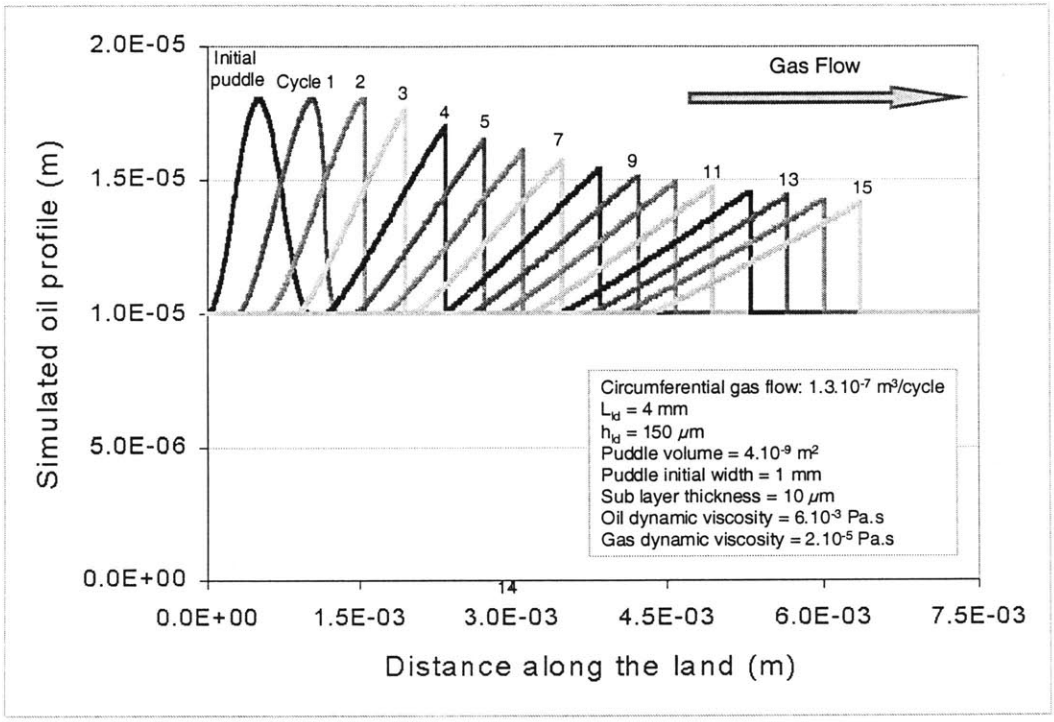


Figure 3.38 – Computed evolution of the shape and position of a two-dimensional oil puddle dragged by gas flow (Initial shape corresponding to the wave-type oil distribution).

Spreading action of the gas flow: The spreading of the oil and thus the reduction of the puddle aspect ratio results from the rolling-over process that occurs at the puddle front edge. Figure 3.39 shows the computation results for a large puddle (1.10^{-8} m^2) of $2.2.10^{-2}$ initial aspect ratio. One can see that after 40 cycles the puddle aspect ratio becomes 5% of the original one (down to $1.2.10^{-3}$). In the case of small puddles ($0.4.10^{-8}$ m^2), for which results are plotted in Figure 3.38, we can see that in 40 cycles the aspect ratio was decreased from $1.8.10^{-2}$ to $7.7.10^{-4}$. Accordingly, in both cases it can be pointed out that in a few engine cycles the dragging action of the blow-by gases significantly reduces the amplitude of the oil surface disturbances.

Here, it can be concluded that the gas flow dragging action and the resulting rolling-over process occurring at the steep edge of the oil puddles smoothen the irregularities of the oil layer covering the piston lands. Consequently, an oil layer where the lubricant is initially unevenly distributed may become uniform after a large number of engine cycles. This latter conclusion is in fact conditioned by the rate at which the non-uniform oil accumulations are generated. For instance, if the amount of oil accumulated on the land is large enough so that Raleigh-Taylor instabilities can develop every engine cycle, then the oil layer will never be uniform (see Figure 3.1). On the other hand, in the case where the formation of oil puddles only results from non-uniform oil supply to the land, if the rate of oil supply is small enough, then every cycle the gas dragging action will spread most of the added oil. Consequently no oil accumulation will build up, and the oil layer will become and/or remain uniform.

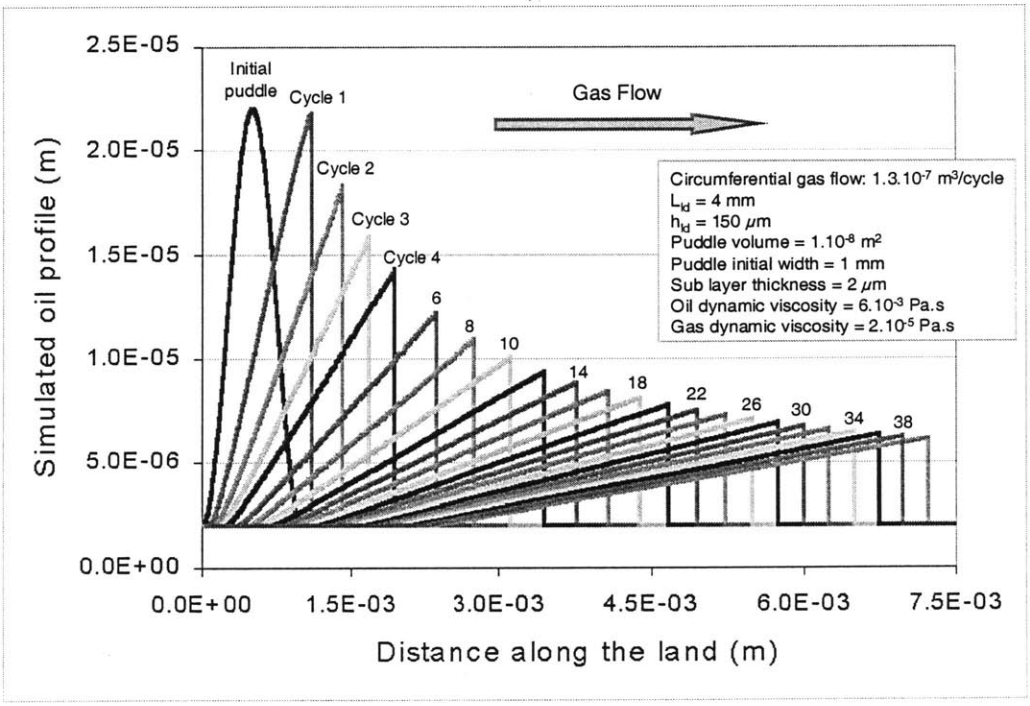


Figure 3.39 – Computed evolution of the shape and position of a two-dimensional oil puddle dragged by gas flow (Initial shape corresponding to the puddle-type oil distribution).

Ring rotation effect: In reality due to the ring rotation, different areas of the piston lands are periodically exposed to low and high circumferential gas flow rate. Considering a situation in which the ring gaps are positioned such that most of the circumferential gas flow travels on one side of the piston, there would be one side of the second land exposed to a strong gas dragging action while the other side would be exposed to a weak one. In this case, on one side of the piston second land there would be no or little spreading effect and thus non-uniform oil accumulation could develop, while on

the other side the oil layer would remain fairly uniform. Furthermore, in a running engine, the top two ring are almost always rotating [56]. Consequently, in any region of the piston lands, there will be periods when the uniformity of the oil layer will deteriorate and periods when it will be enhanced. The comparison of oil distribution images acquired with pinned and non-pinned ring confirmed the effect of ring rotation on the uniformity of the oil layer. In none of the experimental visualizations conducted with non-pinned rings the oil distribution on the piston lands was uniform. In experiments where the top two rings were pinned 180° from each other, the gas dragging action was consistent and significant on both sides of the piston. Accordingly, the oil layer was observed to be very uniform on both the thrust and anti thrust sides. This confirms the fact that if the gas dragging effect is steady, it can overcome the effect of non-uniform oil supply and maintain a uniform oil distribution on the lands. Moreover, it shows that even though the action of gas dragging tends to evenly distribute the oil on the lands, due to the ring rotation uniform oil distribution is very unlikely to exist on the piston lands of a real engine.

Overall, we can conclude that:

1- Due to the rolling-over process occurring at the front edge of the oil puddles, the amplitude of oil surface disturbances can be significantly reduced by the dragging action of the blow-by gases.
2- The uniformity of the oil layer is determined by the rate at which oil puddles are created and the amplitude of the spreading action resulting from the gas flow dragging effect.
3- Ring rotation results in continuous variations of the rate of gas flow sweeping each sector of the lands. Consequently, the spreading action of the blow-by gases is usually not consistent enough to keep the oil layer uniform.

3.1.2.4 Effect of the uniformity of the oil layer on the oil transport rate

As discussed in the previous section due to the ring rotation, the existence of irregular oil supply and/or the development of Raleigh-Taylor instabilities the oil distribution on the piston lands is inherently non-uniform. It appeared necessary to investigate the effect of the oil distribution non-uniformity on the rate of oil transport induced by the gas dragging effect. For both types of oil distribution previously described, namely, the wave-type distribution and the puddle-type distribution, the cycle after cycle evolution of the oil flow rate across the land was computed and averaged over

one wavelength λ. Results were compared with the oil flow rate $\tilde{Q}_{oil}$ predicted for a flat oil layer of thickness $\tilde{h}$.

$$\tilde{h} = \int_{x}^{x+\lambda} h \cdot dx$$

Definition of the oil transport rate: As it can be seen from Equation 3.40, the oil motion is related to the cumulated and not the instantaneous gas flow rate. Therefore, the oil flow rate is not directly dependent on time. For instance, considering the dragging action of the gas flow on the top on the uniform oil layer, the instantaneous oil flow rate can be expressed as:

$$\frac{dQ_{oil}}{dt} = q_{oil} = q_{gas} \cdot \frac{6 \cdot \mu_{air} \cdot h_{oil}}{\mu_{oil} \cdot h_{ld}^2 \cdot L_{ld}} \tag{3.45}$$

with q_{oil}: instantaneous oil flow rate (m^3/s)

q_{gas}: instantaneous gas flow rate (m^3/s).

As one can see from Equation 3.45, the time dependency of the instantaneous oil flow rate is through the instantaneous gas flow rate. Therefore, the rate of oil transport may as well be expressed as:

$$\frac{dQ_{oil}}{dQ_{gas}} = \frac{q_{oil}}{q_{gas}} = \frac{6 \cdot \mu_{air} \cdot h_{oil}}{\mu_{oil} \cdot h_{ld}^2 \cdot L_{ld}} \tag{3.46}$$

This latter expression does not have the unnecessary time dependency, and is therefore more appropriate to describe the rate of oil transport. Accordingly, to study the effect of the oil distribution pattern on the rate of the oil transport resulting from the gas flow dragging action, the oil transport rate was defined as dQ_{oil}/dQ_{gas} and was plotted as function of the cumulative gas flow rate Q_{gas}.

Puddle-type oil distribution: Figure 3.40 shows the evolution of the rate of oil transport for a puddle-type initial oil distribution. Three different zones can be distinguished. First, for very small value of Q_{gas}, no rolling-over occurs at the front edge of the puddle, and thus the puddle aspect ratio is constant. Consequently, the oil flow rate does not change and its value is about twice of $\tilde{Q}_{oil}$. Second, for the value of Q_{gas} greater than about 1.10^{-7} m^3, the front edges of the puddles start to rollover and therefore the puddle aspect ratio significantly decreases. As a result the oil flow rate decreases. Eventually, for large value of Qgas (>$1.3.10^{-6}$ m^3), due to the spreading of the oil puddles, the oil surface is becoming more and more uniform and thus the oil flow rate approaches the asymptotic value $\tilde{Q}_{oil}$ that corresponds to a flat oil layer.

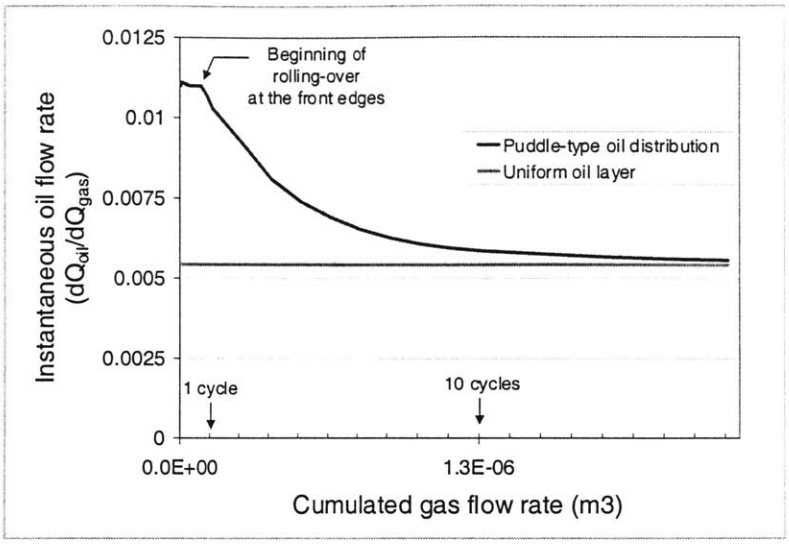


Figure 3.40 – Computed evolution of the rate of oil transport with the cumulative volumetric gas flow (Initial puddle shape corresponding to the puddle-type oil distribution).

For the PSA single-cylinder engine running at 2500 rpm 500 mbar AIP, the integrated gas flow per cycle sweeping the second land is about $1.3.10^{-7}$ m^3. If we consider that this value is representative of the cumulative gas flow for one engine cycle, we can see from Figure 3.40 that the rolling-over process will start within the first engine cycle and that after 10 cycles the oil flow rate is almost equal to $\tilde{Q}_{oil}$. Furthermore, it can be noticed that the maximum oil flow rate, which is obtained with the initial oil distribution and thus during the first engine cycle, is about twice of the oil flow rate that would be predicted using the average oil layer thickness $\tilde{h}$.

The puddle-type oil distribution used to compute the results plotted in Figure 3.40 is representative of the oil distribution recorded in the Kubota engine while Raleigh-Taylor instabilities were developing every cycle at the surface of the oil layer accumulated on the second land. Therefore, it is representative of one of the least uniform oil layer experimentally observed on the piston lands. Consequently, it is believed that in a running engine, the circumferential oil flow rate induced by the gas dragging action should not exceed twice of the flow rate $\tilde{Q}_{oil}$. The fact that the ratio of Q_{oil} and $\tilde{Q}_{oil}$ is decreasing within a few engine cycles shows that if the non-uniformity of the oil layer is not regenerated every few engine cycles the rate of oil transport induced by the dragging action of the blow-by gases is fairly well estimated by $\tilde{Q}_{oil}$.

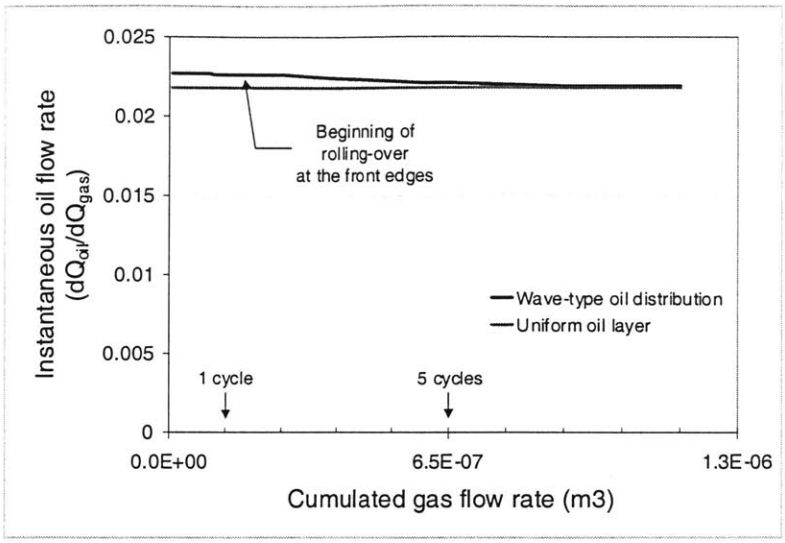


Figure 3.41 – Computed evolution of the rate of oil transport with the cumulative volumetric gas flow (Initial puddle shape corresponding to the wave-type oil distribution).

Wave-type oil distribution: In the case where oil surface disturbances are mainly created by non-uniform oil supply, which occurred in all the tests conducted with the PSA engine, the oil distribution is best represented by the wave-type oil distribution for which the oil thickness varies from 10 to 18 μm. In Figure 3.41, which shows the evolution of the rate of oil transport for a wave-type initial oil distribution, it can be seen that the oil surface non-uniformity has a small effect on the oil flow rate. With the initial oil distribution (first engine cycle) the oil flow rate Q_{oil} is only 4% greater than $\tilde{Q}_{oil}$. After 10 engine cycles the difference between Q_{oil} and $\tilde{Q}_{oil}$ is negligible. Consequently, if the degree of non-uniformity of the oil layer covering the piston lands corresponds to the wave-type oil distribution, the effect of oil surface disturbances on the rate of oil transport induced by gas dragging can be neglected.

Conclusions: Overall we can conclude that the rate of circumferential oil flow induced by the dragging effect of the blow-by gases increases with the degree of non-uniformity of the oil distribution. The minimum oil flow rate $\tilde{Q}_{oil}$ is obtained with a perfectly flat oil layer, and according to experimental observations of the oil distribution the maximum flow rate should not exceed $2.\tilde{Q}_{oil}$. Eventually, in the case where the oil surface disturbances only result from non-uniform oil supply, the oil flow rate computed using a 1-dimensional flow representation always provides a good estimation of the rate of circumferential oil transport.

3.1.2.5 Practical Results

The discussion conducted in the following section applies for both the second and the third land whenever the main component of the gas flow sweeping the land is in the circumferential direction.

Simplified computation of the rate of oil removal: According to the modeling results described in the previous section, when the oil layer is fairly uniform, the circumferential variation of the oil layer thickness can be ignored when computing the oil flow rate induced by the gas dragging action. In particular, the two-dimensional aspect of the oil flow rate oil flow can be ignored and thus a one-dimensional fully developed viscous flow representation can be used. Accordingly, the average rate of circumferential oil transport induced by the dragging action of the blow-by gases in a land sector defined by the gap positions can be expressed as follows:

$$Q_{oil} = Q_{gas} \cdot \left(1 - \frac{\theta_g}{2\pi}\right) \frac{3 \cdot \mu_{air}}{\mu_{oil}} \cdot \frac{\tilde{h}_{oil}^2}{h_{ld}^2} \tag{3.47}$$

With $\tilde{h}_{oil}$, the average thickness of the oil layer covering the land sector defined by the relative gap angle θ_g defined as:

$$\tilde{h}_{oil} = \frac{1}{\theta_g \cdot R_{ld} \cdot L_{ld}} \int_0^{L_{ld}} \int_0^{\theta_g} h_{oil} \cdot R_{ld} \cdot dy \cdot d\theta$$

And with Q_{oil}: cumulative oil flow over one cycle (m^3/cycle)

Q_{gas}: cumulative gas flow over one cycle flowing from one gap to the other (m^3/cycle)

θ_g: angle between the ring end gaps (see Figure 3.36)

Considering the sector of the second or third land defined by the angle θ_g, Q_{oil} represents the amount of oil removed every cycle from this sector by the dragging action of the gas flow. Except when the throttle is closed or near to be closed, the flow of blow-by gases on the second and third land is going from gap to gap toward the crankcase. Consequently, in most engine operating conditions the gas dragging action carries oil lying on the piston lands toward the crankcase.

Effect of the ring gap location: From Equation 3.47, one can see that, the amount of oil removed from a specific sector of a piston land depends on the angle θ_g and thus on the relative position of the gaps of the adjacent rings. The gap positions determine the portion of the total gas flow that sweeps a specific part of the piston second or third land. As the angle θ increases (see Figure 3.47), the portion

of Q_{gas} sweeping the land sector defined by θ is proportionally decreasing and therefore the amount of oil removed every cycle from this sector is decreasing as well.

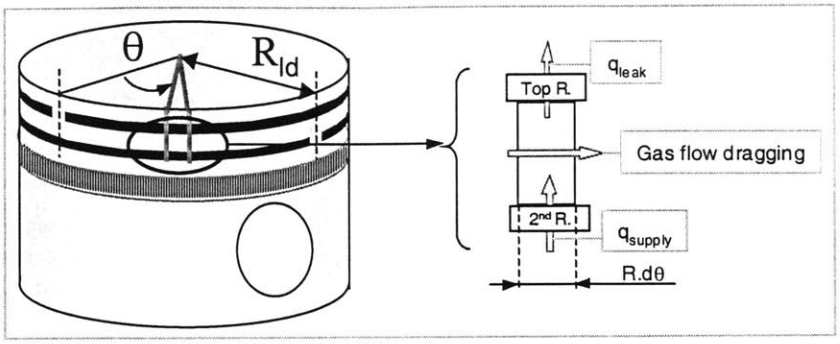


Figure 3.42 – Definition of the control volume for the evaluation of the second land circumferential oil distribution.

In order to study further the effect of the relative gap positions on the amount of oil accumulated in each sector of the piston lands, a simplified oil balance was established (see Figure 3.42). In most cases, experimental observations showed that oil was supplied to the piston lands through one of the adjacent ring groove and that part of the oil accumulated on the land was leaking through the ring groove opposite to the oil supply. Considering either the second or the third land, the simplified oil balance was established assuming that the rate at which oil was supplied to the land through one of the adjacent ring groove q_{supply} was identical all around the circumference of the piston. The rate at which oil leaks through the groove opposite to the oil supply q_{leak} usually varies around the piston circumference since it depends on the amount of oil locally available on the land. Because the rate at which oil leaks away from the land is believed to be much less than the rate at which oil is supplied to the land, the fact that oil flows from the lands to the grooves depends on the amount of oil available was neglected. Accordingly, the rate of oil leakage through the groove opposite to the oil supply was assumed to be constant around the piston circumference. Using the above assumptions the axial oil flows affecting the land oil balance was expressed as:

$$q_{supply} - q_{leak} = K \cdot R_{ld} \cdot d\theta \qquad \text{(K: constant)}$$

With q_{supply}: rate of oil supply per unit of circumference length (m^2/cycle)

q_{leak}: rate of leakage per unit of circumference length (m^2/cycle)

$d\theta$: angle of the control volume as defined in Figure 3.42.

Mass conservation applied to the control volume defined in Figure 3.42 gives the following differential equation:

$$K = Q_{gas} \cdot \left(1 - \frac{\theta_g}{2\pi}\right) \cdot \frac{\mu_{air}}{\mu_{oil}} \cdot \frac{3}{h_{ld}^2 \cdot R_{ld}} \cdot \frac{dh_{oil}^2}{d\theta} \qquad (3.48)$$

Integrating Equation 3.48 gives:

$$h_{oil}(\theta) = \sqrt{\frac{\pi}{(\pi - \theta_g/2)} \cdot \frac{K \cdot \theta \cdot R_{ld} \cdot h_{ld}^2}{3 \cdot Q_{gas}} \cdot \frac{\mu_{oil}}{\mu_{air}}} \tag{3.49}$$

Equation 3.49 is obtained assuming that h(0) = 0 which was found to be true from experiments. The effect of the ring gap relative positions on the circumferential oil repartition can be seen in Figure 3.43 that shows the evolution of the oil layer thickness around the circumference of the piston for three value of θ_g (30, 90 and 180°).

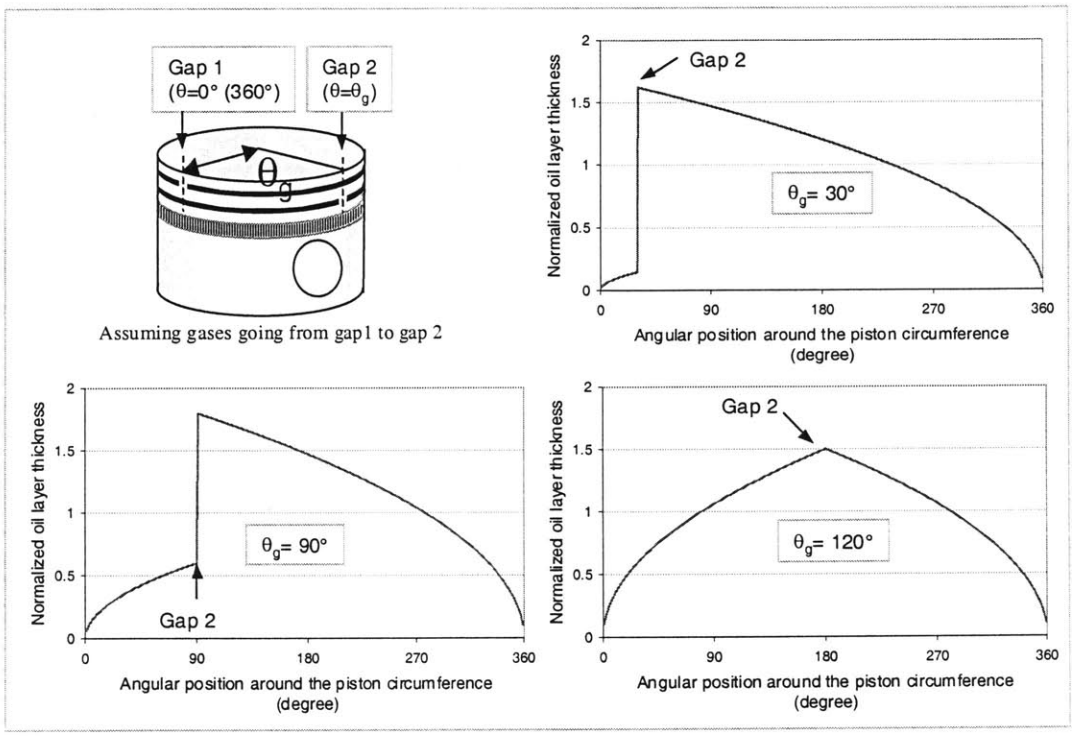


Figure 3.43 – Circumferential repartition of the oil around a piston land (second or third) plotted as a function of the relative positions of the ring gaps.

In Figure 3.43, the local oil thickness was normalized by the average thickness $\tilde{h}_{oil}$. As one can see from the plots, when the ring gaps are not positioned on opposite side of the piston ($\theta_g \neq \pi$), the dragging action of the blow-by gases creates an uneven oil repartition along the piston land circumference. For instance for θ_g= 30° it can be seen that the amount of oil accumulated in the small sector (30°) of the land represents about 2% of the total oil accumulated on the land. Correspondingly, 98 % of the oil is stored in large sector (330°).

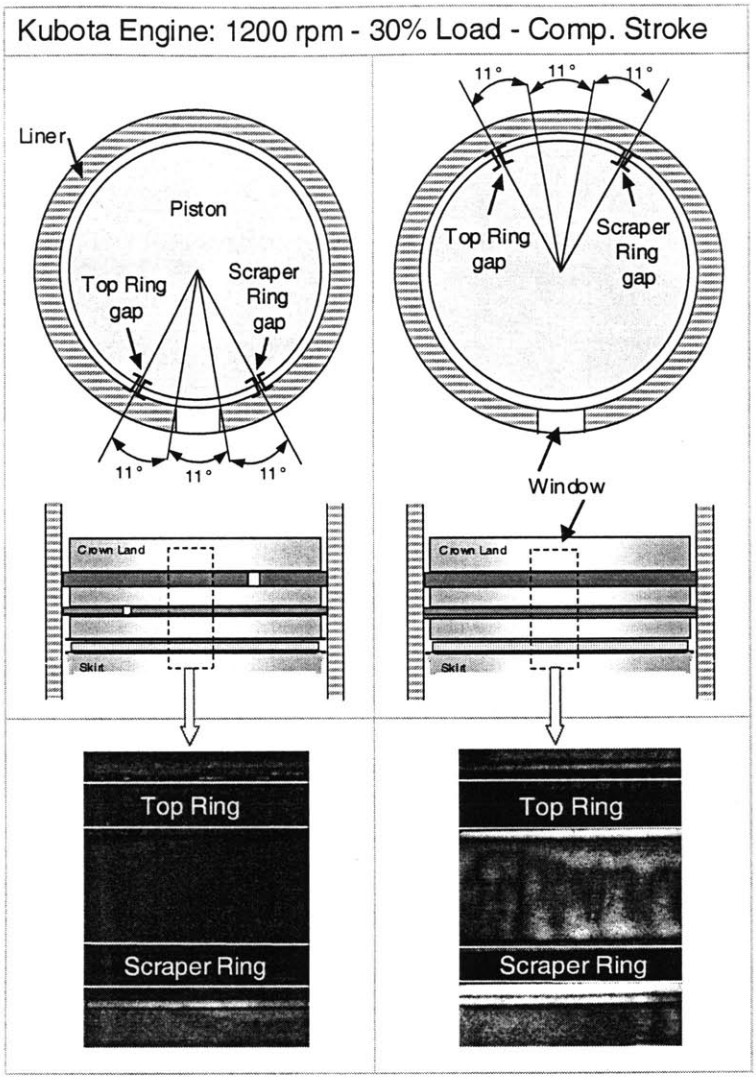


Figure 3.44 – Effect of the relative position of the top two ring gaps observed in the Kubota engine.

This result was confirmed with numerous experimental data. For example, Figure 3.44 shows the oil distribution on the second land of the Kubota engine at 1200 rpm 30% load. On the left image, where the top two rings were pinned on each side of the window such that θ_g was equal to 33°, almost no oil could be detected on the part of the second land located in front of the viewing area. This was the result of the fact that most of the gases flowing from the top ring gap to the second ring gap were sweeping this part of the second land and thus most of the oil supplied to this region was dragged away. On the other hand, where the top two rings were pinned 327° apart, away from the window, only a very small portion of the blow-by gases was flowing between the second land and the window. As a result, as it can be seen on the right image a significant quantity of oil could accumulate on the part of the second land located in front of the viewing area. The same observation was made for the 9 sets of engine operating conditions (from 1200 rpm to 2800 rpm, no load to 70 % load) tested with

these two different ring gap positions. As a conclusion, we can say that non-symmetrical positioning of the ring gaps results in uneven distribution of the oil around the piston lands. Finally, it is interesting to notice that if two ring gaps are lined up, the amount of oil removed by gas flow dragging from the land bounded by these two rings is zero.

The total amount of oil accumulated on one land directly affect the rate at which oil may leak through the upper adjacent groove. Therefore, it is a critical parameter for oil transport toward the combustion chamber. Using Equation 3.49 the total amount of oil accumulated in both sectors of one piston land was computed as a function of θ_g. The results are plotted in Figure 3.45. It can be seen that the total oil volume accumulated on the land reaches a minimum when the ring gaps are located on opposite side of the piston ($\theta_g = \pi$). Furthermore, the computation shows that around $\theta_g = \pi$ the volume of accumulated oil is very little affected by the relative gap positions. On the other hand, when the gaps are close to each other the amount of oil accumulated on the land is very sensitive to the gap location and increases dramatically as θ_g decreases.

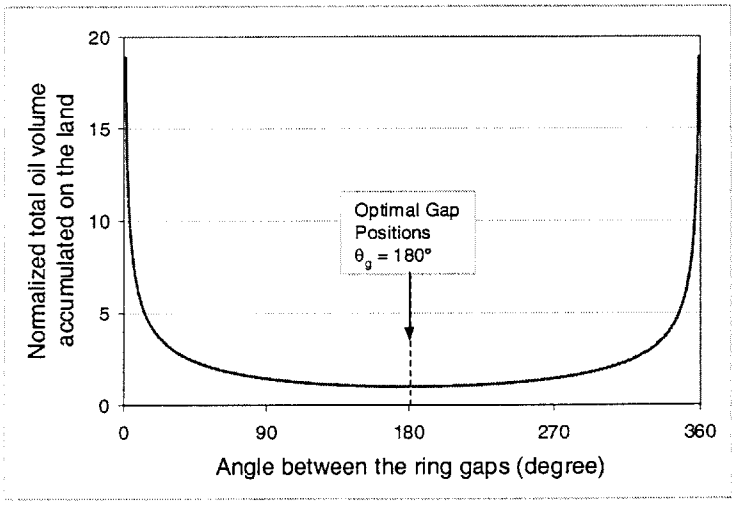


Figure 3.45 – Total volume of oil accumulated on a land plotted as a function of the relative positions of the gaps.

Effect of ring rotation: In a running engine, the rings rotate and therefore the amount of oil accumulated in a specific part of the piston second or third land evolves with time. Assuming that the gas-driven oil removal is the only oil transport mechanism that may affect the circumferential oil repartition, two extreme cases can be distinguished according to the speed of the ring rotation:

1- The time scale of the ring rotation is much larger than the time constant associated with the gas-driven oil removal. In this case, the balance between the oil supply and the gas-driven oil removal is always achieved. Consequently the thickness of the oil layer

these two different ring gap positions. As a conclusion, we can say that non-symmetrical positioning of the ring gaps results in uneven distribution of the oil around the piston lands. Finally, it is interesting to notice that if two ring gaps are lined up, the amount of oil removed by gas flow dragging from the land bounded by these two rings is zero.

The total amount of oil accumulated on one land directly affect the rate at which oil may leak through the upper adjacent groove. Therefore, it is a critical parameter for oil transport toward the combustion chamber. Using Equation 3.49 the total amount of oil accumulated in both sectors of one piston land was computed as a function of θ_g. The results are plotted in Figure 3.45. It can be seen that the total oil volume accumulated on the land reaches a minimum when the ring gaps are located on opposite side of the piston ($\theta_g = \pi$). Furthermore, the computation shows that around $\theta_g = \pi$ the volume of accumulated oil is very little affected by the relative gap positions. On the other hand, when the gaps are close to each other the amount of oil accumulated on the land is very sensitive to the gap location and increases dramatically as θ_g decreases.

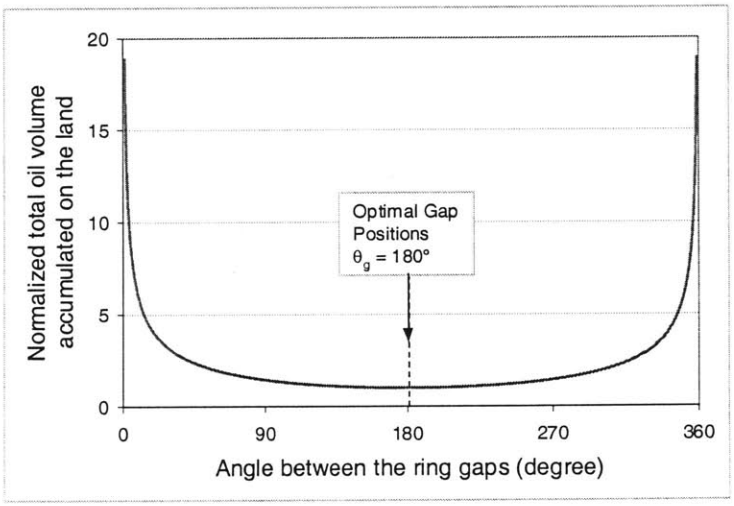


Figure 3.45 – Total volume of oil accumulated on a land plotted as a function of the relative positions of the gaps.

Effect of ring rotation: In a running engine, the rings rotate and therefore the amount of oil accumulated in a specific part of the piston second or third land evolves with time. Assuming that the gas-driven oil removal is the only oil transport mechanism that may affect the circumferential oil repartition, two extreme cases can be distinguished according to the speed of the ring rotation:

1- The time scale of the ring rotation is much larger than the time constant associated with the gas-driven oil removal. In this case, the balance between the oil supply and the gas-driven oil removal is always achieved. Consequently the thickness of the oil layer

$\mu_{oil} = 5.6.10^{-3}$ Pa.s

$\tilde{h}_{oil} = 20\ \mu m$

$R_{ld} = 43.3$ mm

$L_{ld} = 4$ mm

$h_{ld} = 200\ \mu m$

Equation 3.50 gives $\tau_{sor} \sim 100$ seconds. First of all, according to this result the period of the ring rotation is never much smaller than T_{sor}. Consequently, any ring rotation will result in an unsteady repartition of the oil around the circumference of the piston lands. This result was confirmed by the experimental observations of the oil distribution conducted in both the PSA and the Kubota engine. In all tests conducted with non-pinned rings, the oil accumulation on the piston lands was observed to change over periods of several minutes whenever one or several rings started to rotate.

Second, the ring may rotate fast enough so that the period of the ring rotation and the time constant associated with the dragging action of the blow-by gases are in the same order of magnitude. In this situation, locally the rate of supply and the rate of gas-driven oil removal are not balanced and thus there is either oil accumulation or oil depletion.

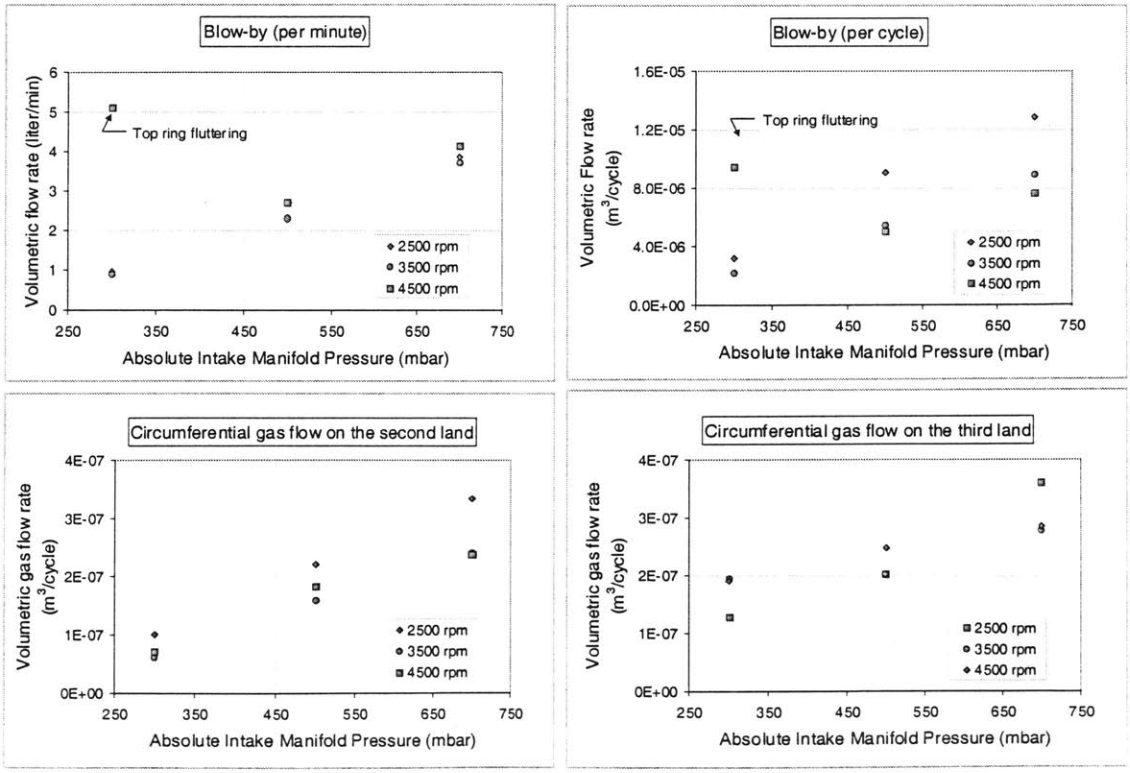


Figure 3.46 – Blow-by flow rate measured in the PSA engine and rate of the circumferential gas flows sweeping the second and third land (calculated with RINGPACK-OC).

Effect of engine running conditions: From Equation 3.47, we can see that the amount of oil removed every cycle from the piston lands by the gas flow dragging effect is increasing with the cumulative gas flow rate Q_{gas}. Figure 3.43 shows the evolution with speed and load of the blow-by flow rate measured in the PSA engine equipped with the standard ring pack, and the computed circumferential gas flow on the second and third land. As one can see, the blow-by and thus Q_{gas} increases with engine load. Consequently, the amount of oil dragged away from the piston land also increases with engine load.

As the engine speed goes up, the time for the blow-by gases to flow through the ring gaps decreases. As a result, if the ring stability is preserved, at constant engine load the volume of blow-by displaced every cycle and the amount of gases sweeping the piston lands should decrease while the engine speed increases. Consequently, the rate of the circumferential oil transport induced by the dragging action of the blow-by gases should decrease as the engine speed augments.

From the results plotted in Figure 3.46, a decrease in the blow-by per cycle and in the volume of gases sweeping the second and the third land can be seen from the measurement and computations results when the engine speed is raised from 2500 to 3500 rpm. The blow-by at 4000 rpm 300 mbar AIP is out of the trend because the top ring flutters in this particular running condition. The blow-by data presented in Figure 3.46 also show that the difference of blow-by per cycle between 3500 and 4500 rpm is very small. This is due to the fact that the speed dependency of the blow-by is not only determined by the time during which the gases can flow through the ring gaps but also by changes in the ring dynamics and by the thermal expansion of both the piston and the liner.

Overall, we may conclude that the rate of circumferential oil transport induced by the dragging action of the blow-by gases increases with the engine load and usually decreases with the engine speed.

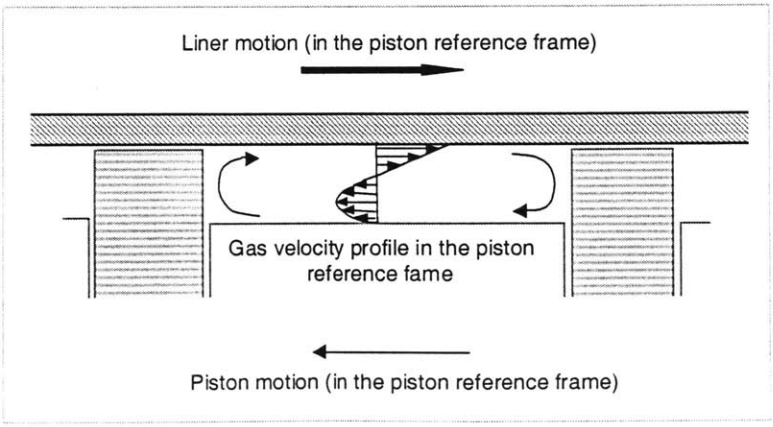


Figure 3.47 – Description of the axial gas flow induced by the piston/liner relative motion (secondary gas flow).

3.1.3 Gas Flow Driven Axial Oil Transport

In the clearances between the piston lands and the liner, blow-by gases are not only flowing around the circumference of the piston but also along its axial direction. The axial gas flows sweeping the piston lands have three origins:

1. Due to the relative motion of the piston and the liner, the gas layer trapped between the lands and the liner is sheared in the axial direction. In the piston reference frame, this shear stress drags the gases from one side of the land (upper or lower) to the other. Since, for most engine running conditions during most part of the engine cycle there is no or little flow through the ring groove, the mass flow rate along the axial direction of the lands may be considered to be zero. As a result, as gases are sheared between the lands and the liner, a rolling flow is created (see Figure 3.47). As shown in Figure 3.47, this gas flux travels upward along the land when the piston moves downward and vice versa. This flow pattern exists on the crown, the second and the third lands. In the following discussion, the gas flow induced by the relative motion of the piston and the liner was referred to as the secondary gas flow.
2. When the rings are moving in the their groove, gases are flowing from the lands to the back of the rings or vice-versa to balance any pressure difference between the connected regions. In particular, if a ring looses stability and flutters, due to the pressure difference between adjacent piston lands large amount of blow-by gases will flow from one land to another directly through the ring groove clearance [14]. Additionally, as rings are moving in their groove, gases are pumped in and out of the ring groove side clearances. All these gas exchanges between the lands and the ring grooves results in axial gas flows on the piston lands.
3. If a ring collapses in the radial direction, a large amount of blow-by gases will flow axially through the clearance opened between the collapsed ring and the liner. This sudden gas displacement, which is driven by the pressure difference between two adjacent lands will result in axial gas flows on the two lands separated by the collapsed ring.

Whenever one of these gas flows occurs, the oil lying on the lands may be dragged along the axial direction of the piston. As it was explained in Section 3.1.1, the axial motion of the oil lying on the piston lands was found to be primary driven by the inertia force resulting from the alternating piston motion. In this paragraph, we will evaluate separately the magnitude of the dragging action of the various axial gas flows and compare it with the effect of the inertia force.

3.1.3.1 Effect of the axial gas flow resulting from the piston/liner relative motion

Description of the gas flow: In order to evaluate the magnitude of the oil displacement induced by the secondary gas flow, an estimation of the shear stress at the surface of the oil layer and thus the gas velocity profile had to be computed. Due to the aspect ratio of the lands ($L_{ld} >> h_{ld}$), away from the rings the gas flow may be considered to be one-dimensional. The Reynolds number based on the average piston velocity at 4000 rpm and a land/liner clearance of 200 μm was found to be in the order of 150. Therefore, the flow is laminar. Moreover, the viscous diffusion time was found to be small compared to the duration of a stroke. Consequently, the acceleration of the fluid is negligible compare to the viscous forces. Eventually, when comparing the convection and the viscous dissipation terms, we found that depending on the vertical angle β formed by the liner and the piston lands the momentum convection may not be negligible. β depends on the liner deformation, on the conic shape of the piston and on the piston tilt. The maximum value of β.Re, which represents the ratio of the convection and viscous terms was estimated to be around 2. Since the purpose here was to get an order of magnitude estimation of the dragging action of secondary gas flow, the effect of the momentum convection was neglected for simplicity. It was understood that this assumption might have led to an underestimation of the shear stress at the oil surface.

Using a one-dimensional fully developed viscous flow representation the axial gas flow resulting from the piston/liner relative motion was computed with the following set of equations:

$$\frac{dP}{dx} = \mu_{gas} \frac{\partial^2 u}{\partial y^2} \tag{3.51}$$

$$u(h_{gas}) = V_l \quad \text{and} \quad u(0) = 0$$

With V_l: liner velocity (in the piston reference frame)

Using the above equations and the fact that the net mass flow rate along the axial direction of the land is zero, the following equations can be derived:

$$u = \frac{1}{2 \cdot \mu_{gas}} \cdot \frac{dP}{dx} \left(y^2 - y \cdot h \right) + \frac{V_l}{h} \cdot y \tag{3.52}$$

$$Q = \int_0^{h_{gas}} u \cdot dy = -\frac{1}{12} \cdot \frac{dP}{dx} \cdot h_{gas}^{\ 3} + \frac{V_l}{2} \cdot h_{gas} = 0 \tag{3.53}$$

Equation 3.53 gives:

$$\frac{dP}{dx} = \frac{V_l \cdot \mu_{gas}}{6 \cdot h_{gas}^{\ 3}} \tag{3.54}$$

Using equation 3.52 and 3.54, the shear stress at the surface of the oil layer τ_{gas} can be computed

$$\tau_{gas} = -\frac{2\mu_{gas} \cdot V_l}{h_{ld}} \tag{3.55}$$

Description of the oil flow: For the purpose of the comparison between the effect of the inertia force and the dragging action of the secondary gas flow the oil layer was assumed to be flat. Accordingly, the oil flow was considered by a one-dimensional. Considering values of the Reynolds number, the viscous diffusion time, and the ratio of the convection and viscous terms, the axial oil flows were found to be fully developed viscous flows for both the inertia and the shear driven flows. Therefore, the oil flow rate resulting from the dragging effect of the axial gas flow was expressed as:

$$q_{oil} = -\frac{\mu_{gas}}{\mu oil} \cdot \frac{h_{oil}^2}{h_{ld}} \cdot V_l \tag{3.56}$$

With q_{oil}: instantaneous oil flow (m^3/s)

h_{oil}: thickness of the oil layer

As one can see from Equation 3.56, due to the alternating motion of the piston, the net oil displacement induced by the secondary gas flow after one engine revolution is zero. Therefore, to evaluate the relative effects of the inertia force and the secondary gas flow, the maximum amplitude of the oil displacement induced by both driving forces were compared. Accordingly, the amount of oil displaced every stroke by the dragging action of the secondary gas flow was computed (see Equation 3.57).

$$Q_{oil}^{s} = -\frac{\mu_{gas}}{\mu oil} \cdot \frac{h_{oil}^2}{h_{ld}} \cdot S \tag{3.57}$$

With Q^s_{oil}: volume of oil displaced during one stroke by the dragging effect of the secondary gas flow (m^3)

S: Length of the stroke (m)

Similarly, the volume of oil displaced by the action of the inertia force during one period of either upward or downward inertia force was computed (see Equation 3.58).

$$Q^{i}_{oil} = -\frac{2 \cdot h^{3}_{oil}}{3\upsilon_{oil}} \cdot Vp_{max} \tag{3.58}$$

With Q^{i}_{oil}: volume of oil displaced by inertia during one inertia period (m^3)

As one can see from Equations 3.57 and 3.58, Q^{s}_{oil} is function of h^{2}_{oil} while Q^{i}_{oil} is function of h^{3}_{oil}. Therefore, the inertia force is expected to have a dominant effect on thick oil accumulation while the secondary gas flow have more effect on the thin oil layers. The ratio of Q^{s}_{oil} and Q^{i}_{oil} was computed for the geometry of the PSA single-cylinder engine for engine speed up to 6000 rpm and oil thickness ranging from 1 to 15 μm. As one can see from Figure 3.48, except for very thin oil layer (< 3 μm), the effect of the inertia force is always dominant over the dragging action of the secondary gas flow. Therefore, if the oil layer covering the piston lands is in average more than a few microns thick, the inertia force will dictate the repartition of the oil along the axial direction of the land. In the case where the average thickness of the oil layer covering the lands is less than a few microns, the amplitude of the oil displacements resulting from both the inertia force and the secondary gas flow are negligible. Consequently, the dragging action of the axial gas flow induced by the relative piston/liner motion can always be neglected.

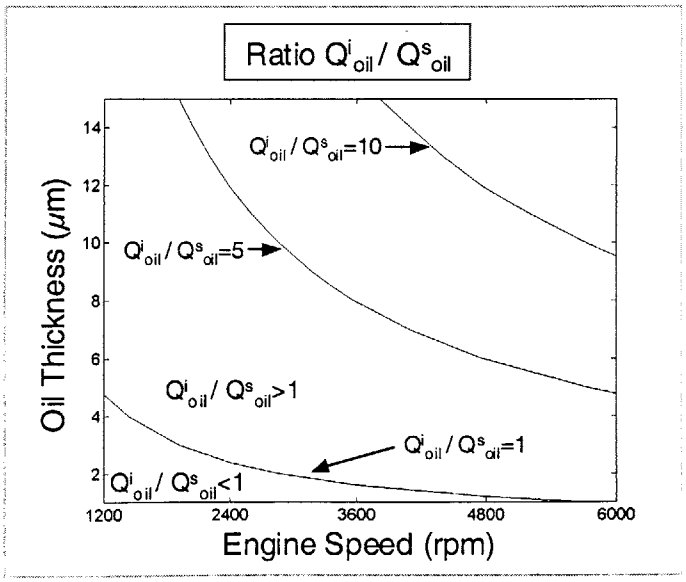


Figure 3.48 – Comparison between oil displacement induced by the secondary gas flow and the inertia force.

3.1.3.2 Effect of gas exchange with the ring grooves and with adjacent lands

In this section, the discussions will focus on the effect of axial gas flows resulting from gas exchanges between the lands and the grooves and between adjacent lands during ring collapse or ring flutter.

Effect of gas flux between the ring grooves and the lands: Gas flow rates between the lands and the ring grooves were computed with RINGPACK-OC for the all the engine operating conditions tested on the PSA single-cylinder engine. When there was no ring flutter, volumetric flow rates were found to be between 1.10^{-8} and 2.10^{-7} m^3/cycle. For comparison, at 4500 rpm 300 mbar AIP where the top ring was fluttering the gas flow rate between the top ring groove and the second land was found to be about 1.10^{-6} m^3/cycle. The Reynolds number associated with these gas flows was computed using the land/liner clearance as characteristic length. The resulting Reynolds number exceeded 10~20 when there was no ring flutter and was about 1500 on the second land when the top ring was fluttering.
In order to estimate the effect of land/groove gas flows on the land oil distribution, one need to estimate the shear stress at the surface of the oil layer. To do so, the gas flow was represented as a one-dimensional fully develop viscous flow. Because the duration of the gas flow between the land and the groove can be as short as a few milliseconds, the acceleration of the fluid is not always negligible. Consequently, the gas flow may not be fully developed and therefore this assumption is only appropriate to provide an order of magnitude estimation of the shear stress at the oil surface. When ring flutter occurs, not only the flow is not fully developed but also the momentum convection and the entrance effects may not be negligible. However, for simplicity the gas flow was represented as a fully developed viscous flow and thus the computed value of the shear stress at the oil surface was very probably underestimated when ring flutter occurs.
Using the previously described assumptions the shear stress at the interface between the gases and the oil was estimated by Equation 3.59.

$$\tau_{gas} = -\frac{3\mu_{gas} \cdot q^{g}_{gas}}{h^{2}_{ld} \cdot R_{ld} \cdot \pi} \tag{3.59}$$

With q^{g}_{gas}: Instantaneous volumetric gas flow rate (m^3/s)

Using Equation 3.59, the volume of oil displaced by the dragging action of the land/groove axial flow was estimated by Equation 3.60.

$$Q^{g}_{oil} = -\frac{3\mu_{gas} \cdot Q^{g}_{gas} \cdot h^{2}_{oil}}{2 \cdot \mu_{oil} \cdot h^{2}_{ld} \cdot R_{ld} \cdot \pi} \tag{3.60}$$

With Q^g_{oil}: Volume of oil displaced on the land by the dragging action of the groove/land gas flow (m^3/cycle)

Q^g_{gas}: Volume of gas flowing between the groove and the land per cycle (m^3/cycle)

The effect of the land/groove gas flow on the land oil repartition was compared with the effect of the inertia force by evaluating the ratio Q^i_{oil} / Q^g_{oil}. First, the comparison was made using the gas flow rate between the top ring groove and the second land computed for the PSA engine running at 2500 rpm 500 mbar. In these running conditions the top ring was stable, and the gas flow rate from the back of the top ring to the second land was about $1.2.10^{-7}$ m^3/cycle. For 2-μm thick oil layer, Q^i_{oil} / Q^g_{oil} was evaluated to be in the order of 10. Therefore, it can be concluded that if there is no ring flutter the gas flow rate between the grooves and the lands is too small for the dragging effect of the gases to significantly affect the oil repartition along the axial direction of the piston lands.

Another comparison was made using the gas flow rate from the top ring groove to the second land computed for the PSA engine running at 4500 rpm 300 mbar AIP. In this particular case, the top ring was fluttering and the gas flow rate was about 1.10^{-6} m^3/cycle. The ratio Q^i_{oil} / Q^g_{oil} was evaluated for a 2-μm thick oil layer and was found to be in the order of 3. At 2500 rpm the ratio would have been in the order of 1. Taking into account the fact that the shear stress of the gas may have been significantly underestimated when ring flutter occurs, it appears that the dragging action of the groove/land may affect the axial oil distribution on the land when a ring loses stability. However, this result was found using a very thin oil layer (2 μm). Considering a 20-μm thick oil layer, the value Q^i_{oil} / Q^g_{oil} is about 25. Therefore, we can conclude that when there is a non-negligible amount of oil accumulated on the land, the axial distribution of the oil is always controlled by the inertia force.

Effect of axial gas flow resulting from ring collapse: Ring collapse was not encountered in any of the running conditions tested on the Kubota and the PSA engine. An order of magnitude of the gas flow rate that may result from top and second ring collapse was estimated using data acquired on a different spark ignition engine of 0.52-liter displacement. In this engine, top and second ring collapse were found to occur at 6000 rpm low load. The resulting gas flow rates were about 5.10^{-9} m^3/cycle from the crown land to the second land and about 3.10^{-7} m^3/cycle from the second to the third land. By comparison with gas flow rates resulting from top ring flutter, we can conclude that gas flows resulting from ring collapse may only affect very thin oil layer (< 2 μm).

Conclusions: Overall, we can conclude that whenever there is a appreciable amount of oil on the lands (greater than a few μm) the dragging action of the gases going in and out of the ring grooves has a negligible effect the axial oil repartition on the piston lands. Even when ring flutter and/or ring collapse occurs, the inertia force dictates the axial oil motion.

3.2 Oil Transport between the Liner and the Piston Lands

3.2.1 Ring Scraping

3.2.1.1 Description

Oil scraping is the mechanical action by which a sliding ring removes oil from the liner. This phenomena was fully described and modeled by T. Tian [14, 25, 26]. According to T. Tian work, ring scraping can occur in two ring/liner lubrication configurations (see Figure 3.49):

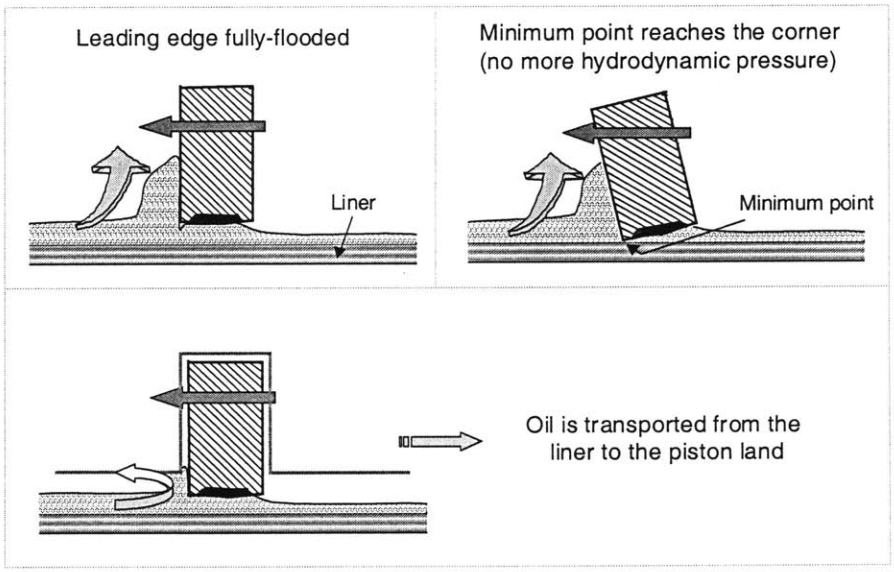


Figure 3.49 – Scraping mechanism.

1- Leading edge fully flooded: When the leading edge of a sliding ring becomes fully flooded, oil is removed from the liner and accumulated on the front side of the ring. This usually occurs when the oil film in front of the ring is thick enough so that the hydrodynamic pressure is not able to lift the ring leading edge above the surface of the oil layer. The lubrication conditions encountered at the leading edge of a sliding ring mainly depend on the thickness of the oil layer in front of the ring and the position of the ring running surface profile relative to the liner. The instantaneous ring profile relative to the liner depends on the ring static profile, the piston tilt and the liner deformation. Accordingly, ring scraping is affected by the ring and piston motion and therefore by the engine running conditions. The amount of oil in front of the ring is in most cases the amount of oil left by the previous ring and thus depends on the lubricating condition of the previous ring. The exception is for the top ring sliding up-stroke when the lubricating film is left by the top ring itself during the

previous down stroke. However, in every cases the occurrence of ring scraping with leading fully flooded results from the succession of two processes. First, an excessive amount of oil is left on the liner by one ring and secondly part of the oil is scraped off by the following ring. The amount of oil scraped depends on the ability of the following ring to slide above the excess of oil and therefore on the position of its profile relative to the liner. Additionally, gas pressures and local ring load variation due to bore distortion play an important role is scraping.

2- Lost of hydrodynamic lift: During the engine cycle, the position of the ring profile relative to the liner changes according to the piston tilt and the ring twist. Accordingly, the location of the point of the ring running surface that is the closest to the liner (called minimum point hereafter) moves up and down along the ring surface. If the minimum point reaches the upper corner of the profile during up strokes or the lower corner during down strokes, the converging wedge that creates hydrodynamic lift disappears. As a result, the ring is only supported by asperity contact and the corner of the ring scrap oil from the liner. In this case, the occurrence of the scraping only depends on the relative geometry of the ring and the liner and is not affected by the amount of oil in front of the ring. This type of scraping greatly depends on the shape of the ring profile and its occurrence usually result from excessive wear of the running surface [17].

3.2.1.3 Scraping observations

When ring scraping occurs, oil accumulates on the front side of the ring. Consequently, scraping should be easily identified on LIF images of the oil distribution. In reality, oil can be transported to the side of the ring by of other mechanisms such as ring squeezing (see Section 3.3.2.1) and/or inertia driven oil transport on the lands. Therefore, one has to be careful when trying to identify ring scraping from oil distribution images. Figures 3.50 and 3.51 show two cases where an excessive amount of oil was left on the liner by one ring and where a clear scraping process could be identified at the leading edge of the following ring. In Figure 3.51, oil, which may have been squeezed out of the OCR groove, was left on the liner right behind the OCR upper land while the piston was moving downward. The pattern of the oil left on the liner and the oil accumulation at the leading edge of the second ring clearly show that the excessive oil deposited on the liner was being scraped by the second ring. Figure 3.50 shows two other images acquired in the PSA engine at 3500 rpm 300 mbar. On this two images, oil, which was released on the liner from the second ring hook, was being scraped by the oil control ring.

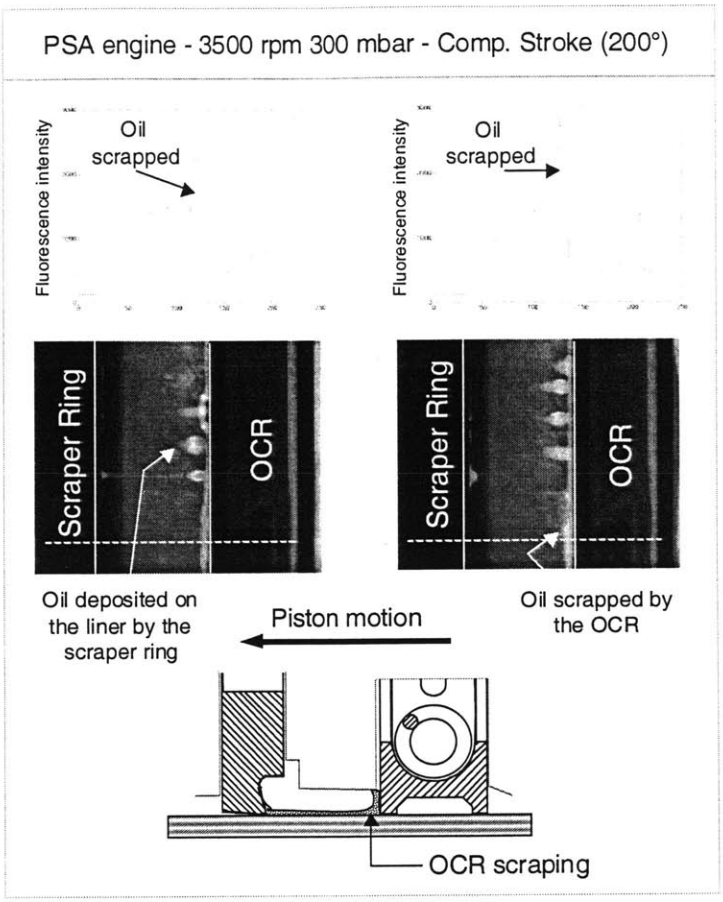


Figure 3.50 – Oil scraping by the upper land of the OCR observed in the PSA engine.

3.2.1.4 Implications for oil transport on the piston

Ring scraping creates an oil accumulation on the front side of the ring and on the part of the piston land located next to the ring. Assuming that one ring scraps during upward strokes, oil will accumulate on the upper side of the ring and as the piston slows down toward TDC oil will be transported by the inertia force from the ring side onto the piston land. If scraping occurs during downward stroke, the oil is transported on the land located below the scraping ring when the piston is around BDC. Consequently, when ring scraping occurs, oil is removed from the liner and is transported to the piston. Consequently, scraping can be considered as a mechanism of oil supply to the piston lands.

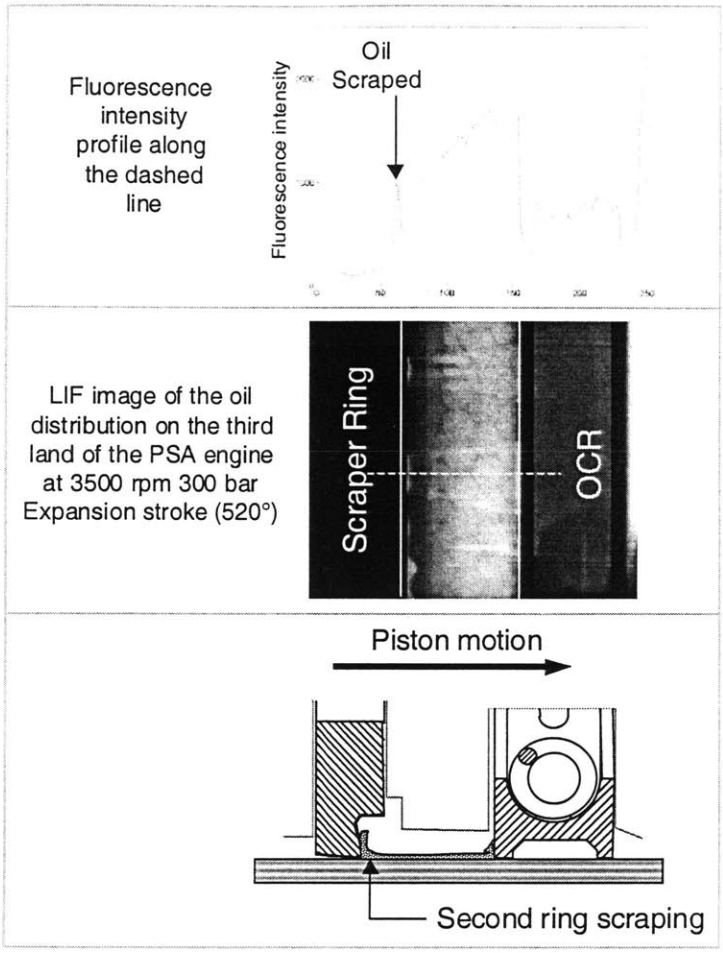


Figure 3.51 – Oil scraping by the scraper ring observed in the PSA engine.

3.2.2 Oil Release

As it was described in the previous section, since the rings physically connect the piston lands and the liner oil may be easily transported from the liner to the piston. The reverse transport, namely oil being transported from the land or the ring side to the liner can also occur. It was observed in both the PSA and the Kubota engine when a Napier ring was used.

3.2.2.1 Observations

In both engines, when a Napier ring was used observations showed that part of the oil that was initially accumulated in the hook could be released to the liner. Figure 3.52 shows images of the oil distribution acquired in the PSA engine during each stroke when the piston was close to the BDC. On all images, one can see puddles of oil that were dropped onto the liner by the scraper ring. Figure

3.53 shows two oil distribution images acquired in the Kubota engine during compression and exhaust stroke. On both images, large puddles of oil that were left on the liner from the scraper ring can be identified. In both cases, the oil left on the liner was released from the hook of the Napier ring by the action of the inertia force. One may notice that the pattern of the oil puddles left on the liner in both engines were different. This is due to the fact that the oil release mechanisms were slightly different in these two cases.

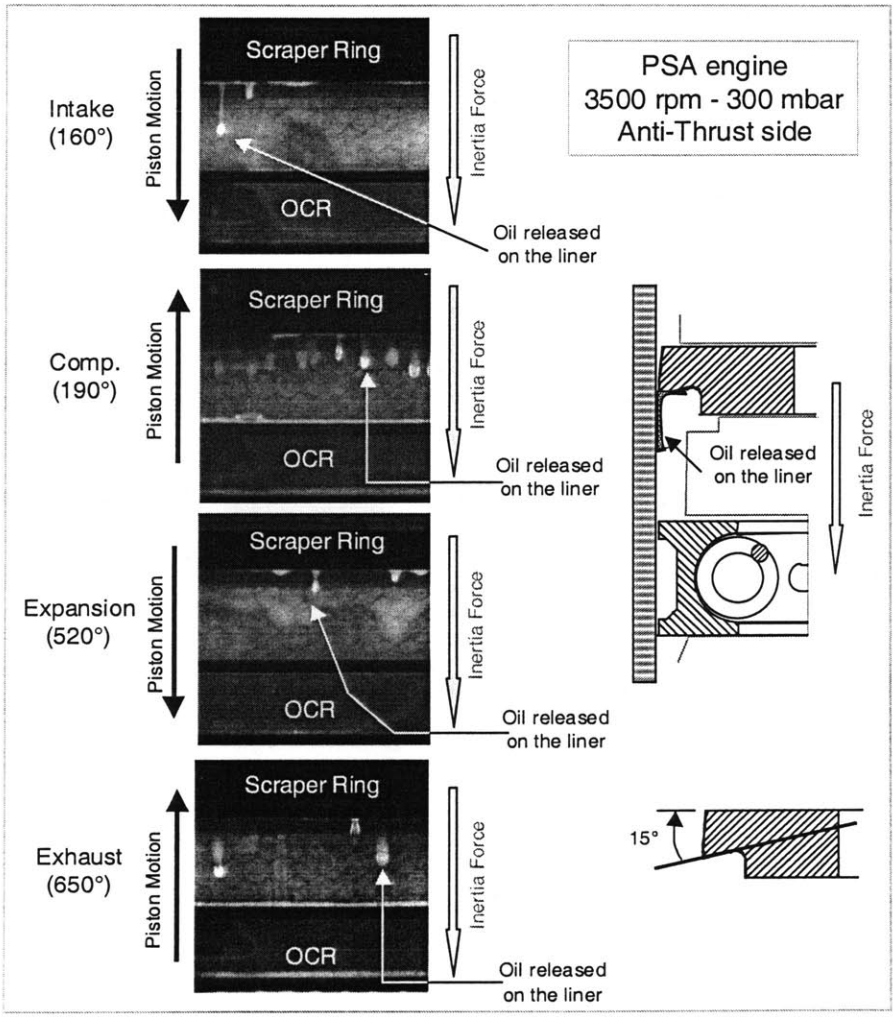


Figure 3.52 – Oil release from the hook of the Napier ring observed in the PSA engine.

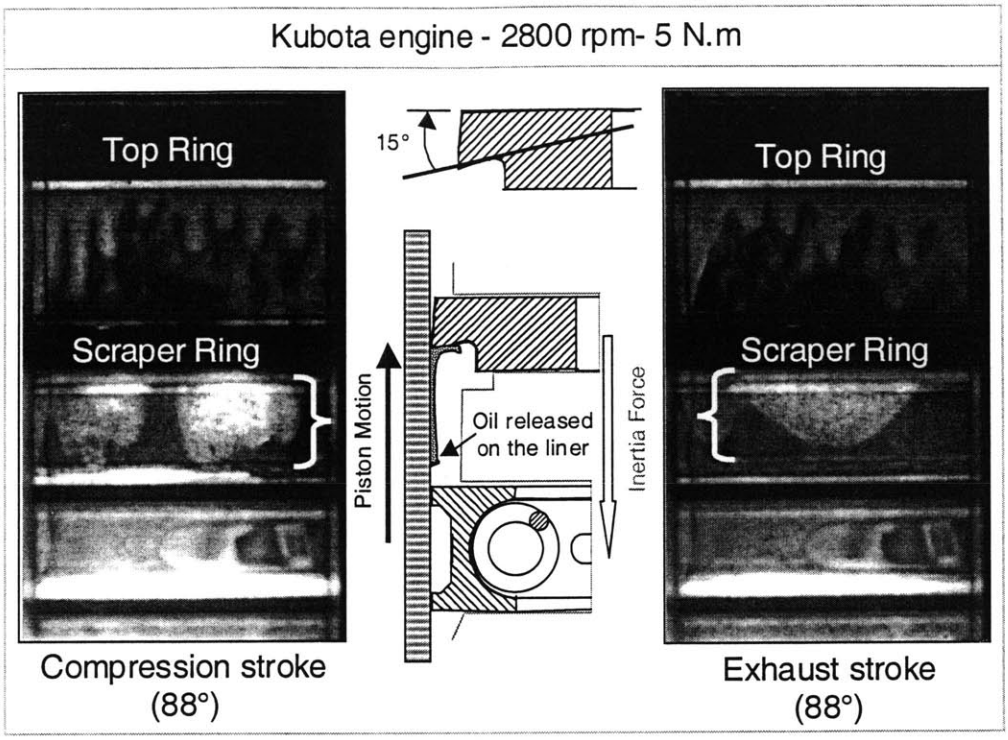


Figure 3.53 – Oil release from the hook of the Napier ring observe in the Kubota engine.

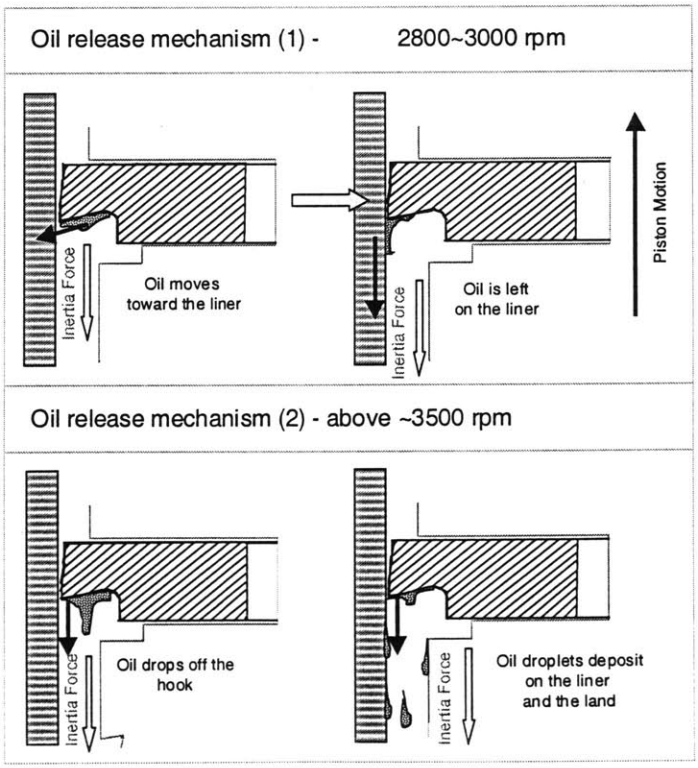


Figure 3.54 – Description of the oil release mechanism.

3.2.2.2 Description

Figure 3.54, describes the mechanisms of oil release that lead to the oil patterns observed in both engines. Oil accumulated in the hook is subject to the inertia force and thus tends to moves downward when the piston is around the BDC. Due to the action of surface tension, oil accumulated on the upper side of the hook stick to the hook and moves toward the liner along the 15°-degree slope. The distance traveled along the upper side of the hook will depends on the angle γ (see Figure 3.54), the amount of oil accumulated in the hook and the intensity of the inertia force. From here three situations can be encountered:

1. If the action of the inertia force is strong enough to bring the oil in contact with the liner, oil will be released on the liner. Oil may be released right at the bottom dead center or during the first part of the upward strokes while inertia is still pointing downward. In this case, during early compression or exhaust stroke, the Napier ring will leave a thick oil layer on the liner as it was observed in the Kubota engine. This type of oil release was not observed below 2800 rpm. Accordingly, it is believed that at lower engine speed, the inertia force was not strong enough to force the oil out of the hook.
2. If the inertia force is strong enough to overcome the surface tension oil droplets will break away from the hook before reaching the liner. The droplets will fall from the hook onto the third land or in the clearance between the land and the liner. The effect of the inertia force can be compare to surface tension forces by estimating the following ratio:

$$R = \frac{\rho \cdot a_p \cdot h \cdot r}{\sigma} \tag{3.61}$$

With a_p: the piston acceleration

h: height of the oil accumulated in the hook

r: radius of curvature of the oil accumulation

If the ratio R is much larger than one, oil droplets will break away from the surface of the oil accumulated in the hook and will drop under the action of inertia in the third land cutoff or in the land liner clearance. In this case, oil is more likely to separate from the hook when the inertia force is close to its maximum, which is around the BDC. Due to the small size of the land/liner clearance, droplets will very likely hit either the third land or the liner. On the images of Figure 3.52, droplets of oil that leaves the Napier ring hook can be seen during the end of intake and expansion stroke. On images acquired at the very beginning of compression and exhaust stroke,

one can see droplets that had separated from the hook and hit the liner. The separation of oil droplets from the hook was observed at 3500 and 4500 rpm in the PSA engine.

3. The inertia force is too small for the oil accumulated in the hook to reach the liner by sliding along the angled part of the hook or by forming droplets. In this case, no oil is transported outside the hook. This situation was encountered in the PSA engine at 2500 rpm and in the Kubota engine at low engine speeds.

3.2.2.3 Implication for oil transport

The fact that oil release was never observed during tests conducted with a second ring without hook shows that it is necessary to have of a angled surface ($\gamma > 0$) to displace oil accumulated on the side of the ring away from the land and potentially release it on the liner. If the ring side is perpendicular to the liner, the action of the inertia force most likely drives the oil directly onto the piston lands.

The oil residing in the hook of a Napier ring comes from the land, the ring/groove clearance and/or the liner. When oil release occurs, part of the accumulated oil is transported to the liner instead of only being transported to the land. In both engines, the hook angle of the tested Napier rings γ were about 15°. Based on this analysis, one may expect an increase in the proportion of oil transported to the liner by increasing the angle of the hook.

Experiments have showed that a minimum engine speed of about 3000 rpm was necessary for the onset of oil release from the Napier ring hook. Since the oil release mechanism is inertia driven, the proportion of oil released to the liner from the hook is expected to increase with the engine speed. However, as it was seen on the PSA engine, at high engine speed (>3500 rpm), the oil accumulated in the hook can break up into droplets and deposit either on the liner or on the third land. Therefore, increasing the engine speed may as well increase the proportion of oil that is transported to the third land. With the experimental data available, it was not possible to establish a clear correlation between the proportion of oil released on the liner and the engine speed. Consequently, we can only conclude that a minimum inertia force and thus a minimum engine speed are required for the oil release mechanism to occur.

Finally, the oil released from the hook locally forms thick oil puddle in front of the oil control ring. Consequently, part of the released oil is scraped off the liner (see Figure 3.50) while the other part passes by the oil control ring. The portion of the released oil that is scraped from the liner by the OCR is usually transported back to the third land. The maximum thickness of oil that can be passed by the OCR depends on the size of the converging region between the upper land of the OCR and the liner. Consequently, the net amount of oil that stays on the liner is limited by the ability of the OCR

to slide above the oil that is released from the hook. Nonetheless, hook of the Napier ring may reduce the oil flow rate to the second ring groove through collecting and releasing the oil moving toward the lower clearance of the second ring g roove.

3.3 Oil Transport Through the Ring Grooves

Oil flows from one land to another through the ring grooves were consistently observed during the engine tests and are thus considered to be a key part of the oil transport along the axial direction of the piston. As it can be seen in Figure 3.55 and 3.56, oil flow through the ring grooves was observed for the three rings and for most engine operating conditions. Oil flow through the ring groove involves three steps that may result from various driving forces. First of all, oil has to be driven from one land into a ring/groove side clearance. Second, oil has to be transported from the clearance on one side of the ring to the clearance on the other side through the back of the ring. Eventually, oil has to be driven from the ring/groove clearance of the other side of the ring to the adjacent piston land.
In steady state engine operation, one may assume that oil flows in and out of the ring grooves reach a balance so that the amount of oil accumulated in the back of the ring is a constant. Then, the rate of oil transport through the grooves may be fully characterized by studying oil flows between the lands and the grooves only. Accordingly, the following sections (3.3.1 and 3.3.2) focuses on oil flows in and out of the ring grooves respectively. The large volume located at the back of the ring may be considered as a buffer region. The amount of oil accumulated in this buffer region may have an effect on the net oil flow through the ring groove. However, because our experimental setup could not be used to study oil transport on the back of the rings, this effect was not thoroughly investigated. Only in the particular situation where the top ring was observed to flutter, the effect of oil filling percentage of the groove were studied by correlating oil distribution observation and simulation results from RINGPACK-OC. These results are discussed in Section 3.3.2.2.

3.3.1 Oil Transports from the Lands into the Grooves

Four potential mechanisms of oil transport from the lands to the ring/groove side clearance were proposed:

1- Ring mechanical pumping.
2- Oil flow driven by the pressure gradient created by the inertia force in the vicinity of the ring/groove clearance.
3- Dragging action of the gas flow from the land to the groove.
4- Shear driven oil flow due to the lateral motion of the piston relative to the rings.

The capability of each of these mechanisms to carry oil from the piston lands to the ring grooves was investigated.

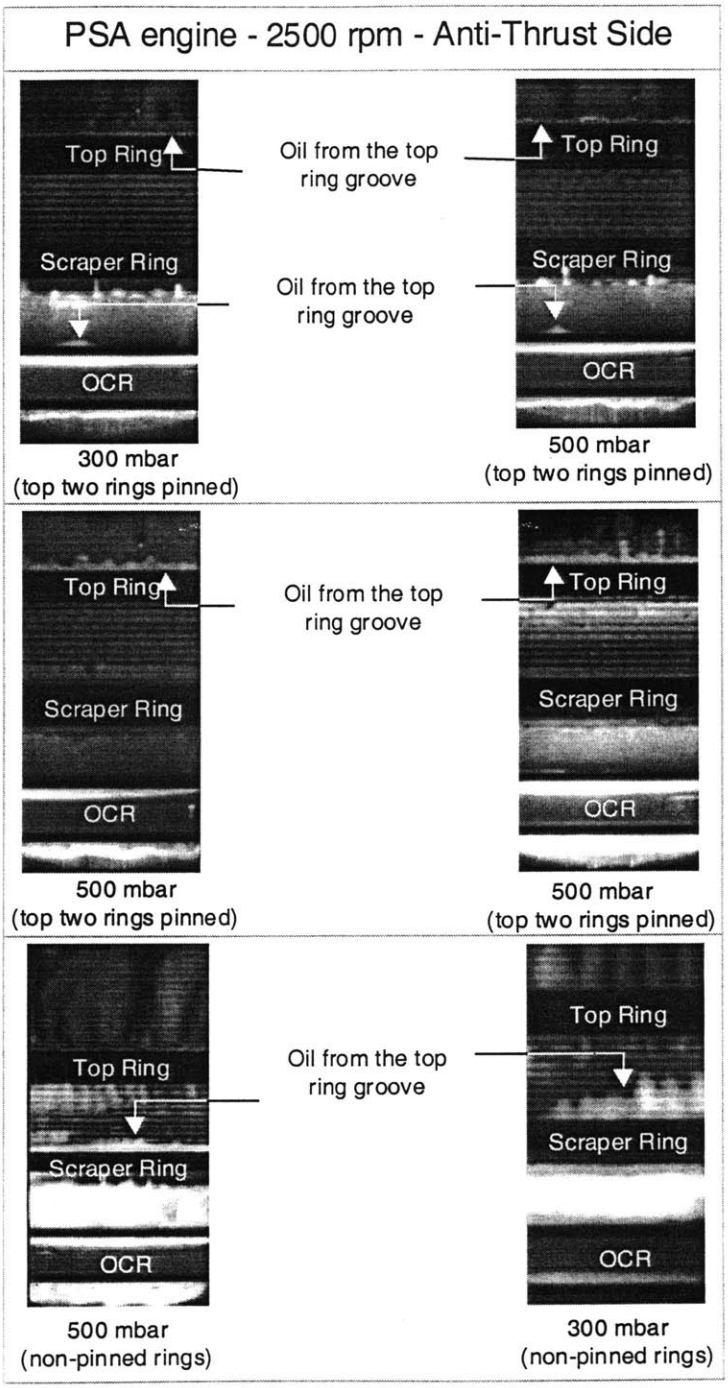


Figure 3.55 - Oil flow out of the ring grooves observed in the PSA engine (I).

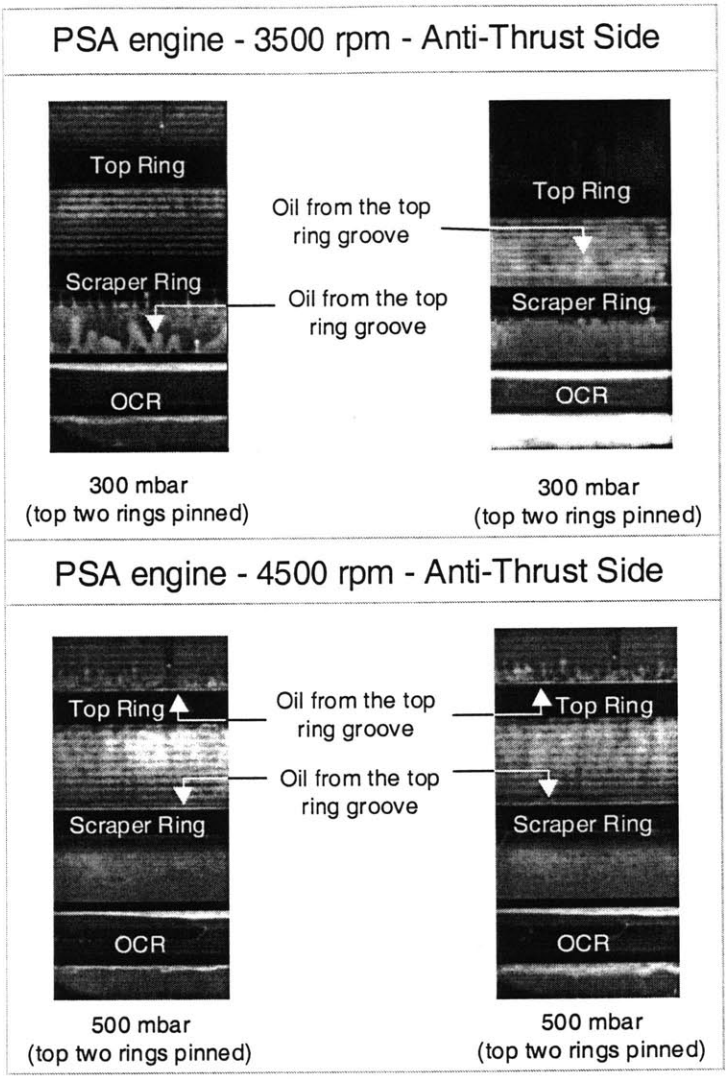


Figure 3.56 - Oil flow out of the ring grooves observed in the PSA engine (II).

3.3.1.1 Ring pumping

As described in Section 3.1.1, inertia can force the oil lying on the piston lands to accumulate against the rings and thus in the vicinity of the ring/groove clearance. The position of the ring relative to the entrance of the ring/groove clearances changes as rings twist and move up and down in their grooves. Depending on the timing of the ring motion and the inertia-driven oil flow, there may be oil accumulated in the vicinity of the ring/groove clearance when the ring moves away from the groove. Then, part of the oil accumulated on the side of the ring will be pumped into the gap opening between the ring and the groove (see Figure 3.57). The amount of oil pumped in the groove will depend on

the amplitude of the ring motion and the amount of oil available. The amplitude of the ring motion, or in other words, the volume opened by the ring as it moves depends on the ring and groove geometry as well as on the ring dynamics. The amount of oil available depends on the oil motion that takes place on the land prior to the ring lift. If the amount of oil available is greater than the volume opened by the ring, the volume of oil pumped in the groove will be controlled by the ring motion. On the other hand, if the volume opened between the ring and the groove is greater than the amount of oil available, axial oil transport occurring on the land will limit the flow into the groove.

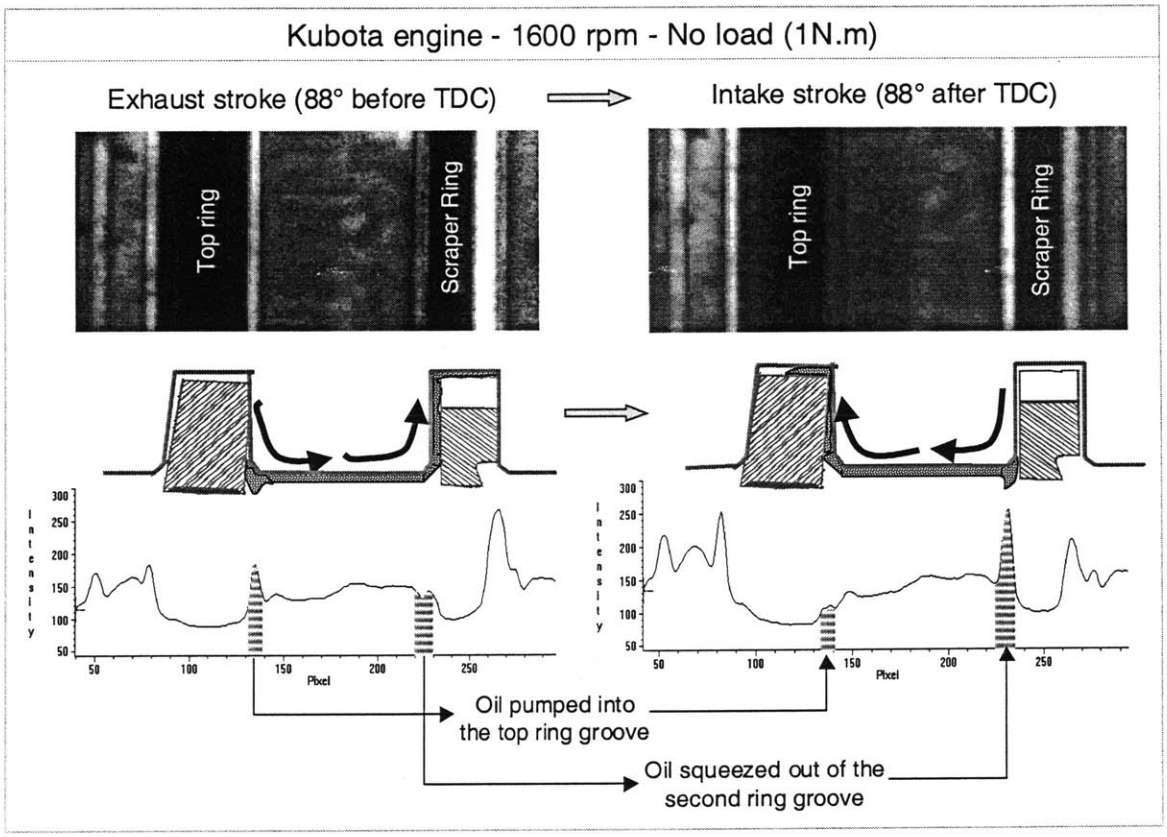


Figure 3.57 – Oil pumping and squeezing observed in the Kubota engine.

A rough estimation of the maximum amount of oil that could be pumped into the ring groove clearance can be computed using typical ring and groove geometry (ring/groove clearance 40 μm, ring radial width 3mm and cylinder bore 86 mm). Assuming that there is enough oil available to fill up half of the ring groove clearance during the ring reversal, the maximum amount of oil that can be pumped into the groove is in the order of 20 000 μg/cycle. This value is three orders of magnitude higher the typical oil consumption rate for this size engine (~ 40 μg/cycle). Therefore, the oil pumping mechanism is very probably limited by the oil availability and not by the ring motion.

Oil availability: The amount of oil available for ring pumping depends on the distribution of the oil on the piston lands at the time of the ring lift. Therefore, in a running engine, it is affected by the inertia force, the uniformity of the oil supply to the land, the ring rotation and the intensity and direction of the gas flows sweeping the lands. Consequently, estimating the amount of oil available for the pumping action of each ring is a very difficult task. However, using the model developed in Section 3.1.1.3 to describe the evolution of the oil distribution along the axial direction of the lands, an attempt to characterize the availability of oil for ring pumping was conducted. The following discussion focuses on the oil flow from the second to the crown land through the top ring groove. Similar reasoning may be applied to the oil flow through any grooves.

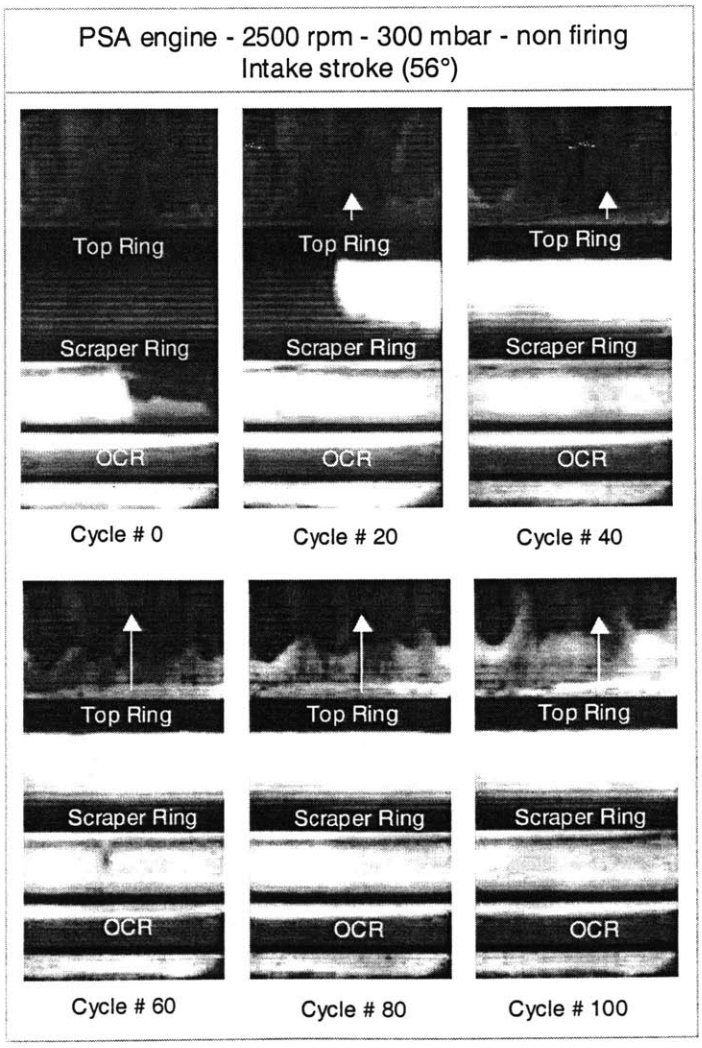


Figure 3.58 – Oil flow through the top ring groove following a sudden increase of the amount of oil on the second land.

As observed in most engine tests, it is assumed that oil is supplied at the bottom of the second land through the second ring groove. According to the modeling work conducted in Section 3.1.1.3, a minimum volume of oil V_{oil_min} is required on the second land for the oil to reach the vicinity of the top ring groove. If the amount of oil accumulated on the second land is below this threshold, the oil supplied to the second land through the second ring groove will not reach the top ring and thus no oil will be transported through the top ring groove. It is important to notice that the existence of this threshold was not clearly proven experimentally. However, during many engine tests, it was observed that a sudden increase of the amount of oil on the second land resulted in a significant increase of the oil flow through the top ring groove (see Figure 3.58).

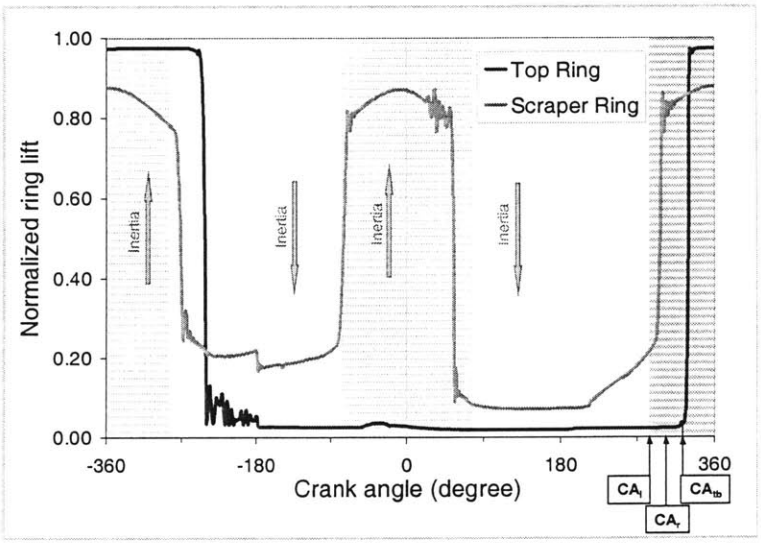


Figure 3.59 – Ring lift and inertia force computed for the Kubota (2000 rpm).

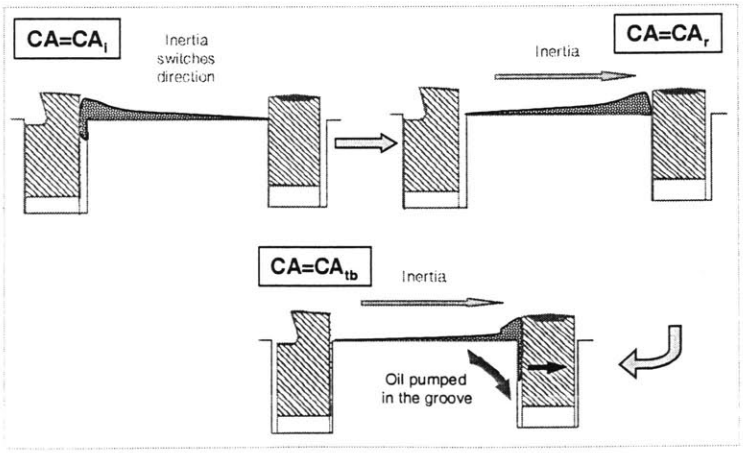


Figure 3.60 – Oil transport to the ring groove, timing of the inertia force and ring lift.

In the situation where the volume of oil accumulated on the second land is greater than V_{oil_min} oil crosses the second land back and forth within one engine revolution. The amount of oil available to be pumped into the lower clearance of the top ring groove depends on how much oil can reach the top ring groove before the ring lifts. As it is described in Figures 3.59 and 3.60, crank angle CA_i represents the moment at which the inertia force is switching from downward to upward direction. At CAi the oil on the second land is accumulated against the scraper ring. At crank angle CA_r, the oil front reaches the top ring. After crank angle CA_r and until inertia switches direction oil accumulates against the top ring. If the top ring twists or lifts away from the bottom side of its groove before CA_r, no oil is available for ring pumping. If the top ring moves away from the bottom of its groove at a crank angle CA_{tb} such that CA_{tb} is after CA_r, the amount oil that has accumulated against the top ring between CA_r and CA_{tb} may be pumped into the groove. An accurate calculation of the amount of oil V_{oil_av} accumulated in front of the lower clearance of the top ring groove would require a complex two-dimensional flow computation. However, using a one-dimensional fully viscous flow representation, an order of magnitude of V_{oil_av} can be obtained with the following equation:

$$V_{oil_av} \sim \frac{\tilde{h}_{oil}^3}{\upsilon_{oil}} \cdot \int_{CA_r}^{CA_{tb}} a_p \cdot d\theta \cdot R_{ld} \cdot \frac{30}{N \cdot \pi}$$

With V_{oil_av}: order of magnitude of the amount of oil available for top ring pumping (m^3)

$\tilde{h}_{oil}$: average thickness of the oil layer on the second land (m)

N: engine speed (rpm)

Volume opened by the rings: The space opened between the groove and the side of the ring defined a maximum volume of oil that could be pumped into the ring groove clearance. In reality, as the ring moves away from the groove, part of the opened space is filled up with gases and/or oil coming from the back of the ring. Therefore, even if there is enough oil available on the land to fill up the gap opening on the side of the ring, it is very likely that the amount of oil pumped into the groove will be much less than the volume swept by the ring.

The twist and lift motions of rings relative to their grooves, which defined the volume swept by the rings, has been described in details in a previous work by T. Tian [17, 14, 27] and can be calculated with the simulation code RINGPACK-OC.

Conclusions: First, the ring pumping process can displace very large amount of oil from the land to the groove and thus should be considered as one of the major mechanism affecting the oil distribution in the piston ring pack. Second, experimental observations showed that there is a strong correlation

between the amount of oil accumulated on one piston land and the oil flow through the adjacent ring grooves. Eventually, based on the model of the oil motion under inertia effect, a characterization of the amount of oil available for ring pumping as a function of the volume of oil accumulated on the land was proposed. The results suggest that there is a minimum volume of oil required for oil supplied on one side of a piston land to be pumped into the groove located on the other side. Furthermore, the timing of the inertia-driven oil motion on the land and the ring dynamics were found to be critical to the amount of oil available for ring pumping.

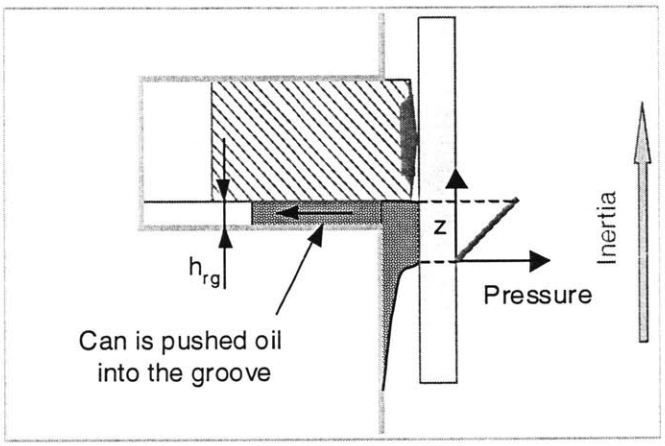


Figure 3.61 – Description of the oil transport into the ring groove resulting from the pressure gradient generated by the inertia force.

3.3.1.2 Pressure gradient due to inertia force

As it is described in Figure 3.61, when oil accumulates against the side of a ring, the inertia force creates a pressure gradient inside the oil accumulation. This pressure gradient may drive oil into the ring groove if the clearance between the ring and its groove is opened. This oil transport occurs when the ring has moved away from the groove and thus after the ring pumping process. Two conditions are required for the pressure to build up at the entrance of the ring groove clearance. First, the entrance of the gap between the flank of the ring and the groove must be fully flooded with oil. To satisfy this condition a large amount of oil has to be available at the outside end of the ring/groove clearance when the ring pumping occurs. Second, since the pressure is proportional to z (see Figure 3.61), a significant amount of oil must be accumulated against the ring. Consequently, this process requires a large amount of oil to be accumulated in the vicinity of the ring/groove clearance before and after the ring lift. From the numerous oil distribution observations conducted, such conditions were never encountered either around the top ring or on the upper side of the second ring, and even rarely on the lower side of the second ring. Consequently, this type of mechanism may only be

considered to be important for the oil flow into the OCR groove or into the lower clearance of the scraper ring groove when there is sufficient oil on the third land.

In order to determine if this oil transport mechanism could have a significant impact on the global oil transport scheme, an estimation of the oil flow rate that can result from the inertia-generated pressure gradient was computed and compared with a typical oil consumption rate. The pressure gradient in the oil accumulation (see Figure 3.61) is given by Equation 3.62.

$$\frac{dP}{dz} = \rho_{oil} \cdot a_p \tag{3.62}$$

The flow rate of oil into the ring groove clearance for a Poiseuille flow is given by Equation 3.63.

$$\frac{q_{oil}}{2\pi \cdot R_{ld}} = \frac{h_{rg}^3}{12\mu_{oil}} \cdot \frac{dP}{dx} \tag{3.63}$$

With q_{oil}: Volumetric oil flow rate between in the ring/groove clearance (m^3/s)

h_{rg}: clearance between the ring and the groove (m).

Using a_p = 3400 m/s^2 (average piston acceleration at 3500 rpm) and z = 0.2 mm, the pressure build up in front of the ring/groove clearance was estimated to be about 500 Pa. Considering that the radial width of the ring was 3 mm, the pressure gradient in the ring/groove clearance was fond to be about 1.8 bar/m. This calculation of the pressure gradient dp/dx assumes that there is no pressure difference between the land and the back of the ring. The value of 0.2 mm for z is typical for oil that may be accumulated on the upper side of the OCR. For oil accumulated on the lower side of the OCR, z may be as large as a few millimeters.

Using h_{rg} = 40 μm, the oil flow rate resulting from the effect of the inertia generated pressure gradient was estimated with Equation 3.63. The results was the following:

$$q_{oil} = 4.10^{-8}\ m^3/s$$

Assuming that this oil flow exists for the time during which the ring stays on one side of its groove, which is approximately half of the engine cycle duration, the oil flow rate per cycle was estimated to be:

$$Q_{oil} = 274\ \mu g/cycle$$

This number is to be compared with the oil consumption per cycle per cylinder at this engine speed that is typically in the order of 40 μg/cycle. Accordingly, we may conclude that the pressure gradient generated by the inertia force at the entrance of the OCR/groove clearance can drive oil into the OCR groove at a rate that is large enough to significantly affect the oil distribution in the piston ring pack.

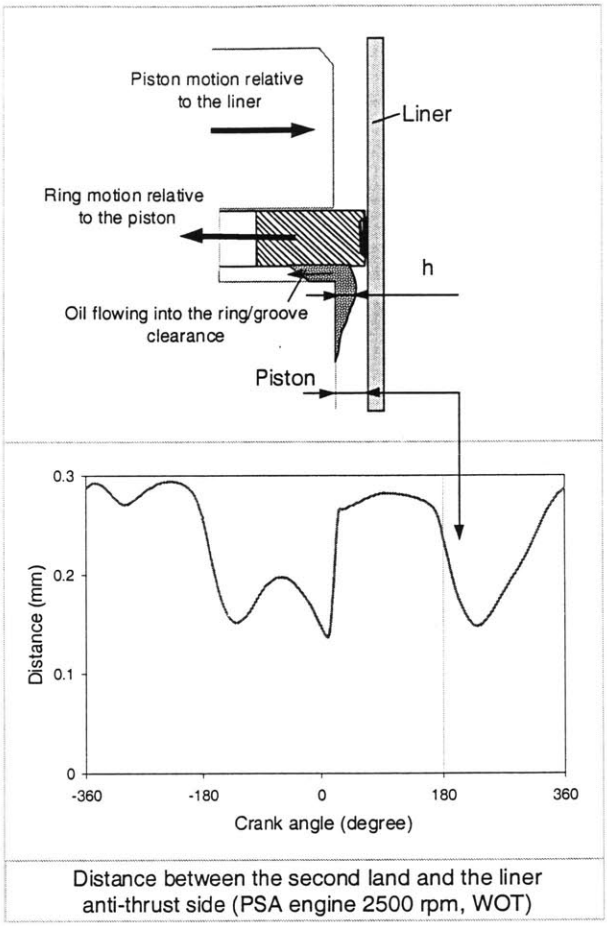


Figure 3.62 – Description of the oil transport into the ring groove resulting from the lateral motion of the piston relative to the rings.

3.3.1.3 Lateral motion of the piston relative to the rings

As it is described in Figure 3.62, due to the piston secondary motion, oil that is accumulated against the rings can be transported inside the ring/groove clearances by the shearing action resulting from the lateral motion of piston relative to the rings. For this kind of transport to occur, oil has to be available in the vicinity of the ring/groove clearance. The inertia force dictates the repartition of the oil along the axial direction of the piston land. Therefore, the amount of oil available in front of the ring/groove clearance at the time the piston moves from side to side is determined by the timing of the piston secondary motion and the inertia force. If the piston lateral motion occurs while the oil on the land is moving away from the ring or before the oil reaches the ring, then no oil will be transported inside the ring groove. Assuming that the piston lateral motion occurs while oil accumulates against the ring, the amount of oil displaced into the ring/groove clearance will depend

on the thickness h (see Figure 3.62) of the oil accumulation and on the amplitude of the lateral piston motion d_{lp} at the considered location. If h is smaller than d_{lp}, then the volume of oil transported inside the groove will be limited by the amount of accumulated in front of the ring groove clearance. Furthermore, the amount of oil displaced into the ring groove depends on the clearance between ring and its groove and thus on the ring position.

An estimation of the rate of transport that can be generated by this mechanism was computed assuming the oil accumulation to be thicker than d_{lp}. Using a Couette flow representation, the oil volume carried is the groove can be written as:

$$dQ_{oil} = \frac{d_{lp} \cdot h_{rg}}{2} \cdot R_{ld} \cdot \cos(\theta) \cdot d\theta \tag{3.64}$$

With dQ_{oil}: oil volume transported inside the ring groove in the angular sector of piston $d\theta$

Accounting for the fact that d_{lp} is varying along the circumference of the piston, the oil volume transported into the groove is given by:

$$Q_{oil} = d_{lp} \cdot h_{rg} \cdot R_{ld} \tag{3.65}$$

Q_{oil} is the amount of oil that would be transported into the ring groove on the side of the piston where this one moved by d_{lp} toward the liner. On the other side, oil may be transported out of the ring groove by a similar mechanism. Using the maximum displacement of the piston second land along the thrust/anti-thrust axis calculated for the PSA engine at 2500 rpm full load (see Figure 3.62), the estimation of Q_{oil} gave the following result:

$$Q_{oil} = 220\ \mu g/cycle$$

This number is in the same order of magnitude as the oil consumption rate in these engine running conditions (~ 40 μg/cycle). Therefore, we can conclude that the relative lateral motion of the rings to their grooves has a significant effect on the oil transport through the piston ring pack and that this mechanism should be considered as one of the main mode of oil transport into the ring groove.

3.3.1.4 Dragging of the gas flow from the lands to the grooves

As it was explained in Section 3.1.3.2, the dragging action of gases flowing between the lands and the grooves has no or very little effect on the repartition of the oil along the axial direction of the piston lands. Therefore, oil accumulated on the piston lands can not be dragged at a significant rate into the ring grooves. In the experiments conducted at 2500 rpm 300 mbar AIP, the top ring was observed to flutter intermittently. While the top ring was fluttering gases were flowing from the combustion chamber to the second land through the back of the top ring groove. The observation of the oil

distribution on the crown land showed that the occurrence of the top ring flutter and the resulting gas flow from the combustion chamber to the top ring groove had no effect on the oil lying on the crown land. Consequently, it can be concluded that even in the case where the gas flow rate from the land/liner clearance to the ring groove is high due to ring fluttering, the dragging action of the gases generates a negligible oil transport into the ring grooves.

3.3.1.5 Conclusions

Overall, we can conclude that three mechanisms were identified as potential modes of oil transport from the piston lands to the ring/groove clearances:

1- Ring pumping. This mechanism may exist for any of the three rings
2- Flow resulting from the inertia-generated pressure gradient. Due to the large amount of oil required for this mechanism to take place, it is mainly expected to occur around the OCR.
3- Flow resulting from the lateral motion of the piston relative to the rings.

These three mechanisms rely on the availability of oil in the vicinity of the ring groove clearance during a specific period of the engine cycle. Moreover, the repartition of the oil along the axial direction of the piston lands is driven by the inertia force. Consequently, the rate at which the oil is transported into the ring groove is strongly dependent on the timing of the inertia force in regards to the ring twist, ring lift and the piston secondary motion.

3.3.2 Oil Transports from the Grooves to the Lands

Two potential mechanisms of oil transport from the ring/groove clearances to the lands were identified and investigated:

1- Ring squeezing action

2- Gas flow dragging in the ring/groove clearances

These two mechanisms were characterized using experimental data and simulation results obtained from the RINGPACK-OC code.

3.3.2.1 Ring squeezing

Description: When one ring is moving toward one side of its groove, part of the oil layer covering the side of the groove and the ring is being squeezed out of the ring/groove clearance. Oil is squeezed toward the inside and the outside of the groove. The oil squeezed out of the groove onto the piston land constitutes a net transport of oil from the ring groove to the piston lands. In most engine operating conditions this type of oil flow was found to be the main mechanism by which oil was transported from the ring grooves to the piston lands. Figure 3.57 shows two images of the oil distribution acquired in the Kubota engine during two following exhaust and intake strokes. Between the two images the second ring had moved from the bottom to the top of its groove. As a result, oil was squeezed out of the upper side of the scraper ring groove. The oil squeezed out can be identified on both the LIF image and the florescence intensity profile. In Figures 3.55 and 3.56, one can clearly see the oil that was squeezed out of the upper side of the OCR, the scraper ring and the top ring groove in various engine operating conditions.

The amount of oil squeezed every cycle out of the ring grooves is determined by the thickness of the oil layer covering the groove sides and the motion of the rings relative to their grooves. The amount of oil trapped in the ring groove clearances depends on the rate at which oil is supplied to these regions. Therefore, it is determined by the oil flows from the lands to the grooves occurring on both sides of the rings and oil transport taking place behind the rings.

Effect of ring/groove geometry: As described in Figure 3.63, the geometry of the squeezing region, which is determined by the groove tilt and the ring twist, greatly affects the portion of the oil being squeezed out at each end of the ring/groove clearances. For instance, if on the upper side of one ring the angle between the ring and its groove is as drawn in Figure 3.63a (inside diameter sealing), more

oil will be squeezed toward the outside of the ring groove than toward the inside. For a rectangular ring, the relative angles between the ring and its groove on both sides of the ring are opposite to each other (see Figure 3.64). Therefore, one side favors oil squeezing toward the back of the ring while the other one favors oil squeezing toward the land. Figure 3.64 shows how oil squeezing on both sides of the rings is affected by the ring twist in a case where there is no groove tilt. For positive-twist ring (Figure 3.64a), more oil will be squeezed out of the groove on the lower side than on the upper side of the ring. On the other hand, with a negative-twist ring more oil will be squeezed out on the upper side than on the lower one. As a result, we may conclude that the ring twist defines a preferred squeezing direction.

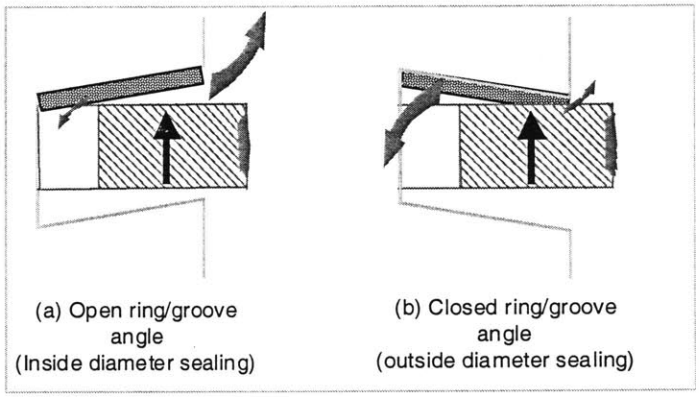


Figure 3.63 – Main squeezing direction for inside and outside sealing configurations.

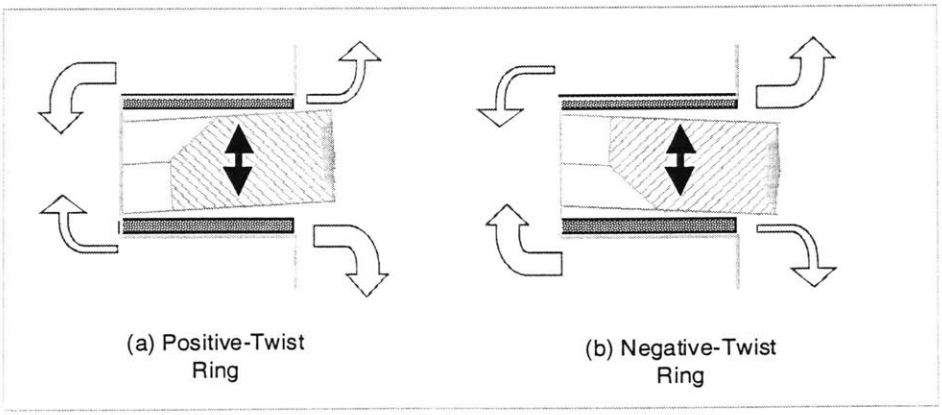


Figure 3.64 – Effect of the ring static twist on the rate of oil squeezing on both side of the ring (assuming rectangular groove).

Direction of the net oil flux through the ring groove: Even though the choice of the ring twist greatly affects the rate at which oil may be transported through the ring groove in each direction, it may not determine the direction of the net oil flux. The net oil transport through one ring groove is the result of the summation all the flows in and out of this groove. The amplitudes of the flows going into the ring grooves were found to be greatly dependent on the amount of oil available in the vicinity of ring/groove clearances. Assuming that the gas dragging effect in the ring/groove clearances (which is described in Section 3.3.2.2) is negligible, the ring squeezing mechanism is the main mode of oil transport from the ring grooves to the lands. In this situation, the direction of the net oil flux through the ring grooves may be determined by the preferred oil squeezing direction as well as by the amplitudes of the rates of oil supply to each side of the ring (see Figure 3.65). In particular, if oil is only supplied on one side of the ring, for instance from the land located below the ring, the net oil flux through the groove will always go from the lower land to the upper one. This will be true even if the ring twist favors ring squeezing from the upper land to the lower one (positive twist ring). In this case, the relative ring/groove angle can only affect the rate at which oil is transported through the groove.

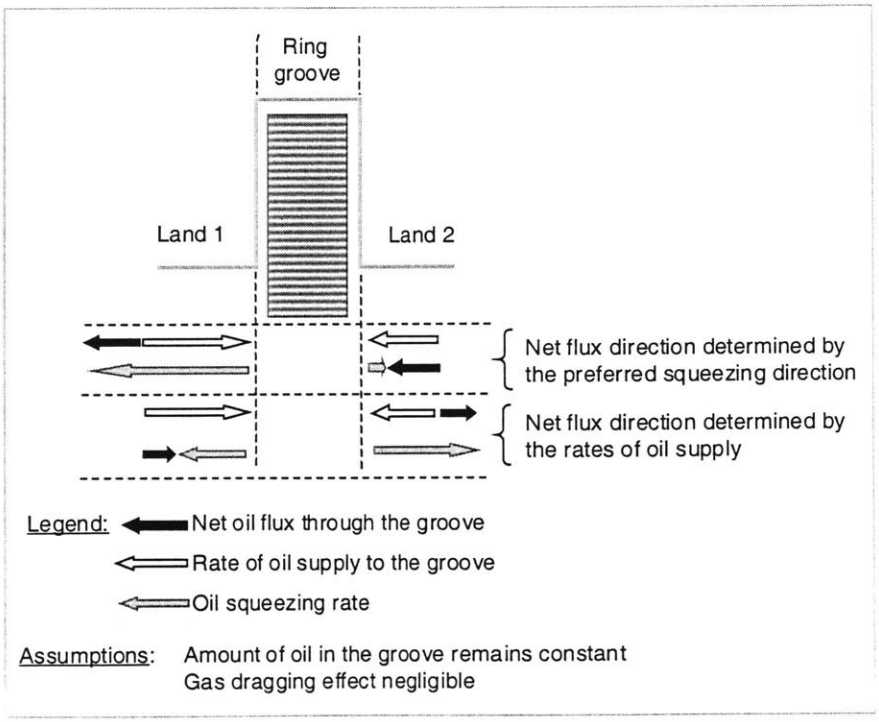


Figure 3.65 – Determination of the direction of the net oil transport through the ring groove (assuming that there is no ring flutter).

Simulation results: The effect of the ring twist on the oil squeezing process occurring on the lower side of the top ring groove was illustrated using the simulation code RINGPAC-OC [33]. Given the thickness of the oil layer covering the ring grooves, this computer code solves the Reynolds equation to determine the oil flow inside the ring/groove clearance. The results presented in Figures 3.66 and 3.67 were computed for the PSA single cylinder engine for two types of top ring, one without static twist and one with 0.005-rad positive twist. The top ring groove was given a 0.1 degree negative tilt to account for thermal deformation of the piston. In Figure 3.66 which shows the instantaneous oil squeezing flow rate along the radial direction of the lower clearance of the top ring groove, one can see the effect of the top ring dynamic twist on the squeezing process. Around the combustion top dead center (0° crank angle), under the effect of the rising pressure in the combustion chamber the top ring twists toward the bottom of its groove and as a result the oil-squeezing rate is increased. In Figure 3.67, which shows the average oil flow rate at different location along the side of the ring, one can see the effect of the top ring static twist on the amount of oil squeezed at both end of the ring groove clearance. First of all, for the two cases plotted in Figure 3.67, the amount of oil squeezed at the outside limit of the squeezing region is larger than the one squeezed at the inside limit. Therefore, as it could be expected from the ring groove relative angle, more oil is squeezed outward than inward. Secondly, it can be seen that the positive-twist top ring squeezes more oil outward than the non-twisted ring.

Furthermore, the calculation shows that even with an oil layer as thin as 2 μm covering the groove sides, the amount of oil squeezed onto the land per cycle can be in the order of 200 μg/cycle. This amount is larger than the typical rate of oil consumption for these engine running conditions (~ 40 μg/cycle). Therefore, it can be concluded that the ring squeezing mechanism constitutes one of the major modes of oil transport from the ring grooves to the piston lands.

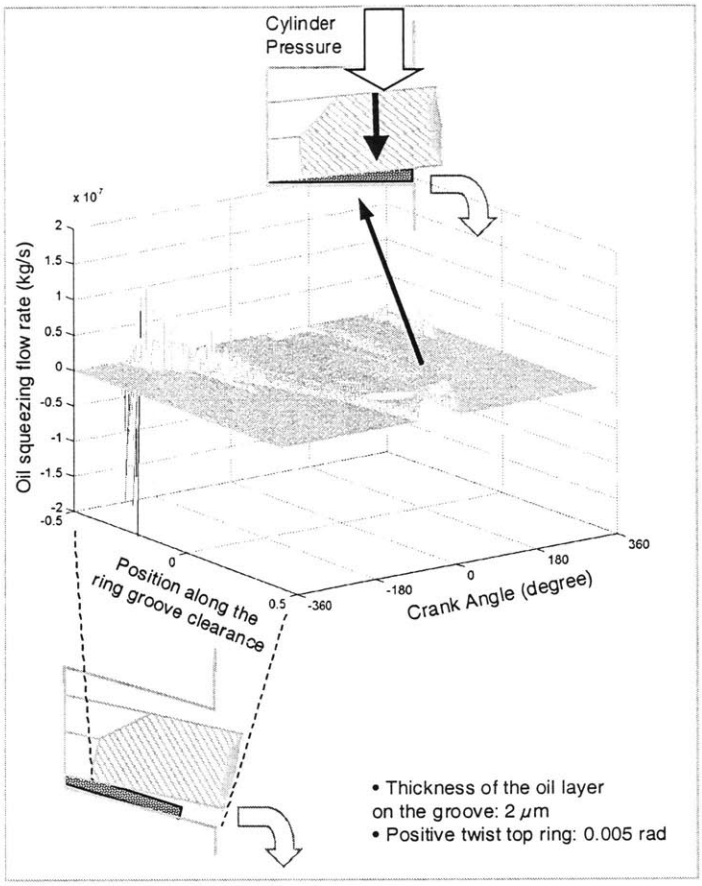


Figure 3.66 - Instantaneous oil squeezing rate at the lower clearance of the top ring groove (Calculated with RINGPACK-OC for the PSA engine running at 2500 rpm 500 mbar).

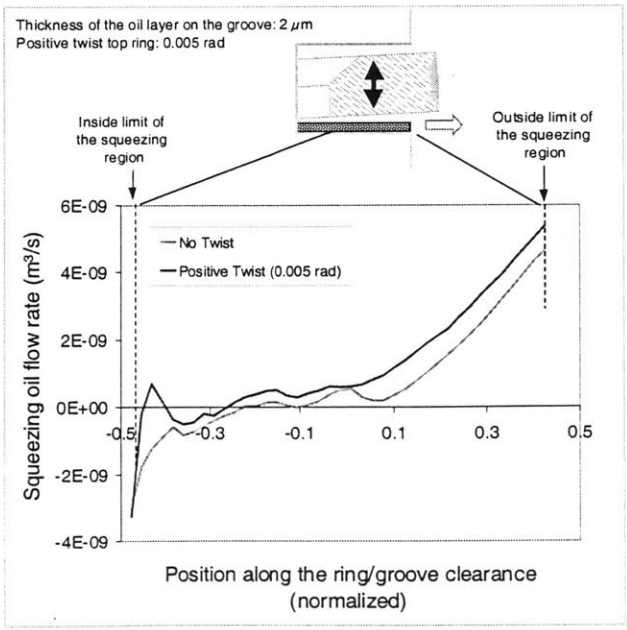


Figure 3.67– Cycle-averaged oil squeezing rate at the lower clearance of the top ring groove (Calculated for the PSA engine running at 2500 rpm 500 mbar).

3.3.2.2 Gas flow dragging in the ring/groove clearances

Description: Gas flow between the grooves and the piston lands have the potential to drag oil covering the sides of the ring/groove clearances and the lands. Previous discussions show that the effect of axial gas flows on the land oil distribution is almost always negligible. Because the ring/groove clearances are much thinner than the land/liner clearances, the friction force applied by the gas flow to the oil layer in the ring/groove clearances is much greater than in the land/liner interstice. Thus, it was worth investigating the effect of gases flowing between the grooves and the lands on the oil layer covering the sides of the ring/groove clearances. To do so, the shear stress induced by the gas flow at the surface of the oil layer had to be estimated. This was done by assuming that the gas flow through the ring groove was a fully developed viscous flow. This assumption was discussed by T.Tian [14] and was found to be appropriate except in the case of top ring fluttering. When the top ring loses stability, the gas flow through the top ring groove is large enough so that convection term and the entrance effect may not be negligible. In this discussion, the gas flow was always represented as a fully developed Poiseuille flow, and thus the dragging action of the gases was underestimated in the case of top ring fluttering. Considering the oil flow as a fully developed Couette flow, the oil flow rate induced by the dragging action of the gases flowing through the ring/groove clearances was estimated by the following equation.

$$q_{oil} = q_{gas} \cdot \frac{3 \cdot \mu_{air} \cdot h_{oil}}{\mu_{oil} \cdot h_{rg}^2 \cdot} \tag{3.66}$$

With q_{oil}: instantaneous oil flow rate (m^3/s)

q_{gas}: instantaneous gas flow rate (m^3/s)

h_{rg}: ring groove clearance (m)

h_{oil}: thickness of the oil layer covering the side of the groove (m)

The rate of oil transport induced by the dragging action the gases flowing through the ring/groove clearances was computed for the PSA engine for the 10 operating conditions that were tested. The gas flow rate through the ring/groove clearance q_{gas} and the height of the channel between the ring and the groove h_{rg} were computed with the RINGPACK-OC simulation code. Since the rings and grooves have a relative angle, the clearance in between them is a converging or diverging channel and thus h_{rg} is varying along the radial direction of the ring/groove clearance. For simplicity, the oil flow rates were estimated using the average height of the channel calculated every crank angle degree.

Figure 3.68 shows the amount of oil removed by the dragging action of the gas flow from the upper and lower side clearances of top ring. The results are plotted for different engine speeds as function of the engine load (intake manifold pressure). As one can see, except for the 300-mbar intake pressure cases, the amount of oil removed from the grooves is about 10 μg/cycle or less, and thus in the order of oil consumption rate but much smaller than the squeezing rates. At 300-mbar intake pressure the top ring flutters. As a result, a large amount of gas is allowed to flow from the combustion chamber to the second land through the top ring groove. Consequently, the amount of oil removed from both sides of the ring groove is greatly enhanced. At 4500 rpm 300-mbar AIP up to 55 μg of oil are carried away from each sides of the ring groove every cycle. On Figure 3.69, which shows the results obtained for the scraper ring, it can be seen that for this type of scraper ring, the amount of oil removed from the second ring groove was negligible in all engine running conditions. It is important to notice that this result can not be extended to other types of scraper ring. For instance, if a negative twist second ring was used, the ring would be very likely to flutter and thus the amount of oil carried by gas flows could be greatly enhanced. Finally, Figure 3.70 shows the results obtained for the OCR. Again these results are very specific to the ring geometry that was used for the computation. Because the twin-land OCR has a tendency to flutter [27], the gas flow rates through the OCR groove can be large enough to drag significant amounts of oil through the groove. The estimations plotted in Figure 3.70 show that for this engine the rate of oil removal from the OCR groove due the gas dragging action could reach 100 μ/cycle.

Overall, we can conclude that the rate of oil transport from the ring grooves to the piston lands resulting from the dragging action of the gases flowing through the ring/groove clearances is:

1. Small but not negligible for the top ring groove
2. Significant for any groove where the ring flutters
3. Usually smaller than the oil squeezing rate.

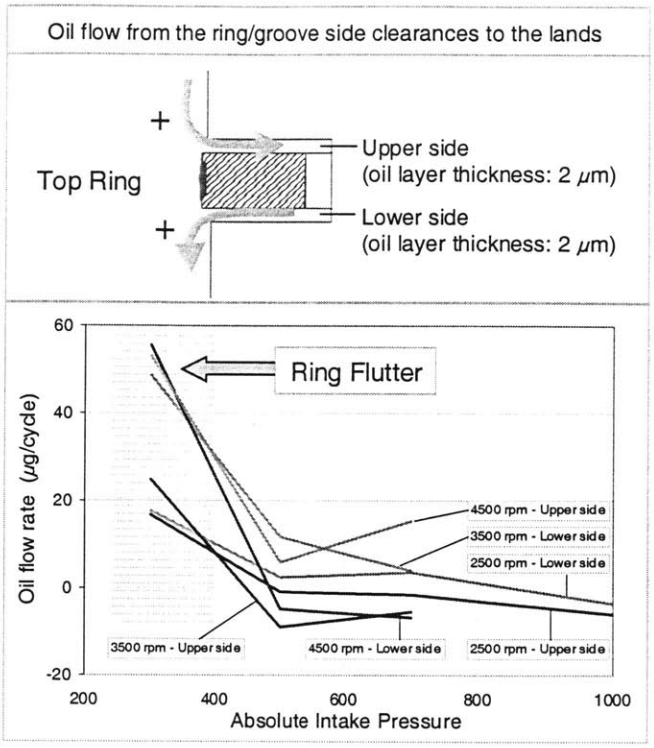


Figure 3.68 – Computed rate of oil transports induced the dragging action of the blow-by gases in the side clearances of the top ring groove (Computed for the PSA engine).

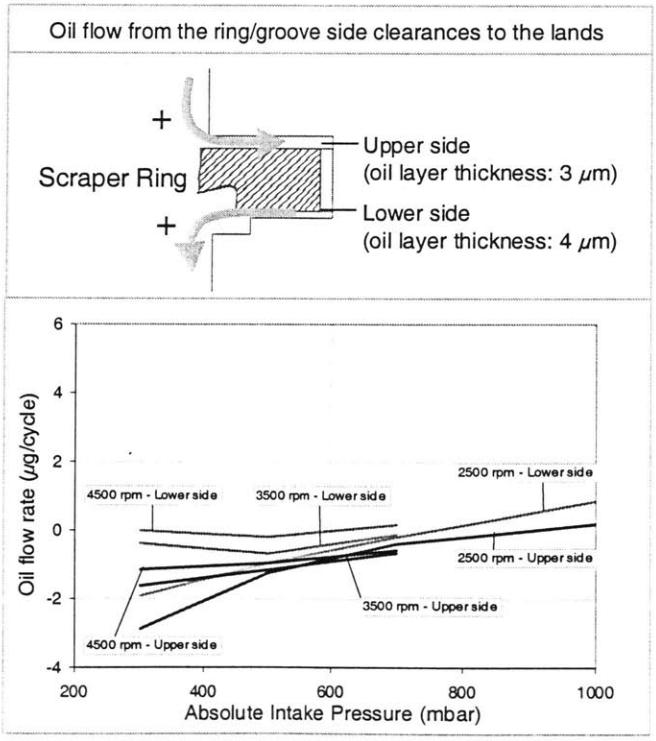


Figure 3.69 – Computed rate of oil transports induced the dragging action of the blow-by gases in the side clearances of the second ring groove (Computed for the PSA engine).

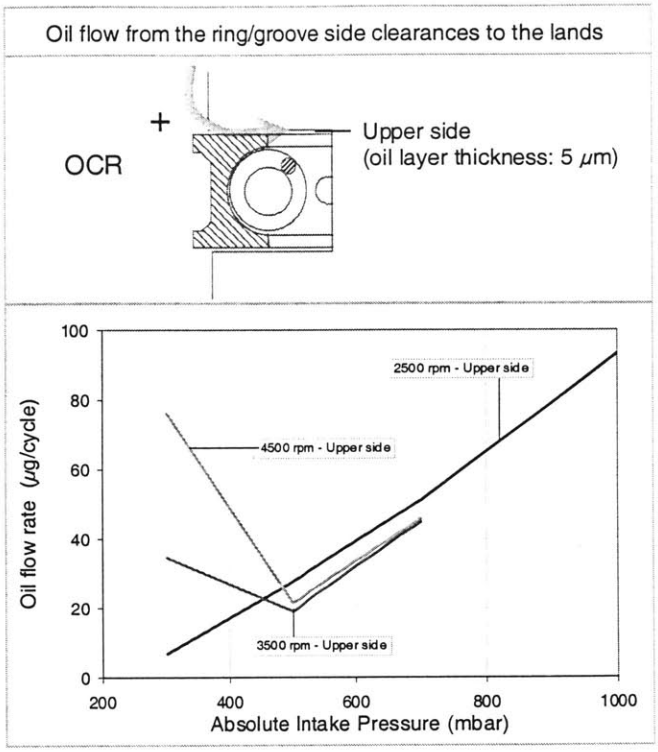


Figure 3.70 – Computed rate of oil transports induced the dragging action of the blow-by gases in the upper side clearance of the OCR (Computed for the PSA engine).

Ring flutter observations: In the PSA single-cylinder engine, at 2500 rpm 300-mbar AIP, the top ring was observed to flutter intermittently. The occasional top ring fluttering was first suspected from the unsteadiness of the blow-by measurements and then was directly observed from the video recording of the evolution of the oil distribution on the piston lands.

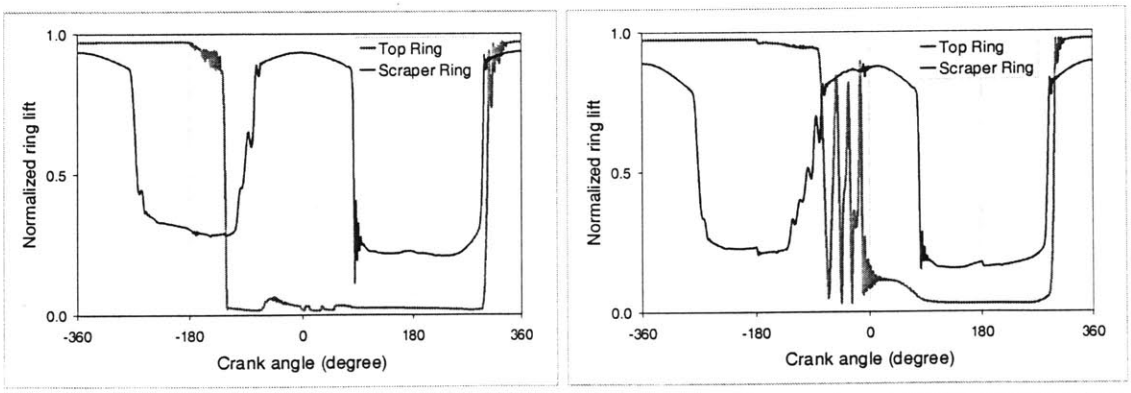


Figure 3.71 – Top and second ring lift computed for the PSA engine running at 2500 rpm 300 mbar.
Left figure: average cylinder pressure trace and top ring groove oil filling 20%.
Right figure: lower than average cylinder pressure trace and top ring groove oil filling 60%.

The blow-by flow rate was measured to be constant at 0.6 liter/min most of the time with peaks around 2 liter/min about every 30 seconds. The simulation code RINGPACK-OC was used to simulate the dynamic behavior of the rings at 2500 rpm 300-mbar AIP. First, the simulation was conducted using a cylinder pressure trace that was the average of 100 measured traces and an oil filling percentage of the first groove of 20%. The results of this first simulation are presented on the left plot of Figure 3.71. As one can see, the computed top ring lift did not show any instability. The predicted blow-by was 0.55 liter/min, which is very close to the measured value of 0.6 liter/min. Consequently, this calculation is believed to be representative of the periods where the blow-by was observed to be constant. Second, simulations were conducted using various single pressure traces picked among the 100 traces that were used to generate the average pressure trace input in the first simulation. Furthermore, these simulations were conducted for various oil filling percentages of the top ring groove (from 10 to 80 %). Using the cylinder pressure traces with lower than average peak pressure and an oil filling percentage of 60%, the top ring was found to flutter during compression stroke (see right plot of Figure 3.71). In this case the predicted blow-by was 1.7 liter/min. This latter simulation is believed to be representative of the periods where the blow-by was measured to reach 2.5 liter/min. Because the blow-by flowmeter was designed to measure steady flow, it was not very accurate when measuring blow-by peak values. Therefore, the agreement between the measured and the computed blow-by flow rates was considered to be satisfying. From the blow-by measurements and the computation results it was concluded that the blow-by variations observed at 2500 rpm 300 mbar AIP were due to intermittent top ring fluttering.

When the top ring is unstable, its position in its groove at a particular crank angle degree may vary from cycle to cycle. Therefore, the oil distribution next to the ring may show some cycle-to-cycle variations as well. Figure 3.72 shows a series of images chosen from the video footage of the evolution of the oil distribution recorded at 2500 rpm 300-mbar AIP. From the first six images of Figure 3.72, one can see that as the top ring was losing stability, its position in its groove was found to vary from cycle to cycle. From images 8 to 15, one can see that the gases flowing through the groove during the ring flutter dragged oil from the lower ring/groove clearance to the second land. Under the effect of the inertia force, the oil carried out of the top ring groove spread over the second land. From the video recording it could be seen that the top ring stopped fluttering around the time where image 15 was acquired. Once the top ring stopped fluttering, oil started to accumulate in the top ring groove. As a result oil that was squeezed out of the upper side of the top ring can be observed on the crown land on images 16 to 20. Eventually, the complete video recording showed that the top ring flutter was occurring every 35 seconds for periods of 3 to 6 seconds.

The periodicity of the fluttering process is believed to result from the effect of the oil filling percentage on the top ring stability. When the top is stable, oil is transported into the top ring groove at a faster rate than it is removed. As a consequence, the amount of accumulated in the groove increases. At some point the oil filling percentage reaches the critical value required for the top ring to lose stability. Then, whenever the cylinder pressure is low enough, the top ring flutters. As the top ring flutters, the amount of oil accumulated in the groove quickly decreases and the ring regain stability.

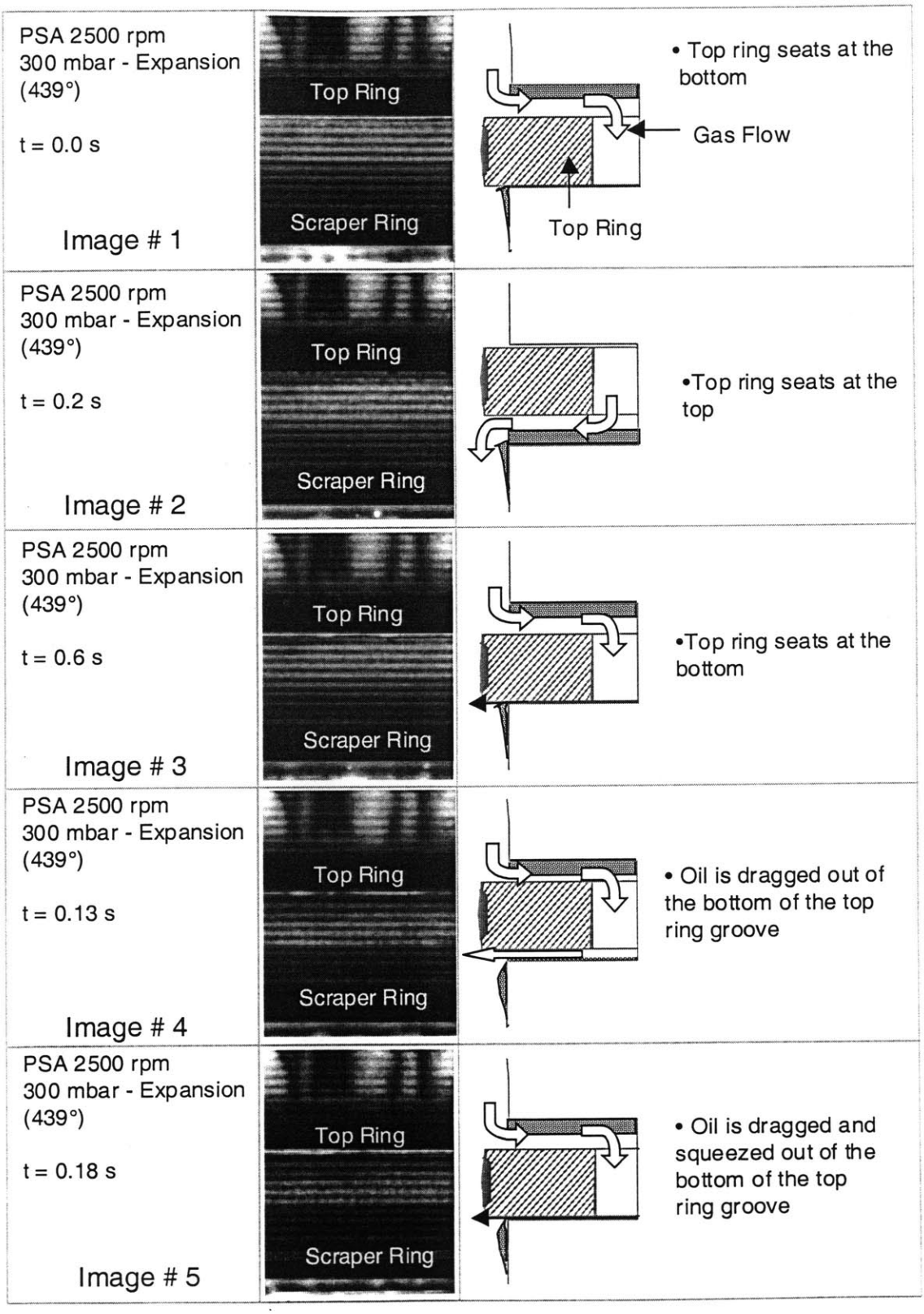


Figure 3.72 (I) – Intermittent top ring fluttering observed in the PSA engine running at 2500 rpm 300 mbar.

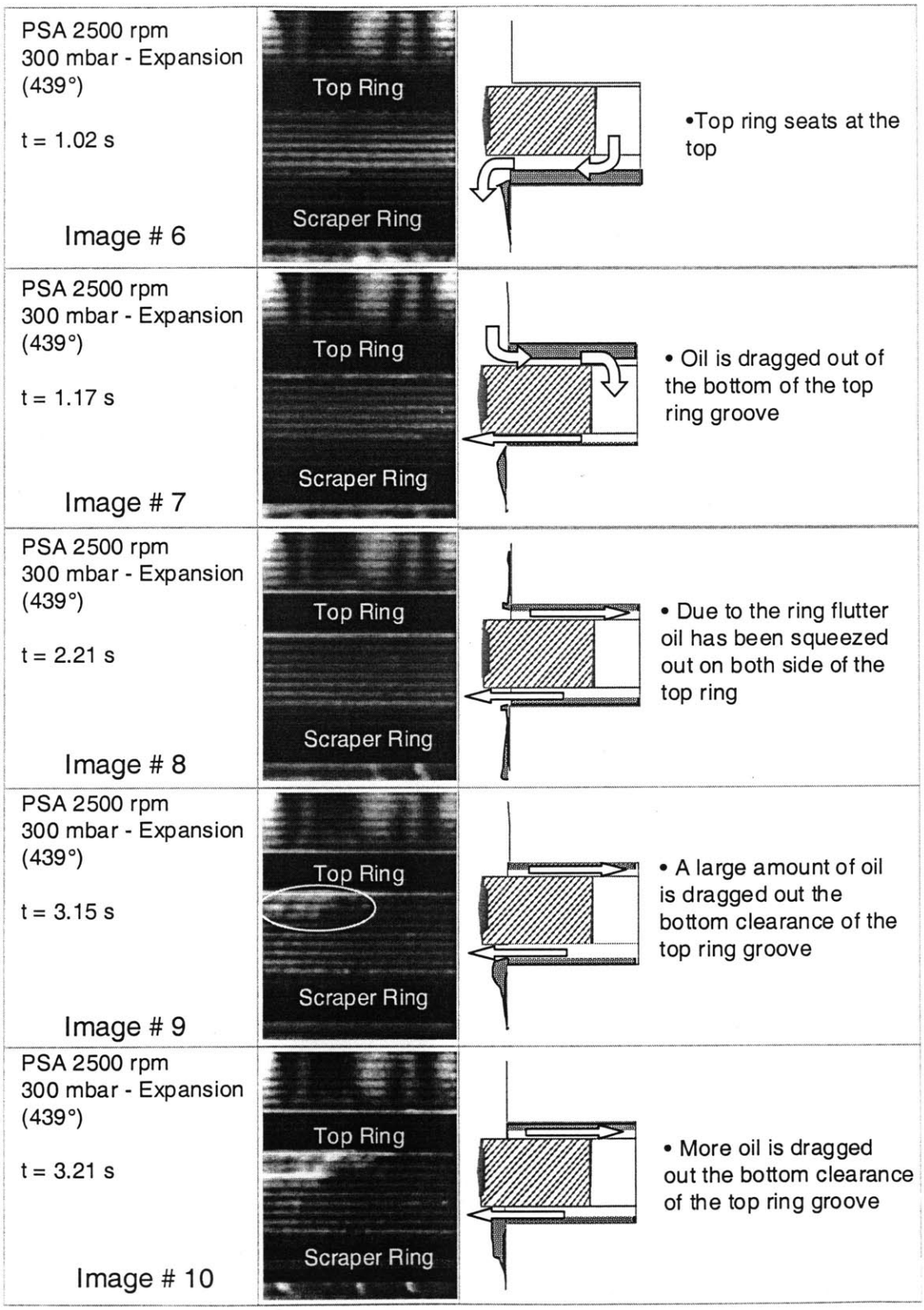


Figure 3.72 (II) – Intermittent top ring fluttering observed in the PSA engine running at 2500 rpm 300 mbar.

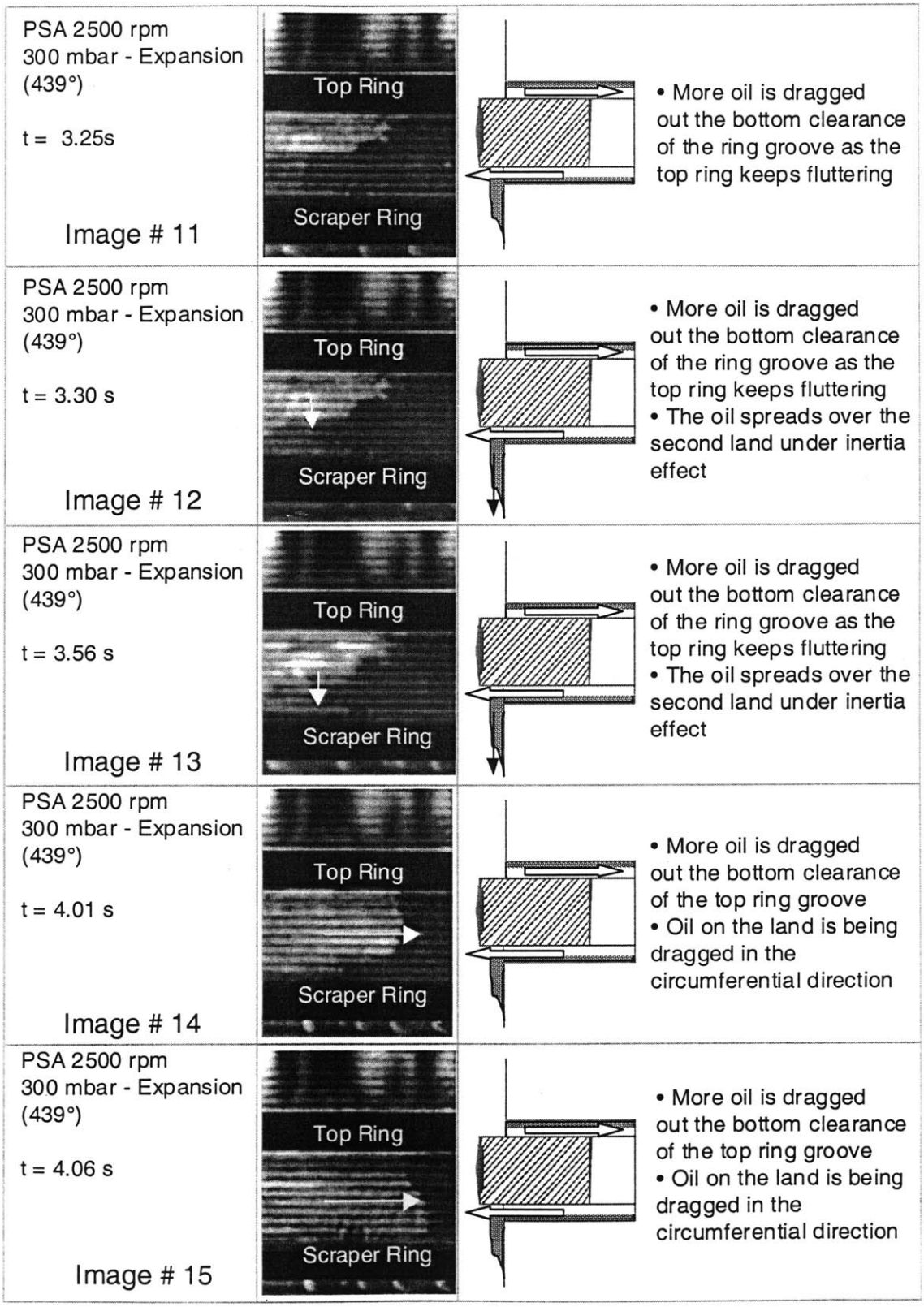


Figure 3.72 (III) – Intermittent top ring fluttering observed in the PSA engine running at 2500 rpm 300 mbar.

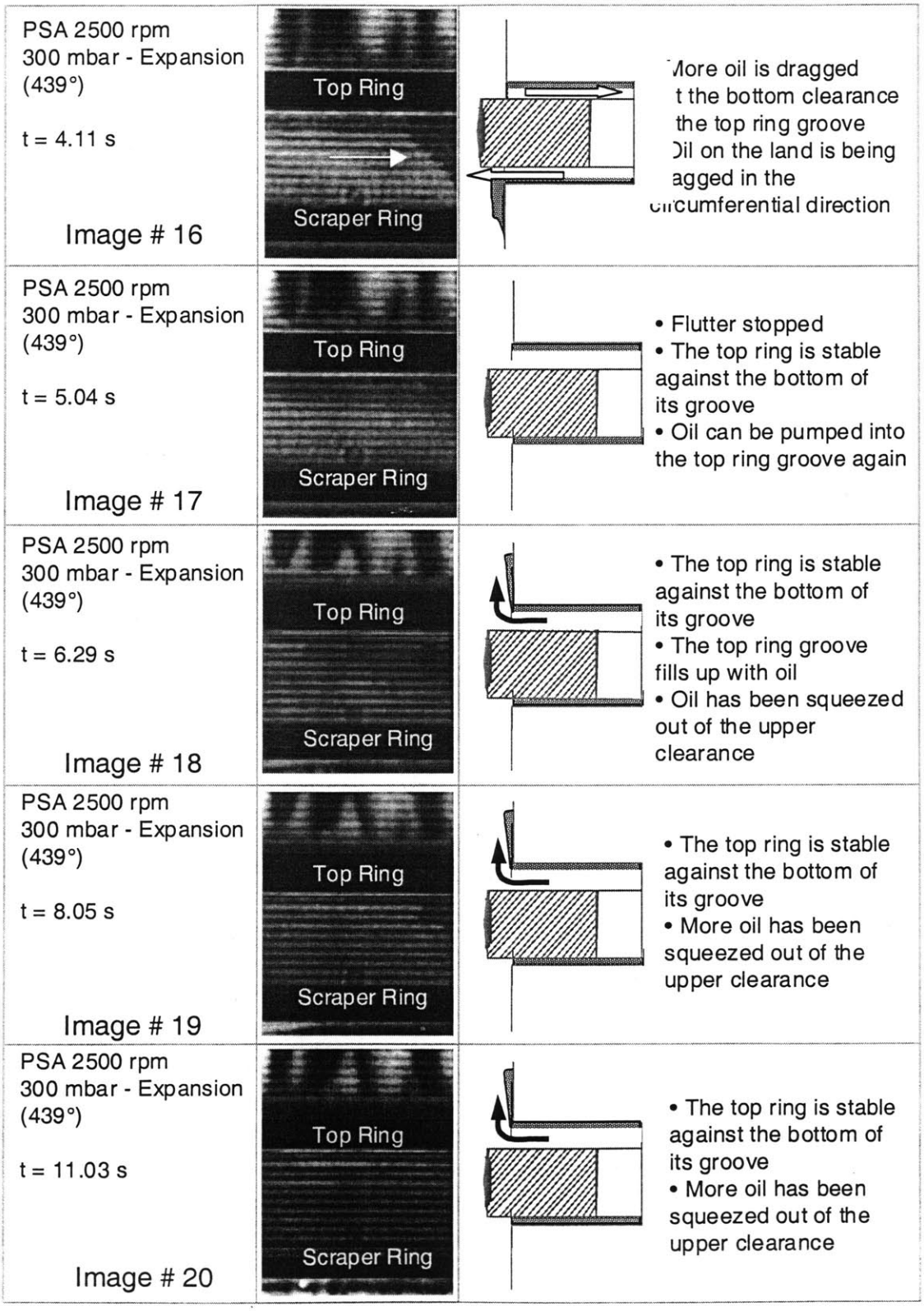


Figure 3.72 (IV) – Intermittent top ring fluttering observed in the PSA engine running at 2500 rpm 300 mbar.

3.3.3 Conclusions

First of all, oil distribution observations have showed that the clearances between the rings and their grooves were a major path for oil to flow from one piston land to another. Three processes that can drive oil from the lands to the ring groove clearances were identified:

1- Ring squeezing (directly observed from the experimental data)
2- Lateral motion of the piston relative to the rings
3- Pressure gradient generated by the inertia force (may only apply to the OCR).

The rates of oil transport resulting from these three mechanisms strongly depend on the amount of oil available in the vicinity of the ring groove clearances, and thus on the effect of the inertia force on the axial distribution of the oil on the piston lands. Moreover, they rely on dynamics of the rings and the piston and therefore vary with engine speed and load.

Second, oil transports from the ring/groove clearances to the lands were found to result from the two following mechanisms:

1- Ring squeezing (main mechanism)
2- Gas flow dragging (particularly significant during ring fluttering)

Eventually, the direction of the net oil transport through one groove depends not only on the relative amplitude of the various flows in and out of the ring groove clearances located on each side of the ring, but also on the relative amplitude of the rates of oil supply to each side of the ring groove.

3.4 Oil Flow Through The Ring Gap

In most engine operating conditions, ring gaps are the main paths through which gases are flowing from the combustion chamber to the crankcase. Correspondingly, we can expect the ring gaps to be one the major path of oil transports between the piston lands. Therefore, oil flows through the piston ring gaps were investigated and characterized for various engine running conditions. Observation of the oil flows through one ring gap requires the gap to be located in front of the window. This condition could have been forced by pinning the ring gaps on the thrust/anti-thrust axis. However, observing the flow through each ring gap in a pinned-ring configuration would have required to setup the rings and/or window position in three different configurations and thus would have been very time consuming. Consequently, in this work, the investigation of the oil flow through the ring gaps was based on observations made as the ring gaps were passing in front of the viewing area during non-pinned ring experiments.

3.4.1 Mechanisms

This section describes the mechanisms by which oil is transported by the gas flows through the ring gaps. The experimental data used in this section were all acquired in the Kubota diesel engine where the reverse blow-by is negligible. As a consequence, the results and conclusions presented in this section apply mostly to diesel engines and spark ignition engines running at WOT (or close to WOT). The effects of significant reverse blow-by, which can be encountered in SI engine operating at low load, are presented in Section 3.4.2.1.

3.4.1.1 Gas driven flow

Observations: As described in Section 3.1.2, oil lying on the piston second and third lands is dragged from gap to gap by the circumferential flow of blow-by gases. Experimental observations (see Figure 3.73) showed that blow-by gases drive the oil from the lands all the way through the ring gaps. In Figure 3.73, one can see that oil accumulated on the second land is transported into the second ring gap region. Moreover, it can be noticed that no significant oil accumulation was detected on the third land below the scraper ring gap. The fact that liquid oil was not detected downstream of the gap shows that oil did not exit the gap as a liquid layer. It is believed that oil entering the gap breaks

down into an oil mist as it flows through the gap with the high velocity gas stream[1]. The breakdown of the oil layer into an oil mist, which was proposed from observation of the oil distribution around the scraper ring gap, may also occur at the top ring gap where the blow-by gases flow at higher velocity. Observations of the oil distribution around the OCR gap did not provide any insight on mist formation since there is always a large quantity of oil accumulated in the chamfer located right below the OCR.

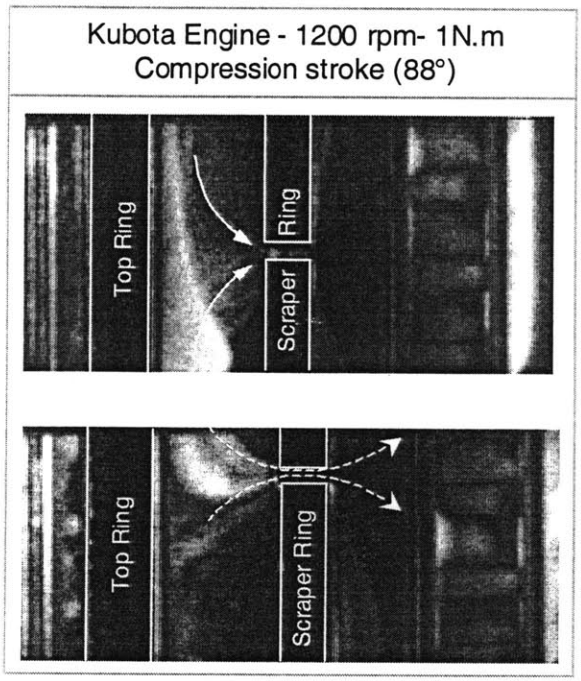


Figure 3.73 – Oil flow through the second ring gap and mist formation observed in the Kubota engine.

Gas dragging action upstream of the gap: The action of the blow-by gases on the oil covering the lands was found to result from the shear stress applied by the gases at the surface of the oil layer. Assuming that the gas flow was a one-dimensional fully developed Poiseuille flow and the oil flow a one-dimensional fully developed Couette flow, the oil flow rate induced by the gas dragging action was evaluated by the following equation (from Equation 3.47):

$$Q_{oil} = Q_{gas} \cdot \frac{3 \cdot \mu_{air}}{\mu_{oil}} \cdot \frac{\tilde{h}_{oil}^2}{h_{ld}^2} \tag{3.67}$$

With Q_{oil}: cumulative oil flow from one gap to another over one cycle (m^3/cycle)

Q_{gas}: cumulative gas flow from one gap to another over one cycle (m^3/cycle)

[1] because the volumetric concentration of dye in an oil mist is much lower than in a liquid layer, fluorescence emitted from an oil mist could not be detected with the equipment used in this project.

$\tilde{h}_{oil}$: average thickness of the oil layer covering the land (m)

h_{ld}: clearance between the land and the liner

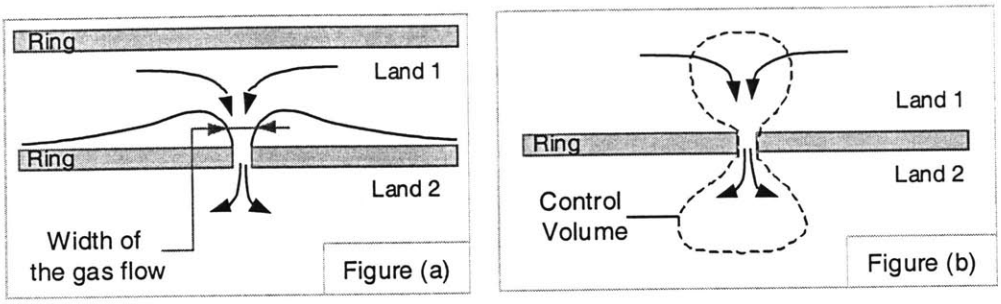


Figure 3.74 – Left figure: width of the gas flow close to the gap.
Right figure: description of the oil control volume used to
compute the rate of oil transport at the gaps.

The oil flow rate given by Equation 3.67 assumes that the convection of the gas momentum is negligible and that the gas flow is laminar. As it is described on Figure 3.74a, as gases approach a gap, the width of the flow shrinks down to the width of the ring gap. The reduction of the gas flow width has two consequences on the gas flow structure. First of all, as the flow width shrinks, the momentum convection becomes dominant over the viscous dissipation. Consequently, the gas velocity gradient right above the oil surface increases and so does the shear stress exerted on the oil layer. Second, as the flow section decreases, the flow accelerates and therefore the Reynolds number increases. Right before the gap, the Reynolds number can be as high as 50000. Consequently, the gas flow becomes turbulent and the dragging action is enhanced. Overall, we can say that in the region where the width of the gas flow shrinks, the shear stress exerted by the blow-by gases is underestimated when using the Poiseuille flow assumption. As a result, in the region close to the ring gaps, the oil flow rate resulting from the gas dragging action is larger than the one predicted by Equation 3.67, and thus, larger than the oil flow rate in areas located away from the gaps.

The enhancement of the gas dragging action in the regions located upstream of the gaps has two major consequences on the oil distribution and transport (when the reverse blow-by is negligible):

1. The oil layer covering the lands becomes thinner and thinner as it gets closer to the ring gaps.
2. The presence of the gaps does not restrict the rate at which oil is removed from the piston lands by the dragging action of the blow-by gases, and therefore, oil should not accumulate upstream of the ring gaps.

This result was confirmed by many of the oil distribution observations conducted in the Kubota engine. In most cases where one ring gap was in the viewing area, due to the enhancement of the gas-

driven oil removal no or very little oil could be detected on the areas of the lands adjacent to the ring gap. Figure 3.75 shows the oil distribution around the OCR gap of the Kubota engine at 1200 rpm 1N.m load. As one can see no oil had accumulated upstream of the OCR gap. On the oil distribution images shown in Figure 3.73, the large oil accumulation that can be seen in front of the scraper ring gap existed before the ring gap rotated in the viewing area and is therefore not related to the presence of the gap.

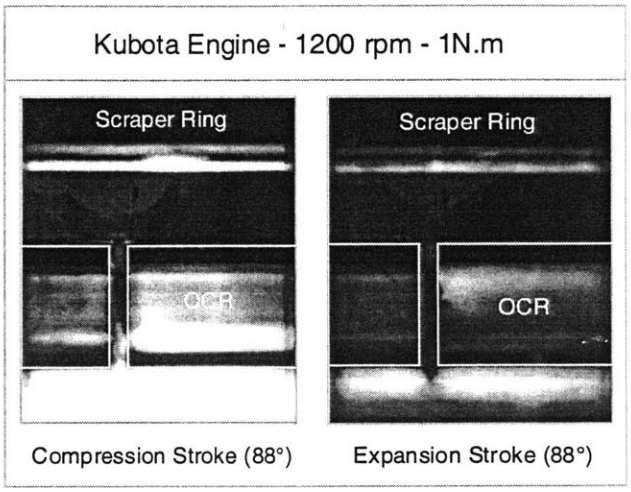


Figure 3.75 – OCR gap observed in the Kubota engine.

Oil entrainment in the gas stream: Since experimental data showed that oil could be transported out of the ring gap as an oil mist, it was clear that oil was entrained in the gas stream either in the gap area or in the region located upstream of the gap. We first looked at the likelihood of oil lying on the land to be entrained in the gas flow. Four correlations for the onset of droplet entrainment from a thin liquid film were found in the literature [57, 58, 59, 60]. All of them mentioned that there is a critical Reynolds number for the liquid phase below which droplets can not separate from the liquid film. The minimum critical Reynolds numbers were reported by Ishii [61] and Hewitt [59]:

$$\text{Ishii: } \mathrm{Re}_c = \frac{\tilde{h}_l \cdot \tilde{u}_l}{\upsilon_l} \sim 160$$

$$\text{Hewitt: } \mathrm{Re}_c = \frac{\tilde{h}_l \cdot \tilde{u}_l}{\upsilon_l} \sim 155$$

With $\tilde{h}_l$: average thickness of the liquid film (m)

$\tilde{u}_l$: average velocity of the liquid film (m/s)

Estimation of the average oil layer velocity showed than even near the ring gaps where the gas dragging effect reach its maximum, the Reynolds number of the oil film can never reach value as high as 150. Consequently, it can be concluded that the entertainment of oil into the gas stream only occurs inside the ring gaps. Due to the complex geometry formed with the ring gaps and the grooves, the existing correlations on liquid entrainment could not be used to characterize the interactions between the high velocity gas flow and the oil dragged into the ring gaps. Consequently, the mist formation process was not further investigated.

Oil flow out of gap: Once oil enters a ring gap, oil may either accumulate in the volume defined by the ring gap and the groove or be entrained across the gap by the high velocity gas stream. Because no oil accumulation was ever observed in the top two ring gaps, it is believed that most part of the oil entering one of the top two ring gaps is entrained in the gas flow and flows with the gas stream. The droplets of oil exiting the gaps can either be transported along with the gas stream or deposited on the land and the liner. The deposition rate of oil droplets depends on the gas flow structure and size and velocity of the droplets.

The complete picture on the mechanism of gas-driven oil transport through the ring gaps that is described above is summarized in Figure 3.76.

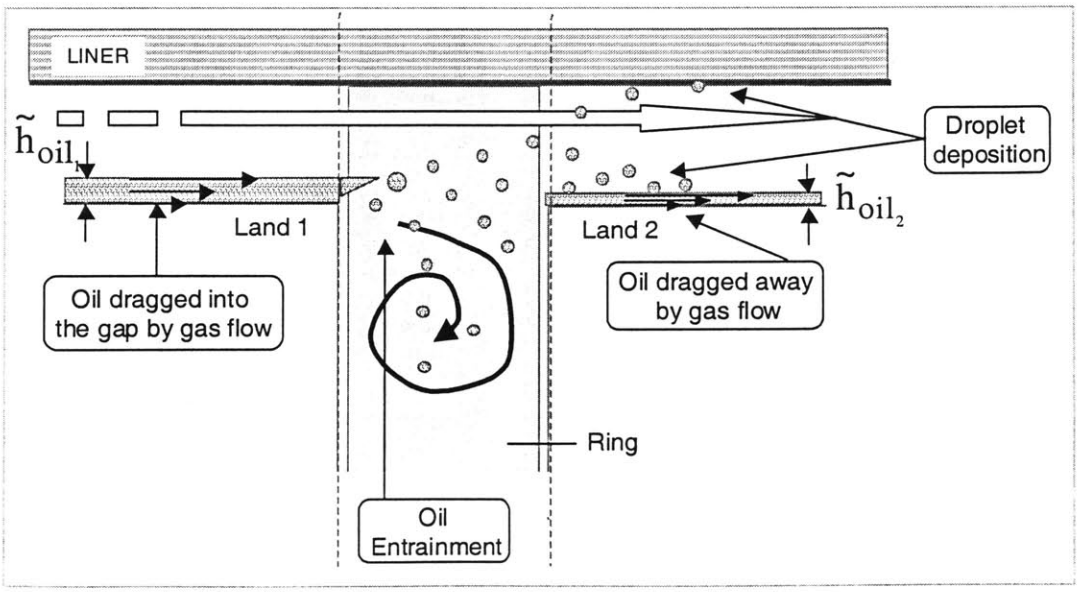


Figure 3.76 – Description of the gas-driven mechanism of oil transport through the ring gaps.

Net oil flow through the ring gaps: Assuming that there is no oil accumulation in the ring gap areas, the net amount of oil transported through each ring gap every cycle can be evaluated by using a control volume as defined on Figure 3.74b. This control volume is defined far enough from the gap so that the rate of oil transport across the borders of the control volume can be estimated by Equation 3.67. Furthermore, it is defined close enough from the gap so that it can be considered than oil does not accumulate inside the control volume. Accordingly, the net oil transport through the ring gaps may be estimated by the following equation (notation refers to Figure 3.76 and 3.74b):

$$Q_{\text{oil_thg_gap}} = Q_{\text{g_ld 1to ld2}} \cdot \frac{3.\mu_{air}}{h_{ld_1}^2 \cdot \mu_{oil}} \cdot \tilde{h}_{\text{oil}1}^2 - Q_{\text{g_ ld 2to ld1}} \cdot \frac{3.\mu_{air}}{h_{ld_2}^2 \cdot \mu_{oil}} \cdot \tilde{h}_{\text{oil}2}^2 \qquad (3.68)$$

With $Q_{oil_thg_gap}$: Net oil transport through the gap per cycle (m^3/cycle)

$Q_{g_ld1\ to\ ld2}$: Total volume of gas flowing from land 1 to land 2 per cycle (m^3/cycle)

$Q_{g_ld2\ to\ ld1}$: Total volume of gas flowing from land 2 to land 1 per cycle (m^3/cycle)

$\tilde{h}_{oil_1}$: Average thickness of the oil layer covering land 1 (m)

$\tilde{h}_{oil_2}$: Average thickness of the oil layer covering land 2 (m)

h_{ld_1} : Clearance between land 1 and the liner (m)

h_{ld_2} : Clearance between land 2 and the liner (m)

If lands 1 and 2 are defined such that in average the blow-by gases flow from land 1 to 2, $Q_{g_ld2\ to\ ld1}$ will be called reverse blow-by. When the amount of reverse blow-by $Q_{g_ld2\ to\ ld1}$ is negligible, $Q_{g_ld1\ to\ ld2}$ is approximately equal to the average flow rate of gases going through the ring gap Q_{gas} (see Equation 3.67). Accordingly, the amount of oil that is driven through the ring gap $Q_{oil_thg_gap}$ is roughly equal to the amount of oil from land 1 dragged toward the ring gap Q_{oil} (see Equation 3.67). Gas flow simulations conducted with RINGPACK-OC showed that for diesel engines and spark ignition engines running at more than half load, the flow rate of reverse blow-by is usually negligible compare to the average blow-by. Therefore, in these situations, the amount of oil transported through the ring gaps is roughly equal to the amount of oil removed from the upstream piston lands by the dragging action of the circumferential gas flows.

3.4.1.2 Inertia driven flow

During experiments conducted at low load in the PSA engine, it was often observed that oil was supplied to the third land through the OCR gap at a relatively high flow rate. In these conditions, the blow-by gases were flowing toward the crankcase and the reverse blow-by was too small to explain the rate at which oil was transported from the skirt region to the third land. For instance, in Figure 3.77, which shows the oil distribution on the third land during compression stroke at 4500 rpm 300 mbar AIP, one can see that a large amount of oil that was supplied through the OCR gap and had accumulated on the third land. It is believed that this oil was transported though the OCR gap by the action of the inertia force.

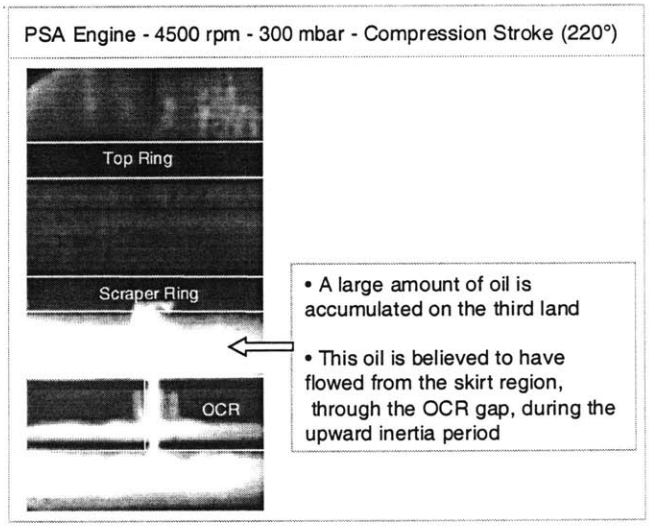


Figure 3.77 – Large oil accumulation observed above the OCR gap in the PSA engine running at low load.

In most cases, the region right below the OCR was observed to be fully flooded with oil. Consequently, during the upward inertia period, oil located in the chamfer below the OCR can move to the third land. This type of oil transport can only occur if one side of the gap is partly flooded with oil and therefore can only take place at the OCR gap during upward inertia period. Furthermore, this type of oil transport requires the OCR gap to be fully or partly flooded with oil. Consequently, it can not occur when the flow of blow-by gases is strong enough to clear the OCR gap (see Figure 3.75). Finally, this type of transport requires a straight open path from the skirt region to the third land and thus can only exist when a twin-land OCR is used.

The rate at which oil may be transported to the third land by this mechanism was estimated assuming that the oil flow was a fully developed viscous flow. The geometry of the oil passage formed by the ring gap and the groove is complex. For simplicity, the oil flow rate was estimated assuming that the

oil passage was a round tube of section equal the area of the OCR gap opened to the third land. For a Poiseuille flow driven by a body force through a round tube, the following relationship can be derived [Mills]:

$$q_{oil} = \frac{D_h^2 \cdot A}{\mu_{oil} \cdot 32}(f_i) \tag{3.69}$$

With q_{oil}: oil flow rate (m^3/s)

D_h: hydraulic diameter

A: section of the tube

f_i: body force ($kg.m^{-2}.s^{-2}$)

Replacing A and f_i by the variables specific to this problem, Equation 3.69 becomes:

$$q_{oil} = \frac{D_h^2 \cdot h_{ld3} \cdot d_{g3}}{\mu_{oil} \cdot 32}(-\rho_{oil} \cdot a_p) \tag{3.70}$$

With h_{ld3}: clearance between the third land and the liner (m)

d_{g3}: size of the OCR gap (m)

a_p: piston acceleration (m/s^2)

Using the geometry of the PSA engine and the average inertia force at 3500 rpm, and assuming that this oil transport was taking place for about half the engine cycle, the amount of oil transported to the third land was estimated to be about 2500 μg/cycle. This number, which is two order of magnitude above the typical oil consumption rate for one cylinder (40 μg/cycle), it probably largely overestimated since is assumes that the OCR is fully flooded with oil. However, this estimation shows that in SI engines running at low load the inertia force can be responsible for a large portion of the oil supply to the third land when a twin-land OCR is used.

3.4.2 Low load and closed throttle situations

3.4.2.1 Low load engine operation

The low load situations described here refer to spark ignition engines only. The experimental data used to investigate oil transport through the ring gaps in low load situations were acquired in the PSA engine at 300-mbar absolute intake pressure (AIP). For reference, at 300 mbar AIP, a 2-liters spark-ignited engine output a small but positive torque. In these running conditions, the average blow-by flows toward the crankcase. But since the cylinder pressure is significantly lower than the crankcase

pressure during more than 25% of the engine cycle, the amount of reverse blow-by is not negligible. From Equation 3.68, it can be seen that the direction of the net oil flux through the ring gaps depends on the relative values of:

- the forward and reverse blow-by
- the land/liner clearance on both lands
- the average oil thickness on both lands.

Correspondingly, the net oil flow may or may not be in the same direction as the net gas flow.

Top ring gap: The rate of gas-driven oil transports on the lands and through the gaps is function of the volumetric gas flow rate. Except, in closed throttle operation (intake manifold pressure ~ 200 mbar or lower), the net mass flow of gases through the top ring gap always goes from the crown land to the second land. However, blow-by gases flow from the crown to the second land during the period where the combustion chamber is pressurized and back to the crown land when the pressure on the second land and the combustion chamber is low. Consequently, the net volumetric flow rate can go from the second land to the combustion chamber while the net mass flow rate goes in the opposite direction. Calculations conducted for the PSA engine with the RINGPACK-OC code showed that the net volumetric gas flow through the top ring gap was positive (toward the crankcase) from WOT down to 500~600 mbar AIP. Below 500~600 mbar AIP, the net volumetric gas flow through the top ring gap was found to be negative (the pressure upstream of the gap was used to compute the volumetric gas flow rate).

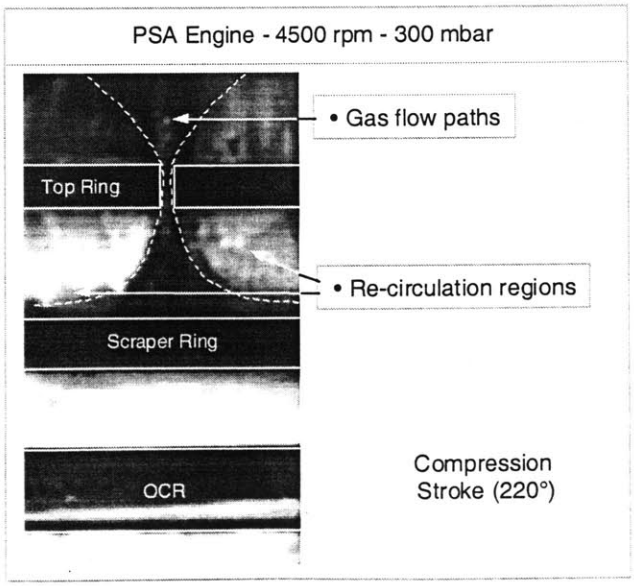


Figure 3.78 – Top ring gap observed at low load in the PSA engine.

Images of the oil distribution around the top ring gap were acquired at 4500 rpm 300 mbar AIP while the net volumetric flow through the gap was going from the second to the crown land at a rate of $5.3.10^{-7}$ m^3/cycle. From Figure 3.78, we can see no significant oil accumulation was detected on the crown or the second land on the path of the blow-by gases. Therefore, it is believed that because there was no oil available on the lands neither the blow-by nor the reverse blow-by were carrying any significant amount of oil through the gap. From simulation results it was found that even though the average volumetric gas flow at the gap was going from the second to crown land, the average volumetric gas flow on the second land was going from the top to the second ring gap at a rate of 3.10^{-7} m^3/cycle. Accordingly, the fact that there was no oil the region on the second land located below the top ring gap can be explained by the direction of the circumferential oil flow.

Overall, we can conclude that the fact that the net volumetric blow-by flow through the top ring gap goes toward the combustion chamber at low engine load does not generate oil transport from the second to the crown land. This conclusion is valid as long as the average gas flow on the second land goes toward the crankcase and thus drags the oil away from the top ring gap.

Scraper ring gap: Because the upward and downward gas flows through the scraper ring gap occur with gases of similar densities, the net volumetric gas flow through the second ring gap is usually in the same direction as the net mass gas flow. However, the amount of oil lying on the third land may be much larger than the amount of oil on the second land, in which case $\tilde{h}_{oil_2}$ is greater than $\tilde{h}_{oil_1}$.

From Equation 3.68, one can see that the net oil flow through the scraper ring gap may goes from the third land to the second land while the average volumetric blow-by flow goes from the second to the third land.

This situation was observed in the PSA engine at 2500, 3500 and 4500 rpm 300 mbar AIP. First of all, Figure 3.79 shows the evolution of the oil distribution on the second land of the PSA engine recorded while the engine was running at 4500 rpm 300 mbar AIP. In these conditions the blow-by gases were flowing toward the crankcase at about 4.5 liter/min. On the sequence of images of Figure 3.79, it can be clearly seen that 1) the oil layer on the third land was much thicker than the one on the second land, 2) that oil was transported through the scraper ring gap from the third to the second land. Second, Figure 3.80 shows the evolution of the oil distribution on the second and third land of the PSA engine at 2500 rpm 300 mbar AIP. On the first image of Figure 3.80, there is little oil on the third land and correspondingly little oil above the scraper ring gap. From image 2 to 5 (cycle 2 to 5), an oil accumulation was building up below the scraper gap. As a result, we can see that once oil was available below the scraper ring gap, oil was transported with the reverse blow-by onto the second

land. Finally, in Figure 3.81, which shows the evolution of oil distribution on the second land at 3500 rpm low load, one can see that oil transported through the scraper ring gap deposits on the second land. In the three examples described above, the average volumetric gas flow on the second land was flowing from the top ring gap to the scraper ring gap. Accordingly, oil lying on the second land was dragged toward the scraper ring gap. Moreover, in these three cases the reverse blow-by was carrying some oil from the third to the second land. Therefore, the net oil flow at the gap was limited by the effect of the reverse blow-by and as a consequence oil could accumulate above the scraper ring gap. This was confirmed by the experimental observations presented in Figures 3.79 and 3.80. In both cases, the amount of oil accumulated on the second land around the scraper ring gap was found to increase cycle after cycle. In the case of Figure 3.79, the ring was rotating and as a consequence the oil transported by the reverse blow-by was spread over the second land.

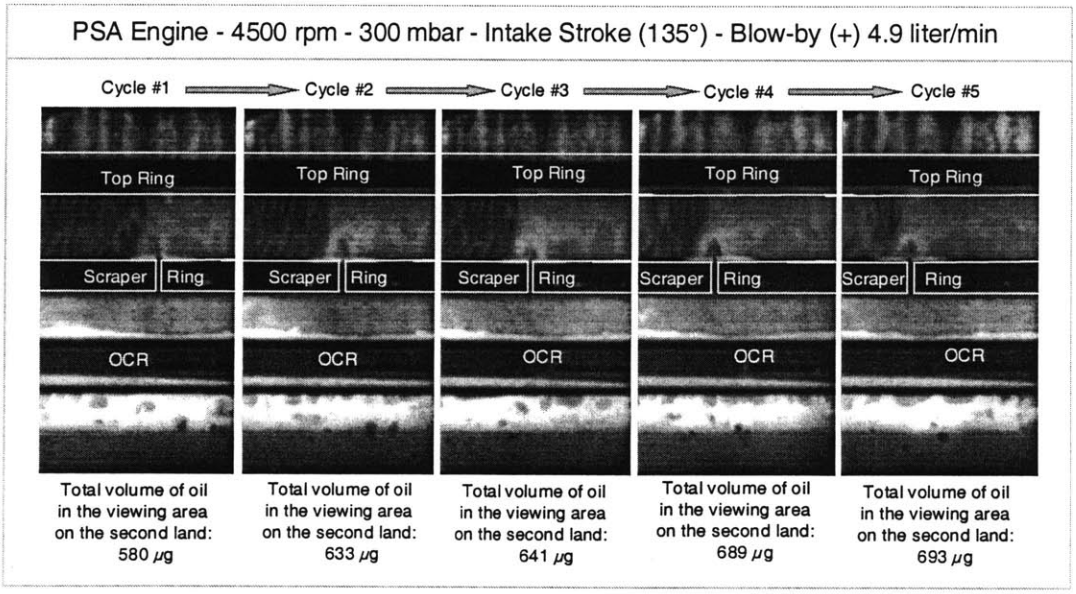


Figure 3.79 – Oil flow from the third to the second land observed at the second ring gap in the PSA engine running at low load (4500 rpm).

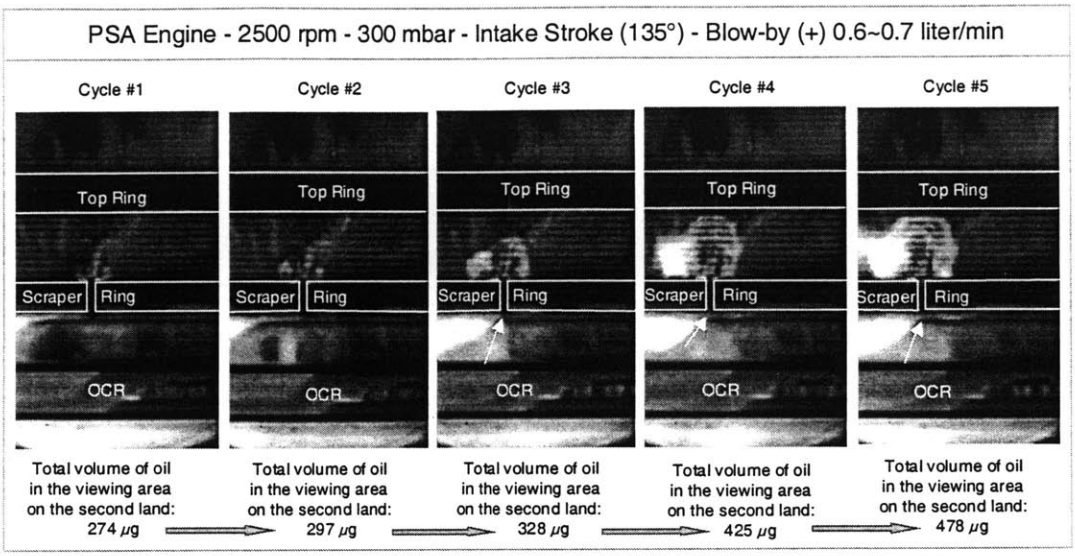


Figure 3.80 – Oil flow from the third to the second land observed at the second ring gap in the PSA engine running at low load (2500 rpm).

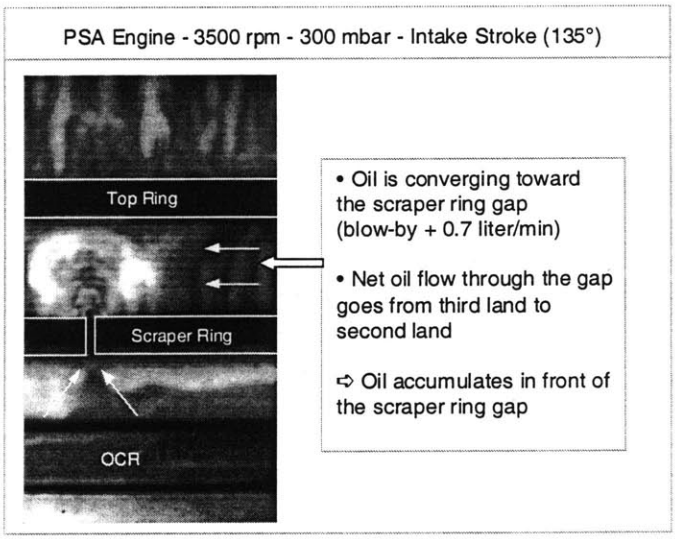


Figure 3.81 – Oil flow from the third to the second land observed at the second ring gap in the PSA engine running at low load (3500 rpm).

Oil control ring gap: Since the thickness of the oil accumulation below the OCR is always greater than the thickness of the oil layer covering the third land, the reverse blow-by may transport oil upward through the OCR gap as it does through the scraper ring gap. However, it is believed that in low load condition, the main mode of oil transported to the third land is the inertia-driven mechanism described in Section 3.4.1.2.

3.4.1.2 Closed throttle situation

As it is explained in Section 2.2.1, in passenger car engines closed or nearly closed throttle engine operations, which leads to intake manifold pressure of 200 bar or lower, are only encountered for short periods of time. With such intake manifold pressure, the blow-by is usually negative and as a result the gases flowing through the piston ring pack drag oil around the lands and through the gaps from the skirt region all the way to the combustion chamber.

Observations of the oil distribution conducted at 4500 rpm during transient from 700 to 200 mbar AIP showed that the oil flow on the lands and through the gap was changing direction at the time the throttle was closed. Once the reverse flow of blow-by gases was established, oil was seen flowing from the skirt region to the upper part of the piston mainly through the ring gaps. It was observed that the longer the engine runs with closed throttle, the more oil accumulates on the third, second and finally crown land. Since it takes more than a few seconds for the oil to travel from gap to gap all the way to the crown land, we can conclude that the dramatic effect on oil consumption of the reverse oil flow trough the ring gaps depends on the duration of the period during which the throttle position is maintained. For instance, during the transient operation tested in this work, the oil accumulation on the crown land was found to dramatically increase 4 to 7 seconds after the throttle was closed. If the throttle was maintained closed for more than 30 seconds to a minute, the oil accumulations on the piston lands were observed to reach such levels that the rings lost any ability to regulate the oil flow through the grooves.

We can conclude that in closed or nearly closed throttle engine operation, the reverse oil flow driven by the reverse blow-by through the ring gaps becomes the main mechanism of oil supply to the piston lands. Moreover, the rate at which oil is carried up the ring pack is significantly greater than in normal engine operating conditions. Finally, we can say that the time required for oil to reach the crown land, a few seconds, is in the same order of magnitude than the time during which passenger car engine usually operates with a close or nearly close throttle.

CHAPTER 4. OIL TRANSPORT ROUTES IN THE PISTON RING PACK

4.1 Dividing the Ring Pack into Three Regions

The purpose of the oil transport process occurring in the piston ring pack is to supply a controlled amount of lubricant to areas that are critical in terms of lubrication requirements, namely the liner and the top ring groove. A minimum liner oil film thickness is required to allow hydrodynamic lubrication to occur and therefore to limit friction and wear. Oil is needed in the top ring groove to lubricate the ring/groove contact and to enhance heat flux from the piston to the liner. Continuous oil oxidation process occurring above 150°C and the resulting risk of ring sticking impose a limit on the oil residence time in the top ring groove. Consequently, to ensure minimum lubricant refreshment rate oil must be continuously supplied to the top ring grove region. Eventually, the amount of oil supplied to the critical regions must be limited in order to control the oil loss to the combustion chamber and thus oil consumption.

In order to describe the main paths of oil transport and define a mass-conserving oil transport scheme, the piston ring pack was divided into three regions. The regions were defined according to the ring pack geometry and the specific function of the region components in the ring pack lubrication process (see Figure 4.1).

- Region 1: Region 1 includes the upper half of the OCR and its groove, the third land, the lower half of the scraper ring and its groove and the portion of the liner located between the upper rail/land of the OCR and the scraper ring. Region 1 is located between the oil supplying region (upper piston skirt) and the upper ring pack (second land and above). Accordingly, oil transports in Region 1 determine the oil supply to the part of the liner and the ring pack located above the scraper ring. In particular, the various elements of Region 1 control the thickness of the oil film left on the liner for the lubrication of the top ring running surface.
- Region 2: Region 2 includes the upper half of the second ring and its groove, the second land and the lower half of the top ring and its groove. Oil transports in Region 2 determines the lubrication condition of the top ring and its groove and the amount of oil supplied to Region 3.
- Region 3: Region 3 includes the upper half of the top ring and the crown land. Region 3, which has no function in terms of lubrication, is the area of the ring pack where oil transported along the piston is lost to the combustion chamber.

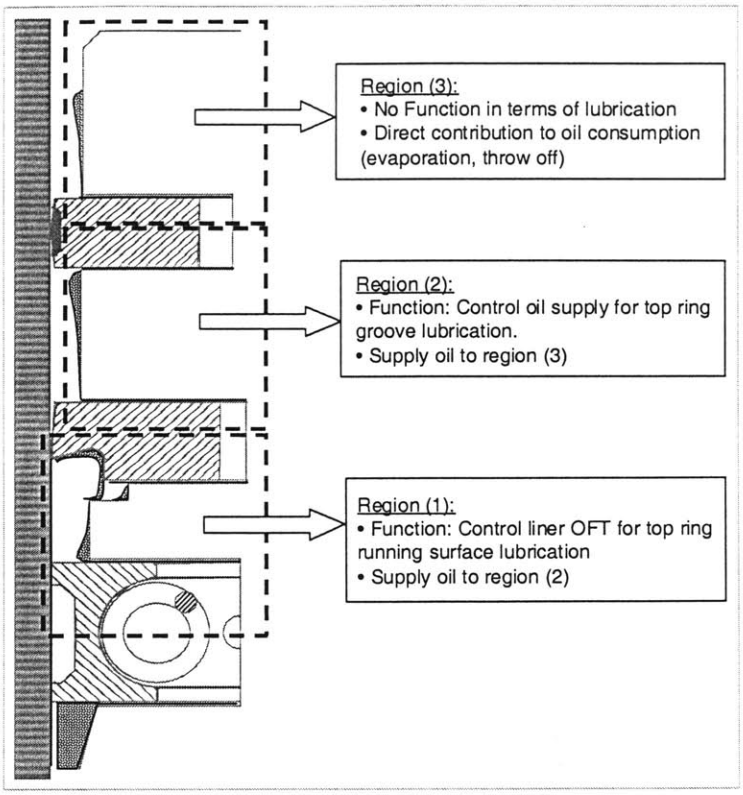


Figure 4.1 – Definition of the ring pack regions.

In this chapter, the effects of ring/piston design and engine operating conditions on the relative importance of the different oil routes and oil transport rates were discussed. Furthermore, the oil transport routes within and between the different regions were described in terms of their contribution to oil consumption and to the fulfillment of the critical lubrication objectives.

Finally, in this analysis the oil reservoir located below Region 1, namely the lower half of the OCR and its groove and the upper part of the piston skirt, was considered to always provide a non-restricted oil supply to both the OCR/liner interface and the OCR/groove upper clearance. The validity of this assumption was confirmed by every experimental observations of oil distribution carried in this project. Accordingly, oil transports in this region was not discussed. For information, oil supplied to this region is transported from the lower part of the liner by the piston primary and secondary motion and has two origins.

1- Oil coming from the connecting rod end bearings that has impinged on the liner.
2- Oil coming from the piston cooling jet.

4.2 Region 1: Controlling the Oil Supply to the Upper Ring Pack

4.2.1 Oil Supply

Experimental observations showed that the oil supplied to Region 1 was coming from the piston skirt region and was flowing through three different paths:

1- First of all, in most engine operating conditions oil was found to be supplied to the third land by the squeezing action of the OCR pushing oil out of the upper side of its groove. The rate at which this transport mechanism supplies lubricant to the third land depends on the OCR dynamics and on the supply of oil to the upper clearance of the OCR and its groove. Consequently, it is strongly dependent on the ability of the OCR to seal the upper ring/groove clearance.

2- If the thickness of the oil film left on the liner by the OCR during downward stroke is greater than the oil thickness left by the scraper ring at the same liner location, oil accumulates on the lower side of the scraper ring. The amount of oil accumulated against the scraper ring constitutes a net oil supply to Region 1. The amount of oil scraped from the liner by the second ring can be considered as an excess of oil left by the OCR. This amount of oil depends on the lubrication condition between the upper rail/land of the OCR and the liner and on the size of the converging region of the scraper ring running surface. In the case where the second ring is a Napier ring, the excess of oil removed from the liner by the scraper ring temporarily accumulates in the hook.

3- Eventually, for the particular case of spark ignition engines running at low load, it was found that oil flowing from the upper skirt region to third land through the OCR gap could constitute a major mode of oil supply to Region 1.

The remaining part of the oil supplied to Region 1 comes from the second land and is transported through the scraper ring gap by the stream of blow-by gases. The rate at which this type of oil transport supplies oil to the third land area is mainly determined by the oil transport balance in Region 2 and is therefore discussed in Section 4.3.

In the three following sections, experimental data obtained in this project and results from the modeling work previously conducted by T.Tian [14, 26, 33] were combined to describe how the three most common OCR designs affect the oil supply to Region 1 through the OCR groove and the OCR/liner interface. Since a large portion of the experimental work done in this work was conducted with twin-land OCRs, oil transports around this type of OCR were given a more detailed description.

In Section 4.2.1.4, the effect of the OCR design on oil supply through the OCR gap(s) in spark ignition engine running at low load is discussed.

4.2.1.1 Twin-Land Oil Control Ring

Oil supply at the ring/liner interface: As it was described by T.Tian [27], the position of the twin-land OCR relative to the liner is a function of the ring twist and the piston tilt. Accordingly, the distance between each land and the liner varies along the circumference of the piston. Figure 4.2 shows the piston tilt and the land/liner clearances computed for PSA engine running at 2500 rpm 500 mbar AIP. The piston tilt was computed using a piston secondary motion model developed in the Sloan Automotive Lab by C.McNally [62] and improved by L.Liu. The position of the OCR relative to the liner was computed with a model developed by T.Tian [27]. As one can see on the lower plot of Figure 4.2, on the anti-thrust side during intake stroke and most part of expansion stroke the upper land of the OCR is further away from the liner than the lower land. Consequently, oil accumulated between the two lands of the OCR can be released on the liner during the downward stroke. This phenomena may be particularly significant during the early part of intake stroke where the gap open between the upper land and the liner reach 1.65 μm, and where the inertia force pushes oil upward making the leading edge of the upper land fully flooded. As a result, during the early part of intake stroke, the twin-land OCR is very likely to leave an excessively thick oil film on the liner. Due to the limited size of the converging region of the scraper ring, the excess of oil left by the OCR will be scraped off from the liner by the scraper ring. In Figure 4.3, which shows the computed wetting conditions of the scraper ring, it can be seen that the leading edge of the second ring becomes fully flooded during intake stroke and thus that oil removed from the liner accumulates against the lower side of the scraper ring. Oil removed from the liner will be transported to the third land or to the hook in the case of a Napier ring and thus constitutes a net oil supply to Region 1. Consequently, from the simulation results it can be concluded that the design of the twin-land OCR and its dynamics favor oil supply to Region 1 through the OCR/liner interface. This oil supply mechanism, which results from the piston tilt action on the ring position relative to the liner can only happen on the anti-thrust side of the piston.

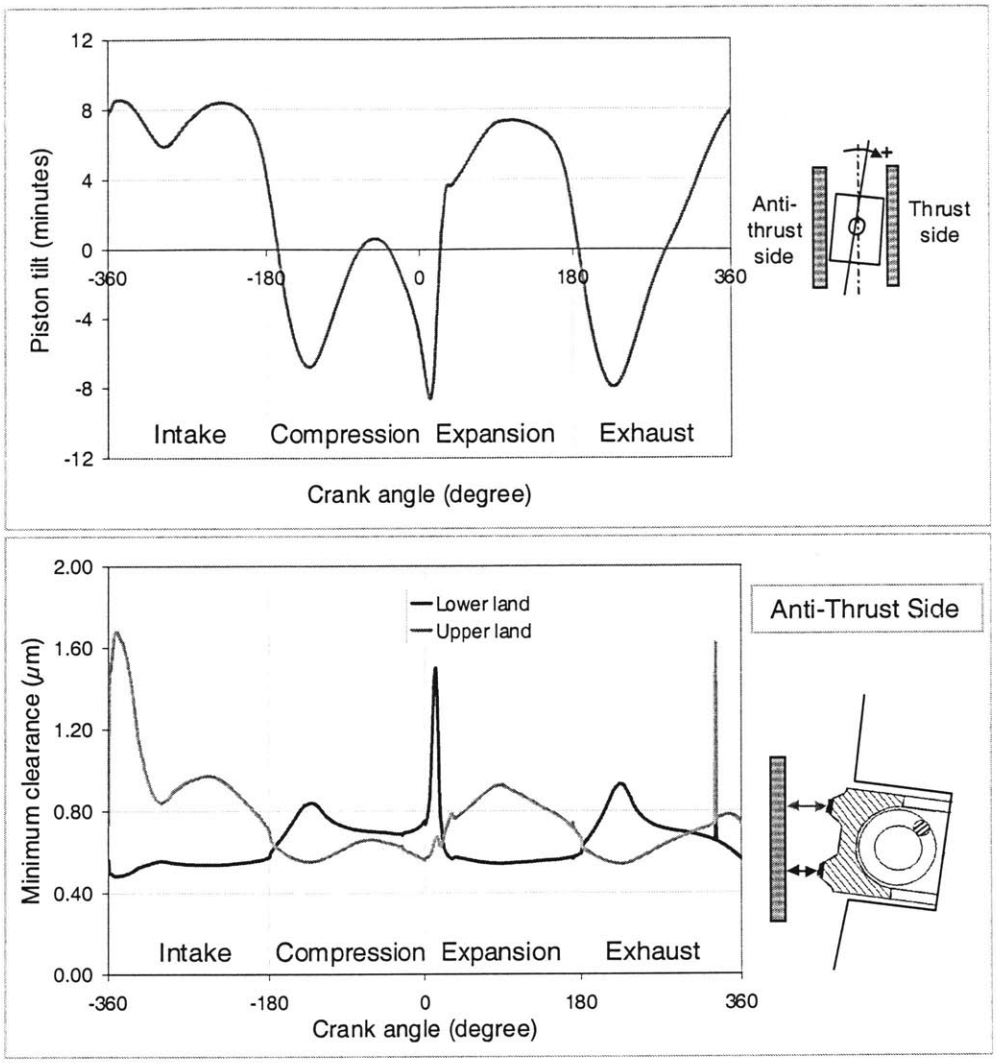


Figure 4.2 – Piston tilt and land/liner clearances of the twin-land OCR, calculated for the PSA engine running at 2500 rpm 500-mbar intake pressure.

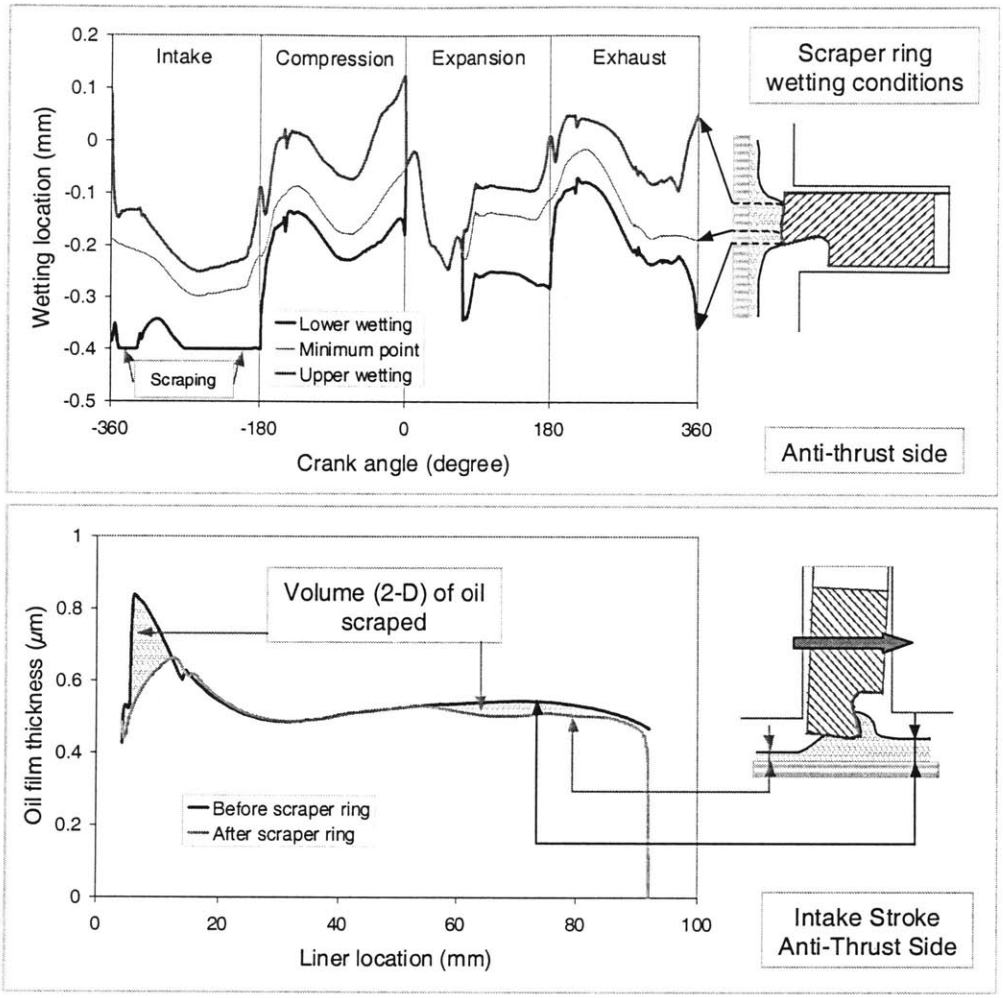


Figure 4.3 – Wetting conditions of the scraper ring when used with a twin-land OCR, calculated for the PSA engine at 2500 rpm 500-mbar intake pressure.

Oil scraping resulting from the combine use of a twin-land OCR and a scraper ring was observed in both the Kubota and the PSA engine. Figure 4.4 shows an image of the oil distribution acquired in the PSA engine on the anti-thrust side of the piston ring pack. As one can see, oil scraped off the liner during the early part of intake stroke formed an oil accumulation at the leading edge of the scraper ring. On the LIF image of Figure 4.5, which was acquired during intake stroke on the anti-thrust side of the Kubota piston ring pack, one can see that oil left on the liner by the twin-land OCR is scraped off from the liner and accumulates in the hook of the Napier ring.

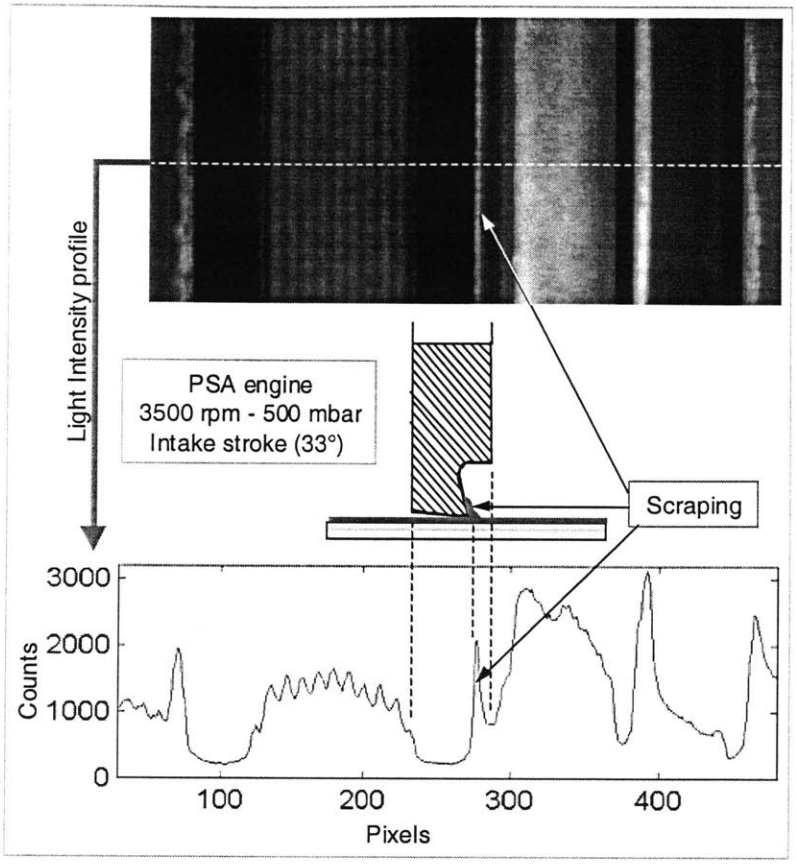


Figure 4.4 – Second ring scraping observed in the PSA engine.

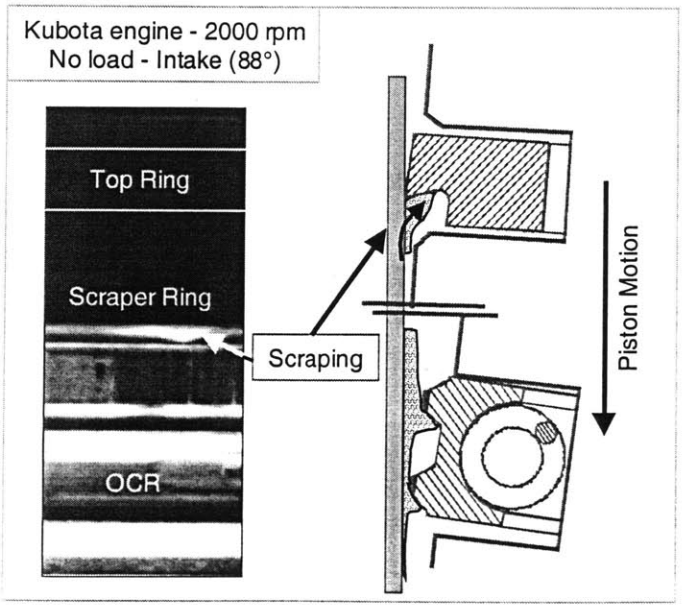


Figure 4.5 – Second ring scraping observed in the Kubota engine.

The effect of the oil supply through the OCR/liner interface on the third land oil accumulation was demonstrated by testing twin-land OCRs of three different tensions in the Kubota engine. During these tests the calibration operations were not conducted. As a consequence, the fluorescence intensity could not be translated into oil film thickness. However, since the settings of the optical setup were maintained constant for all the tests, the level of fluorescence intensity was a reliable indication of the relative amount of oil accumulated on the piston lands. Accordingly, the average level of fluorescence intensity (photon counts) on the second and third lands was calculated for the three sets of tests (see Figure 4.6). To eliminate the influence of pulse-to-pulse laser intensity variations, the numbers were averaged over 50 consecutively acquired images. The results obtained are presented in the table of Figure 4.6. It can be seen that decreasing the OCR tension significantly increased the amount of oil accumulated in the third land region. Since decreasing the ring tension reduces the ability of the twin-land OCR to seal the ring/liner interface, the change in the third land oil accumulation shows the increase of oil supply through the OCR/liner interface. Moreover, the fact that the second land oil accumulation was not affected by the change of the OCR tension shows that the additional oil left on the liner by the OCR was transported to the third land region by the scraping action of the second ring. Quantitatively, the change in the average fluorescence intensity shows that the amount of oil accumulated on the third land could change by roughly 50% by changing the OCR tension by 30%. Overall, it can be concluded that when a twin-land OCR is used, the scraping of excess of oil left on the anti-thrust side of the liner during intake or expansion stroke can constitute one of the major oil supply to the third land region (Region1).

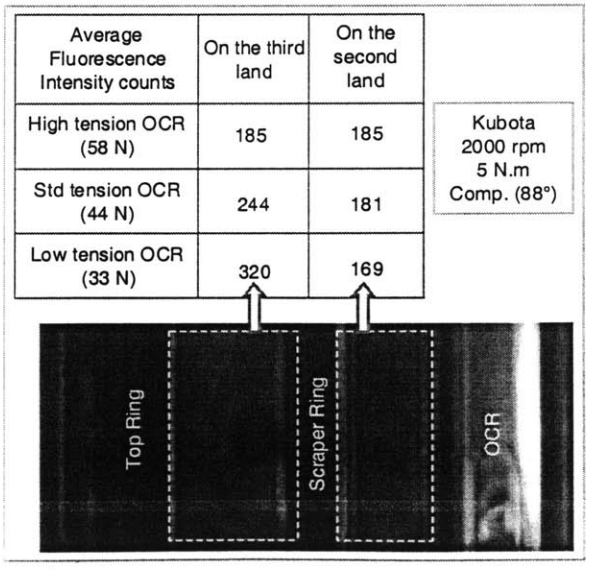


Figure 4.6 – Effect of the twin-land OCR tension on the second and third land oil accumulation (observed in the Kubota engine).

Oil supply through the ring groove: Oil leaking from the OCR groove onto the third land was observed in both engines during most of the conducted oil distribution observations. Examples can be seen in Figures 3.55 and 3.56. Therefore, oil flow through the OCR groove should always be considered as a significant mode of oil supply to the third land region when a twin-land OCR is used.

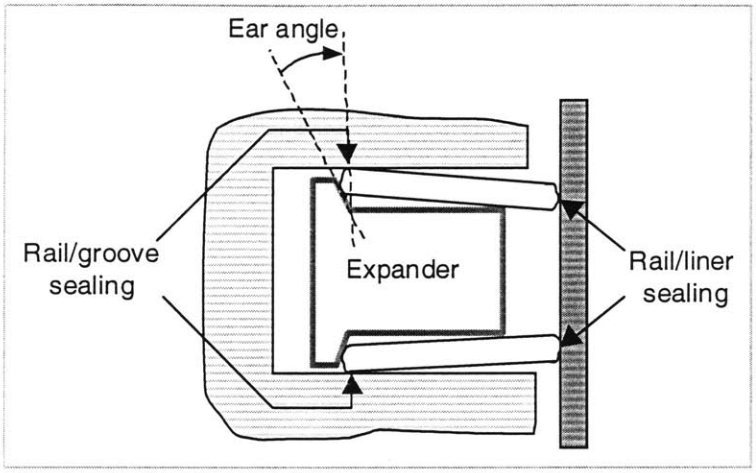


Figure 4.7 – Three-piece OCR side sealing.

4.2.1.2 Three-Piece Oil Control Ring

Oil supply through the OCR groove: As it can be seen on Figure 4.7, three-piece OCRs are designed with an ear angle to seal both the upper and the lower ring groove clearances. Due to the presence of an ear angle (see Figure 4.7) on the expander, the rails are pressed against the sides of the groove and thus prevent oil flow though the ring/groove clearance. However, in his modeling work T.Tian [25] showed that under specific engine operating conditions the inner end of the rails could move away from the groove sides. As a result, the three-piece OCR can loose its side sealing ability. In particular, T. Tian reported [25] that:

- At low engine speed, the inner end of the rail may leaves the side of the groove temporarily around the bottom and top dead centers due the sudden change of magnitude and direction of the rail/liner friction force.
- At high engine speed, the rails may move away from the groove around mid-stroke due to the sudden change of the inertia force.

When the upper rail loses contact with the groove, a gap is opened for oil to flow through the ring/groove clearance either toward the third land or toward the crankcase. Therefore, in these conditions oil may be supplied to the ring/groove clearance. T.Tian also reported that due to their low

torsional resistance, the rails exhibit a large amplitude dynamic twist. According to the position of the rails relative to the grooves, the twisting motion of the upper rail is very likely to squeeze oil trapped in the upper rail/groove clearance toward the outside of the groove. Such squeezing action would result in oil being supplied to the third land region. Therefore, from the modeling results reported by T.Tian we can conclude that when a three-piece OCR is used, depending on the engine running conditions, oil may be supplied to the upper ring pack through the OCR groove.

Oil supply through the rail/liner interface: Since the two rails of a three-piece OCR are independent, their position relative to the liner is not or little affected by the piston tilt. Consequently, if the bore distortion is limited three-piece OCR should not leave an excessively thick oil layer on the liner during downward strokes. Accordingly, oil scraping of the second ring should not constitute an significant oil supply to the third land region (Region 1). On the other hand, in his modeling work T. Tian suggested that depending on the shape of the rail running surface, oil that is left on the liner by the OCR during a downward stroke may be scraped off the bore by the upper rail during the upward strokes. In particular, T.Tian pointed out that this phenomenon was very likely to occur with new rings, or at high engine speed with expanders that have ear angles. If oil scraping by the upper rail occurs, part of the scraped oil will be transported to the third land. Therefore, we can conclude that depending of the geometry of the rail running surfaces, oil may be transported to the upper ring pack via the rail/liner clearance when a three-piece OCR is used.

A few sets of oil distribution LIF images were acquired while using a three-piece OCR. Since the amount of collected data was limited, it was not possible to study in details the effect of the three-piece OCR on oil supply to the third land region. Nevertheless, it can be reported that no significant difference in the third land oil distribution was observed when comparing the data acquired with three-piece OCRs and twin-land OCRs.

4.2.1.3 U-flex Oil Control Ring

Oil supply through the OCR groove: A U-flex OCR was tested in the Kubota engine at three different speeds (1200, 2000, 2600 rpm) and two different loads (1 N.m and 10 N.m). Images of the ring pack oil distribution were acquired for all four strokes. In all the tested engine running conditions, oil being squeezed out of the upper clearance of the OCR/groove clearance was identified on the third land during the intake stroke. In Figure 4.8, one can see the oil on the third land that was squeezed

out of the OCR groove when the ring was lifted during the second half of exhaust stroke. The squeezed oil spread upward on the third land under the effect of the inertia force. These results show that oil flow through the OCR groove may be one of the major oil supply mechanism to the third land region when a U-flex OCR is used.

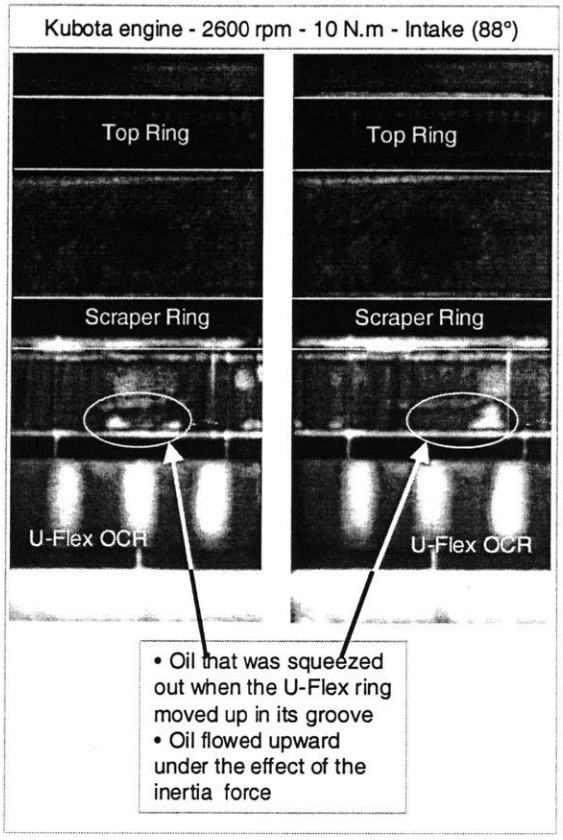


Figure 4.8 – Oil squeezed from the OCR groove to the third land, observed in the Kubota engine while using a U-flex OCR.

U-flex OCRs do not provide permanent side sealing. Therefore, it can be expected that the ring pumping/squeezing action, which results from the motion of the ring relative to its groove, will drive oil from the back of the OCR to the third land. Moreover, finite-element modeling conducted at Dana-Perfect Circle Europe showed that U-Flex rings are significantly deformed once they are assembled in the piston/liner system. As a result, the flanks of U-flex rings, which are flat when the ring is disassembled, have a wavy pattern once they are mounted in the engine (see Figure 4.9). The waviness, which is in the order of 25 μm, creates gaps through which oil and gases can easily flow during engine operations. The reduced side sealing ability of U-Flex ring resulting from the flank waviness may enhance oil flow through the ring groove and thus oil supply to the third land region via the OCR/groove clearance.

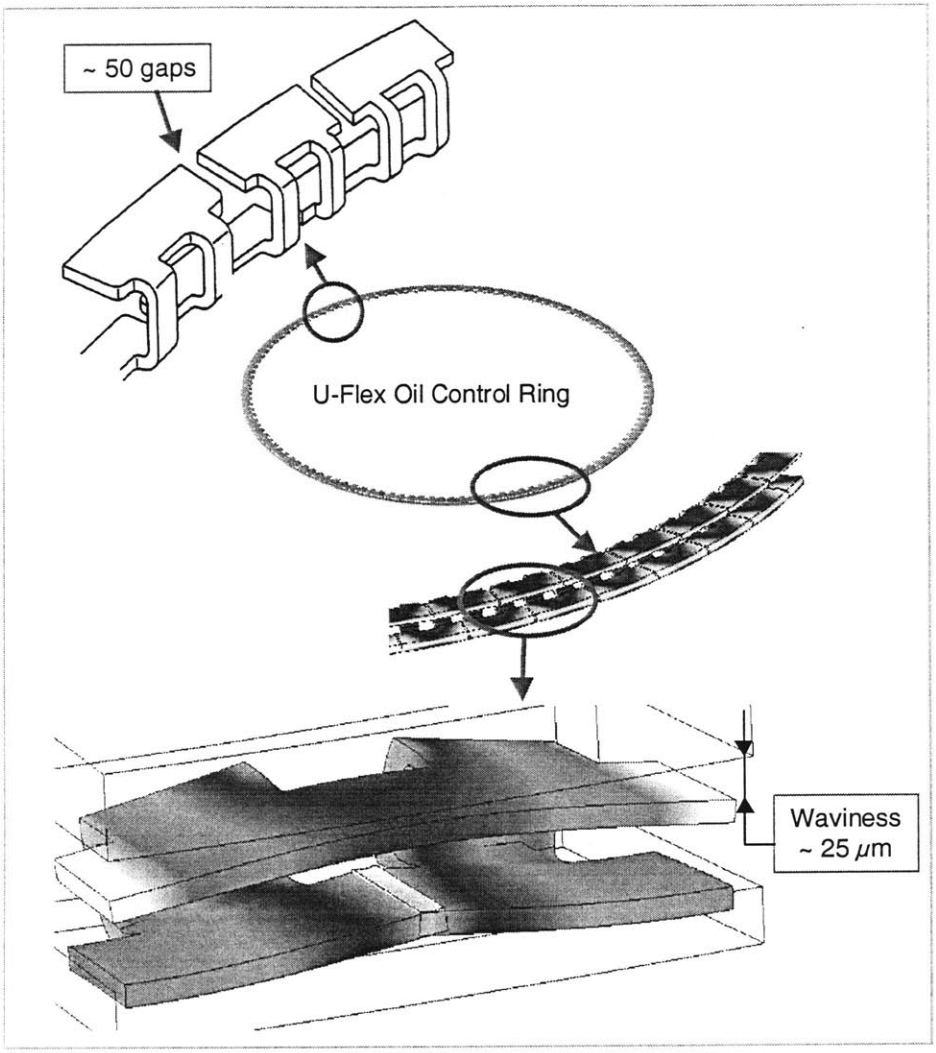


Figure 4.9 – U-flex structure and deformation of the U-flex flanks.

Oil supply through the ring/liner clearance: Like the two lands of twin-land OCRs, the two running surfaces of U-flex rings are mechanically attached. However, since U-flex rings have a relatively small torsional resistance, once the ring is constrained into the cylinder bore the relative position of the two lands is almost independent of the piston tilt. Therefore, contrary to twin-land OCRs U-flex rings can provide good ring/liner sealing all around the piston. Moreover, since U-flex rings have a limited range of dynamic twist, the up-scraping process described by T.Tian for three-piece OCRs is very unlikely to occur when using U-flex type ring. Eventually, U-flex OCRs have excellent liner conformability that further enhances their ring/liner sealing ability. Overall, it can be concluded that

U-flex OCRs are very unlikely to allow oil supply to the third land region through the ring/liner interface.

4.2.1.4 Oil Supply through the OCR Gap

In Section 3.4.2, experimental data showing direct oil supply to the third land region through the gap of a twin-land OCR were discussed. It was found that in the spark ignition engine running at low load (low intake manifold pressure), the flow of blow-by gases through the OCR gap was not strong enough to remove oil accumulating below and in the OCR gap. As a result, oil was transported by the action of the inertia force directly from the upper piston skirt region, which is usually partly or fully flooded with oil, to the third land. Moreover, order of magnitude estimation showed that this transport mechanism could supply oil at a tremendous rate and therefore initiate a dramatic oil flow to the upper ring pack. This type of oil transport can only occur if a straight path exist between a region where oil accumulates in large quantity, which in this case was the chamfer below the OCR, and the third land. The gaps of the two rails of three-piece OCRs are usually not lined up since the two rails are independent. U-flex OCRs are made such that the gaps of the two lands are offset (see Figure 4.9). Furthermore, in all the tests conducted with three-piece and U-flex OCRs, large accumulation of oil between the two the lands (rails) were never observed, and thus the only oil reservoir located in the OCR vicinity was the upper skirt region. Consequently, it can be concluded that the gap configurations of three-piece and U-flex OCRs do not provide a straight path between an oil filled region and the third land. As a result, inertia-driven oil supply to the third land region through the OCR gap(s) can only occur when a twin-land OCR is used. The fact that this type of oil supply only takes place in SI engines running in low or negative load conditions may be a negative aspect of using twin-land OCRs in SI engines.

4.2.2 Internal Flow Pattern

Region 1 may be divided into three sub-regions:

- The portion of liner located between the OCR and the scraper ring.
- The third land.
- The hook of the Napier ring (if a Napier ring is used) and the cutoff in the upper part of the third land (if there is a cutoff).

Throughout the experimental observations, it was determined that significant oil flux driven by the inertia force could take place between these various sub-regions. In this work, two types of scraper

ring designs were tested: one with a hook (Napier ring) and one without hook (simple taper face ring). The presence of a hook in the second ring was found to greatly affect the oil flow pattern in Region 1. Accordingly, in the two following sections, the oil distribution along the axial direction of the third land region is described for both types of scraper rings.
Finally, effects of the OCR design on circumferential oil flow are discussed in Section 4.2.2.3.

4.2.2.1 Scraper Ring with Hook

First of all, within each of the two sub-regions located on the piston, namely the third land and the hook/cutoff area, oil was found to be displaced according to the amplitude and direction of the inertia force. The details of the mechanism of this type of oil transport are described in Section 3.1.1. Second, various oil flux between the sub-regions were observed. These oil flux, which were found to result from the effect of the inertia force and the motion of the second and oil control ring relative to the liner, are described below.

Liner/hook oil transports: As any other scraper rings, Napier rings have the ability to scrap off excess of oil left on the liner by the OCR and thus to generate a transport of oil from the liner to the third land region. Furthermore, the hook of the Napier ring was found to have two major effects on the oil distribution within Region 1. First of all, it acts as a buffer region where oil scraped off the liner may be temporarily stored before being transported to the third land, to the liner and the second ring groove. Secondly, the upper side of the hook, which slopes toward the liner at a 15° angle (see Figure 3.54), was found to direct part of the oil accumulated in the hook onto the liner during the periods where the inertia force is pointing downward (see Section 3.2.2). Furthermore, it was determined that the oil transport between the hook and the liner, namely oil scraping and oil release, usually occur repeatedly on a time scale of one engine cycle or less.

Third land/hook oil transports: Experimental data showed that the alternating inertia force could drive oil accumulated on the third land into the hook and vice versa. For instance, Figure 4.10 shows LIF images of oil being transported from the third land region to the hook of the Napier ring. It can be seen that under the action of the inertia force, the surface of the oil that reaches the edge of the third land breaks either into droplets and/or an oil film that flow straight to the upper side of the Napier ring hook. In most cases, when oil was observed to flow from the third land to the hook during the upward inertia period, the opposite transport was seen to occur during the downward inertia period. Figure 4.11 shows images of oil distribution acquired in the PSA engine at three different crank angle degrees during the late part of intake stroke. One can see on the left image that oil that was originally

accumulated in the hook/cutoff sub-region had flown onto the third land over the outside edge of the cutoff. A cycle-resolved sequence of LIF images showing the evolution of the third land oil distribution under the effect of the inertia force can be seen in Figure 3.5.

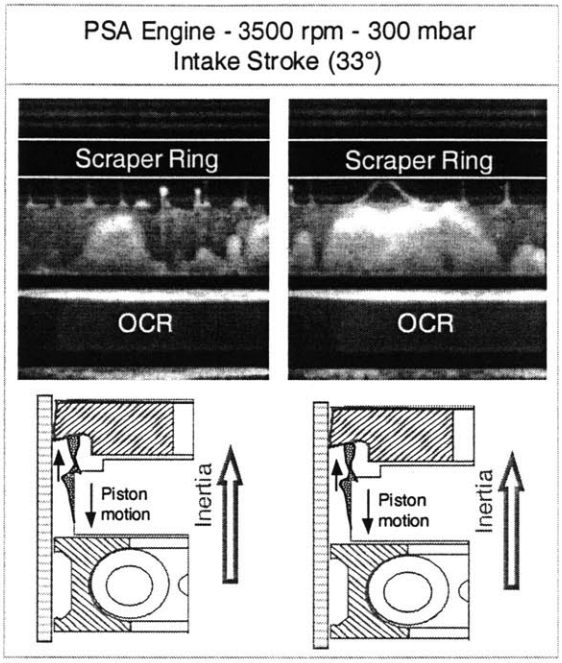


Figure 4.10 – Oil transport from the third land to the hook of the Napier ring.

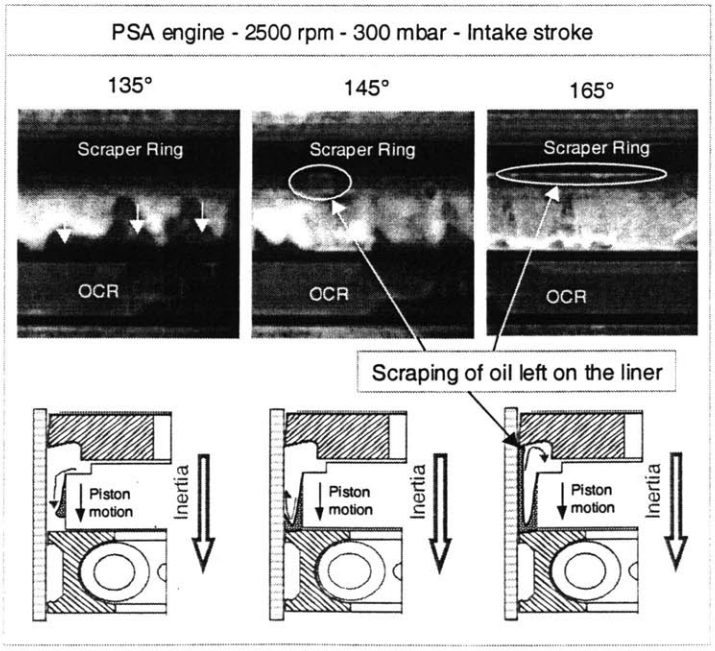


Figure 4.11 – Oil transport from the hook to the third land and to the liner (Observed in the PSA engine).

Third land/liner transport: In the case where the amount of oil accumulated on the third land is large enough so that the inertia force can drive oil from the cutoff across the third land, oil may accumulate against the upper side of the OCR during the downward inertia periods. As a result, two types of oil transports may be enabled. First, oil may be transported into the OCR groove and then back to the piston skirt region. Second, if the amount of accumulated oil is large enough so that oil can fill up the clearance between the third land and the liner oil will be transported to the liner and potentially scraped off by the scraper ring. The latter phenomenon was often observed in the PSA engine and is presented in the three-image sequence of Figure 4.11.

1. On the left image acquired at 135° degree after the intake TDC, we can see oil that flows out of the cutoff and downward on the third land under the action of the inertia.
2. On the middle image (145° after TDC), one can see that in some location oil has crossed the third land and reached the upper side of the OCR. In one particular location the amount of oil accumulated was large enough so that oil was transported to the liner and left behind the OCR while the piston was moving toward the BDC.
3. On the right image (160° after TDC), oil has accumulated against the upper side of the OCR and locally filled up the gap between the third land and the liner. As a result oil is transported from the third land to the liner as the piston is approaching the BDC. Furthermore, the LIF image clearly shows that part of the oil that was left on the liner is removed by the scraping action of the second ring and therefore transported back to the hook/cutoff region.

The whole cycle described above has to occur in less than 90 crank angle degrees since it requires both the piston motion and the inertia force to be in the downward direction. Particularly, in the case described in Figure 4.11, the whole process occurs over 30 crank angle degrees. The onset of such loop transport mostly depend on the ability of the inertia force to accumulate enough oil against the OCR and is thus mostly dependent on the engine speed and the amount of oil accumulated in the third land region (Region 1).

Here, we can conclude that when a Napier ring is used:

1. The oil repartition in Region 1 is determined by thee oil fluxes that occur among all three sub-regions on time scales equal or smaller than the engine cycle.
2. Oil fluxes between the hook/cutoff area and the third land are determined by the direction and the amplitude of the inertia force. Oil fluxes between the liner and the piston (oil scraping and release) result from the combined effect of the inertia force and the ring/liner relative motion.

3. If the volume of oil accumulated in the third land region is large enough, an oil flux looping through the various sub-regions can be established.

4.2.2.2 Scraper Ring without hook

There are two types of scraper ring without hook:

- The negative-twist scraper ring (see Figure 2.7). This type of ring, which has a chamfer at its lower inside corner to create a negative static twist, is commonly used in diesel engines.
- The simple taper face ring (see Figure 2.7). This type of ring, which has no torsion chamfer, has a small negative static twist resulting from the presence of the taper face. This design was tested in the Kubota engine.

The twist of the scraper ring mostly affect the ring dynamics and therefore the oil and gas flows through the second ring groove. Consequently, it may significantly affect oil flow out of Region 1 through the second ring groove (see Section 4.3.). Nevertheless, as it was explained in Section 3.1.3.2 the oil distribution on the land is little or not affected by land/groove gas flows. Accordingly, the following discussion may apply for both the simple taper face and the negative twist scraper ring.

Images of the oil distribution with a simple taper face second ring were acquired in the Kubota engine in nine different engine operating conditions ranging from 1200 to 2800 rpm and from minimum to 70% load. The experimental data showed that the evolution of the third land axial oil distribution mostly resulted from the action of the alternating inertia force. When a second ring without hook is used, the edge of the ring running surface that may potentially scrap oil is located at the corner of the ring lower flank. Consequently, in oil distribution images, second ring scraping is difficult to identify because one can not separate scraped oil from oil squeezed out of the second ring groove or oil remaining on the side of the ring. Accordingly, from the oil distribution observations it was difficult to determine the effect of second ring scraping on the third land oil flow pattern. However, careful analysis of the experimental data suggested that whenever the second ring scraped excess of oil left by the OCR, oil removed from the liner accumulated at the lower side of the second ring. Then, as the piston reached the BDC, the inertia force spread the oil accumulated against the lower side of the scraper ring onto the third land. Eventually, after the inertia force reversed in the following stroke, oil moved back toward to the second ring. No oil release to the liner was ever observed without hook in the second ring.

Oil flow from the third land to the liner occurring on the upper flank of the OCR was only observed in the PSA engine in which a Napier ring was used (see Section 4.2.2.1). Nonetheless, it is believed

that the presence of the hook is not required for this type of the flow to occur, and the land/liner loop transport could as well occur with other type of scraper rings.

To summarize, we can conclude that when a scraper ring without hook is used:

1. The oil distribution in the third land region mostly results from the effect of the inertia force.
2. If there is not enough oil on the third land to locally fill up the gap between the land and the liner, oil flow from the third land to the liner can not occur.

4.2.2.3 Third Land Circumferential Oil Flow.

Experimental observations conducted with twin-land OCRs occasionally showed that oil lying on the third land was dragged from the second to third ring gap by the flow of blow-by gases. This type of oil transport can only occur if the dominant gas flow sweeping the third land is along the circumferential direction. Since U-flex OCRs have about 50 tiny gaps evenly distributed all around the piston circumference, gas flows sweeping the third land can be considered to be mostly in the axial direction when a U-flex ring is used. Consequently, circumferential oil flow on the third land may only occur with three-piece and twin land OCRs. Furthermore, simulations of twin-land OCRs dynamics, which were conducted for the PSA engine ring geometry, showed that the OCR likely flutters during compression and/or expansion stroke in a wide range of engine speed and load. From the simulation results, it was found that when the twin-land OCR flutters the main stream of blow-by gases flows to the crankcase directly through the OCR groove, and therefore the circumferential aspect of the gas flow is partly lost.

4.2.3 Outward oil flows and Net oil transports

Oil flows out of the third land region (Region 1) either by passing the second or the oil control ring. The oil flowing from Region1 to the upper skirt region goes out of the piston ring pack and is thus considered to be recycled to the crankcase region. Oil flowing pass the second ring constitutes the oil supply for the lubrication of the upper ring pack and the source for potential oil consumption. In particular, the amount of oil supplied for the lubrication of the top ring running surface is controlled by the combined action of the running surfaces of the scraper and the oil control ring during downward strokes. Furthermore, oil flowing from the third to the second land constitutes an oil supply for the lubrication of the top ring groove and for potential transport of liquid oil to the combustion chamber.

The two following sections describe effects of the OCR, second ring and third land design on the oil flows toward the upper skirt region and the second land. Furthermore, the direction of the net oil transports through the different paths linking the third land region to the upper skirt area and the second land are discussed.

4.2.3.1 Oil Flow Pass the OCR

Through the ring groove: Oil accumulated on the third land may flow out of Region 1 through the OCR groove. First, to flow out of the third land region through the OCR groove oil has to flow from the land to the upper clearance of the OCR and its groove. This type of oil transport, which may result from the pumping action of the OCR or the relative motion of the OCR and the piston, strongly depends on the availability of oil in front of the ring/groove clearance (see Section 3.3.1). Consequently, it is strongly affected by the timing of the oil motion and the dynamics of the piston and rings. Second, oil trapped in the upper clearance of the OCR groove can be transported to the back of the OCR either by the squeezing action of the ring or by gas flow dragging. As it is explained in Section 3.3.2.2, the oil flows out of the OCR grooves resulting from the dragging action of blow-by gases are only significant when the OCR flutters.

If we first consider the case where the action of gas flows is negligible (no flutter), the squeezing action of the upper land of the OCR creates two competing flows: one flowing to the third land region and one flowing out to the back of the OCR. The direction of the net oil flow will be determined by the relative amplitude of the oil supply rate and squeezing rate at the inside and outside ends of the upper clearance of the OCR groove. Since there is undoubtedly much more oil available on the back of the OCR than there is on the third land, most of the oil supplied to the upper clearance of the OCR groove comes from the inside of the groove. Accordingly, the net oil flow resulting from the squeezing action of the upper land of the OCR most likely result in oil transport from the back of the ring to the third land region. This was confirmed by multiple experimental observations that clearly showed that the squeezing action of the OCR was in fact supplying oil to the third land.

When a twin-land OCR is used and the engine running conditions are such that the OCR flutters, the rate at which oil is removed from the upper groove clearance by the dragging effect of blow-by gases is not negligible. However, the oil flow rate induced by gas dragging is much less than the oil flow rate induced by the ring squeezing action (see Section 3.3.3). Accordingly, it is believed that when a twin-land OCR flutters the direction of the net oil transport through the OCR groove remains toward the third land, and that the rate at which oil is supplied to Region 1 is reduced by the dragging action of the gases flowing through the OCR/groove clearance.

Through the OCR gap: With any kind of OCR, oil lying on the third land is dragged along with the gas stream and through the OCR gap(s). Except in SI engines running in low load conditions (intake pressure < ~300 mbar), the net oil flux at the OCR gap(s) is always going from the third land region to the crankcase. In fact, this oil transport mechanism is believed to account for most of the oil return to the crankcase region. The rate at which the oil is carried toward the crankcase through the OCR gap mostly depends on the rate at which oil is dragged to the entrance of the gap and is therefore roughly proportional to the flow rate of blow-by gases going through the OCR gap(s). The images of Figure 4.12, which were acquired in the Kubota engine in the expansion stroke while using a U-flex OCR ring, show oil carried through one of the gaps by the blow-by gases going toward the crankcase. One may notice that the oil in a liquid layer form on the third land forms droplets as it is dragged through the gap.

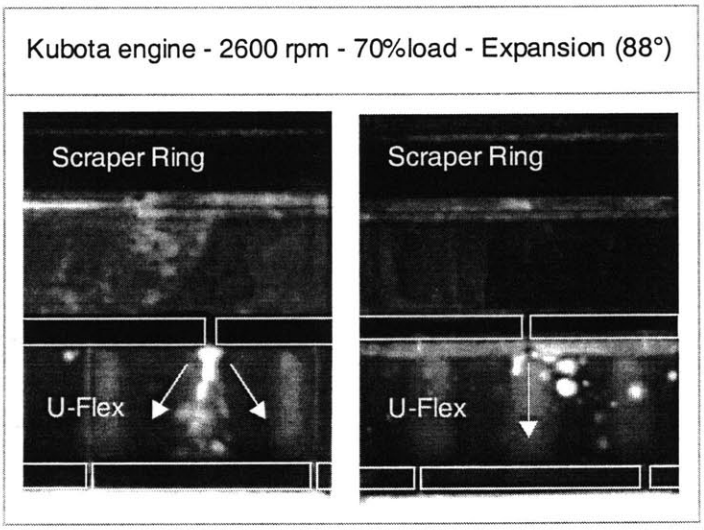


Figure 4.12 – Oil and gas flows through gaps U-flex OCR.

Through the OCR/liner interface: When a Napier second ring is used, the oil is released onto the liner during the early part of upward strokes. Part the oil released can be passed over by the OCR. Therefore, the oil can be returned to the region located below the ring pack through the OCR/liner interface. The portion of the released oil that is allowed through the ring/liner interface is determined by the size of the converging region of the upper rail/land running surface. This type of oil transport out of the third land region is beneficial for oil consumption since it allows part of the oil accumulated in the hook to be transported back to the upper skirt region. The direction of the net oil flux though the OCR/liner interface is determined by the relative amplitude of 1) the excess of oil left by the OCR and scraped by the second ring during the downward strokes, 2) the amount of oil

released on the liner that is allowed pass the OCR during upward strokes. Accordingly, when a Napier ring is used, a detailed simulation of the scraper and OCR lubrication is needed to determine the net oil transport through the OCR/liner interface.

For the three types of OCR discussed in this work, an overview of the various oil transports in and out of the third land region occurring around the OCR is presented in Figure 4.13.

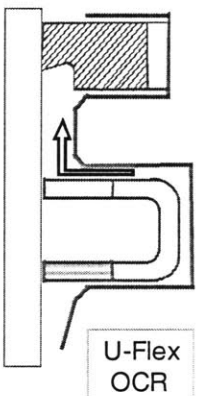
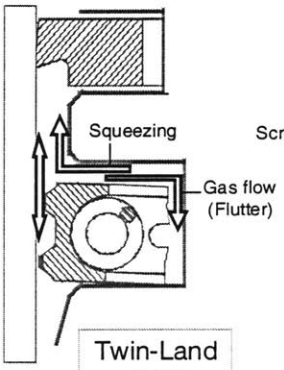
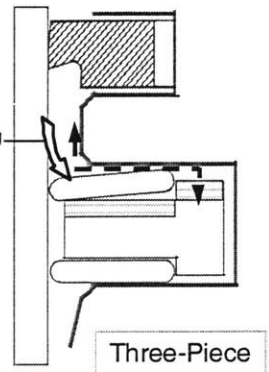
	U-Flex OCR	Twin-Land OCR	Three-Piece OCR
Specific characteristics affecting oil transport	• Excellent liner conformability • Waviness of the flanks	• Two rails solidly attached • Straight gap	• Enhanced side sealing • Potential up scraping (rail dynamic twist)
			
Supply to Region 1	• Oil leakage from OCR groove • Oil from OCR gap (low load)	• Oil leak from OCR groove • Second ring scraping excessive oil left by OCR • Oil from OCR gap (low load)	• Upper rail scraping • Oil from OCR gap (low load)
Oil return to the crankcase region	• Gas flow through the gaps (~50)	• Gas flow through the gap • Oil flow through the OCR groove (if flutter) • Oil passing the OCR running surface	• Gas flow through the gaps

Figure 4.13 – Effect of various OCR designs on oil transports between the upper skirt region and the third land region.

4.2.3.2 Pass the Scraper Ring

The oil can be transported from Region1 to Region 2 either through the second ring groove or through the gap. The rate at which oil flows from the third to the second land through the scraper ring groove depends on:

1. The rate at which the oil from the third land region is supplied to the lower clearance of the second ring groove.
2. The rate at which oil is squeezed out of the upper and lower clearances of the scraper ring groove.
3. The amplitude and direction of the flux of blow-by gases flowing through the groove.

In this section the effects of the presence of a hook, of a third land cutoff and of second ring negative twist on the various oil transport processes affecting the rate at which oil flow through the scraper ring groove are discussed. First, the effects of the hook and the third land cutoff on the amount of oil pumped into the lower clearance of the scraper ring groove are described using experimental data acquired in the Kubota engine with three different scraper ring/third land configurations. Then, with the support of simulation results obtained with the RINGPACK-OC code, the effect of the second ring twist is analyzed. Finally, the amplitude and the direction of the net oil flow through the scraper ring gap are discussed.

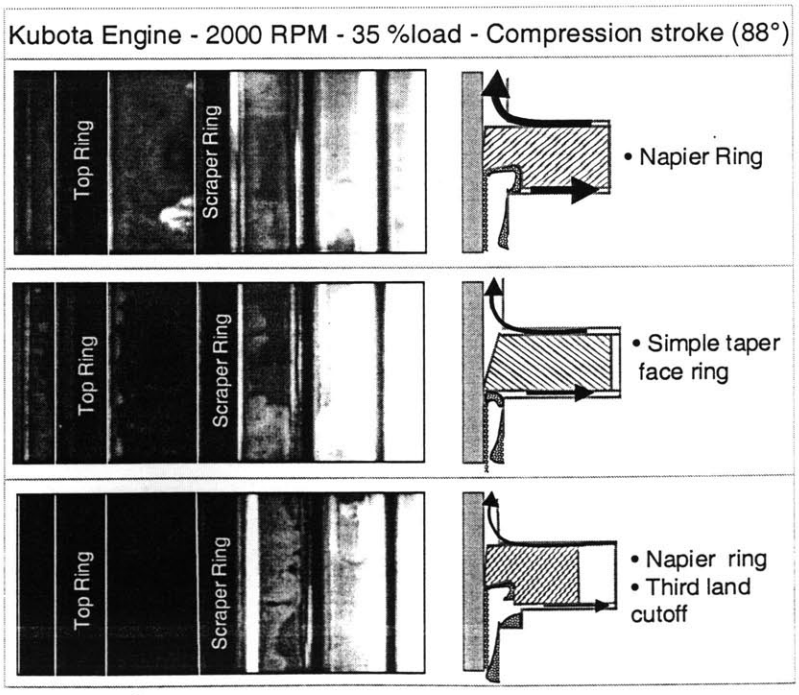


Figure 4.14 – Effect of the second ring/third land geometry on the second land oil accumulation (I).

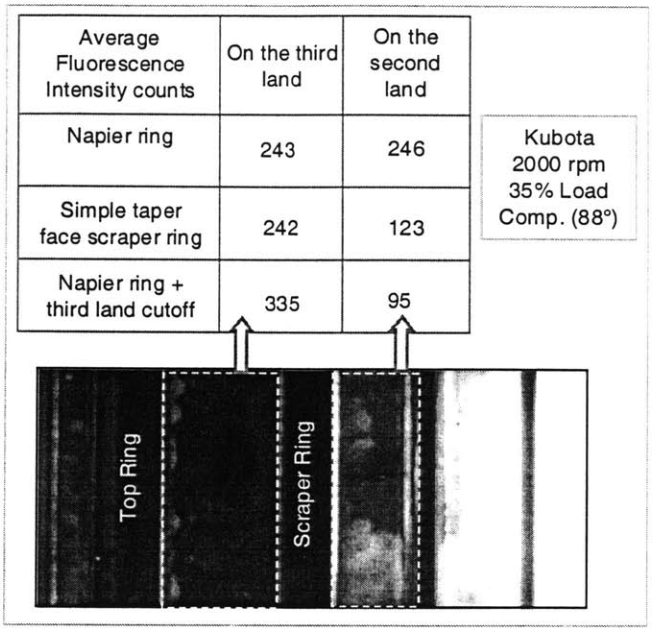


Figure 4.15 - Effect of the second ring/third land geometry on the second land oil accumulation (II).

Hook and third land cutoff: The effect of the hook and third land cutoff on the oil flow through the second ring groove were studied by testing the configurations presented in Figure 4.14. Figure 4.15 reports the level of fluorescence intensity measured on the second and third land of the Kubota engine for the second ring and third land geometry tested. Over the viewing area for each piston land, the level of fluorescence was the average of 50 consecutively acquired images. Since the same tuning of the optical setup was used for the three sets of tests, the fluorescence intensity level provides a good estimation of the relative amount of oil accumulated on second and third land in each configuration. The test conducted with the simple taper face scraper ring and without third land cutoff was used as a reference.

From the top image of Figure 4.14 and the table in Figure 4.15, we can see that when the simple taper face ring is replaced by a Napier ring, the amount of oil accumulated on the second land is greatly increased. This shows that when there is no cutoff at the top of the third land, using a Napier ring enhances the rate of oil supply to the second land through the second ring groove. Since in both cases the gas flows have a negligible effect, the increase of the oil flow through the second ring groove is either due to an increase in the oil supply to the lower ring/groove clearance or a change in the squeezing action of the ring. Comparing the ring/groove relative angle for the Napier (positive twist) and the simple taper face ring (small negative twist), we find that using a Napier ring should decrease the rate at which oil from the upper ring/groove clearance is squeezed toward the second land.

Consequently, the changes in the squeezing action of the second ring are not responsible for the increase of oil supply to the second land.

In order to understand the effect of the hook geometry on the rate of oil supply to the lower ring/groove clearance we can look at the amount of oil that can be pumped into the groove when the ring lifts up. When a simple taper face ring is used, the amount of oil accumulated in front of the of ring/groove lower clearance depends on the phasing of scraper ring dynamic and the inertia force, which drives oil along the axial direction of the third land. Accordingly, since oil has the ability to spread on the third land only a small fraction of the oil located in the third land region may accumulate in front of the lower clearance of scraper ring groove. As a result the amount of oil pumped into the groove is limited and so is the rate at which oil is transported to the second land. When a Napier is used, oil transported from the third land to the hook or scraped from the liner is trapped in the hook. Consequently, significant amount of oil may accumulate in the hook. Moreover, the displacement of the oil in the hook is very limited. As a result, oil can be easily be accumulated in front of the lower clearance of the scraper ring groove and therefore the rate at which oil is pumped into the groove is greatly enhanced. Figure 4.16 shows the second ring lift computed for the Kubota engine running at 2000 rpm 35 % load. On can see that during the early part of exhaust stroke the scraper ring twists away from the lower side of its groove. Since this inertia force is pointing downward, all the oil trapped in the hook is accumulated in front of the ring/groove clearance. As a result, the second ring can efficiently pump large amount of oil into the ring/groove clearance.

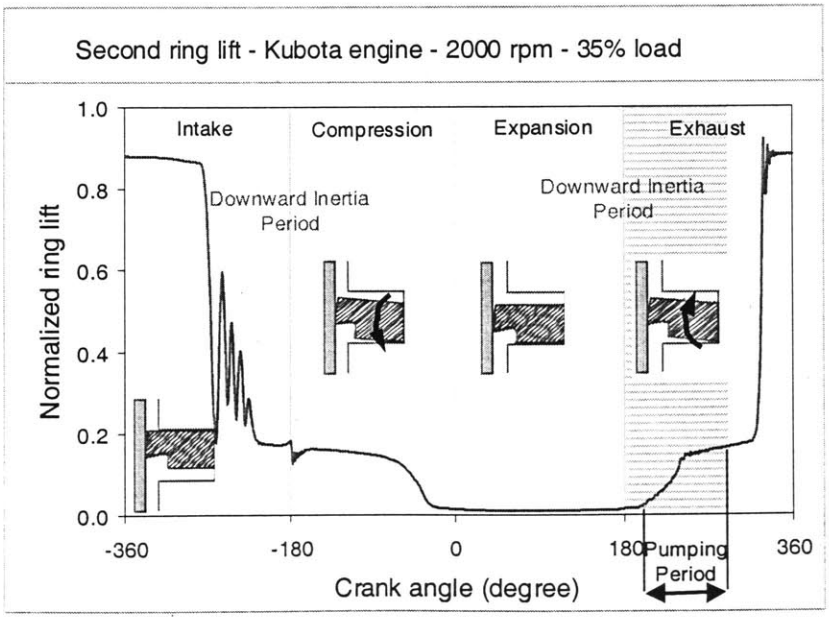


Figure 4.16 – Computed second ring lift for the Kubota engine running at 2000 rpm 35% load.

In the third configuration, which is commonly used in SI engines, a Napier ring was used and a cutoff was machined at the top of the third land. As one can see in Figures 4.14 and 4.15, this configuration minimizes the oil flow through the second ring groove and therefore the amount of oil accumulated on the second land. Once again, the results can be explained by examining the amount of oil available for ring pumping on the lower side of the scraper ring groove. During the upward inertia period oil is stored in the upper part of the hook while during the downward inertia period oil is stored in the third land cutoff. Therefore, with this design oil never accumulates in front of the lower clearance of the second ring groove and thus the amount of oil that can flow into the second ring groove is minimized.

To summarize, we can say that when oil transports driven by gas flows are negligible:

1. The rate at which oil is transported to the second land through the scraper ring groove is primarily determined by the rate at which oil is supplied to the lower ring/groove clearance. Accordingly, it is limited by the amount of oil available in front of the lower clearance of the scraper ring groove.
2. The availability of oil that may potentially flow into the ring groove can be controlled by detailed geometrical features added on the ring and the land such as the hook of the Napier ring and a cutoff at the top of the third land.
3. The hook of Napier rings and the third land cutoff act as a buffer region that allow the oil to be stored away from the ring /groove clearance, and their ability to control the oil flow through the second ring groove diminishes if they are filled up with oil.

Second ring twist: The scraper ring twist has two potential effects on the rate of oil transport through the second ring groove. First, it changes the rate at which the oil is squeezed out of the clearances of the second ring groove on the lower and the upper sides of the ring. Assuming that the rate of oil supply to the groove remains unchanged, positive twist decreases the rate at which oil is squeezed out to the upper land and negative twist increases it. Second, simulations conducted with RINGPACK-OC showed that negative twist second rings have the ability to flutter in a wide range of engine operating conditions. When the scraper ring loses its stability, a large amount of blow-by gases is allowed to flow from the second land to the third land through the second ring groove. Negative twist second ring were not tested in this work and consequently there is no experimental data showing the effect of second ring flutter on the second land oil distribution. However, experimental observations of the oil distribution conducted while the top ring was fluttering showed that the stream of gases flowing around the ring could drag a significant amount of oil out of the groove (see Figure 3.72). Accordingly, it is believed that the gas flow induced by second ring fluttering can drag a significant

amount of oil from the second ring groove to the third land and thus greatly reduce the rate of oil transport to the second land.

For the three types of scraper ring discussed in this work, an overview of the various oil transport processes between the third and the second land is presented in Figure 4.17.

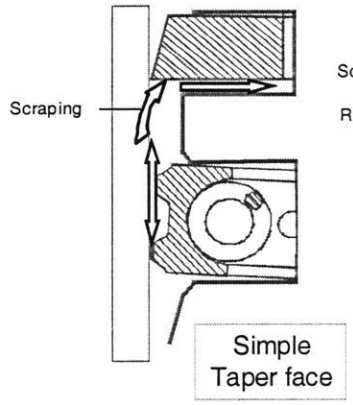
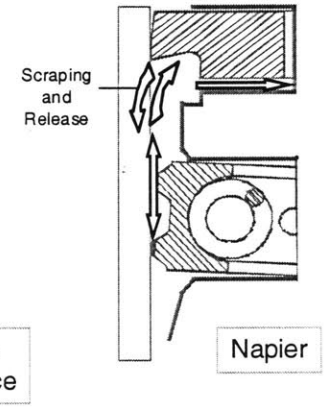
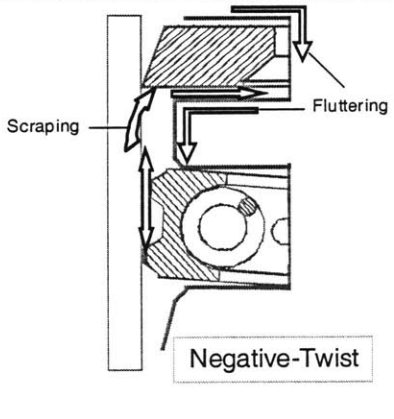
Specific characteristics affecting oil transport	• Taper face favors scraping	• Hook and third land cutoff acts as buffer regions • Hook allows oil release • Taper face favors scraping	• Negative static twist affect squeezing and allow flutter • Taper face favors Scraping
			
Supply to Region 2	• Through the groove	• Through the groove, reduced oil supply to the groove due to hook and third land	• Through the groove, reduced oil transport to the second land when flutters
Oil return to the crankcase region	• (no effect)	• Oil released on the liner can be passed by OCR	• (No effect)

Figure 4.17 – Effect of various scraper ring design on oil transports in and out of the third land region.

Oil flow through the scraper ring gap:

(The rate and the direction of oil transport through the scraper ring gap is discussed in Section 4.3.1.2)

4.3 Region 2: Controlling the Oil Supply to the Top Ring Groove

The second land (Region 2) is the oil source for the lubrication of the top ring groove. Moreover, part of the oil transported from the second land to the top ring groove is squeezed out onto the crown land and thus constitutes a source of liquid oil consumption. Consequently, the rate at which oil is transported from the second land to the top ring groove is of primary importance for the performance of the ring pack system. In this section, we first discuss the characteristics of the various oil transports between the second land and the adjacent regions. Then, a simplified oil balance is established to describe how the rate at which oil is supplied to the top ring groove is controlled by the competing oil flows on the second land.

4.3.1 Oil Flows In and Out of Region 2

4.3.1.1 Through the Second Ring Gap

The oil flow driven by the stream of blow-by gases through the second ring gap was found to be the only oil transport that removes oil from the second land and carries it to the third land. It is therefore an essential mechanism in the process of returning oil supplied to the upper ring pack back to the crankcase region. As it is explained in Section 3.4, the rate at which the oil is transported through the second ring gap depends on:

1. The volume of gases going every cycle through the gap from the second to the third land (blow-by) and the volume going from the third to the second land (reverse blow-by).
2. The amount of oil available in the regions located directly upstream and downstream of the ring gap.

In diesel engines and in SI engines running with high enough intake pressure (intake pressure > ~500) mbar), the flow rate of reverse blow-by is negligible and therefore oil transport through the scraper ring gap only occurs from the second to the third land. Furthermore, since in these conditions the effect of the reverse blow-by can be neglected, the rate at which oil is carried through the gap is equal to the rate at which oil lying on the second land is dragged toward the scraper ring gap (see Section 3.4.1.1). Consequently, in these conditions the scraper ring gap does not restrict the amount of oil removed from the second land by the circumferential flow of blow-by gases.

In SI engines running at low intake manifold pressure (< ~400 mbar), the flow rate of reverse blow-by becomes significant and consequently oil transports through the gap occur in both directions.

Therefore, as the intake manifold pressure decreases the net oil flow going from the second to the third land may becomes lower than the amount of oil dragged from the second land to the region located upstream of the scraper ring gap. As a result, in SI engine running in low load condition oil may accumulate above the scraper ring gap.

In the extreme cases where the throttle is near to be closed, the average blow-by is reversed and consequently gas and oil flow passing the scraper ring gap are going from the third to the second land. In this particular situation, there is no more oil transport going toward the crankcase region and thus it is possible that none of the oil supplied to the ring pack is returned to the sump.

4.3.1.2 From the Second Ring Groove

Except for the SI engines running near to closed throttle condition, where oil is carried by the reverse blow-by from the third to the second land through the scraper ring gap, experimental observations showed that oil is supplied to second land region through the scraper ring groove. The squeezing action of second ring was found to be the mechanism driving the oil from the upper clearance of the scraper ring groove onto the second land. As it is explained in Section 4.2.3.2, the rate at which oil flows to the second land through the second ring groove greatly depends on the rate at which oil is supplied to the lower clearance of the second ring groove, and thus it is strongly affected by oil transports in the third land region (Region 1).

4.3.1.3 To the Top ring Groove

The oil transport rate through the top ring groove depends on:

1. The rate at which the oil is supplied to the lower clearance between the top ring and its groove.
2. The rate at which oil is squeezed out of the upper and lower clearances of the top ring groove.
3. The amplitude and direction of the flux of blow-by gases flowing through the groove.

Oil supply: The rate at which oil is supplied to the lower clearance of the top groove mainly depends on the amount of oil available in front of the top ring groove clearance at the time where the top ring lifts and/or the piston moves laterally (see Section 3.3.1). Accordingly, the phasing of the inertia-driven oil displacement and the motions of the top ring and piston are critical to the amount of oil supplied to the top ring groove. Moreover, the amount of oil that may accumulate in front of the top

ring groove clearance depends on the total volume of the oil lying on the second land. Therefore, it depends on the oil supply from the second ring groove and the oil removal resulting from the dragging action of the blow-by gases. The effect of the gas-driven circumferential oil flow on the amount of oil to be transported from the second land to the top ring groove is discussed in details in Section 4.3.2.

Top ring twist and oil squeezing: As it is explained in Section 3.3.2.1, the relative angle between the rings and their grooves affects the rates at which oil is squeezed out of the upper and lower sides of the grooves. Accordingly, changing the top ring static twist can reduce or enhance the net oil flow through the top ring groove. The two most commonly used top ring designs for SI engines and small diesel engines are the rectangular top ring (no twist) and the positive twist top ring. Using a positive twist top ring enhances the oil squeezing toward the outside of the lower clearance of the top ring groove. As a result, it reduces the rate at which oil is transported to the crown land.

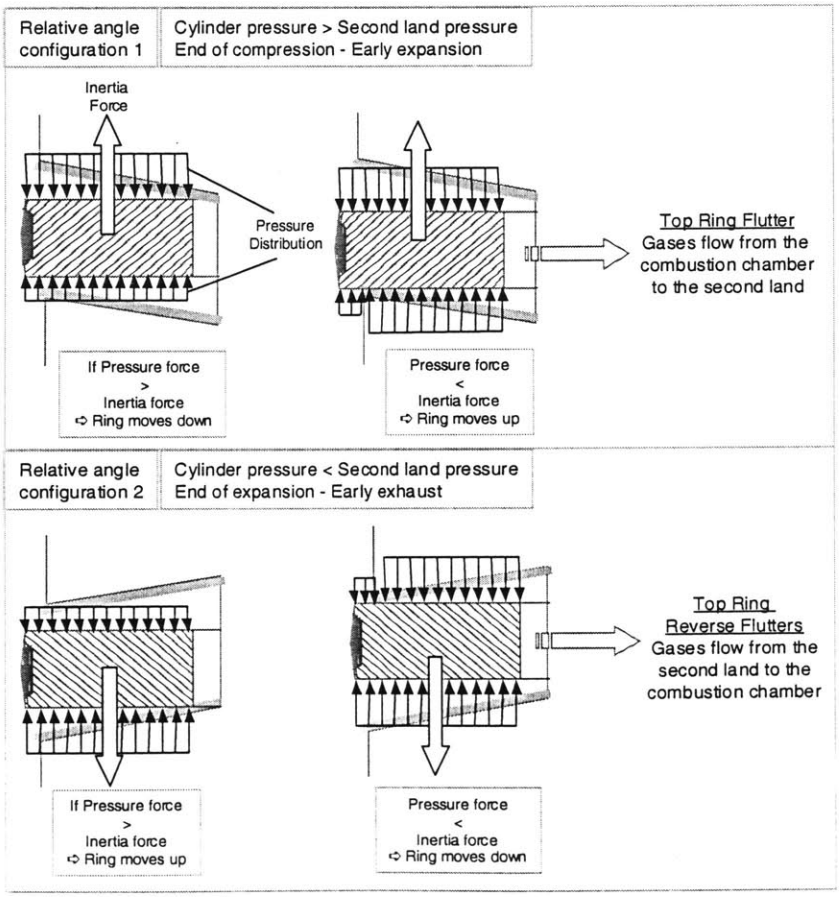


Figure 4.18 – Description of top ring flutter and reverse flutter.

Top ring flutter: The top ring may lose its stability in the two different force balance configurations presented in Figure 4.18.

- Top ring flutter: If the relative angle between the top ring and its groove is as presented in the top figure (configuration 1), the top ring may flutter around the combustion top dead center. This type of top ring flutter, which usually occurs at high speed and low load (SI engines), induces gas flows from the combustion chamber to the second land and therefore reduces the rate of oil transport to the crown land. Experimental data showing the effect of the top ring flutter were shown and discussed in Section 3.3.2.2.
- Top ring reverse flutter: If the relative angle between the top ring and its groove is as drawn in the bottom figure (configuration 2), the top ring may flutter around the expansion bottom dead center. This type of top ring flutter, which usually occurs at high speed high load, induces gas flows from the second land to the combustion chamber and therefore enhances the rate of oil transport to the crown land. The effect of top ring reverse flutter on oil transport to the crown land and oil consumption was characterized by E.Yilmaz using real-time oil consumption measurement and ring dynamics simulation [63].

In both cases, the gas flow resulting from the top ring instability affects the oil flow through the top ring groove by dragging oil accumulated inside the top ring groove. However, according to estimations conducted in Section 3.1.3.2, axial gas flows resulting from the flutter of the top ring have no or little effect on the oil transports on the adjacent lands and therefore on the oil flows going into the top ring groove.

The relative angle between the top ring and its groove depends on the top ring static twist, the top ring dynamic twist and the groove tilt. Due to the piston thermal deformation, the groove tilt is changing with engine running conditions. Moreover, the top ring dynamic twist changes with engine speed and load. As a result, a rectangular top ring may flutter at high speed low load and "reverse flutter" at high speed high load. Therefore, ring motion simulations and thermal deformation calculations are necessary to predict the exact dynamic behavior of the top ring.

4.3.1.4 Through the Top Ring Gap

Positive blow-by situations: In all tested engine operating conditions where the blow-by gases were flowing from the combustion chamber to the second land, no oil accumulation was ever observed either upstream or downstream of the top ring gap. Therefore, it is believed that there was no significant transport of liquid oil trough the gap of the top ring. The absence of oil transport through

the top ring gap was a result of the lack of oil supply to the part of the crown located above the gap. Because, there is no circumferential gas flow to drag oil accumulated on the crown land no oil is supplied to the region located upstream of the gap.

If the top ring rotates, the oil that accumulates away from the gap may be exposed to the stream of blow-by gases flowing through the top ring gap and thus be transported to the second land. This type of oil transport may carry oil from the crown to the second land. However, the resulting rate of oil transport is restricted by the ring rotation speed and is thus believed to be small compare to the rate of oil transport through the top ring groove. Overall, it is safe to say that when the blow-by is positive, which is the case in most engine operating conditions, the oil transport through the top ring gap is very limited and therefore do not significantly affect the amount of oil accumulated on the second land.

Negative blow-by situations: In the tests conducted at 200-mbar absolute intake manifold pressure (almost closed throttle) the blow-by gases were flowing toward the combustion chamber. Such low intake manifold pressure levels correspond to a negative engine torque output and thus can only be encountered during transient engine operation (see Section 2.2.1). Experimental observations showed that if the throttle position was maintained, the volume of oil accumulated on the second land was dramatically increasing and that liquid oil was carried to the crown land by the stream of reverse blow-by gases. In transient tests where the intake manifold pressure was decreased from 700 down to 200 mbar while the engine was running at 4500 rpm, oil was observed to flow upward through the top ring gap between 45 seconds to 1 minute after the action on the throttle. Consequently, we can conclude that the onset of liquid oil transport from the second to the crown land through the top ring gap depends on the duration of the period during which the engine is maintained in negative blow-by operating conditions.

4.3.1.4 Top Ring Down Scraping

The barrel shape of the top ring profile is designed so that top ring scraping can not occur. However, as the top ring wears down, its running surface becomes flatter and flatter. As a result, after a large number of running hours, it may occur that the upper or the lower corner of the ring running surface comes in contact with the liner. This phenomenon is more likely to happen in diesel engines where the wear rate is higher than in spark ignition engine [17]. When the lower corner of the top ring profile contacts the liner during downward stroke, hydrodynamic lubrication can not occur and the top ring scrap the oil from the liner. Consequently, oil is supplied to the top of the second land. Since

the top ring does not have the ability to release oil on the liner, the top ring down-scraping constitutes a net oil transport from the liner to the second land.

Every tests conducted in this project were started with a new ring pack and were completed in less than 40 hours of engine operation. As a result, the top ring running surface profile was never significantly worn down and top ring scraping was never experimentally observed in this work.

4.3.2 Effect of the total amount of oil stored on the second land

4.3.2.1 Oil supply to the top ring groove lower clearance

The rate at which the oil is transported to the top ring groove lower clearance is of primary importance since it determines the lubrication condition of the top ring groove and the rate at which oil is lost to the crown land. Oil is transported into the top ring groove lower clearance either by the pumping action of the top ring and by the motion of the piston relative to the top ring. In both cases, the rate at which the oil is transported into the groove strongly depends on the amount of oil available in front of the lower clearance of the top ring groove at the time when either the piston or the ring moves. Accordingly, the duration of the period during which oil accumulates in front of the lower clearance of the top groove and the volume of the resulting oil accumulation are critical parameters in determining the oil supply to the top ring groove.

According to the description of the inertia-driven axial oil transport conducted in Section 3.1.1.3, the period T_{acc} (in crank angle degree) during which oil accumulates against the top ring can be defined as CAi - CA_r. Where CA_r is the crank angle at which oil, which was originally accumulated against the scraper ring, reaches the top ring and CA_i is the crank angle following CA_r at which the inertia force switches from the upward to the downward direction. CA_r decreases as the oil volume on the second land and/or the engine speed increases. Accordingly, T_{acc} increases with the amount of oil accumulated on the second land and with the engine speed. Moreover, since the oil motion toward the top of the second land is driven by the inertia force, the rate at which oil accumulates against the lower side of the top ring during Tacc increases with the engine speed and with the average thickness of the second land oil layer. Therefore, because T_{acc} and the rate at which oil flows toward the top of the second land both increase with the total volume of oil accumulated on the second land and the engine speed, the rate at which oil is supplied to the top ring groove also grows with the amount of oil stored on the second land and the engine speed. Eventually, since the amount of oil stored on the second land is determined by the various oil transports between the second land and the adjacent

regions, we can conclude that the second land oil balance controls the rate of oil supply to the top ring groove.

4.3.2.2 Second land oil balance

In this Section a simplified second land oil balance was established to describe how competing actions of the various oil transport processes taking place on the second land affect the rate at which oil is supplied to the top ring groove.

Assumptions: First, the circumferential gas flow sweeping the second land was considered to always flow from the top to the second ring gap. Accordingly, the following discussion applies to all engine operating conditions except SI engines running in closed or near to closed throttle condition. Second, the balance between the oil transport processes affecting the second land was always assumed to be achieved and thus the amount of oil stored on the second and its circumferential repartition was assumed to be steady. In particular, this assumption implies that the rings do not rotate. According to the analysis of the experimental observations conducted in Section 4.3.1, three oil transport mechanisms were considered:

1. The oil supply from the second ring groove resulting from the squeezing action of the scraper ring.
2. The circumferential oil transport resulting from the dragging action of the blow-by gases flowing from gap to gap.
3. The oil leakage toward the top ring groove.

- The oil flow from the second ring groove to the second land was assumed to be uniform all around the piston circumference. Moreover, since the rate of oil transport through the second ring groove was found to be mostly determined by oil transport processes occurring in the third land region and the dynamic of the scraper ring, it was considered to the independent of the amount of oil accumulated on the second land. Accordingly, it was expressed as:

$$q_{supply} = K \cdot R_{ld} \cdot d\theta \qquad \text{(K: constant)} \tag{4.1}$$

With q_{supply}: rate of supply to the second land per unit of circumferential length (m^2/cycle)

$d\theta$: angle defined by an infinitesimal section of the land (see Figure 3.42)

- The rate of circumferential oil transport is given by (see Section 3.1.2.4):

$$q_{dragged} = Q_{gas} \cdot \left(1 - \frac{\theta_g}{2\pi}\right) \frac{3 \cdot \mu_{air}}{\mu_{oil}} \cdot \frac{h_{oil}^2(\theta)}{h_{ld}^2} \tag{4.2}$$

With $q_{dragged}$: rate of circumferential oil transport at the circumferential location θ located within the land sector defined by θ_g (angle between the second and the top ring gap)

$h_{oil}(\theta)$: Average oil thickness along the axial direction of the land at the circumferential location θ.

- According to the analysis conducted in Section 4.3.2.1, the rate of oil transport to the top ring groove was expressed as an increasing function of the oil layer thickness and the engine speed:

$$q_{leak} = f(h_{oil}, N) \cdot R_{ld} \cdot d\theta \quad \text{with} \quad \frac{df}{dh_{oil}} > 0 \quad \text{and} \quad \frac{df}{dN} > 0 \tag{4.3}$$

With q_{leak}: rate of oil transport to the top ring groove at the circumferential location θ

Mass conservation: Applying mass conservation to a control volume defined as an infinitesimal angular section of the second land (see Figure 3.42), the following relationship was derived:

$$q_{supply} - q_{leak} = \frac{dq_{dragged}}{d\theta} \tag{4.4}$$

Then, using Equations 4.1, 4.2, and 4.3 Equation 4.4 was expressed as: n

$$K - f(h_{oil}, N) = Q_{gas} \cdot \left(1 - \frac{\theta_g}{2\pi}\right) \cdot \frac{\mu_{air}}{\mu_{oil}} \cdot \frac{6 \cdot h_{oil}}{h_{ld}^2 \cdot R_{ld}} \cdot \frac{dh_{oil}}{d\theta} \tag{4.5}$$

Because f(hoil,N) is not explicitly known, Equation 4.5 can not be integrated and thus the distribution of the oil around the second land $h_{oil}(\theta)$ can not be computed.

As it was explained in Section 4.3.1.1, in most engine running conditions, all the oil dragged from both sectors of the second land to the region located upstream of the second ring gap is carried to the third land with the stream of blow-by gases. Therefore, the amount of oil removed from the land by the blow-by gases is equal to the amount of oil dragged into the scraper ring gap. Since $h_{oil}(\theta)$ is not known, we may estimate the total amount of oil removed every cycle from the second land $Q_{dragged}$ using the average thickness of the oil layer:

$$Q_{dragged} = Q_{gas} \cdot \left(1 - \frac{\theta_g}{2\pi}\right) \frac{3 \cdot \mu_{air}}{\mu_{oil}} \cdot \frac{\tilde{h}_{oil}^2}{h_{ld}^2} \quad (m^3/\text{cycle}) \tag{4.6}$$

With: $$\tilde{h}_{oil} = \frac{1}{2\pi \cdot R_{ld} \cdot L_{ld}} \int_0^{L_{ld}} \int_0^{2\pi} h_{oil} \cdot R_{ld} \cdot dy \cdot d\theta$$

Similarly, the total amount of oil transported to the top ring groove Q_{leak} may be considered to be a function of the average thickness of the oil layer:

$$Q_{leak} = \cdot \int_0^{2\pi} f\left(h_{oil}(\theta)\right) \cdot R_{ld} \cdot d\theta \approx F(\tilde{h}_{oil}) \qquad \text{with} \quad \frac{dF}{d\tilde{h}_{oil}} > 0 \tag{4.7}$$

Using the approximations given by Equations 4.6 and 4.7, mass conservation applied to the entire second land can be expressed as a function of the average thickness of the oil layer $\tilde{h}_{oil}$:

$$2\pi \cdot R_{ld} \cdot K - F(\tilde{h}_{oil}, N) = Q_{gas} \cdot \left(1 - \frac{\theta_g}{2\pi}\right) \cdot \frac{\mu_{air}}{\mu_{oil}} \cdot \frac{3 \cdot \tilde{h}_{oil}^2}{h_{ld}^2 \cdot R_{ld}} \tag{4.8}$$

Graphically, the second land oil balance given by the above equation can be represented as in Figure 4.19.

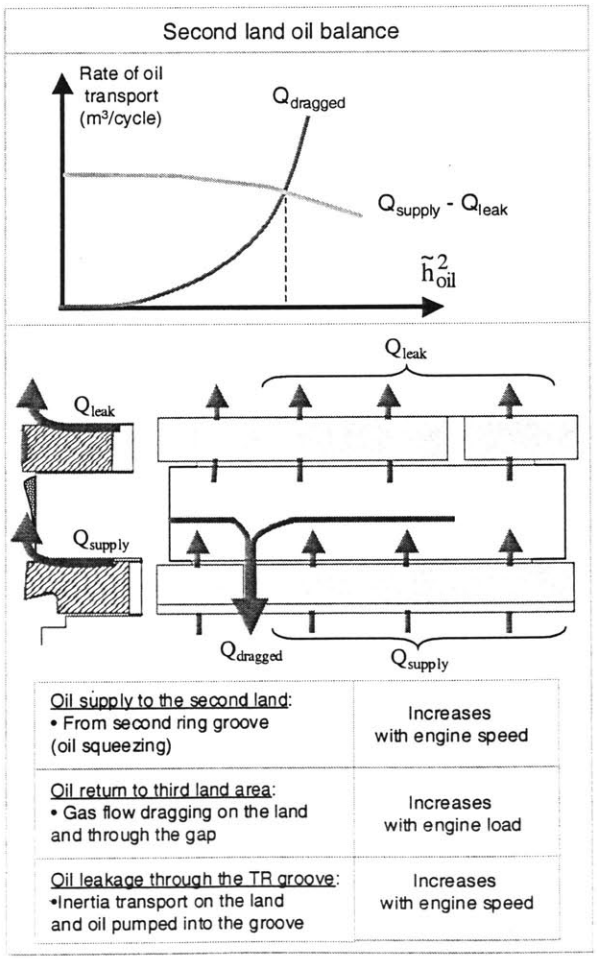


Figure 4.19 – Second land oil balance.

Effect of engine load: Considering the various oil transport processes affecting the second land oil balance, changing the engine load while maintaining the engine speed mainly affects the rate at which the oil is removed by the dragging action of the blow-by gases. In fact, increasing the engine load usually results in an increase of the amount of gas sweeping the second land Qgas and therefore causes an increase of the oil removal rate $Q_{dragged}$. Consequently, as one can see from Figure 4.20, which graphically shows the effect of a load increase on the second land oil balance, increasing the circumferential flow of blow-by gases reduces the average thickness of the oil layer covering the second land $\tilde{h}_{oil}$.

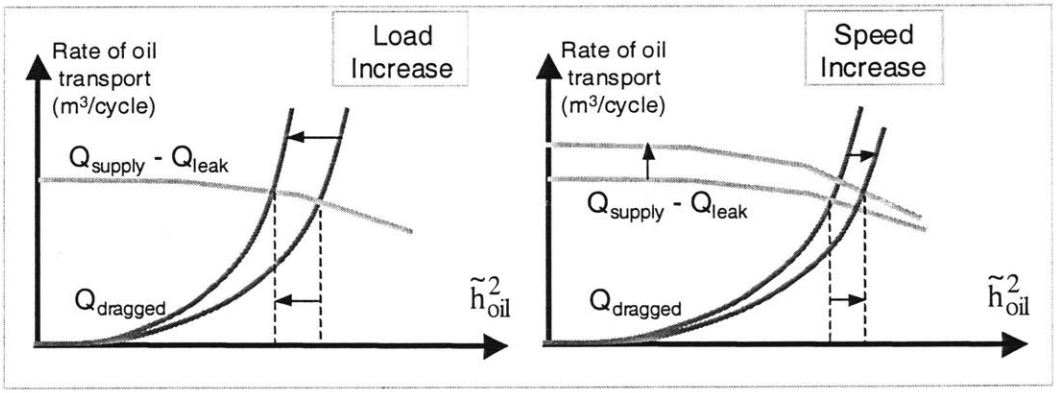


Figure 4.20 – Schematic description of engine speed and load effect on the second land oil balance

This trend was confirmed by experimental data acquired in the PSA engine (see Figure 4.21). The average thickness of the oil layer covering the part of the second land located in front of the window was measured in various engine operating conditions while the top two rings were pinned. The rings were pinned such that θ_g was equal to π and the gaps were located along the piston pin axis. The LIF observations showed that with this ring configuration the oil distribution was perfectly steady and the oil layer was uniform. Consequently, this configuration was particularly appropriate to study the variation of the amount of oil accumulated on the second land with the engine speed and load. For each running condition the average thickness of the oil layer covering the second land $\tilde{h}_{oil}$ was determined using 4 sets of 50 LIF images acquired in each of the four strokes. In Figure 4.21, which shows the measured evolution of $\tilde{h}_{oil}$ with the engine load (intake manifold pressure) at three different engine speeds, one can see that $\tilde{h}_{oil}$ was systematically observed to decay as the engine load increases.

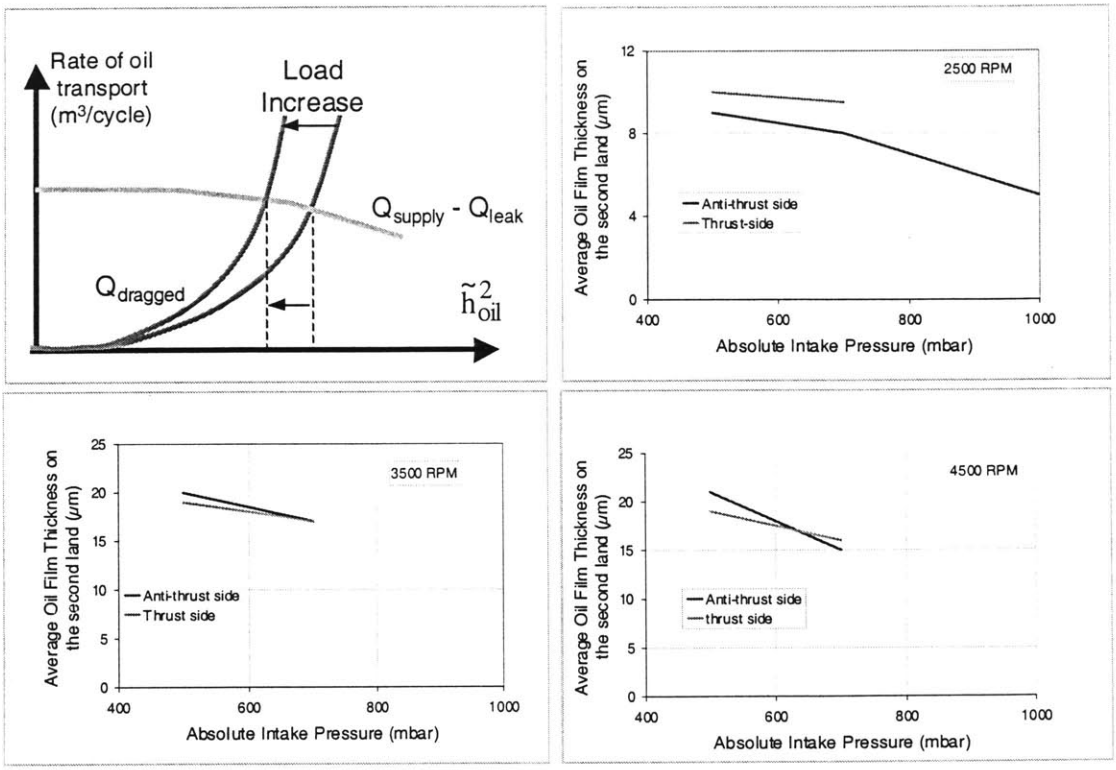


Figure 4.21 – Effect of engine load on the second land oil accumulation (measured in the PSA engine).

Since the rate of oil transport through the top ring groove was found to be an increasing function of the second land oil volume, we can conclude that increasing the engine load should result in a decrease of the amount of oil flowing into the top ring groove.

Eventually, the fact that the oil layer was found to be very uniform shows that approximating the local oil thickness h_{oil} by the average thickness of the oil layer $\tilde{h}_{oil}$ is appropriate when there is no ring rotation. Accordingly the approximations used to derived Equations 4.6 and 4.7 do not affect the validity of the analysis of the second land oil balance.

Effect of the engine speed: Changing the engine speed affects all three oil transports related to the second oil balance.

1. Increasing the engine speed usually results in a reduction of the volume of blow-by gases flowing through the top and the scraper ring gap. Accordingly, it is expected to reduce the rate of oil removal (per cycle) induced by dragging action of the blow-by gases.
2. It enhances inertia-driven oil transport and thus oil flows across the piston lands and through the ring grooves. Therefore, as the engine speed goes up the rate of oil supply to the second land and the rate at which oil is flowing to the top ring groove should increase.

In order to analyze the effect of the engine speed on the average thickness of the second land oil layer measured in the PSA engine, $\tilde{h}_{oil}$ was plotted versus the rate of oil removal $Q_{dragged}$. The simulation code RINGPACK-OC was used to calculate Q_{gas} for each engine operating condition tested and $Q_{dragged}$ was estimated from Equation 4.6. The results are plotted in Figure 4.22. Due to the uncertainties involved in both the calibration of $\tilde{h}_{oil}$ and the computation of Q_{gas} only significant variations of Qdragged and $\tilde{h}_{oil}$ could provide relevant analysis. Accordingly, only the effect of increasing the engine speed from 2500 to 3500 rpm was discussed.

From 2500 to 3500 rpm, both $\tilde{h}_{oil}$ and $Q_{dragged}$ were found to significantly increase. Since Q_{leak} is an increasing function of both the engine speed and the average oil layer thickness $\tilde{h}_{oil}$, this results shows that from 2500 to 3500 rpm Q_{leak} increased. Moreover, since $Q_{supply} = Q_{leak} + Q_{dragged}$ the results of Figure 4.22 also show that increasing the engine speed from 2500 to 3500 rpm resulted in an increase of the oil supply from the second ring groove Q_{supply}. Overall, in this particular case raising the engine speed resulted in an increase of the amount of oil accumulated on the second land. However, the extent of this result is limited since it was observed from experimental data obtained over a 1000-rpm speed range.

Nonetheless, even though the evolution of the amount of oil accumulated on the second land with the engine speed could not be established over a wide range of engine operating conditions, it is believed that in most cases increasing the engine speed results in an greater rate of oil transport to the top ring groove.

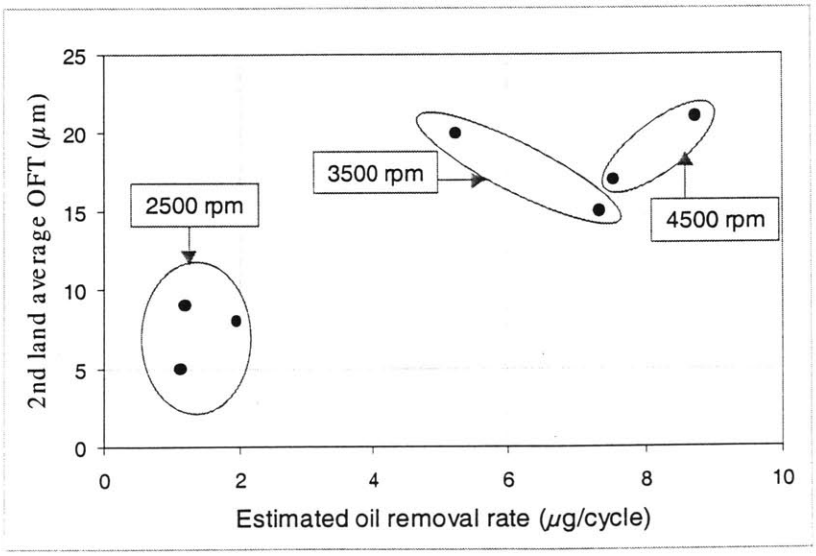


Figure 4.22 – Effect of engine speed on the second land oil balance (measured in the PSA engine).

4.4 Region 3: The Oil Consuming Region

4.4.1 Oil Supply

From the top ring groove: Except in maintained closed throttle engine operation where liquid oil may flow upward through the top ring gap, the oil is supplied to the crown land through the top ring groove. The squeezing action due to the top ring moving up in its groove is responsible for the transport of the oil from the upper groove clearance to the crown land. As a result, in most engine operating conditions, oil is supplied to the crown land during the late part of the exhaust stroke. At is was discussed in Sections 4.3.1.3 and 4.3.2.1, the rate at which oil is transported through the ring groove depends on:

1. The oil supply to the lower clearance of the top ring groove that is strongly dependent on the amount of oil accumulated on the second land and inertia-driven oil flows.
2. The top ring static and dynamic twist.
3. The flow of blow-by gases through the top ring groove.

Figure 4.23 shows images on the oil distribution in the upper ring pack of the PSA engine. On each of the three LIF images, which were acquire at 2500 rpm at three different engine load, one can identify the oil located at the bottom part of the crown land that had been squeezed out of the top ring groove.

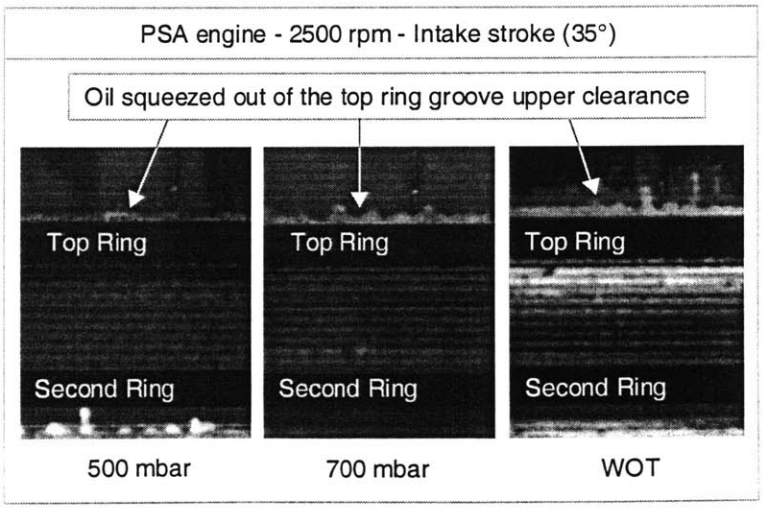


Figure 4.23 – Oil squeezed out of the top ring groove toward the crown land (observed in the PSA engine).

Top ring up scraping: When top ring up scraping occurs, the oil removed from the liner is supplied to the lower part of the crown land. Top ring up scraping may occur in two situations:

1. When the ring running surface has suffered enough wear so that the upper corner of the ring profile contacts the liner during upward strokes [17].
2. When the bore is significantly distorted and as a result the top ring conformability is strongly affected by the pressure in the combustion chamber.

Since oil accumulated on the crown land is not returned to the crankcase, top ring up-scraping constitutes a direct source of oil consumption.

4.4.2 Oil Flow to the Combustion Chamber

Only the oil located very near the region upstream of the top ring gap may be carried to the second land by the stream of blow-by gases. Consequently, most of the oil supplied to the crown land is never returned to the lower part of the piston ring pack and ends up being transported to the combustion chamber. There are two mechanisms by which oil accumulated on the crown land may be lost to the combustion chamber:

1. Oil that reaches the upper edge of the crown land can be thrown off to the combustion chamber by the action of the inertia force.
2. In engine running conditions where the crown land temperature is high enough (high load) oil evaporates and mixes with the combustion chamber gases.

Depending on the residence time of the oil on the crown land (see Figure 2.20), the lubricant may be oxidized as it evaporates. As a result, the heaviest components of the oil may contribute to the formation of carbon deposits on the crown land.

Transport to the upper edge of the crown land: The only force having a significant effect on the oil accumulated on the crown land is the inertia force resulting from the piston alternating motion. Consequently, the oil supplied to the lower part of the crown land moves up and down according to the direction and amplitude of the inertia force. The distance traveled by the oil is determined by the engine speed and the volume of oil accumulated on the crown land (see Section 3.1.2.4). Therefore, at constant engine speed the distance reached by the lubricant increases every time additional oil is supplied to the crown land. Figure 4.24 shows three images of the oil distribution acquired during the intake stroke 20 cycles apart. One can see that due to the repeated top ring squeezing process the total amount of oil accumulated on the crown land was increasing cycle after cycle. Moreover, it can

clearly be observed that the distance traveled by the oil lying on the crown land was increasing with the total volume of oil. In the situation where enough oil is accumulated on the crown land so that the oil can reach the upper edge of the piston, oil may be thrown off to the combustion chamber during the upward inertia period. The throw off process will continue as long as the oil is supplied to the crown land.

In the PSA engine, it was observed that if the oil supply to the crown land stopped as a result of an engine load or speed change, the oil accumulated on the crown land would stop spreading. The oil would remain on the crown land as long as a change in the engine operating conditions allows the oil supply to resume. Consequently, depending on the previous conditions in which the engine was run, there could be oil accumulated on the crown land while there was no oil flow through the top ring grove.

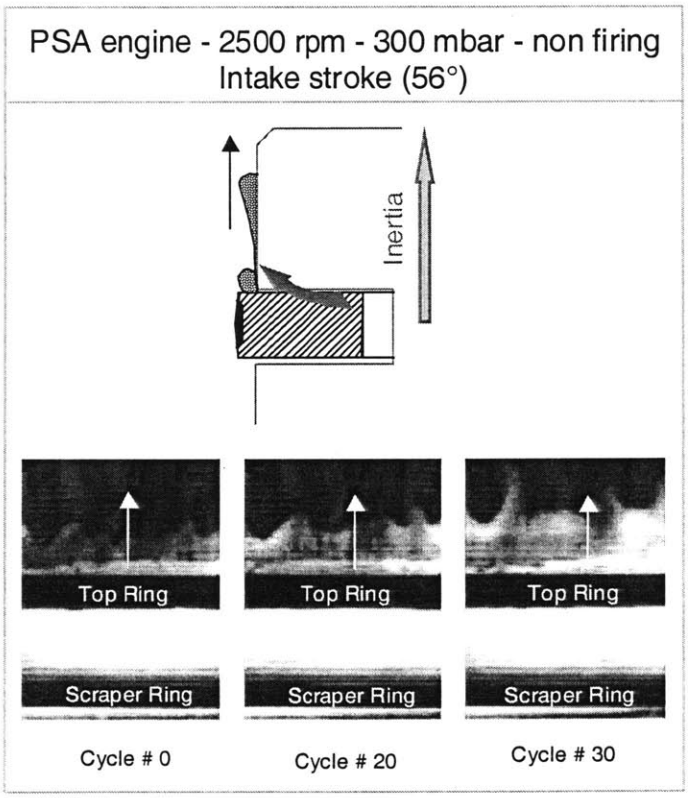


Figure 4.24 – Top ring oil squeezing and inertia-driven oil transport observed on the crown land of the PSA engine.

Oil evaporation and oxidation: At high engine load the crown land temperature can reach 280 ~ 300°C and therefore the oil may evaporate and/or be oxidized. The lighter the oil components are more likely to evaporate. Meanwhile the heavier components are more likely to be oxidized on the land and form carbon deposits. The rate at which the oil is oxidized depends on the oil temperature and the time during which the oil is exposed to high temperatures (see Figure 2.20). Consequently,

the rate at which the oil layer covering the crown land is refreshed greatly affects the carbon deposit build up.

Figure 4.25 shows a summary of the various oil transports affecting the crown land region.

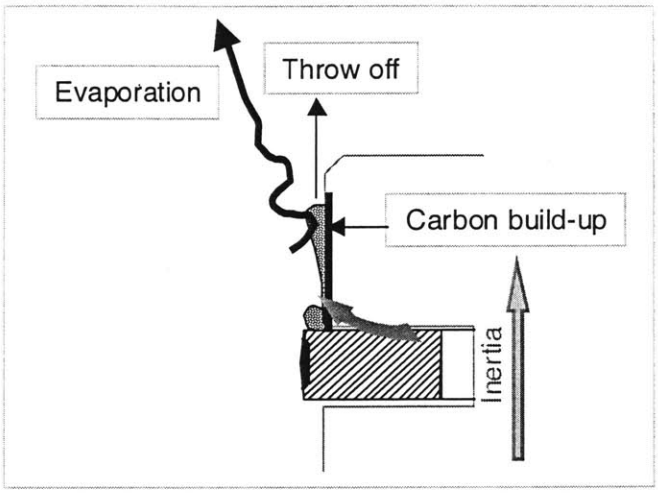


Figure 4.25 – Description of oil transport on the crown land.

4.5 Global Oil Transport Scheme

Using the knowledge gained from the extensive experimental investigation and the results from characterizing and modeling various oil transport mechanisms, a mass-conservative scheme describing the main routes and modes of oil transport through the piston ring pack was proposed. Since in spark ignition engines, the engine load, which is determined by the intake manifold pressure, was found to greatly affect the direction and the amplitude of the gas-driven oil transport, the mass-conservative scheme was presented in three different figures corresponding to three ranges of engine operating conditions. In this section, to describe the general oil transport pattern we first refer to the oil transport scheme presented in Figure 4.26, which apply for diesel engines and SI engines running at high load. Then, the variations of the oil transport scheme occurring at low load and in closed throttle engine operation (Figures 4.27 and 4.28) are discussed.

4.5.1 Reference case: Diesel engine and SI engines at high load

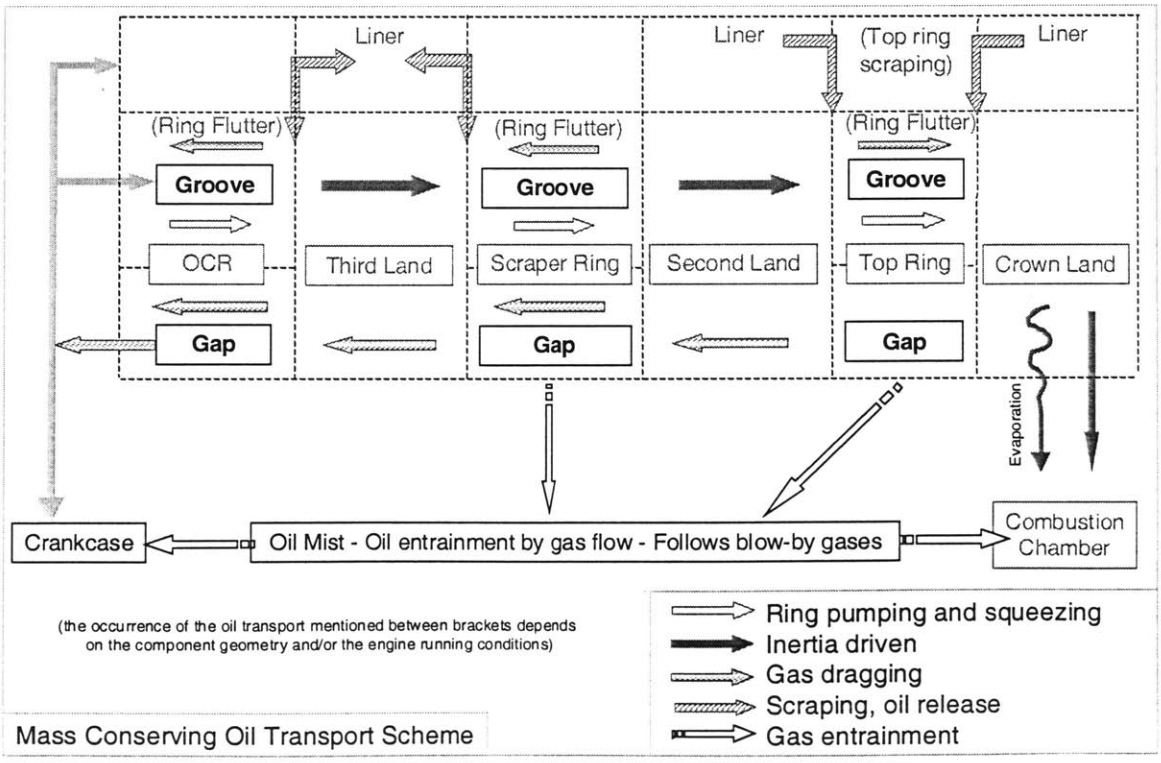


Figure 4.26 – Global oil transport scheme for diesel engine and spark ignition engine at high load (Intake pressure > ~500 mbar).

4.5.1.1 Upward oil transport

In all engine running conditions other than closed throttle operation, the oil was found to flow from the upper skirt region to the crown land by flowing through the ring grooves and across the lands. Oil flows across the piston lands are driven by the inertia force while in most cases oil flow through the ring grooves results from the ring dynamics and the piston/ring relative motion. The direction of the net oil transport along the axial direction of the piston is determined by the location of the oil source. In other words, because oil is supplied at the bottom of the ring pack, more oil is always supplied at the bottom than at the top of the piston lands and ring grooves. Consequently, the net oil transport due to the inertia force and the ring pumping/squeezing process is toward the combustion chamber. Since the oil motions across the piston lands and thus the oil supply to the lower clearances of the grooves of top two rings both depends on the intensity of the inertia force, the rate at which the oil is transported toward the combustion chamber increases with the engine speed.

4.5.1.2 Downward oil transport

Over the whole range of engine operating conditions the major oil transport toward the crankcase was driven by the dragging action of the blow-by gases. The oil accumulated on the piston is dragged around the lands and carried through the ring gaps by the gas stream all the way to the upper skirt region. The rate (g/cycle) at which oil is transported by the dragging action of the blow-by gases is determined by the volumetric blow-by flow rate. Accordingly, it increases with the engine load and usually decreases with the engine speed.

4.5.1.3 Occasional oil transport processes

Depending on the ring geometry and engine running conditions some very specific oil transport may take place and affect the oil distribution and flow pattern in the piston pack.

Ring flutter: Depending on the relative angle between the rings and their grooves, rings may flutter in some specific operating conditions. The large amount of blow-by gases flowing through the groove of a ring that flutters drags the oil accumulated in the ring groove clearances and therefore strongly affect the rate of oil transport through the back of the ring. Depending on the direction of the gas flow ring fluttering can either be beneficial (negative-twist scraper ring flutter) or detrimental (top ring reverse flutter) to oil consumption (see Figure 4.26).

Top ring scraping: Top ring scraping may occur in case of excessive wear of the ring running surface or at high engine load in the presence of bore distortion. In both cases, it creates an additional oil supply to the upper ring pack region and therefore favors the oil transport to the crown land (see Figure 4.26).

Note: On the three figures showing the global oil transport scheme, potential transports of oil mist generated at the top two ring gaps were added for completeness. The generation of oil mist at the ring gaps was found experimentally.

4.5.1.4 Liquid oil consumption and Main controlling points

The rate at which the oil is lost to the combustion chamber results from the competition between the inertia-driven oil transports that drives the oil toward the combustion chamber and the gas-driven oil removal that carries oil back to the crankcase region. Accordingly, the rate of liquid oil consumption through the piston/liner interface is expected to increase with the engine speed and decrease with the engine load. These trends make high speed low load engine operation critical for liquid oil consumption through the piston/liner interface.

In a typical three-ring passenger-car engine ring pack, the control of the upward oil transport rate is achieved at three different locations:

1. The geometry/design of the OCR determines the oil supply to the third land and to the part of the liner located between the OCR and the scraper ring (see Figure 4.13).
2. The geometry of the second ring and the top part of the third land determine the rate of oil supply to the scraper ring groove and thus to the second land (see Figure 4.17)
3. The second land oil balance determines the oil supply to the top ring groove and thus to the crown land.

Additionally, by affecting the squeezing rate and potentially inducing ring flutter, the relative angle between the rings and their grooves affects the rate of oil transport through the ring grooves.

4.5.2 SI engines running at low load and Closed-throttle engine operation

(See Figure 4.27 and 4.28)

The oil transport scheme presented in Figure 4.26 applies for spark ignition engines running with intake manifold pressure greater than ~ 500 mbar (See Figure 4.27). When the intake manifold pressure is lowered below ~ 500 mbar the flow of reverse blow-by starts to have a non-negligible effect on the oil flow through the second and third ring gaps. As a consequence, the rate at which the oil is removed from the second and the third land is limited and the rate of oil return to the crankcase region decreases.

Furthermore, in the case when a twin-land OCR is used, around 300 mbar intake pressure, oil driven by the inertia force starts to flow upward through the OCR gap.

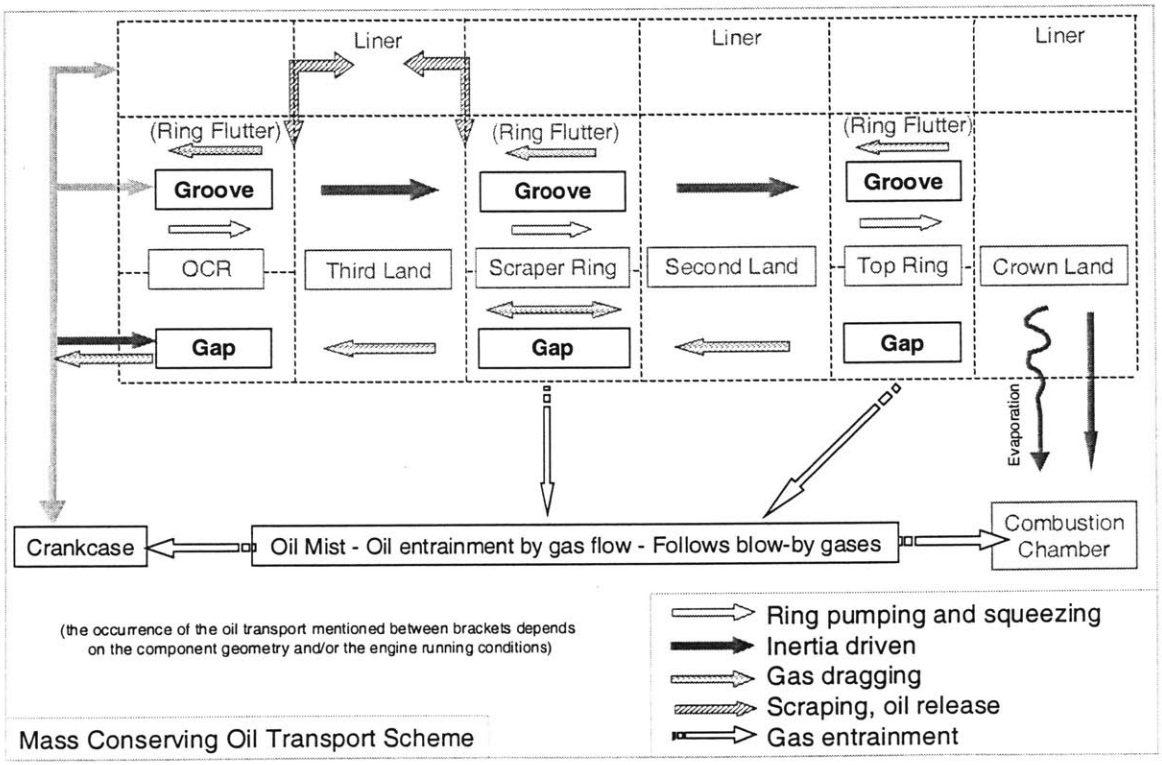


Figure 4.27 – Global oil transport scheme for spark ignition engine running at low load (Intake pressure 300 ~500 mbar).

When the throttle is closed or near being closed (intake manifold pressure ~200 mbar or lower), the blow-by flow is reversed and consequently the dragging action of the blow-by gases transports oil in the direction of the combustion chamber (See Figure 4.28). In this situation, there is no transport mechanism to carry oil back to the crankcase region, and therefore the piston ring pack quickly becomes flooded with oil. As a result large amount of liquid oil are lost to the combustion chamber.

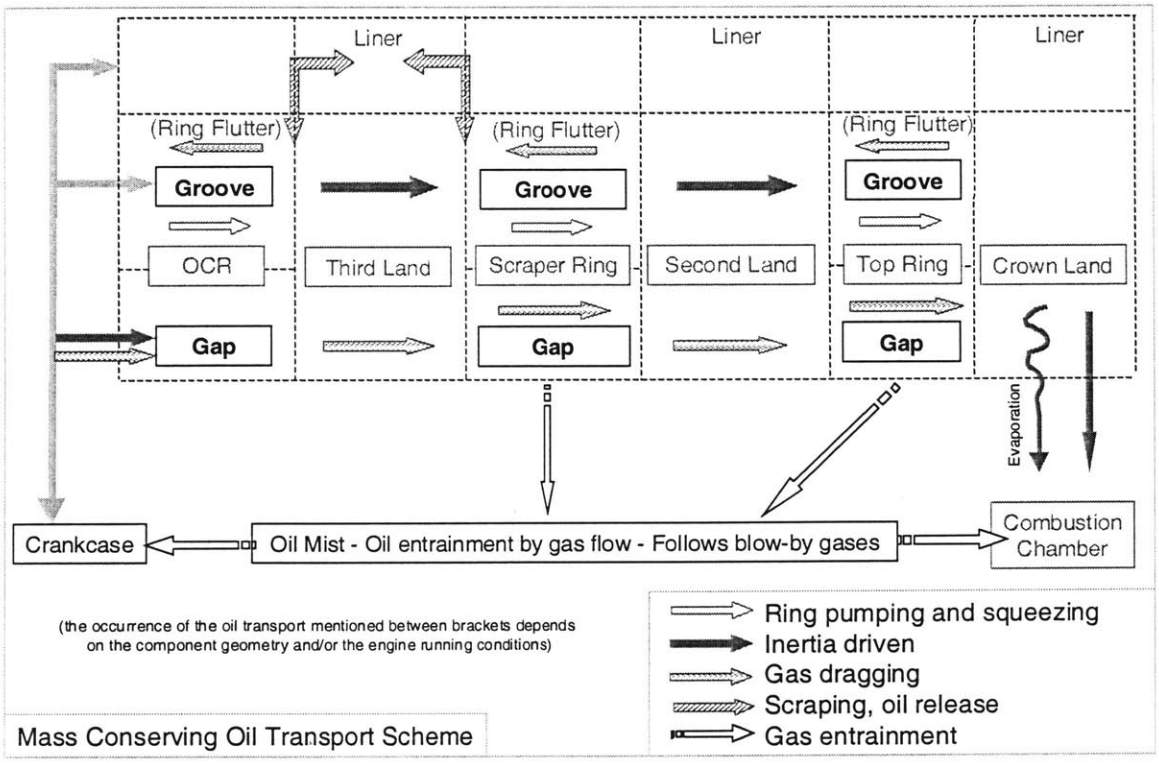


Figure 4.28 - Global oil transport scheme for spark ignition engine with closed or near to closed throttle (intake pressure < ~200 mbar).

CHAPTER 5. CONCLUSIONS

In this work, a unique experimental facility dedicated to the study of oil transport in the piston ring pack of internal combustion engines was built. A visualization system using multiple-dye Laser-Induced-Fluorescence was implemented to observe oil displacements among various regions of the piston ring pack of a diesel and a spark ignition engine. High-resolution (30 μm/pixel) images and video recordings of the oil distribution were acquired over a range of running conditions representative of passenger-car engine operation. To bring understanding of the oil transport processes on the piston lands, through the grooves and gaps, and their interactions, a great deal of effort was made in identifying and characterizing the mechanisms responsible for the oil flows along the piston.

On the piston lands, oil was observed to move in both axial and circumferential directions. The axial oil displacements were found to be driven by the inertia force resulting from the piston alternating motion. The circumferential flow appeared to result from the dragging action of the blow-by gases. Through experimental observations, it was established that the inertia force dictates the oil repartition along the axial direction of the piston lands. In particular, it forces oil to repeatedly accumulate against the rings and spread over the piston surface. The spreading of oil puddles by the inertia force was carefully modeled taking into account the two-dimensional aspect of the oil flow occurring at the front edge of the puddles. The developed model was used to predict the aspect ratio and the distance traveled by the oil accumulated on the piston lands. The predictions were in good agreement with the oil distribution profile measured during engine operation. Furthermore, the model suggests that for each engine speed and land width there is minimum oil volume required for the inertia force to establish a net oil transport across the land. Using simulation results and dimensional analysis, an analytical relationship expressing the inertia-driven oil displacements as a function of the piston speed and the oil volume was derived. As a result, the evolution of the oil distribution along the axial direction of the piston lands can now be computed through the engine cycle and therefore correlated with the oil supply to the ring/groove clearances. Such information will be of great use for the future development of oil transport simulation tools.

Two major mechanisms were found to be responsible for oil flows from the piston lands to the ring grooves: the ring pumping, which was observed experimentally, and the lateral motion of the piston relative to the rings. The quantity of oil flowing into the ring grooves appeared to be mostly

determined by the amount of oil available in front of the ring groove clearances at the time of the ring lift and/or the piston lateral motion. Accordingly, it can be concluded that the rate at which oil from the lands is supplied to the grooves of the top two rings is strongly dependent on the timing of the inertia-driven oil displacements and the ring and piston dynamics. By changing the second ring and third land geometry, it was experimentally proven that the amount of oil that accumulates in front of the lower clearance of the second ring groove greatly affect the oil flow rate through the back of the scraper ring. In particular, the combined use of a Napier ring and a cutoff at the top of the third land was found to minimize the rate of oil transport from the third to second land.

The oil flow from the ring grooves to the piston lands appeared to be governed by the ring squeezing action and the dragging effect of the gases flowing through the ring groove clearances, this latter mechanism being only significant when ring flutter occurs. The experimental observations of the land oil distribution during top ring fluttering clearly showed that gas flows resulting from ring instability could remove most of the oil accumulated in the top groove, preventing oil from flowing to the crown land. Furthermore, it was found from engine test results and analytical calculation that the axial gas flow resulting from ring fluttering has little effect on the land oil distribution. The experimental observation further suggested that the direction of the net oil flows through the back of the rings was determined by the location of the main oil supply to the ring groove. Typically, because more oil was supplied to the lower clearance of the ring grooves oil was flowing from the lower to the upper land. The ring/groove relative angle, which affect the squeezing process, and the flutter-induced gas flow appeared to affect the rate at which the oil was flowing through the ring grooves but not the direction of the net transport.

Overall, the combination of the oil flows across the piston lands and through the ring grooves appeared to be the main path of oil transport toward the crown land. Since oil displacements across the lands and thus oil supply to the lower clearances of the ring grooves depend on the intensity of the inertia force, it was concluded that the rate at which oil is transported to the combustion chamber increases with the engine speed.

The oil flows along the circumferential direction of the piston lands were first modeled taking into account the wavy pattern of the oil distribution. Calculation results based on measured oil distribution pattern showed that in most cases the effect of the non-uniformity of the oil layer was negligible. Accordingly, a simplified one-dimensional approach was proposed to compute the rate of oil removal resulting from the gas dragging action. The model suggested that the rate at which oil is dragged around the lands is proportional to the volumetric blow-by flow rate and thus increases with engine load. Furthermore, it was found that cycle after cycle the cumulative effect of the blow-by

gases carries the oil around the lands and through the gaps all the way to the upper skirt region. In fact, the dragging action of the blow-by flow appeared to be the only mechanism by which oil supplied to the upper ring pack can be recycled to the crankcase region. Experimental observation showed that in diesel and spark ignition engines running at high load, the presence of the ring gaps do not limit the rate of oil removal from the piston lands. On the other hand, it appeared that when the intake manifold pressure is lowered below about 500 mbar, the increasing reverse blow-by can create some non-negligible upward oil transport through the second and third ring gap. As a result the rate at which oil may be returned to the crankcase region is restricted. Accordingly, it was concluded that as the intake pressure is lowered in spark ignition engine, the rate at which oil is returned to the crankcase decreases because of lower blow-by flow rate and flow restriction at the ring gaps. Eventually, in closed throttle engine operation where the blow-by is negative, due to the absence of oil transport toward the crankcase, the total amount of oil accumulated on the piston lands was found to increase with time. Furthermore, engine tests showed that liquid oil could reach the top ring gap and flow to the combustion chamber in less than one minute.

Then, a comprehensive oil transport scheme showing the main path and mechanisms of the oil transport within the piston ring pack was proposed. It highlighted that the rate at which oil is lost to the combustion chamber results from the competition between the inertia driven oil transport, which carry oil across the land and through the ring grooves toward the top of the piston, and the gas-driven oil removal, which returns oil to the crankcase. Eventually, a region by region analysis of the piston ring pack indicated that there are three main locations where the rate of oil transport to the combustion chamber can be controlled:

1. The oil control ring which determines the oil supply to the third land and the part of the liner located between the scraper ring and the OCR.
2. The second ring and its groove where the rate of oil transport from the third to second land can be controlled by detailed geometrical features and/or second ring flutter.
3. The second land where the balance between the oil supply and the gas-driven oil removal determines the total amount of oil accumulated on the second land and thus the rate of oil supply to the top ring groove.

This work was the first comprehensive investigation of the mechanisms of oil transport in the piston ring pack of internal combustion engines. It provides an extensive analysis and description of the physical processes responsible for the oil flow through the piston ring/liner interface. It constitutes a major step in the development of analytical tools for oil consumption reduction. Additionally, this

thesis proposes a region by region oil transport analysis which has potential for providing practical guidance for the piston and ring designs.

REFERENCES

[1] Burnett, P.J., 1992, "Relationship Between Oil Consumption, Deposit Formation and Piston Ring Motion for Single-Cylinder Diesel Engines", SAE paper 920089.

[2] Munro, R., 1990, "Emissions Impossible – The Piston and Ring Support System", SAE paper 900590.

[3] Mayer, W.J., Lechman, D. C., and Hilden, D. L., 1980, " The Contribution of Engine Oil to Diesel Particulate Emissions", SAE 800256.

[4] Schneider, E. W., Sell, J. A., Siekkinen, J., W., 1998, "The Contribution of Lubricating Oil to Exhaust Deposits and Exhaust Particulates from Gasoline Engines – A Radiotracer Medthod", SAE paper 982580.

[5] Drury, C., and Withehouse, S., 1994, "The Effect of Lubricant Phosphorus Level on Exhaust Emissions in a Field Trial of Gasoline Engine Vehicles", SAE Paper 940233.

[6] Ueda, F., Sugiyama, S., Arimura, K., Hamagushi, K., Akiama, K., "Engine Oil Additive Effects on Deactivation of Monolithic Three-Way Catalysts and Oxygen Sensors", SAE Paper 940746.

[7] Hill, S. H., Sytsma, S, J., 1991, " A System Approach to Oil Consumption", SAE Paper 910743.

[8] Takiguchi, M. et al., 1999, "Effect of Piston Ring Tension on Oil Consumption and Piston Friction in Diesel Engines", ASME Vol.32-3.

[9] Nakada, M., 1993, "Piston and Piston Ring Tribology and Fuel Economy", Proceedings of International Tribology Conference, Yokohama, 1993.

[10] Heywood, J. B., 1988, *Internal Combustion Engines Fundamentals*, McGraw-Hill.

[11] Sasaki, M. et al., 1997, " The Effect of EGR on Diesel Engine Oil and its Countermeasures", SAE Paper 971695.

[12] Tamai, G., 1995, "Experimental Study of Engine oil Film Thickness Dependence on Liner Location, Oil Properties, and Operating Conditions", M.S. Thesis, Department of Mechanical Engineering, MIT, September 1995.

[13] Noordzij, L. B., 1996, " Measurement and Analysis of Piston Inter-Ring Pressures and Oil Film Thickness and their Effects on Engine Oil Consumption", M.S. Thesis, Department of Mechanical Engineering, MIT, June 1996.

[14] Tian, T., 1997, "Modeling the Performance of the Piston Ring-Pack in Internal Combustion Engines", Ph.D. Thesis, Department of Mechanical Engineering , MIT, June 1997.

[15] Yoshida, H., Kusama, K., Kobayashi, H., 1991, "Diesel Engine oil Consumption Depending on Piston Ring Design", SAE Paper 911699.

[16] Fesser, R. C., 1988, " Small Engine Piston Ring Design for Reduced Oil Consumption", SAE Paper 881372.

[17] Tian, T., Rabute, R., Wong, V. W., Heywood, J. B., 1997, "Effects of Piston-Ring Dynamics on Ring/Groove Wear and Oil Consumption in a Diesel Engine.

[18] Rabute, R., Tian T., " Challenges Involved in Piston Top Ring Designs for Modern SI Engines", Transactions of ASME, Journal of Engineering for Gas Turbine and Power, April 2001, Vol. 123.

[19] Yoshida, H., et al. 1996. "Effect of Second Land Shape on Oil Consumption", ICE-Vol. 27-2, October 1996 ASME Fall Technical Conference, Volume2.

[20] Schneider, E. W., Blossfeld, D. H., Lechman, D. C., Hill, R., Reising, R., Brevick, J. E., 1993, "Effect of Cylinder Out-of-Roundness on Piston Ring Rotation and Engine Oil Consumption", SAE Paper 930716

[21] Ishizuki, Y., Sato, F., Takase, K., 1981, "Effect of Cylinder Liner Wear on Oil Consumption in Heavy Duty Diesel Engines", SAE Paper 810931.

[22] Dowson, D., Economou, P. N., Ruddy, B. L., Strachan, P. J., Baker, A. J. S., 1979, "Piston Ring Lubrication – Part II. Theoretical Analysis of a Single Ring and a Complete Ring Pack", *Energy Conservation Through Fluid Film Lubrication Technology: Frontiers in Research and Design*, Winter Annual Meeting of ASME, pp. 23-52.

[23] Ting, L. L., Mayer, J. E., 1974, "Piston Ring Lubrication and Cylinder Bore Wear Analysis, Part I – Theory", ASME Transaction – Journal of Lubrication Technology, Vol. 96, pp 305.

[24] Rhode, S. M., 1980, "A Mixed Friction Model for Dynamically Loaded Contacts with Application to Piston Ring Lubrication", Proc. Of the 7th Leeds-Lyon Symposium on Tribology, Westbury House, 1980, p262.

[25] Tian, T., Wong, W. V., Heywood, J. B., 1998, " Modeling the Dynamics and Lubrication of Three Piece Oil Control Ring in Internal Combustion Engines", SAE Paper 982657.

[26] Tian, T., Wong, V. W., Heywood, J. B., 1996, "A Piston Ring-Pack Film-Thickness and Friction Model for Multigrade Oil and Rough Surfaces", SAE Paper 962032.

[27] Tian, T., Wong, V. W., 2000, " Modeling the Lubrication, Dynamics, And Effect of Piston Tilt of Twin-Land Oil Control Rings in Internal Combustion Engines", Transactions of ASME, Journal of Engineering for Gas Turbines and Power, January 2000, Vol. 122, pp 119.

[28] Artzner, D., "Investigation of Oil Consumption Mechanisms in a Spark-Ignition Engine", M.S. Thesis, Department of Mechanical Engineering, MIT, May 1996.

[29] Keribar, R., Dursunkaya, Z., Flemming, M.F., 1991, "An Integrated Model of Ring Pack Performance", Transactions of ASME, Journal of Engineering for GAas Turbines and power, Vol. 113, pp 382-389.

[30] Dursunkaya, Z., Keribar, R., Richardson, D., 1993, "Experimental and Numerical Investigation of Inter-Ring Gas Pressures and Blow-by in a Diesel Engine", SAE Paper 930792.

[31] Ariga, S., 1996, " Observation of Transient Oil Consumption with In-Cylinder Variables", SAE Paper 961910.

[32] Zelenka, P., Kriegler, W., Herzog, P. L., Cartellieri, 1990, "Ways Toward the Clean Heavy Duty Diesel", SAE Paper 900602.

[33] Tian, T., Noordzig, B. L., Wong, V. W., Heywood, J. B., 1996, " Modeling Piston-Ring Dynamics, Blow-by, and Ring-Twist Effects", ICE-Vol. 27-2, October 1996 ASME Fall Technical Conference, Volume 2, pp 67-80, Fairborn, Ohio.

[34] Hoult, D. P. et al., 1988, "Calibration of Laser Fluorescence Measurements of Lubricant Film Thickness in Engines", SAP Paper 881587.

[35] Hoult, D. P., Takigushi, M., 1991, "Calibration of Laser Fluorescence Technique Compared with Quantum Theory", STLE Tribology Transactions, Volume 34 (1991), 3, pp440-444.

[36] Shaw, B. T., Hoult, D. P., Wong, V. W., 1992, " Development of engine Lubricant Film Thickness Diagnostics Using Fiber Optics and Laser Fluorescence", SAE 920651.

[37] Casey, S., 1998, "Analysis of lubricant Film Thickness and distribution along the Piston/Liner Interface in a Reciprocating Engine", Department of Mechanical Engineering, MIT.

[38] Takigushi, M., Nakayama, K., Furuhama, S., Yoshida, H., 1998, "Variation of Piston Ring Oil Film Thickness in an Internal Combustion Engine", SAE Paper 980563.

[39] Richardson, D. E., Borman, G. B., 1991, "Using Fiber Optics and Laser Fluorescence for Measuring Thin Oil Films with Application to Engines", SAE Paper 912388.

[40] Arcoumenis, C. et al., 1998, " Measurements of Lubricants Film Thickness in the Cylinder of a Firing Diesel Engine Using LIF", SAE Paper 982435.

[41] Nakayama, K. et al., 1998. " Effect of Oil Ring Geometry on Oil Film Thickness in the Circumferential Direction of the Cylinder", SAE Paper 982578.

[42] Inagaki, H., Saito, A., Murakami, M., and Konomi, T., 1995, " Development of Two Dimensional Oil Film Thickness Distribution Measuring System," SAE Paper 952346.

[43] Takiguchi, M., Nakayama, K., Furuhama, S., Yoshida, H., 1998, "Variation of Piston ring Oil Film Thickness in an Internal Combustion Engine – Comparison between Thrust and Anti-Thrust Sides", SAE Paper 980563.

[44] Saito, K., Igashira, T., Nakada, M., 1989, " Analysis of Oil Consumption by Observing Oil Behavior Around the Piston Ring Using a Glass Cylinder Engine", SAE Paper 892107.

[45] Mulgrave, P., 1997, "Development of a Laser Induced Fluorescence System for Measuring Oil Film Thickness in Two Dimensions in a Reciprocating Engine", M.S. Thesis, Department of Mechanical Engineering, MIT.

[46] Haugland, R. P., 1999, "Handbook of Fluorescent Probes and Research Chemical", Seventh Edition, Molecular Probes.

[47] Guilbault, G. G., 1990, "Practical fluorescence", Second Edition, Marcel Dekker, Inc., New-York.

[48] Saeki, S., Hart, D. P., 2001, "Investigation on YAG(532) Laser Dyes for Oil Film Thickness and Temperature Measurement", Proceeding of PSFVIP-3, March 2001, Maui. Hawaii, USA, F3096.

[49] Schafer, F. P., 1973, "Topics in applied physics Volume 1", "Dye Lasers", Springer-Verlag New-York/Heidelberg/Berlin 1973, pp 20 and pp 147.

[50] Duarte, F. J., Hillman, L. W., 1990, "Dye Laser Principles with applicationa", Quantum Electronics-Principles and Applications, Academic Press.

[51] Malhe, "Mini Piston Manual", Issue 1995, Mahle Gmbh, D-70369 Stuttgart.

[52] Chang, H., S., Wayte, R., Spikes, H. A., 1993, "Measurement of Piston Ring and Land Temperatures in a Firing Engine Using Infrared", Tribology Transactions, Vol. 36 (1993), 1, pp 104-112.

[53] Coppeta, J., Rogers, C., 1998, "Dual Emission Laser Induced Fluorescence for Direct Planar Scalar Behavior Measurements", Experiments in Fluids, Vol. 25, Issue 1, pp 1-15.

[54] Hidrovo, C. H., Hart, D. P., 2000, "Dual Emission Laser Induced Fluorescence Technique (DELIF) for Oil Film Thickness and Temperature Measurement", Proceeding of ASME FEDSM'00, ASME 2000 Fluids Engineering Division Summer Meeting June 2000.

[55] Sanda, S., Inagaki, H., 1997, "Simultaneous Measurement of a Piston oil Film Thickness and a Temperature Using a Dual Fluorescence Method", World Tribology Congress, London 1997.

[56] Min, B. S., Kim, J. S., Oh, D. Y., Choi, J. K., Jin, J. H., 1998, "Dynamic Characteristics of Oil Consumption-Relationship Between the Instantaneous Oil Consumption and the Location of Piston Ring Gap", SAE Paper 982442.

[57] Kataoka, I., Ishii, M., Nakayama, A., 2000, "Entrainment and deposition rates of droplets in annular two-phase flow", International Journal of Heat and mass Transfer, Vol. 43, pp 1573-1589.

[58] Dallman, J. C., Laurinat, J. E., Hanratty, T. J., 1984, " Entrainment for horizontal annular gas-liquid flow", International Journal of Multiphase Flow, Vol. 10 (6), pp 677-690.

[59] Hewitt, G. F., Govan, H., 1990, "Phenomenological modeling of non-equilibrium flows with phase change", International of Heat and Mass Transfer, Vol. 33 (2), pp 229-242.

[60] Nigmatulin, R. I., Nigmatulin, B. I., Khodzhaev, YA. D., Kroshilin, V. E., 1996, " Entrainment and Deposition Rates in a Dispersed-Film Flow", International Journal of Multiphase Flow, Vol. 22 (1), pp 19-30.

[61] Ishii, M., Grolmes, M. A., 1975, "Inception Criteria for Droplet Entrainment in two-Phase Concurrent Film Flow", AIChe Journal, Vol. 21.

[62] McNally, C., 2000, " Development of a Numerical Model of Piston Secondary Motion for Internal Combustion Engines", M.S. Thesis, Department of Mechanical Engineering, MIT.

[63] Yilmaz, E., Thirouard. B., Tian, T., Wong, V., Heywood, J. B., Lee, N., 2001, "Analysis of Oil Consumption Behavior during Ramp Transients in a Production SI Engine," To be Presented in 2001 SAE Fall Fuel and Lubricant Meeting and Exposition, San Antonio, TX, September 2001.

ANNEX 1

Function $f(h,x,\lambda 1)$ for the computation of the fluorescence mission of dye 2 resulting from dye 1 excitation:

$$f(h,x,\lambda_1) = e^{-\sigma \cdot x} \cdot \left(\frac{-2 \cdot \sigma'}{\sigma^2 - \sigma'^2} \right) + \frac{1}{\sigma - \sigma'} \cdot e^{-\sigma' \cdot x} - \frac{1}{\sigma + \sigma'} e^{-(\sigma+\sigma') \cdot h + \sigma' \cdot x}$$

With: $\sigma = C_{dye1} \cdot \varepsilon_{d\ ye1}(\lambda_{laser}) + C_{dye2} \cdot \varepsilon_{d\ ye2}(\lambda_{laser}) + _{oil}$

and $\sigma_{g1} = \alpha \cdot_2 \cdot C_{dye2} \cdot \varepsilon_{dye2}(\lambda_1) + \sigma_{oil}$

ANNEX 2

Tested Engine Configurations

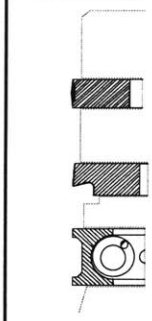
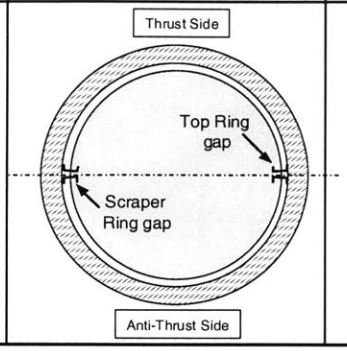
PSA Single-Cylinder Engine					
Ring Types	Ring Positions	Speed (RPM)	Intake Pressure (mbar)	Anti-Thrust Side Observations	Thrust Side Observations
		2500	300	1	1
			500	1	1
			700	1	1
			1000	1	1
		3500	300	5	7
			500	2	6
			700	1	2
		4500	300	1	1
			500	1	1
			700	1	1

Table 2.2a

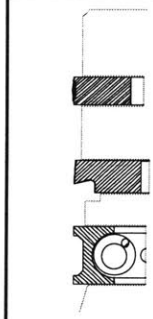
PSA Single-Cylinder Engine					
Ring Types	Ring Positions	Speed (RPM)	Intake Pressure (mbar)	Anti-Thrust Side Observations	Thrust Side Observations
	NON-PINNED RINGS	2500	300	2	
			500	2	
			700	1	
			1000		
		3500	300	1	
			500	1	
			700	1	
		4500	300	2	
			500		
			700		

Table 2.2b

Table 2.2 – Description of the engine configurations and running conditions tested in the PSA single-cylinder engine.

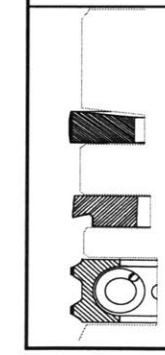
KUBOTA Engine				
Ring Types	Ring Positions	Speed (RPM)	Load (N.m)	Anti-Thrust Side Observations
	NON-PINNED RINGS	1200	0.1	1
			5	1
			10	1
		2000	0.1	1
			5	1
			10	1
		2800	0.1	1
			5	1
			10	1

Table 2.3a.

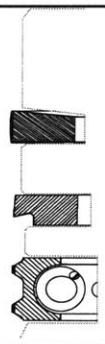
KUBOTA Engine				
Ring Types	Ring Positions	Speed (RPM)	Load (N.m)	Anti-Thrust Side Observations
 Low Tension 30 N	NON-PINNED RINGS	1200	0.1	1
			5	1
			10	1
		2000	0.1	1
			5	1
			10	1
		2800	0.1	1
			5	1
			10	1

Table 2.3b.

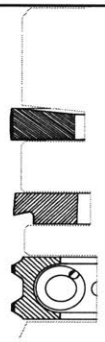
KUBOTA Engine				
Ring Types	Ring Positions	Speed (RPM)	Load (N.m)	Anti-Thrust Side Observations
 High Tension 58 N	NON-PINNED RINGS	1200	0.1	1
			5	1
			10	1
		2000	0.1	1
			5	1
			10	1
		2800	0.1	1
			5	1
			10	1

Table 2.3c.

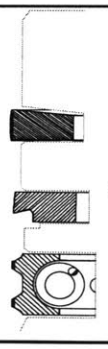
KUBOTA Engine				
Ring Types	Ring Positions	Speed (RPM)	Load (N.m)	Anti-Thrust Side Observations
 Third Land Cut-off Standart Tension 45 N	NON-PINNED RINGS	1200	0.1	1
			5	1
			10	1
		2000	0.1	1
			5	1
			10	1
		2800	0.1	1
			5	1
			10	1

Table 2.3d.

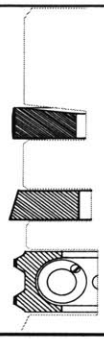
KUBOTA Engine				
Ring Types	Ring Positions	Speed (RPM)	Load (N.m)	Anti-Thrust Side Observations
 No Hook High Tension 45 N	NON-PINNED RINGS	1200	0.1	1
			5	1
			10	1
		2000	0.1	1
			5	1
			10	1
		2800	0.1	1
			5	1
			10	1

Table 2.3e.

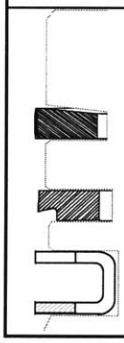
KUBOTA Engine				
Ring Types	Ring Positions	Speed (RPM)	Load (N.m)	Anti-Thrust Side Observations
 U-Flex	NON-PINNED RINGS	1200	0.1	1
			5	1
			10	1
		2000	0.1	1
			5	1
			10	1
		2800	0.1	1
			5	1
			10	1

Table 2.3f.

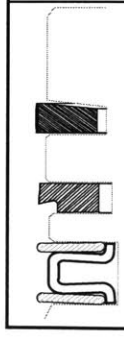
KUBOTA Engine				
Ring Types	Ring Positions	Speed (RPM)	Load (N.m)	Anti-Thrust Side Observations
 ıree-piece	NON-PINNED RINGS	1200	0.1	1
			5	1
			10	1
		2000	0.1	1
			5	1
			10	1
		2800	0.1	1
			5	1
			10	1

Table 2.3g.

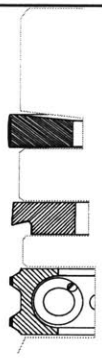
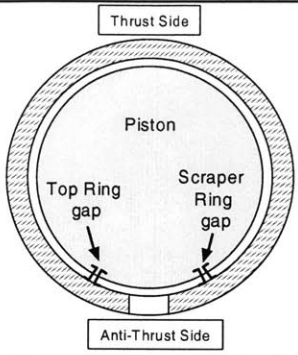
KUBOTA Engine				
Ring Types	Ring Positions	Speed (RPM)	Load (N.m)	Anti-Thrust Side Observations
		1200	0.1	1
			5	1
			10	1
		2000	0.1	1
			5	1
			10	1
		2800	0.1	1
			5	1
			10	1

Table 2.3h.

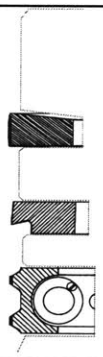
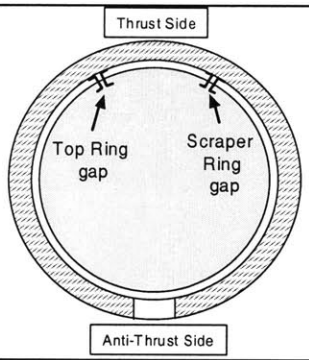
KUBOTA Engine				
Ring Types	Ring Positions	Speed (RPM)	Load (N.m)	Anti-Thrust Side Observations
		1200	0.1	1
			5	1
			10	1
		2000	0.1	1
			5	1
			10	1
		2800	0.1	1
			5	1
			10	1

Table 2.3i.

Table 2.3 – Description of the engine configurations and running conditions tested in the Kubota single-cylinder engine.